Development of a Mathematical Model for Compressible Liquid Transients and Its Numerical Implementation

A thesis submitted

in partial fulfillment for the award of the degree of

Doctor of Philosophy

by

Jishnu Chandran R.

Department of Aerospace Engineering

Indian Institute of Space Science and Technology

Thiruvananthapuram, India

August 2021

Certificate

This is to certify that the thesis titled ***Development of a Mathematical Model for Compressible Liquid Transients and Its Numerical Implementation*** submitted by **Jishnu Chandran R.**, to the Indian Institute of Space Science and Technology, Thiruvananthapuram, in partial fulfillment for the award of the degree of **Doctor of Philosophy** is a bona fide record of the original work carried out by him under my supervision. The contents of this thesis, in full or in parts, have not been submitted to any other Institute or University for the award of any degree or diploma.

Dr. A. Salih
Professor
Dept. of Aerospace Engineering

Dr. Aravind Vaidyanathan
Professor & Head
Dept. of Aerospace Engineering

Place: Thiruvananthapuram
Date: August 2021

Declaration

I declare that this thesis titled ***Development of a Mathematical Model for Compressible Liquid Transients and Its Numerical Implementation*** submitted in partial fulfillment for the award of the degree of **Doctor of Philosophy** is a record of the original work carried out by me under the supervision of **Dr. A. Salih**, and has not formed the basis for the award of any degree, diploma, associateship, fellowship, or other titles in this or any other Institution or University of higher learning. In keeping with the ethical practice in reporting scientific information, due acknowledgments have been made wherever the findings of others have been cited.

Place: Thiruvananthapuram
Date: August 2021

Jishnu Chandran R.
(SC13D016)

"Real knowledge is to know the extent of one's ignorance."

-Confucius

Acknowledgements

I would first of all like to express my sincere gratitude to my research supervisor Dr. A Salih., for making the PhD experience intellectually challenging as well as enjoyable. He has been a consistent source of inspiration for all these years and I am highly indebted to his exceptional teaching and immense patience. I would also like to acknowledge my deep gratitude to my Doctoral Committee members Dr. T Jayachandran, Dr. Raju K. George, Dr. Aravind Vaidyanathan, and Dr. Deepu M, for their valuable suggestions and encouragement. It was a great experience for me to have discussions with such eminent personalities. I wish to thank our department HOD, Dr. Aravind Vaidyanathan for his help and support. I would like to thank Dr. V. K. Dadhwal, Director, IIST, for providing me an opportunity to be a part of this institute. I also thank all the faculty members of IIST, especially Dr. Raju K George, Dean (R&D), Dr. Kuruvilla Joseph, Dean (Student Activities), and Dr. Lekshmi V Nair (Head, Department of Humanities), for their timely advices, support, and goodwill. I would like to thank the DOS for the financial support during my research period. I wholeheartedly thank the faculties and staff of the department, and the library and administrative staff, for their timely help, love and support.

I consider myself lucky that I met and became friends with a bunch of really wonderful people at the institute. I would like to specially mention the names of Micky Baisil, Deepak M, Rajesh Rajagopal, Parvathy S P, Risha Raju, Arun Govind Neelan, Sachin, Anuja, Dhanesh, Sarath, Ajin, and Aravind. I thank them all for their love and care. It would be a huge injustice if I don't acknowledge the perseverance shown by my beloved parents, brother, and in-laws when I faced difficulties and delays during my research. I thank them for their unrelenting encouragement that helped me sustain my interest in research. Finally, I thank my wife Rashmi, the one who motivated me whenever I was low in confidence, who stood with me in all my success and failures with unconditional love and support. Her contributions are beyond words. I close the acknowledgement by remembering all my Gurus, whose blessings have helped me reach this far.

'Loka Samastha Sukhino Bhavanthu'

Jishnu Chandran R.

Abstract

This research work report the development and implementation of a mathematical model for the simulation of hydraulic transients in compressible liquids. The work discusses the importance of understanding the hydraulic transients for different theoretical and practical flow situations. The significance of this study is derived from the need for accurate fluid property estimates in liquid transient simulations as there are *unaccounted* liquid compressibility effects and improper pressure damping techniques affecting the reliability of computational models for numerical simulation.

This research work presents a new equation of state (modified NASG) for the compressible modelling of liquid water over wider range of pressures. The proposed compressible model could be applied in theoretical flow modelling and computational flow simulations of the liquid. Theoretical implementation of the model has been demonstrated through the development of an analytical solution to the water shock tube problem. The same problem has been computationally simulated, and the corresponding numerical results are compared and validated against the analytical solution. The research further focuses on improving the simulation accuracy of valve-induced hydraulic surges, a commonly observed liquid transient. Relevant valve-closure experimental cases from the literature are selected for the study. A suitable mathematical model is chosen for simulation of these transients, which is further upgraded with the compressible model. Results from simulation experiments suggested the need for improvement in friction models to achieve better accuracy. In this context, we introduced the concept of adaptive damping by defining 'variable pressure wave damping coefficients' (VPDCs) for unsteady friction formulation. This parameter, VPDC, adds flexibility to the computational solver by providing dissipation to the waves based on prevailing flow conditions. Numerical simulation of hydraulic transients at upstream and downstream locations of closing valves using unsteady friction model with VPDC shows good improvement in the computational accuracy. The mathematical model that accounts the liquid-compressibility effects and equipped with the adaptive damping capability is used to study the transient pressure difference developed across fast-closing valves.

The modified NASG equation of state for water could be used for high accuracy liquid compressibility modelling and for the estimation of wave speed over varied range of applications. The research work presents analytical solution to the water shock tube problem as

a simple yet powerful benchmark solution for testing computational algorithms developed for the simulation of compressible liquid flows. The VPDC definition presented in the work for imparting adaptive damping capability could be applied to improve the accuracy and numerical stability of computational solvers for the simulation of highly transient flows. The research also brings out and explains the variations in surge characteristics based on the location in a system with respective to the closing-valve. Numerical experiments performed as part of the research work also explored the impact of valve closure duration on the pressure difference across closing valves during valve-induced surges.

Contents

List of Figures

List of Tables

Abbreviations

AFT	Applied Flow Technology
AUSM	Advection Upstream Splitting Method
CFL	Courant–Friedrichs–Lewy
EOS	Equation of State
FDS	Flux Difference Splitting
FVS	Flux Vector Splitting
HDPE	High density poly ethylene
HLL	Harten Lax Van Leer
HLLC	Harten Lax Van Leer Contact
HLLE	Harten Lax Van Leer Einfeldt
HPLC	High-performance liquid chromatography
IAPWS	International Association for the Properties of Water and Steam
IBVP	Initial Boundary Value Problem
MC	Monotonized Central
MM	Min Mod
MOC	Method of characteristics
MUSCL	Monotonic Upstream-centred Scheme for Conservation Laws
NASG	Noble-Abel Stiffened Gas
NIST	National Institute of Standards and Technology
PTS	Pressurized thermal shock
PWR	Pressurized water nuclear reactors
SCM	Split-Coefficient Matrix
TPWH	two-phase water hammer
TVD	Total Variation Diminishing
UHPLC	Ultra high-performance liquid chromatography
VA	van Albada
VPDC	Variable Pressure wave Damping Coefficient

Nomenclature

a	Signal propgation speed
a_0	Speed of sound at standard state
A	Coefficient matrix for transient terms
b	Covolume
B	Coefficient matrix for convective terms
c	Speed of sound in medium
$\bar{c}$	Stiffened Speed of sound
C	Jacobian matrix
C_v	Isochoric specific heat
C_p	Isobaric specific heat
d	Diameter
e	Specific total energy
E	Young's Modulus
f	Darcy friction factor
F	Flux vector
k	Constant pressure wave damping coefficient
k_v	Variable pressure wave damping coefficient
K_V	Flow coefficient of valve in metric units
k_{vd}	Variable pressure wave damping coefficient for downstream surge
k_{vu}	Variable pressure wave damping coefficient for upstream surge
K_0	Constant parameter in Tait equation
L	Length
m_1	Tunable parameter for overall dissipation
m_2	Tunable parameter for dissipating trend correction
P	Pressure
$\bar{P}$	Stiffened Pressure
P_0	Pressure at standard state

P_∞	Stiffening constant parameter
$\triangle P_{max}$	Maximum possible pressure fluctuation
$\triangle P_{RLF}$	Relative local fluctuation of pressure
q	Heat bond of liquid water
R_W	Parameter for liquid similar to gas constant
Re	Reynolds Number
s	Pipe thickness
S	Source vector
T	Temperature
T_0	Reference temperature
T_C	characteristic time period
T_V	Actual duration of valve closure
t	Temporal co-ordinate
u	Axial component of velocity
u_S	Shock speed
U	Conservative variable vector
V	Velocity
v	Specific volume
W	Characteristic variable vector
x	Spatial co-ordinate
x_0	Initial location of diaphragm
Z	Eigenvector matrix

Greek symbols

α	Void fraction
ρ	Density
$\bar{\rho}$	Stiffened Density
ρ_0	Density at standard state temperature
ε	Specific internal energy
ε	Specific internal energy at reference temperature
γ	Ratio of specific heats
Γ_A	mass transfer due to air release
Γ_v	mass transfer due to vaporization/condensation
ν	Poisson's ratio
θ	Density exponent in Tait equation
τ	Shear stress due to skin friction

$\wedge$	Matrix of Eigen values
Δ	Operator showing difference in a quantity
Subscripts	
0	Standard state
1	Zone 1
2	Zone 2
A	Zone boundary A
B	Zone boundary B
C	Zone boundary C
D	Zone boundary D
E	Zone E
G	Gas
i	Index for Spatial grid
L	Liquid
L	Left Zone
M	Mixture
R	Right Zone
Superscripts	
$+$	Positive values
$-$	Negative values
-1	Matrix inverse
n	Index for time step
s	Steady condition
us	Unsteady condition

Chapter 1

Introduction

Flow of liquids are generally treated as incompressible flows in which liquid density is assumed to be constant. However, there are several flow situations where compressibility effects in liquids become important and hence the variation of density cannot be ignored when the governing equations for fluid flow are solved. Unsteady flow transients in long hydraulic pipelines, sudden closure of valve in a piping system, and liquid flows at extremely high pressures are some of the examples where the compressibility effects of liquids cannot be ignored. One of the major difficulties in modelling liquid as compressible fluid is the lack of accurate compressible models, particularly the *equation of state* that relate various thermodynamic properties of liquids. Another issue is that the inability of friction models to adapt to dissipative requirements of the flow. A reasonable compressible flow model should be able to estimate transient variations of liquid density and speed of sound in the liquid medium in an accurate manner.

This work intends to develop a mathematical model that could address most of the identified drawbacks in the currently available models for the simulation of compressible liquid transients. We also make a detailed study of the applicability and effectiveness of this compressible model in simulating flow of liquid with compressible effects. Further, this research also aims to develop a friction model capable of achieving adaptive dissipation. Finally, we will present a complete model for the simulation of practical problems involving compressible liquid flow transients.

1.1 Motivation

A majority of liquid transients that we study are generated by practical flow situations like sudden changes in the flow area, closure of valves, etc. in fluid flow and transfer processes. We also come across theoretical studies of the liquid transients in systems like

hydrodynamic shock tubes. Most of these scenarios involve high values of fluid pressure and transiently varying signal propagation speed. In the simulation of liquid flow transients, the variation of fluid pressure with time at different strategic locations in the system needs to be modeled with high accuracy. This is because the transient pressure data is very crucial to the design and safety considerations of the system. Some of the important limitations, we observed, in the mathematical models for simulation of such flows are the lack of adequate compressible models for liquids and the inability of friction models to adapt to the dissipation requirements based on flow physics.

An adequate compressible model for liquids should be capable of capturing density variations accurately during flow transients by relating density to fluid pressure and temperature. Such a compressible model should also be able to calculate transiently varying signal propagation speed by using locally updated fluid properties at every moment. Similarly, a friction model that can adapt to drastically varying flow situations could lead to improved dissipation mechanisms and accurate numerical prediction of pressure surges.

1.2 Objectives

The main objectives of this research work are listed below:

- To develop an accurate compressible model for liquid water for reliable application to a wide range of pressure and temperature.
- To develop an analytical solution for a suitable theoretical problem involving compressibility effects in liquids to establish the appropriateness of the model for related class of problems.
- To demonstrate the relevance of analytical solution developed as a benchmark solution for the evaluation of computational solvers for compressible liquid flows.
- To apply the proposed compressible model for simulation of practically relevant liquid transients such as problems involving sudden closure of valves.
- To develop a 'variable pressure wave damping coefficient' (VPDC) that could enable the dissipation mechanism of unsteady friction models to adapt to the flow requirements of a liquid transient.
- To apply adaptive dissipation enabled friction model for the simulation of valve closure problems and to investigate associated improvements in the model.

- To present an adequate mathematical model for the simulation of liquid transients with accurate modelling of liquid compressibility effects and adaptive damping capabilities for friction model.

1.3 Scope

This research presents an accurate compressible model for liquid water that can be applied in theoretical and computational models for the simulation of various flow conditions of liquid. The proposed compressible model provides accurate fluid property estimates for high-pressure conditions compared to available liquid compressibility models. The accuracy of the proposed equation of state (EOS) for water is demonstrated for a wide range of pressure and temperature to ensure reliable application in modelling flow cases. The availability of an associated speed of sound relation with the EOS helps in accounting for locally and transiently varying signal propagation speed in the system. This capability to model varying signal speed could improve the performance of 'method of characteristics' based flow solvers to which the model is incorporated. The exact analytical solution for water shock tube problem developed as part of this research made it a 'simple and easy to use' test case. Hence, the water shock tube problem together with its exact solution can be used as a benchmark problem for validation of compressible liquid flow solvers. The analytical solution procedure presented here can also be utilised as a template that could be extended to any other liquid, subject to the availability of corresponding equation of state for liquid and the relation for speed of sound.

The variable pressure wave damping coefficient (VPDC) introduced and presented in this research is also a potential area for future research. The studies demonstrate capability of the proposed friction model with VPDC to adapt to varying dissipation requirements of flow. This adaptive dissipation capability could be integrated into many existing mathematical models to generate a class of highly stable computational flow solvers. The resulting solvers would then be capable of modelling highly transient flows involving large property gradients. Different variants of VPDC could be explored and incorporated for improving unsteady friction models.

Application of the compressible liquid model and the VPDC based adaptive friction models could also be extended to multidimensional and multi-fluid cases in a straightforward manner. For example, developing accurate compressible models for industrial liquids like crude oils is very important for designing of transfer pipelines and associated structures.

1.4 Structure of the Thesis

The thesis is arranged in eight chapters closely related to the objectives described above.

In chapter 2, survey of literature is presented. Various high-pressure applications and flow situations involving liquid compressibility effects are presented in this chapter along with information on different compressible models available for liquid water. A section of the chapter explains importance of shock tube studies in compressible flows with special mention to the Sod's problem. Subsequently we discusses various studies and applications related to liquid shocks. Some select Riemann solvers and flux methods are also discussed with the help of related literature. A review of various unsteady friction models from the literature is also presented in this chapter. The final section provides a review of experimental and computational studies on valve-induced hydraulic transients.

In chapter 3, a new equation of state for the compressible modelling liquid water is presented. Through a detailed comparative study with NIST data, accuracy of the proposed EOS over a wide range of pressure and temperature is demonstrated. The new EOS is also compared against a few of the existing EOS for liquid water.

In chapter 4, details on the development of an analytical solution to the water shock tube problem are provided along with the complete solution procedure employed. The solution profiles obtained for varied configurations of the problem are also presented in this chapter.

In chapter 5, the numerical simulation of the water shock tube problem by considering fluid compressibility effects is explained. The numerical results for the problem are further validated against the already developed exact solution to the problem. This chapter demonstrates the water shock tube problem as a new benchmark test case for the family of compressible liquid flows.

In chapter 6, the procedure for hydraulic surge estimation for non-cavitating flow situations using a compressible-liquid model is presented. The latter half of this chapter introduces the concept of an adaptive-damping technique for unsteady friction models and demonstrates its application to selected flow cases.

In chapter 7, implementation of the adaptive-damping technique in numerically modelling different valve-induced hydraulic surge experiments is presented. This chapter also provides a strategy for numerical estimation of transiently varying pressure difference across a fast-closing valve. The impact of valve closure duration on the maximum pressure difference developed across a closing valve is also outlined in this chapter. The major conclusions drawn in this research work are summarised in chapter 8.

Chapter 2

Review of Literature

2.1 Introduction

In this chapter we present information gathered from the literature in the area of flow transients in compressible liquids. Section 2.2 presents details of various applications where liquids are exposed to very high pressures. The subsequent section, section 2.3 provides information on the compressible modelling of liquids using different models such as equations of state. This section gives importance to models and equation of state related to water, due to the liquid's high relevance in industrial and non-industrial applications. Section 2.4 outlines the importance and wide range of applications of shock tube problems in the study of compressible flows. A brief explanation of gas shock tube problem and associated mathematical model is also available in this section. Section 2.5 lists various studies and applications associated with events like shock generation, propagation, interaction etc., observed independently or together in different liquids. Details of different Riemann solvers and flux methods are presented with the help of relevant literature in Section 2.6. The concept of MUSCL (Monotonic Upstream-centred Scheme for Conservation Laws) method and details on the MUSCL type slope-limited solvers are presented in Section 2.7.

Section 2.8 summarises different friction models used in the modelling of liquid transients, with reference to some of the notable contributions in this field. The last section of the chapter, Section 2.9 reviews some important contributions and studies on valve-induced hydraulic surges.

2.2 High-Pressure Applications of Liquids

Pressure is an important thermodynamic variable because of its strong relation with other fluid properties such as temperature and density. The variables in a flow system such as flow velocity and speed of sound in the fluid medium are also closely related to existing pressure in that system. In hydrodynamic studies, it is a common observation that liquid density and speed of sound in the liquid medium are treated as constants with respect to varying fluid pressure. This is because these parameters are usually weak functions of fluid pressure and variations in their magnitude with changing pressure are negligibly small. However, there are flow situations where liquid density and signal speed in the liquid medium exhibit appreciable variation with pressure. Most of such scenarios are associated with high-pressure applications of liquids. In such applications, liquid density and sound celerity vary over a wider scale, and these variations need to be accounted for understanding the underlying flow physics better. Some of the flow scenarios and applications where liquids are exposed to very high pressures are briefly explained here.

High-performance liquid chromatography (HPLC) is an indispensable chemical separation, identification and quantification technique which is used for the investigation of classes of compounds and individual substances in a mixture. Conventional HPLC serves up to pressures of around 350 bar. The more recent technology of Ultra high-pressure liquid chromatography (UHPLC) operates at pressures up to 1000 bar. The basic concepts on HPLC and UHPLC are available in the works [1, 2] and the biochemical and biomedical applications of these processes are outlined in [3]. For a material with two distinct liquid phases of different densities, the experimental observation of liquid-liquid transition is very difficult. To observe the diffuse scattering from both liquid phases in such transitions, extremely high pressure conditions are required [4]. There are numerous studies [5, 6] on achieving metallic state in hydrogen by compressing it to extreme pressure conditions. The work by Weir et al. [7] reports on shock experiments where liquid hydrogen is exposed to pressures of the order of 140 GPa. In highly lubricated contacts as observed in rolling element bearings, gears, cams, constant velocity joints, etc., situations arise where the lubricants are exposed to extreme variations in pressure about 1 GPa and above [8].

There are numerous studies on the use of ionic liquids as operating fluids in high-pressure applications [9, 10] and on their behaviour under such high pressures [11, 12]. The ionic liquids are preferred due to their relatively low compressibility, which is desirable for high-pressure applications. A research on the behaviour of various liquids and solutions at high pressure is presented by Boucher and Murrell in [13]. Information on the physical

and chemical behaviour of various high-pressure liquids and solutions and the details of their thermo-physical properties, relative permittivity etc., were discussed by Taniguchi et al. [14]. More high-pressure studies on different liquids are available in the work by Mao et al. [15].

The existence of liquid water under extreme conditions and associated properties of the liquid are significant in many industrial applications. For instance, liquid water is compressed to extreme pressures in water jet cutting where the pressurized fluid even slices through metals. The U.S. patents [16, 17] reports maximum cutting fluid pressures of the order of 1.5 GPa in water jet cutters. A review of compressible liquid impact on solid surfaces is provided by Lesser and Field in [18]. The impinging jet of water used for quenching process as reported by Ramezanzadeh et al. in [19] also uses liquid water under very high pressure. The underwater explosion is another domain where water gets compressed substantially and associated density variation in the fluid is significant. Study on the water waves generated by underwater explosions presented in [20] considers the flow to be compressible in the initial phase before the shock wave separates from bubble front. The studies [21–23] are also related to underwater explosions where compressible effects in the liquid under pressure are significant. In the medical application called Sonic shock lithotripsy [24], which is also known as Extracorporeal shock wave therapy, liquid water gets compressed above 1000 bars [25].

Sonoluminescence [26, 27], the phenomenon by which light is emitted from imploding bubbles in a liquid when excited by acoustic waves, involves water under very high pressure. Oceanographic studies on the evolution of streams [28], and on the deep-sea explorations [29], require the property variations of sea water based on varying temperature and pressure conditions. The recent studies by Chen et al. [30] and Houqun [31], reveal that for earthquake-induced dynamic responses, neglecting the compressibility of overlying water could underestimate hydrodynamic pressure at the bottom of an ocean and a dam. In pressurized water nuclear reactors (PWR) [32], liquid water is compressed to pressures above 15 MPa, to use it as a coolant at high temperatures. The hydraulic surge analysis due to water-hammer resulting from sudden valve closures [33, 34], is another transient phenomenon involving liquid compressibility effects due to the high-pressure magnitudes involved. Liquid water is compressed substantially, and associated density variations are significant for all the aforementioned cases.

2.3 Compressible Modelling of Liquids

Most liquids behave as though they are gases that are already under extremely high pressures. This explains why most liquids are commonly treated to be incompressible. As external pressure varies by a few atmospheres, from 0.1 MPa to 0.2 MPa for instance, a liquid behaves just like a gas would, when the gas pressure changes in similar way, from 2000.1 MPa to 2000.2 MPa for instance. However, as the applied pressure range reaches considerably high magnitude, this assumption becomes invalid and compressibility effects in the liquids become significant. Compressibility of the fluid plays a crucial role in hydraulic applications. The lower compressibility of the hydraulic liquid in a high-pressure machine result in its higher efficiency [9]. There are numerous industrial applications and scientific studies where the effect of liquid compressibility cannot be ignored. For all such cases, the possibility of including relevant property variations in the liquid should be considered. An early study conducted by N. M. Philip on adiabatic and isothermal compressibilities of 24 different liquids is available in [35]. Compressibility of water was established through experiments by 1762, however, it took almost a hundred years to achieve the precise value for the same even at ambient pressures [36]. The effect of liquid compressibility on acoustics and Kolmogorov spectrum of hydrodynamic turbulence is outlined in [37]. Fluid compressibility is a parameter that affects the performance of reservoirs. The effects of oil compressibility on the production performance of fractured reservoirs is carried out through simulation studies in [38]. The effect of liquid compressibility on bubble dynamics and reactions inside the bubble, is computationally investigated by Fuster et al. in [39] and Merouani et al. in [40]. The role of liquid compressibility in the volumetric and mechanical losses in high pressure displacement pumps is investigated by Paszota in [41]. The effect of compressibility of the drilling mud (treated as a liquid) on the pressure rise in a shut-in well is explored by Henry in [42].

Numerical methods are widely employed in modelling compressible multi-phase flows involving liquid compressibility effects. There are also many computational studies which investigate the effects of liquid compressibility on the stability of mathematical models, and also in determining the related multi-phase physics. Consequences of liquid compressibility consideration on the mathematical well-posedness of multi-fluid equation system for bubbly flows is investigated by Egashira and Kanagawa in [43]. The role of compressible effects in a liquid in determining the interactions between oscillating bubbles is studied by Zhang et al. in [44]. Deng et al. [45] discuss discontinuity-resolving reconstruction for compressible multi-phase flows with moving interfaces. Re and Abgrall [46] present

a novel pressure-based method for weakly compressible multi-phase flows. The effect of liquid phase compressibility in the simulations using a two-fluid model is numerically investigated by Shokri and Esmaeili [47].

2.3.1 Equations of state for liquids

Perceptible variations in density and sound celerity in a liquid medium imply the requirement of additional relations in a mathematical model that could model the compressibility effects in liquid. An equation of state (EOS) is a thermodynamic relation connecting different state variables to specify the state of matter for a given set of physical conditions. We have the ideal gas equation to relate the various state properties of ideal gases and the Van der Waals equation of state [48] for the corresponding case for real gases. Similarly, many of the liquids we encounter in scientific applications also have one or more state equations. A liquid EOS relates the various thermodynamic variables of a liquid such as pressure, volume, temperature, or internal energy [49]. Most state equations also have an associated relation for the speed of sound in the medium. EOS are very useful in estimating unknown properties of fluids from known quantities. These relations can be used to model compressibility effects in a liquid by estimating varying density and speed of sound in the liquid medium from changing pressure values during a process.

A fundamental equation of state for liquid states of argon, nitrogen, and carbon dioxide is available in [50]. A simple analytical EOS is presented in [51] for modelling liquid phase of different metals. The EOS for non-magnetic liquid iron presented in [52] is used in thermo-chemical modelling of the Earth's core. The EOS such as the Van der Waals, the Redlich-Kwong, the Soave, and the Peng-Robinson are among the widely used models in oil industry [53]. Thermodynamic properties of pure ionic liquids can also be estimated using state relations such as the extended SAFT-BACK EOS [54], the ePC-SAFT [55], the fluctuation EOS [56] etc.

2.3.2 Equations of State for Water

There are different equations of state available for liquid water and for the saturation states of water. The works by Rice and Walsh [57], Nowak [58], Gurtman et al. [59], Ree [60], Chen et al. [61], Halbach and Chatterjee [62], Mueller and Gubbins [63], Wiryana et al. [64], Jeffery and Austin [65] etc., are some important contributions to equations of state for water in the last century. Hill et al. [66] presented a fundamental EOS for heavy water and a reference EOS for the same liquid is proposed in [67]. The International Association

for the Properties of Water and Steam (IAPWS) EOS for the estimation of thermodynamic properties of ordinary water for general and scientific use is available in [68]. An analytical state equation for water is developed from the statistical associating fluid theory (SAFT) by Chen eta al. [69]. Davitt et al. [70] introduced an EOS for water under negative pressure. An EOS for water in relation with its quantum molecular dynamic simulations at ultra-high pressures as in planetary interiors is proposed by French et al. [71]. Wide range EOS for water and steam are proposed by Nigmatulin and Bolotnova [72]. Holten et al. [73] proposed an EOS for the prediction of thermodynamic state variables of cold and super cooled water for pressures up to 400 MPa, which can be further extrapolated up to 1000 MPa range. An experimental equation of state for water down to the negative pressure range of -120 MPa is proposed by Pallares et al. [74]. Notable contributions on the state equations for sea water include the works by Millero et al. [75], Fofonoff [76], Nycander et al. [77] etc. Millero provides a historical review on the EOSs for seawater in [78]. A comparative study was carried out by Hayward [79] on different compressibility equations for liquids. The study by Li [80] suggests the suitability of the Tait EOS for representing the $P - V - T$ relationship for water and the Tait-Gibson EOS for sea water respectively.

There are some equations of state which are commonly used to model the compressibility of liquid water, such as the Tait equation, the stiffened gas equation and many of their extensions. The Tait equation for relating the pressure and density of liquid water under isothermal conditions was proposed by P. G. Tait [81]. Since then the Tait EOS has undergone numerous modifications starting with the temperature-dependent version of this EOS presented by Tamman a few years later in [82]. MacDonald [83] has reviewed the utility of the Tait equation and the Murnaghan equation for liquids and solids. The Tumlirz EOS [84] and the Tamman EOS for pure water are rearrangements of the linear secant-modulus equation used by Tait. The historical evolution of the Tait equation is presented in [85]. The Mie–Gruneisen equation is an equation of state relating the volume of a solid to the applied pressure [86]. A Mie-Gruneisen type of EOS for liquid water is developed by Davis in [87]. The Mie-Gruneisen EOS is extended to study liquid water by Huang [88] where the Mie-Gruneisen constant is derived from shock jump condition. The stiffened gas equation proposed by Harlow and Amsden [89] is a modified form of the Grüneisen equation of state. The stiffened gas equation is among the most widely used EOS for water for modelling single phase flows as well as multi-phase flow situations. The Noble Abel Stiffened Gas EOS proposed by Le Métayer and Saurel [90] for the prediction of saturation states of water brings about significant improvement to the stiffened gas equation.

Water is treated to be inviscid and compressible in the works of Liu et al. [21], Mor-

ley and Williamson [91], and Deng et al. [45] where the Mie-Gruneisen EOS is used to determine the pressure of compressed and expanded water. A two-phase compressible flow solver is suggested by Li et al. [22] where they numerically investigate the bubble dynamics in underwater explosion and treats compressible effects in water by using the Tait EOS [81]. Gurovich et al. [23] explains the compression loading of a copper target to extreme pressures of the order of 2×10^{11} Pa using compressed water flow generated by the underwater electrical explosion of a wire array. In that study, a polytropic EOS is used for calculating the variable density of water. A quantitative estimation of hydrodynamic characteristics and value of the nose over-pressure of a planing plate of a finite extension, at subsonic and supersonic velocities with an attached and detached compression shock, is carried out by Maiboroda [92]. This study employs an isentropic EOS for modelling water compressibility. The application of the Stiffend gas EOS can be found in the works of Saurel and Abgrall [93], Allaire et al. [94], Le Métayer et al. [95], FlÅtten et al. [96] etc. The prediction of high-pressure volumetric properties of compressed liquids using a two states model is presented by Jasiok et al. in [97]. Dolan et al. [98] proposed a metastable limit for the compressed form of liquid water. More theory on the compressibility of liquid water is available in the work by Yasutomi [99].

2.4 Shock Tube Problems and Their Importance in Compressible Flows

Shock waves are small transition layers over which the physical quantities such as pressure, density, and temperature change very rapidly. The shock tube [100–102] is a device in which normal shock waves are generated by rupturing a diaphragm separating a high-pressure fluid from a fluid at low pressure. Shock tube facilities are generally used to generate extreme temperature and pressure conditions under which behaviour of materials and objects are investigated. Some of the applications of shock tube are, in the investigation of chemical kinetics of reactions at high temperatures [103, 104], in the performance evaluation of thermal protection systems of a body during re-entry from space back to earth's atmosphere [105–113], in studying the impact of blast waves on biological specimens in biomedical research [114, 115], etc. The applications of shock waves in therapeutical studies are outlined in [24, 116, 117]. Shock tubes are also widely employed in the investigation and theoretical understanding of compressible flow phenomena and fluid transients including gas and shock dynamics. The behaviour of different fluids in their highly compressed

state is experimentally studied using various shock compressing techniques. The wave motion associated with flow conditions like explosions, seismic movements, sudden flow interruptions etc., involves the generation and propagation of shocks through the respective fluid media. A brief history of the development of shock tubes, the device's principle of operation and some important results for high-temperature gas dynamics obtained on shock tubes in recent time are outlined in [118]. The 3D schematic of a typical shock tube geometry is shown in Figure 2.1.

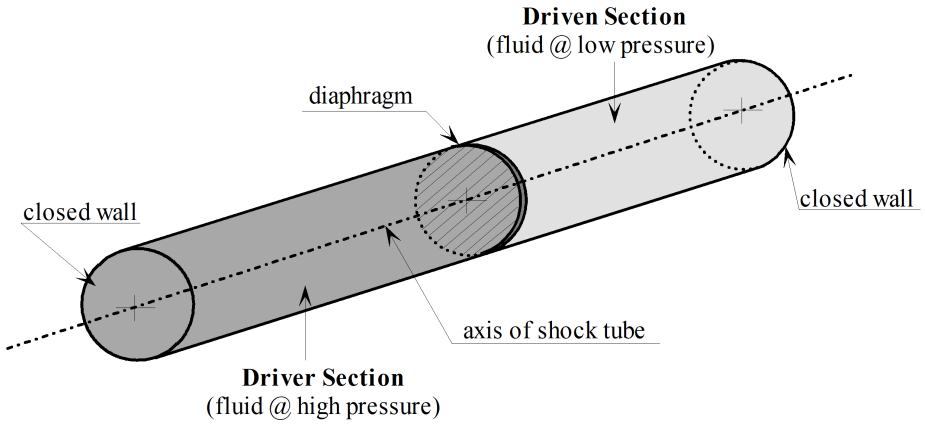

Figure 2.1: The 3D schematic of a shock tube.

A typical shock tube setup consists of a long tube separated into two sections by a diaphragm located inside it. In single-fluid shock studies, these sections will be filled with the same fluid but at different initial states. The initial conditions of temperature and flow velocity may or may not vary between the two sections based on the situation under study. However, the most important parameter that initially varies across the diaphragm is fluid pressure. The section containing fluid under high-pressure is the 'driver section' and the section that holds the fluid at a relatively lower pressure is called as the 'driven section'.

2.4.1 Gaseous Shock Tube Studies

There are many studies available in the literature where the high-temperature, high-pressure behaviour and the chemical kinetics of various gases and gas mixtures are studied with the help of different shock tube configurations. Glass and Patterson [119] presented one of the first studies on the theoretical and experimental aspects of shock-tube flows. A comprehensive study on the geometric forms and structure of different types of shock waves that occur in a perfect gas is presented by Pain and Rogers [120]. The equilibrium air radiation for a selected range of wavelength is experimentally investigated using a shock

tube in [121]. Various shock tube techniques are used in understanding the kinetics and thermodynamics related to the thermal decompositions of acyclic and aromatic fuels as pointed out by Kern and Xie [122]. Davidson and Hanson [123] presented the corrections required for shock tube studies of real gases at high pressures to consider the effects on temperature, pressure, and density. Chojnicki et al. [124] used one-dimensional shock-tube experiments for investigating dynamics of rapidly decompressed gas-particle mixtures and associated shock waves, with application to the initial stages of Vulcanian and Plinian eruptions. Ananthu and Kumar [125] carried out numerical performance analysis of shock tube for different driver and driven gases. Gas shock tubes are used by Kumar and Nedungadi to generate blast wave signatures for studying the interaction between blast waves and human bodies [126].

2.4.2 The Gas Shock Tube Problem of Sod

Gas shock tube problem or simply shock tube problem, is one of the most established and widely used benchmark problems in the field of computational fluid dynamics for compressible flows. This is due to the multiple benefits offered by this problem, like simplicity in the problem setup, ease of computational modelling and most importantly the availability of an exact solution to the problem. Shock tube physics and analytical procedure to obtain the exact solution to the gas shock tube problem are clearly outlined in [127]. The thickness of transition layer for a strong shock is of the order of magnitude of the mean–free path of molecules, which is about 10^{-7} m. Replacing shock waves as mathematical discontinuities is, therefore, a reasonable approximation [128]. However, the discontinuous approximation of very weak shock waves such as sonic booms can be very inaccurate [129]. For an in depth discussion on shock thickness one may refer to [130]. Gary A. Sod investigated the gas shock tube problem numerically using computational tools called the Riemann solvers in [131], due to which the gas shock tube problem is more often referred to as Sod shock tube problem. In his work [131], Sod used the Euler equations as the set of governing equations for transient modelling of the shock tube and solved the problem on a one-dimensional domain. A schematic of the one-dimensional representation of gas shock tube is provided in Figure 2.2.

The initial condition of the shock tube problem consists of a discontinuity separating two uniform states. In a gas shock tube problem, the uniform states on either side of the diaphragm are defined using variables such as pressure, density and flow velocity. The initial conditions of pressure, density and fluid velocity are labelled as P_L, ρ_L, u_L in the

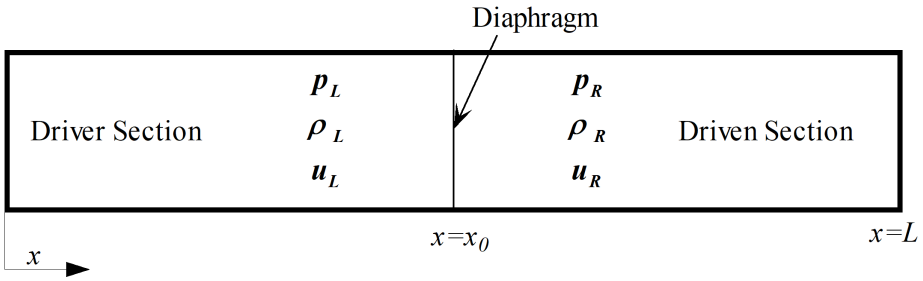

Figure 2.2: The 1D schematic of a gas shock tube.

left side of the diaphragm and P_R, ρ_R, u_R in its right side and these zones are marked $'L'$ and $'R'$ respectively. For the one-dimensional problem model, unit length is chosen for the sealed tube which is the physical domain of the problem, and the diaphragm is positioned half way of the tube i.e., at $x_0 = 0.5$ units from the left boundary. The initial property values on either side of the diaphragm are set as follows:

$$\begin{array}{lll} P_L = 1.0 & & P_R = 0.1 \\ \rho_L = 1.0 & \text{and} & \rho_R = 0.125 \\ u_L = 0 & & u_R = 0 \end{array}$$

Initially the fluid on either side of the diaphragm is at rest. On the rupture of the diaphragm, the pressurised gas on the left is expected to move towards right thus forming a compression wave front. In the mean time, an expansion fan propagates into the left compressed region. The successive compression waves coalesce to form a shock which moves further right at a supersonic speed into the low pressure side. Across the contact surface formed the density and temperature are discontinuous. The waves traversing through the fluid results in the formation of different zones and the extent of each region varies with time. The motive is to predict the transient phenomena prior to shock/expansion wave reflection at the boundaries. The transient problem thus evolved for an ideal gas, with few waves to be captured and their relative effect on the fluid properties, defines the one-dimensional shock-tube problem.

The fluid chosen for the problem is air and is treated as an ideal gas. The viscous effects are considered to be negligible along the tube walls and the tube is assumed to be long enough to avoid wave reflections from the boundaries over the computational time. A set of non-linear hyperbolic conservation laws, the one-dimensional equations of gas dynamics, forms the system of governing equation for the problem. In conservation form, the system of governing equations is given by

$$\frac{\partial \rho}{\partial t} + \frac{\partial (\rho u)}{\partial x} = 0 \tag{2.1a}$$

$$\frac{\partial (\rho u)}{\partial t} + \frac{\partial (\rho u^2 + P)}{\partial x} = 0 \tag{2.1b}$$

$$\frac{\partial (\rho e)}{\partial t} + \frac{\partial (\rho e u + P u)}{\partial x} = 0 \tag{2.1c}$$

where, ρ is the density, u the velocity, P the pressure, and e the specific total energy of the fluid. In the vector form, the system of equations may be expressed as follows:

$$\frac{\partial U}{\partial t} + \frac{\partial F(U)}{\partial x} = 0 \tag{2.2}$$

where U is the vector of conserved variable and $F = F(U)$ is the corresponding flux vector given by

$$U = \begin{bmatrix} \rho \\ \rho u \\ \rho e \end{bmatrix} \qquad \text{and} \qquad F = \begin{bmatrix} \rho u \\ \rho u^2 + P \\ \rho e u + P u \end{bmatrix}.$$

The specific total energy (e) and specific internal energy (ε) are connected by the relation

$$e = \varepsilon + \frac{1}{2} u^2 \tag{2.3}$$

For a perfect gas, the specific internal energy is given by the relation

$$\varepsilon = \frac{1}{\gamma - 1} \frac{P}{\rho} \tag{2.4}$$

where the ratio of specific heats, $\gamma = 1.4$ for air. The expression for the speed of sound in air is given by

$$a = \sqrt{\frac{\gamma P}{\rho}}, \tag{2.5}$$

The governing equation (2.2) forms a coupled non-linear hyperbolic system. The system of equations can be solved analytically for the shock tube problem as discussed in the following section.

The solution structure of one-dimensional shock tube problem is as shown in Figure 2.3. A total of five different regions are observed in the x-t diagram. The regions marked 'L', 'E', '2', '1', and 'R' are all centred at the initial position of the diaphragm i.e., at $x = x_0$. 'L' and 'R' are the unaffected zones of high pressure and low pressure respec-

tively, over which no waves have traversed. Zone '1' is the region over which the shock has traversed. '2' is the zone bounded by the expansion fan 'E' to the left and by the contact discontinuity to the right. The one-dimensional shock tube problem has an exact solution,

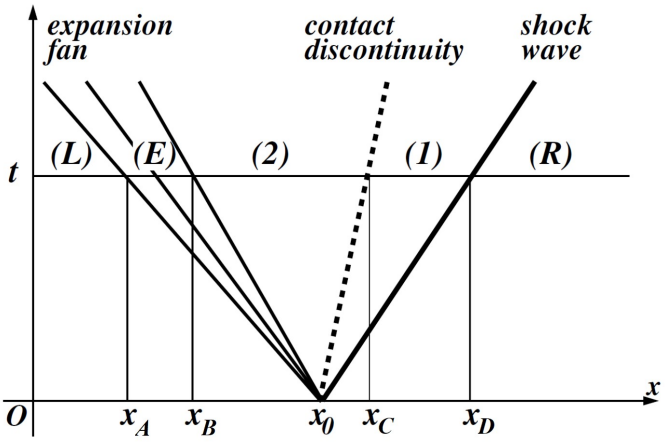

Figure 2.3: x-t diagram for the exact solution of the shock tube problem

which makes this problem the most common benchmark problem for compressible flow solvers. The complete procedure involved in the development of the exact analytical solution to this problem is provided in *Appendix* B. The exact solution to the Sod's problem after 0.2 seconds from the rupture of the diaphragm is shown in Figure 2.4. The velocity, density, pressure and specific internal energy plots are shown for a domain of unit length where the initial position of diaphragm is at $x_0 = 0.5$.

2.5 Studies and Applications Related to Liquid Shocks

The applications and studies related to liquid shock span over varied areas. The study of shock waves in a liquid containing gas bubbles by Campbell and Pitcher [132], and the shock initiation of detonation in liquid explosives by Campbell et al. [133] are some of the early reported works in this field. A reflecting-shock-wave type experimental technique is described by Walsh and Rice [134] to measure the important thermodynamic variables at high pressures. Lyzenga et al. [135] experimentally measured the temperature variations in the shock-compressed water using the optical pyrometry technique. On the studies related to the impact of liquid jet on solid surfaces [18], the liquid is considered compressible with the shocks moving into the liquid interior following collision with solid surface. A review of various techniques used for estimation of the viscosity of var-

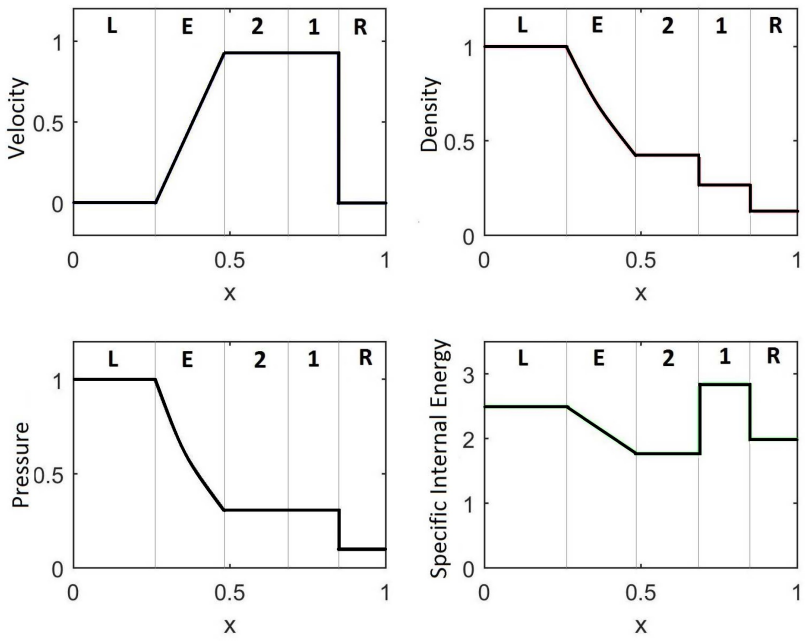

Figure 2.4: Analytical solution of Sod's problem at $t = 0.2\,\mathrm{s}$

ious shock-compressed fluids, which also include liquids, is presented by Al'Tshuler et al. [136]. Cooke and Chen [137], studied on the shock capturing for pure water using general equation of state. The thermal analysis of the shock response of pyrotechnic mixtures by Lee and Finnegan [138], is an application of shock in the field of chemistry. In the case of shock wave lithotripsy, the extracorporeal acoustic shock wave propagates through the liquid and leads to high positive pressures [25]. The electronic conduction studies and the Hugoniot relation for water from shock velocity measurements, in shock compressed high-pressure water, are reported in the work of Celliers et al. [139]. Studies on the water samples undergoing compression from peak pressures achieved with multiple shock waves in nanosecond duration, leading to the ultrafast freezing of the liquid, are carried out by Dolan et al. in [140, 141]. Various researches on underwater shock waves applied to the development of different therapeutic devices are outlined in [142]. Batani et al. [143] studied the variation in liquid refractive index associated with the compression of liquid water to megabar pressure range by using laser-driven shock waves.

The development of shock Hugoniot curves of different liquids needed to perform precise numerical simulations of shock wave/tissue interaction is presented by Gojani et al. in [144]. Gojani et al. also reports the experimental results for the determination of reliable shock Hugoniot curves of liquids. More details on the shock wave generation in liquid water for different biological studies are available in [145]. The handbook of shock waves

by Ben et al. [146] provides further insight into the shock waves in liquids. The elasticity of an inertial liquid shock is explored by Biance et al. in [147]. The simulation studies of shock-waves in water generated by a nanosecond-laser pulse are outlined by Kubecka et al. in [148]. A recent U. S. patent [149], reports the use of shock waves to sufficiently compress a jet of liquid precursor for the high-pressure synthesis of materials. Liquid film breakup induced by shock waves is experimentally investigated by Song et al. in [150], and the detonation combustion wave in liquid kerosene–air mixture is numerically analyzed by Debnath and Pandey in [151]. Investigation of the interface deformation during droplet breakup by Kaiser et al. [152], studies the pressure-wave pattern formation after the passage of shock thorough the liquid using a compressible model. Similarly, the recent article by Ash [153] discusses on how shock-like waves form in the raindrop before it shatters off the hydrophobic surfaces. The study on pressurized thermal shock (PTS) in stratified liquid-vapour systems by El-Said et al. [154], rightly points out the inability of the available CFD codes in modelling the two-phase water hammer (TPWH) flow, due to the strongly compressible nature of the associated flow phenomena. The recent study by Li et al. [155] on the dynamic state of liquids under blast wave loading discusses the shock compression behaviour of liquids, and the interaction of rarefaction waves propagating in the liquid.

2.6 Riemann Solvers and Flux Methods

The classical Riemann problem [156, 157] is an initial-value problem for a system of homogeneous PDEs. The initial setup of this problem consists of two constant states forming a discontinuity [158, 159]. The Riemann problem plays a significant role in the development of numerical methods for the computation of flows with discontinuous solutions. This problem is very helpful for the interpretation of governing relations like the Euler conservation equations. This is because all the important flow features such as the shocks and rarefaction waves appear in the form of characteristics in the solution to this problem. The family of numerical solution techniques used to solve the Riemann problems are known as the Riemann solvers. They employ specific algorithms for computing the numerical flux across a discontinuity in the Riemann problem. Toro [128] provides a comprehensive, coherent and practical presentation of various Riemann solver techniques.

There are exact Riemann solvers as well as approximate Riemann solvers. The exact Riemann solver iteratively solves the Riemann problem and the solution principle is intrinsically linked to the Godunov method. The first exact Riemann solver for the Euler equations was proposed by Sergei K. Godunov [160]. The approximate Riemann solvers

were developed because of heavy computational cost associated with the iterative type exact solvers and the necessity to approximate certain areas in the solution. Exactly solving a single Riemann problem may not seem to be computationally very costly. However, when the Riemann solver is employed as a building block in a finite volume method, it can prove to be prohibitively expensive. Such a case necessitates the solution of a Riemann problem at every cell edge for every time step [161].

Approximate, non-iterative solutions based on the situation modelled, may provide sufficient data for computational purposes. Approximate solution to the Riemann problem can be obtained using the Godunov-type methods through two different approaches. The first approach uses an approximation for numerical flux employed in numerical method. In the second approach, a state is approximated, followed by the evaluation of flux function at this state. A comparison of various approximate Riemann solvers for solving the Riemann problem in a compressible liquid is presented by Ivings et al. in [162]. A brief review of a few approximate Riemann solvers and some numerical flux functions used with these approximate solvers are provided here.

The Roe solver is one of the best–known of all approximate Riemann solvers and it belongs to the class of Flux Difference Splitting (FDS) methods. This approximate solver proposed by Roe [163], is related to the Godunov scheme, using which the inter-cell numerical flux at computational cell interface on a discretised space-time domain is estimated. The method by Roe has undergone a lot of modifications and refinements since its inception. These developments have also made this method versatile, making it suitable for a variety of physical problems. Some of the major refinements to the Roe method were proposed by Roe and Pike [164], which reduced the computational cost associated with the Roe averaged Jacobian matrix. The application of the Roe scheme was extended to a variety of multiphase flow problems by Sainsaulieu [165], which avoided the phase splitting part in the algorithm. The Roe scheme was parallelly implemented to two–dimensional gas dynamic applications by Giraud and Manzini [166]. LeVeque and Shyue [167] implemented this solver related to two-dimensional front tracking computations. Rieper [168] suggested a fix to circumvent the reduced accuracy of the Roe's solver for low-Mach number simulations. A weak formulation of the Roe-type Riemann solver is presented by Castro and Toro in [169] for solving the general hyperbolic systems. A finite volume and unstructured grid-based well-balanced Roe scheme for local inertial equations related to flood modelling is presented by Martins et al. [170].

The Osher solver [171] developed by Osher and Chakravarthy is another method that belongs to the FDS family. Extension of the Engquist–Osher's scheme [172] for the scalar

conservation laws for solving the system of Euler equations led to the development of the Osher method. In the Osher's flux approach, phase expanse between the left region and the right region is sub-divided into simple wave sub-paths. A distinctive feature of the Osher method is the improved performance of this solver near slow-moving shock waves [173, 174]. In the FDS family of methods like the Roe's and Osher's, the flux computation is based on all the three waves according to variable differences at cell interface.

Harten, Lax, and van Leer in 1983 developed an approximate Riemann solver for computing flows with discontinuities, named after them as the HLL solver [175]. The solver has a two-wave model which restricts its ability to capture the intermediate waves like the contact discontinuity. In 1988, the two-wave HLL solver incorporated the wave speed estimates proposed by Einfeldt which came to be known as the HLLE solver [176]. Einfeldt further worked on these methods to propose the HLLEM solver [177]. Following the philosophy of HLL scheme, Toro et al. in 1992 developed a solver based on a three-wave model called the HLLC solver [178]. The new scheme provides better resolution to intermediate waves. The HLLC solver initially computes the slowest and fastest signal speeds (S_L and S_R) respectively, using which it assesses the middle wave speed, S_*. The middle wave speed further divides the central star-region of the Riemann solution profile into two sub star-regions, which are the left star (U_{*L}) and right star (U_{*R}) regions. The three-wave model of HLLC and the formation of different zones in the solution profile are shown using the $x - t$ diagram in Figure 2.5. The flux computation follows an algorithm and the

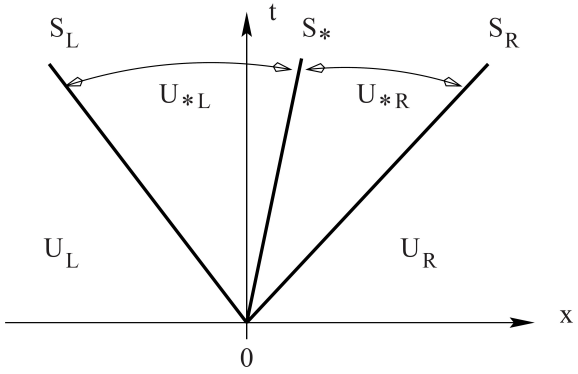

Figure 2.5: The HLLC three wave model

ultimate choice of flux at each cell interface, $F^{hllc}_{i+\frac{1}{2}}$, is based on the sign of computed signal velocities. The HLLC flux is used with Godunov's first-order method for computation. The HLLC scheme can be written in the following generic way:

$$U_i^{n+1} = U_i^n + \frac{\Delta t}{\Delta x}\left(F^{hllc}_{i+\frac{1}{2}} - F^{hllc}_{i-\frac{1}{2}}\right) \tag{2.6a}$$

where

$$F^{hllc}_{i+\frac{1}{2}} = \begin{cases} F_{Li+\frac{1}{2}}, & \text{if } 0 \leq S_{Li+\frac{1}{2}} \\ F_{*Li+\frac{1}{2}}, & \text{if } S_{Li+\frac{1}{2}} \leq 0 \leq S_{*i+\frac{1}{2}} \\ F_{*Ri+\frac{1}{2}}, & \text{if } S_{*i+\frac{1}{2}} \leq 0 \leq S_{Ri+\frac{1}{2}} \\ F_{Ri+\frac{1}{2}}, & \text{if } S_{Ri+\frac{1}{2}} \leq 0 \end{cases} \tag{2.6b}$$

The Euler equations have three distinct characteristic fields in one, two and three space dimensions. This makes the three-wave solver model HLLC a complete Riemann solver, for the Euler equations as approximate wave structure of HLLC contains all characteristic fields of the exact problem. The procedure for computing and selecting the appropriate fluxes at interfaces using the HLLC three-wave model is described in *Appendix* A.

There is another family of methods known as the Flux Vector Splitting (FVS) methods. In the FVS approach, the flux vector at each cell interface is split into two separate components, one with the positive and the other with the negative direction. Splitting of the flux vector into positive and negative vectors is based on the sign of the corresponding eigenvalues. The Steger–Warming [179] is an FVS type splitting method. However, this flux method faces difficulty in solution approach in the vicinity of sonic points due to non-differentiability at such locations. To circumvent this limitation, Van Leer proposed an advanced version of this FVS method in [180], and this method was later named after him. This method had the desirable advancements such as the split Jacobian matrices and that the split fluxes are degenerate for subsonic flow. This flux method is diffusive leading to poorly resolved boundary layer in viscous simulations.

The AUSM$^+$-up flux algorithm is an advanced version of the Advection Upstream Splitting Method (AUSM) by Liou and Steffen [181], which is a flux vector splitting method as the name suggests. The inviscid flux vector $F(U)$ is split into two physically distinct parts, the convective part $F^{(c)}$ and the pressure part $F^{(p)}$, i.e., $F = F^{(c)} + F^{(p)}$. This method takes into account the physical nature of convection and acoustic propagation process while treating them numerically. The convective flux term is treated as a quantity getting advected at velocity $u_{i+\frac{1}{2}}$ at the interface, whereas the pressure flux is governed by acoustic speed a in the medium. AUSM method has undergone many modifications as reported by the works [182–184], and complete evolution of this method is available in [185]. The AUSM method have a notable drawback in the form of pressure oscillations along the grid direction with very small velocity component. This is primarily due to the lack of dissipative mechanism in pressure field. The AUSM$^+$-up proposed by Liou [186], and modified by Chang and Liou [187], mitigates this problem to some extent and is de-

signed to provide high accuracy results at all flow speeds. The AUSM$^+$-up algorithm is given by

$$U_i^{n+1} = U_i^n - \frac{\Delta t}{\Delta x}\left(F^n_{i+\frac{1}{2}} - F^n_{i-\frac{1}{2}}\right) \tag{2.7}$$

where

$$F_{i+\frac{1}{2}} = F^{(c)}_{i+\frac{1}{2}} + F^{(p)}_{i+\frac{1}{2}}.$$

As in the case of basic AUSM scheme, the inviscid flux vector F is split into two physically distinct parts; the convective part, $F^{(c)}$ and the pressure part, $F^{(p)}$. However, the flux terms $F^{(c)}$ and $F^{(p)}$ are redefined as follows

$$F^{(c)}_{i+\frac{1}{2}} = u_{i+\frac{1}{2}} \begin{bmatrix} \rho \\ \rho u \\ \rho e + P \end{bmatrix}_{L/R} = M_{i+\frac{1}{2}} a_{i+\frac{1}{2}} \begin{bmatrix} \rho \\ \rho u \\ \rho e + P \end{bmatrix}_{L/R} \tag{2.8a}$$

$$F^{(p)}_{i+\frac{1}{2}} = \begin{bmatrix} 0 \\ P_{i+\frac{1}{2}} \\ 0 \end{bmatrix}. \tag{2.8b}$$

Here M is the Mach number of flow, which is the ratio of the flow velocity u to the acoustic signal speed a. The detailed algorithm of the AUSM$^+$-up scheme with the complete set of relations is given in the *Appendix* A. A detailed study on different numerical flux functions used in Riemann solvers for ideal gases is presented by Kitamura in [188].

2.7 MUSCL Type Slope Limited Riemann Solvers

The concept of MUSCL type schemes for non-linear conservation laws is developed by Bram Van Leer, and he presented it through a series of papers [189–193] between 1973-1979. The abbreviation MUSCL stands for Monotonic Upstream-centred Scheme for Conservation Laws. The works of Van Leer are among the first attempts to achieve higher order accuracy by modifying the piece-wise data associated with the first-order method of Godunov [160] proposed in 1959. The MUSCL approach relies on data reconstruction for obtaining high–order of accuracy. The MUSCL reconstruction is constrained such that spurious oscillations are avoided, justifying the usage of the word monotone in the name of the method. The flux at each cell boundary is calculated from the left and right states after reconstruction and slope limiting. These fluxes are then assigned as inputs to the Riemann solver, and the solutions thus obtained, are averaged and used to advance the solution in

time.

In a one-dimensional spatial domain $[0, L]$, which is discretized into N computing cells, $I_i[x_{i-1/2}, x_{i+1/2}]$, and assuming a uniform mesh, we have the mesh size, $\triangle x = x_{i+1/2} - x_{i-1/2}$, to be a constant. For the Initial Boundary Value Problem (IBVP) governed by the Euler equations, a system of non-linear hyperbolic conservation laws as follows

$$U_t + F(U)_x = 0 \tag{2.9}$$

the initial condition is given as

$$U(x, 0) = U^{(0)}(x)$$

and the boundary conditions are defined as

$$U(0, t) = U_l(t) \quad \text{and} \quad U(L, t) = U_r(t)$$

the IBVP problem is expressed using an explicit and fully discrete conservative scheme as

$$U_i^{n+1} = U_i^n + \frac{\triangle t}{\triangle x}\left[F_{i-\frac{1}{2}} - F_{i+\frac{1}{2}}\right] \tag{2.10}$$

where $\triangle t$ is the time step size computed based on the CFL criteria.

The objective of using the MUSCL method is to construct a second-order cell interface flux $F_{i+\frac{1}{2}}$ as an extension of the Godunov's first order upwind method. The first step of the MUSCL algorithm is called the data reconstruction step. In this step, the cell average values U_i^n are replaced locally in each cell $I_i[x_{i-1/2}, x_{i+1/2}]$ by the piece-wise linear functions as follows

$$U_i(x) = U_i^n + \frac{(x - x_i)}{\triangle x}\triangle_i, \quad x \,\epsilon\, [0, \triangle x] \tag{2.11}$$

where $\triangle_i$ is a suitably chosen slope vector. The piece-wise linear MUSCL reconstruction step for three consecutive computational cells are illustrated in Figure 2.6

The values of $U_i(x)$ at left and right boundaries of a cell I_i notated respectively as U_i^L and U_i^R, are called the boundary extrapolated values. They are defined as follows:

$$U_i^L = U_i^n - \frac{1}{2}\triangle_i \tag{2.12a}$$

$$U_i^R = U_i^n + \frac{1}{2}\triangle_i \tag{2.12b}$$

The reconstruction process retains the conservation as the integral of $U_i(x)$ over any cell

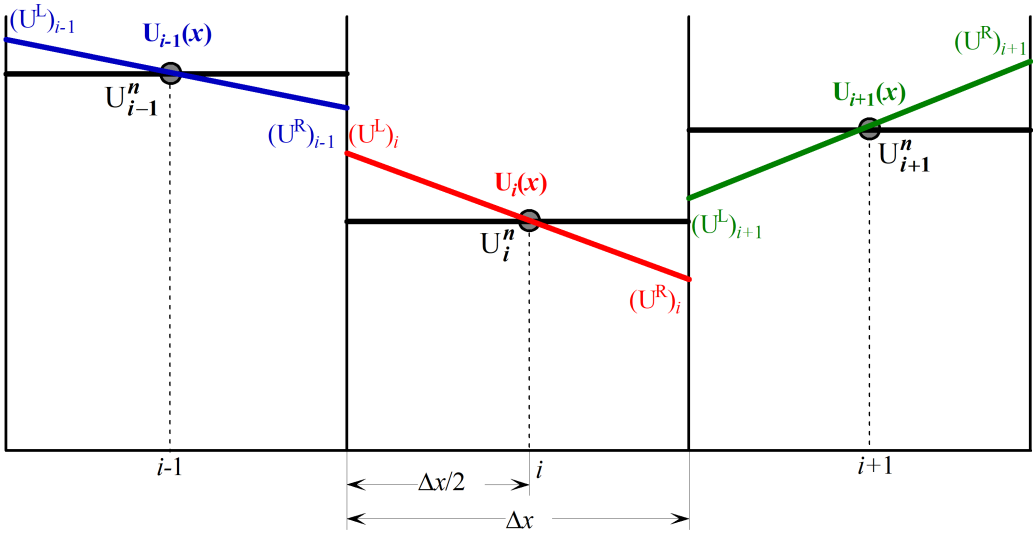

Figure 2.6: Piece-wise linear MUSCL reconstruction for three consecutive computing cells

I_i is same as U_i^n. We also have to remember that for the Euler equations, U and $\triangle_i$ are three-component vectors. For the MUSCL-Hancock method [194, 195], the second step is used to evolve the boundary extrapolated values to a time $\triangle t/2$ as shown below.

$$\overline{U}_i^L = U_i^L + \frac{1}{2}\frac{\triangle t}{\triangle x}\left[F(U_i^L) - F(U_i^R)\right] \tag{2.13a}$$

$$\overline{U}_i^R = U_i^R + \frac{1}{2}\frac{\triangle t}{\triangle x}\left[F(U_i^L) - F(U_i^R)\right] \tag{2.13b}$$

The inter-cell fluxes $F(U_i^L)$ and $F(U_i^R)$ are evaluated from the boundary extrapolated values U_i^L and U_i^R respectively of each cell I_i. These initially extrapolated and further evolved values at the cell boundaries constitute a Riemann problem at each cell interface '$i + 1/2$' where

$$U_L \equiv \overline{U}_i^R \quad \text{and} \quad U_R \equiv \overline{U}_{i+1}^L \tag{2.14}$$

These Riemann problems are solved to obtain the similarity solution of the form $U_{i+\frac{1}{2}}(x/t)$. The inter-cell flux $F_{i+\frac{1}{2}}$ in Equation (2.12) is computed from the Riemann solution as follows

$$F_{i+\frac{1}{2}} = F\left(U_{i+\frac{1}{2}}(0)\right) \tag{2.15}$$

where $U_{i+\frac{1}{2}}(0)$ is the value of $U_{i+\frac{1}{2}}(x/t)$ at $x/t = 0$. By using these values of inter-cell fluxes, the value of the cell-averaged variable vector U is updated to the $n + 1^{th}$ time level

as per Equation (2.12), and the solution is thus marched forward in time.

A possible choice of slope vector $\triangle_i$ is

$$\triangle_i = \frac{1}{2}(1+\omega)\,\triangle_{i-\frac{1}{2}} + \frac{1}{2}(1-\omega)\triangle_{i+\frac{1}{2}} \tag{2.16}$$

where,

$$\triangle_{i-\frac{1}{2}} = U_i^n - U_{i-1}^n \quad \text{and} \quad \triangle_{i+\frac{1}{2}} = U_{i+1}^n - U_i^n$$

and $\omega\,\epsilon\,[-1,1]$. More accurate piece–wise MUSCL data reconstructions are possible, like the piece–wise quadratic reconstruction available in [196].

The higher order spatial discretisation schemes usually exhibit spurious oscillations due to sharp changes in solution domain arising from the presence of shocks, discontinuities etc. The slope limiters have a major role in limiting the solution gradient near shocks and discontinuities. The pioneering works in the field of slope limiters (also called flux limiters) [197–199] are associated with Boris and Book. The limiter functions are usually constrained to be greater than or equal to zero. For cases of sharp gradients, zero gradients, and slope direction changes, the limiter function takes a value of zero, such that the flux is represented by a low-resolution scheme. Similarly, for smooth solutions, the limiter value is equal to 1, which represents a high-resolution scheme for the flux. Based on the difference in switching characteristics, there are numerous limiters available. The selection of a limiter in a computational model is based on the particular problem handled and solution schemes used. As none of the available limiter functions are found to work well for all problems, a particular choice of this function is usually made on a trial and error basis. Harten introduced the concept of Total Variation Diminishing (TVD) schemes in [200] following the flux limiter approach. A comparative study of the TVD-limiters is available in [201,202]. The work by Luttwak and Falcovitz [203] discusses slope limiting for vectors by proposing a novel vector limiting algorithm, and a geometry independent slope limiter for the discontinuous Galerkin method is presented by Aizinger in [204]. The effect of limiting functions in the accuracy of numerical solutions are discussed by Liu et al. [205] and Ladonkina et al. [206]. Advanced slope limiters for Euler equations are presented by Kitamura and Hashimoto in [207] and by Bragin et al. in [208], and a direction-aware slope limiter for three-dimensional cubic grids is proposed by Velechovsky et al. in [209].

2.8 Friction Models for Liquid Transients

In the numerical modelling of liquid transients, properly quantifying frictional losses in the systems is crucial to the accuracy of flow simulations. There are steady and unsteady models available for estimating the transiently fixed and varying losses associated with the flow. There are few points to be considered while applying a friction model for simulating highly transient liquid flows. For flow situations involving high pressures, the liquid can be treated as slightly compressible. Such a treatment of the fluid shall help in accounting for small variations in liquid density and speed of sound during the transient. The assumption that the pipe material exhibits elastic effects and computing the signal propagation celerity inside the pipe based on this, improve the accuracy of characteristics modelling. The importance of including the unsteady friction models and the viscoelastic considerations during the modelling of pipe fluid transients is outlined by Duan et al. [210]. Most of the liquid transients are associated with sharp variations in different flow parameters and neglecting these variations in a few parameters can lead to computational inaccuracies.

In the flow simulations, the steady component of friction is very often modelled using the Darcy-Weisbach relation [211], which defines the steady part of the friction F_s as

$$F_s = \frac{f}{d}\frac{u\,|u|}{2g} \tag{2.17}$$

where, f is the Darcy-Weisbach friction factor, d is the pipe-diameter, u is the flow velocity, and g is the accelaration due to gravity. The quasi-steady friction models assume that the unsteady friction has no contribution to energy losses in the flow. These models include only the quasi-steady part and is thus computationally economical.

During a hydraulic transient in a pipe system, the generated pressure waves propagate inside the pipeline and dissipate down over a period of time. The system consequently reaches another steady state. This dissipation of energy in the system is a result of hydraulic resistance offered by internal fluid friction and the friction at system boundaries. The friction models considering only the steady part are commonly found to be insufficient in accounting for the complete frictional losses associated with transient flows. This is because considerable loss occurs in transient flows due to the unsteadiness of the flow, making it necessary to quantify these losses by including an unsteady component of friction. The unsteady friction models can be classified into two groups based on the timeline of the flow acceleration data used in these models.

The first group of unsteady friction models uses past flow acceleration data for the cal-

culation of unsteady friction value. The unsteady friction models proposed by Zielke [212], Trikha [213], Vardy and Brown [214] etc. all belong to this group. The analytical model developed by Zielke [212] defines unsteady head loss as a function of the flow acceleration and the weighted velocity changes from the previous time instant. The definition of unsteady head loss per unit length, F_{us}, from the Zielke model is expressed as follows

$$F_{us}(t) = \frac{16\nu}{gd^2} \int_0^t \frac{\partial u}{\partial t}(u) * W(t-u)du \tag{2.18}$$

where ν is the kinematic viscosity, W is the weighting function, and $*$ is the convolution operator. Trikha [213] and Vardy and Hwang [215] developed characteristics based models for transient friction in pipes. While Zielke [212] proposed a weighting function appropriate for laminar flows, Trikha [213] simplified this model for better computational efficiency. Vardy and Brown extended the definition of these weighting functions for turbulent flows in smooth pipes through a series of works [214, 216, 217], followed by the application to rough pipes [218]. However, the computation results of Vardy and Brown are of short duration, which is insufficient to understand the trend of energy decay in the transient flow.

The second group of unsteady friction models uses instantaneous value of acceleration as observed with the models of Daily et al. [219], Brunone et al. [220, 221]. Daily et al. [219] were among the first to suggest the dependence of unsteady friction losses on the flow acceleration. The friction model developed by them from experimental studies defines unsteady friction as follows.

$$F_s = \frac{f}{d}\frac{u^2}{2g} + \frac{k_1}{g}\frac{du}{dt} \tag{2.19}$$

where, k_1 is a non-dimensional coefficient which takes a value in the range of 0.01-0.015 for accelerating flows and a value of 0.62 for decelerating flows. Carstens and Roller [222] later proposed the parameter k_1 as a function of the flow Reynolds number.

An additional convective acceleration term was included in the friction model by Brunone et al. [220]. It was included such that, the unsteady friction is present when $u\,\partial u/\partial t > 0$ and the unsteady part is removed for $u\,\partial u/\partial t < 0$. In the derivation of classical water hammer equations, the velocity gradient term, $\partial u/\partial x$, is usually ignored due to its negligible magnitude. This term after multiplying with signal celerity, a, is added to instantaneous acceleration, $\partial u/\partial t$. These two acceleration terms are further combined and then taken product with a constant coefficient, k_2 in the Brunonne's unsteady friction model, as shown

below.

$$F_s = \frac{f}{d}\frac{u^2}{2g} + \frac{k_2}{g}\left(\frac{\partial u}{\partial t} - a\frac{\partial u}{\partial x}\right) \tag{2.20}$$

where k_2 is an experimentally evaluated parameter that plays a crucial role in the friction model. This parameter may be assumed as a constant or can be defined as a function of the initial Reynolds number. The unsteady friction models defined using instantaneous values in the flow is relatively lucid and computationally efficient.

The effects of viscous shear in liquid transients in a cylindrical tube were explored by Holmboe and Rouleau [223] through two different experiments using a rectangular pressure pulse. Schultz [224] tried to understand the impact of unsteady friction on pressure wave propagation inside tunnels. Bergant et al. [225] reviewed various unsteady friction models developed for transient pipe flows and confirmed the valid range of application of these models. Select unsteady friction models for transient pipe flow simulation are experimentally investigated and validated by Adamkowski and Lewandowski [226]. Vítkovskỳ et al. [227] tested various unsteady friction models for their suitability in modelling different types of flow transients using experimental data. Norooz et al. [228] present a review of the different unsteady friction models for one-dimensional transient pipe flows.

2.9 Valve-induced Hydraulic Surges

The fast closure of valves is a common scenario observed in various piping systems. Such closures subsequently result in sudden change of flow conditions in the system. The sudden change in the velocity of the fluid in motion causes a surge in fluid pressure and this phenomenon is commonly known as the Water hammer effect. Water hammer is a perfect example of a liquid transient where the fluid-compressibility effects cannot be neglected. The inertia of the forward-moving fluid before it is brought to rest compresses the fluid volume ahead of it against the changing boundary. During this process of deceleration, kinetic energy of the flow is transformed into equivalent pressure energy. The compression front thus developed propagates as a wave through the pipeline travelling at the speed of sound. The maximum pressures during such a surge can exceed the initial static pressure by several orders of magnitude. This information is very crucial during the design stage to ensure safety to the system components and accessories. Sudden valve closures not only induce high-pressure situations but can also create low pressures due to the formation of rarefaction waves. This may further lead to cavitation if the local pressure at any point in the system drops below the vapour pressure of the liquid.

There are numerous analytical and experimental studies on valve-induced hydraulic surges, where the transient variation of different flow parameters are investigated. Mitra and Rouleau [229] studied the axial and radial variations observed in the transient pressure waves propagating through the liquid transmission lines, generated from valve closures. Jelev [230] presented a hysteretic friction-based method for modelling the damping of pressure oscillation during hydraulic surges. This method considers water column dynamics, compressibility of fluid and energy losses by the elasticity of pipe walls for a pressurized pipe. Liou [231] investigated the maximum pressure head emanating from linear closure of valves using a non-dimensional variable formulation. Brunone et al. [232] experimentally measured the velocity for valve-induced transients to demonstrate the presence of flow recirculation, flow reversal and increase in the turbulence intensity for the transient event. Numerous simulations and experiments carried out by Ramos et al. [233] investigated the dynamic response of pipelines based on different aspects such as pipe materials, diameters, thickness, lengths and transient conditions. Covas et al. presented the dynamic effect of pipe-wall viscoelasticity in valve-induced hydraulic transients in their works [234, 235]. Neuhaus and Dudlik [34] presented data from several valve-closure experiments performed at the PPP test rig at Fraunhofer for different initial temperatures and system pressures. This work also discusses both the importance of including and the difficulty of modelling the numerous effects that can occur during such transient events.

Choi et al. [236] discussed the issues related to pressure monitoring for valve-induced transient flow in water pipelines, such as the influence of sampling location and sampling interval on pressure measurements. Perez and El-Bayoumi [237] studied the effect of valve characteristics of a motor-operated valve such as flow coefficient, valve curve and stroke time on the surge pressures in delivery terminals. Three-dimensional CFD simulation of valve-induced water hammer phenomena in a simple tank-pipeline valve system is presented by Yang et al. [238]. The CFD model used the sliding mesh technique and considered the compressibility effects in water. Jung and Karney [239] clearly outline the key differences and merits of different unsteady pipe flow models such as the water hammer models, the rigid water column analysis, the quasi-steady analysis, and the Joukowski approach. Bertaglia et al. [240] performed a comparative study on the relative accuracy and efficiency of various methods used for numerical simulation of hydraulic transients in visco-elastic pipes.

The impact of valve closure duration and trends on the surge characteristics are explored through different studies. For turbulent conditions, the effect of valve-closure schedule on the surge characteristics was numerically studied by Azoury et al. [241] using the MOC

method. This study also proposed a chart for determining the valve schedule for minimising surge pressure. The study by Liou [231] graphically demonstrated the dependency of maximum head generated during a linear valve closure on the period of closure of the valve. Bazargan-Lari et al. [242] proposed a mathematical curve developed using a multi-objective optimisation model, for the optimal valve closing rule for controlling the surge pressure. A recent study by Yuce and Omer [243] investigated the effect of various valve closure schemes in pipelines such as sudden, linear and stepwise closures on the hydraulic transient characteristics.

Chapter 3

A New Equation of State for Compressible Liquid Water

3.1 Introduction

Water is the most common liquid in daily life situations. Though it is frequently observed in both industrial and non-industrial flow applications, water is rarely modelled as a compressible fluid. From atmospheric pressure up to a few hundred bars of pressure, water is essentially an incompressible liquid as its density does not exhibit a strong functional relationship with its pressure. However, there are flow situations and applications where liquid water is exposed to large variations of pressure and temperature. Different industrial applications where liquid water is exposed to very high pressures are outlined in Section 2.2. For flow situations where water density exhibits a strong association with pressure or temperature or both, adequate equations of state are necessary to address the compressibility effects in the liquid. Details of the compressible modelling of liquid water from different studies and information regarding various EOSs for water are presented in Section 2.3. The main reason for the incompressible treatment of water by most mathematical models is the presence of complexities associated with the use of EOSs. Ideally, an EOS for a liquid should have a relatively simple structure for the ease of incorporation into existing mathematical models along with the ability to provide accurate property estimates. However, there are limitations for most of the available EOSs for water in the form of a limited range of operation, complicated structure etc. In modelling compressible liquid flows, the reliability of the EOS used over the specified property range and the ease of its incorporation into flow model determines the overall efficiency of the model.

This chapter analyses some select equations of state which are frequently used in compressible modelling of water. EOS such as the Tait, the Stiffened Gas, and an EOS de-

veloped by Metayer and Saurel for predicting the saturation states of water, known as the Noble Abel Stiffened Gas (NASG), are considered here. Isothermal density data from National Institute of Standards and Technology (NIST) database for different temperatures within a specified range and over the wide pressure range of 1 bar to 10,000 bar were obtained. A modification to the NASG EOS is proposed to apply it for reliable prediction of liquid water properties away from the saturation conditions. The new EOS so developed is named as the 'Modified NASG EOS'. Accuracy of all the four EOS is quantitatively evaluated by comparing the predicted densities with the corresponding NIST data over the wide pressure range. Performance of the EOS is also evaluated over selected temperature range. This chapter also discusses the qualitative ability of different state equations in reliably modelling isothermal and non-isothermal flow situations.

Section 3.2 of the chapter briefly explains some select EOS for water. The details of the development of 'Modified NASG EOS' is presented in Section 3.3 along with the evaluation strategy adopted for this compressible model. Section 3.4 presents the results from comparative study and discusses the major observations and findings.

3.2 Commonly Used Equations of State for Water

Modelling of water as a compressible liquid requires relations which connect the properties of water such as pressure, density, temperature etc. These relations should also perform satisfactorily at the pressure ranges where compressible effects in water become predominant. There are many EOSs available for water which are applicable over different pressure and temperature ranges. Some of them are defined over a wide range of pressure, and the demerits associated with most of such EOS are either the reduced accuracy in property predictions or their inability to capture complete physics of the problem. Those equations of state which are applicable over a very narrow range of pressure have the advantage of producing accurate results within their stipulated range, but outside this range, the predicted values may be highly inaccurate. Here, three different EOSs are initially considered which are frequently used for compressible modelling of water, viz., the Tait EOS, the Stiffened Gas EOS, and the NASG EOS. The comparatively lucid structure and ease of incorporation into flow equations are the two major attributes considered while these EOS were chosen for the study. Below we provide a brief description of each of these EOS.

3.2.1 The Tait Equation of State

Scottish mathematician and physicist Peter Guthrie Tait proposed this EOS [81]. The equation has gone through a number of modifications over the last century, and one such modification is by R. H. Cole in 1948 for modelling the response of liquid water to underwater explosions as reported in [244]. The historical evolution of the Tait equation is presented in [85]. A latest version of Tait EOS as given in [245] relates pressure P and density ρ as follows:

$$P = K_0 \left[\left(\frac{\rho}{\rho_0} \right)^{\theta} - 1 \right] + P_0 \tag{3.1}$$

In equation (3.1), P_0 and ρ_0 are respectively the pressure and the density of water at the reference temperature. Parameters K_0 and θ are weak functions of temperature and pressure. These parameters are held constant and are assigned the following values, $\theta = 7$ and $K_0 = 3 \times 10^8$ Pa. This is an isothermal EOS due to which there is no coupling established between temperature and density. The caloric equation that is thermodynamically consistent with the pressure-density relation, is a constant specific heat relation which defines the specific internal energy ε as follows:

$$\varepsilon = C_v \left(T - T_0 \right) + \varepsilon_0 \tag{3.2}$$

In equation (3.2) C_v is the specific heat at constant volume for water with a value of 4.183 kJ/kgK and T_0 is the reference temperature taken to be 273.15 K. The value of specific internal energy at the reference temperature, $\varepsilon_0 = 0.617$ kJ/kg. The speed of sound c with the Tait equation is computed from the following relation:

$$c = \left[\frac{\theta \left(P - P_0 + K_0 \right)}{\rho} \right]^{1/2} \tag{3.3}$$

The Tait equation is very accurate despite its isothermal behaviour. The limitation of this EOS is mainly in its application to non-isothermal flow modelling.

3.2.2 The Stiffened Gas Equation of State

The Stiffened Gas EOS is a simplified form of Grüneisen EOS [246]. The Stiffened-gas model proposed by Harlow and Amsden in [89] and used by FlÅtten et al. in [96] relates

pressure P, density ρ, and temperature T as follows:

$$P = \rho\,(\gamma - 1)\,C_v T - P_\infty \tag{3.4}$$

In equation (3.4) P_∞ is a constant parameter representing the molecular attraction between water molecules, C_v is the specific heat at constant volume and γ is the ratio of specific heats for the liquid. The expression of stiffened gas EOS is identical to ideal gas equation for zero value of the parameter P_∞. The speed of sound relation consistent with this EOS is as follows

$$c = \left[\gamma \frac{(P + P_\infty)}{\rho}\right]^{\frac{1}{2}} \tag{3.5}$$

The values of the parameters in equation (3.5) for liquid water are $\gamma = 2.85$, $P_\infty = 8.3302 \times 10^8$ Pa, and $C_p = 4155$ J/kgK. As shown in the section of results, Stiffened gas EOS over-predicts the density of water. Another drawback of this EOS is the returning of negative pressure values for density values lower than reference density. A regularized version of stiffened-gas equation of state is presented by Ghidaglia and Mrabet [247] that corrects this unphysical behaviour of the EOS. Despite these inaccuracies, Stiffened gas equation is amongst the most widely used EOS for water due to its simple structure and ease of inclusion into flow models. An adiabatic version of stiffened gas EOS known as 'Cole equation of state' is also available for liquids [248].

3.2.3 The Noble-Abel Stiffened Gas (NASG) Equation of State

Noble-Abel Stiffened Gas EOS combines the Noble-Abel EOS [249] and the Stiffened Gas EOS. This EOS brings about significant improvement in Stiffened Gas equation and is primarily meant for the prediction of saturation properties of certain liquids. Métayer and Saurel formulated this equation in [90] where the EOS parameters for different fluids are determined from their respective experimental saturation curves. The NASG caloric equation relates the pressure P, the specific volume v, and the specific internal energy ε as follows:

$$P = (\gamma - 1)\,\frac{(\varepsilon - q)}{(v - b)} - \gamma P_\infty \tag{3.6}$$

where γ, P_∞, q, and b are constant coefficients characteristic of the thermodynamic properties of fluid. Specifically, q is the heat bond of liquid water and b represents the co-volume of the fluid. The combined term $(\gamma - 1)(\varepsilon - q)$ represents thermal agitation, $(v - b)$ repre-

sents repulsive short distance effects linked to molecular motion, and γP_∞ corresponds to attractive effects leading to molecular cohesion in condensed states. The value of NASG coefficients for liquid water in temperature range 300-500K is given in Table 3.1. The quantities ε and v are computed from the relevant equations which are available in [90].

Table 3.1: Coefficients for the NASG EOS

C_p (J/kgK)	C_v (J/kgK)	γ	P_∞ (Pa)	b (m^3/kg)	q (J/kg)
4285	3610	1.19	7.028×10^8	6.61×10^{-4}	-1177788

3.3 The Modified-NASG Equation of State

The original NASG EOS proposed in [90] is for the prediction of saturation properties of water. The reference state used for calculating parameter P_∞ for NASG EOS is the saturation state corresponding to pressure $P_0 = 1.0453$ bar at which density $\rho_0 = 957.74$ kg/m^3 and speed of sound $c_0 = 1542.0$ m/s. As a result, this EOS is found to over-predict the density of water at lower pressure range of 1×10^5 Pa which is its major drawback. The NASG EOS thus demands a robust modification which may enable it to predict the property of water away from saturation conditions more accurately, without significantly altering the structure of NASG EOS. Therefore, the proposed modification to this EOS is in line with preserving its basic structure given by Equation (3.6).

The major step in the modification is to recalculate the parameter P_∞ using a new reference state. The NIST values of density and speed of sound at the temperature of 300 K and the pressure of 1×10^5 Pa are 996.56 kg/m^3 and 1501.5 m/s respectively. Therefore, we use a new reference state that is very close to this, which is $\{P_0,\ T_0,\ \rho_0,\ c_0\}$=$\{1 \times 10^5$ Pa, 300 K, 997.0 kg/m^3, 1500 m/s$\}$. The specific volume relation and the speed of sound relation are given as follows:

$$v = \frac{(\gamma - 1)\, C_v T}{P + P_\infty} + b \tag{3.7}$$

$$c = \left[\frac{\gamma v^2 \,(P + P_\infty)}{v - b}\right]^{1/2} \tag{3.8}$$

With the new reference state the value of P_∞ and b are to be recomputed using the set of

equations (3.7) and (3.8). Rearranging equation (3.7) we get:

$$v - b = \frac{(\gamma - 1)\, C_v T}{P + P_\infty}$$

On substituting this expression of $(v - b)$ into the sound speed relation given by equation (3.8), we arrive at the following relation:

$$c = \left[\frac{\gamma v^2 \left(P + P_\infty\right)^2}{(\gamma - 1)\, C_v T} \right]^{1/2}$$

Rearranging the above equation for P_∞ we get:

$$P_\infty = \frac{c}{v} \left[\frac{(\gamma - 1)\, C_v T}{\gamma} \right]^{1/2} - P$$

On substituting the reference property values and the fixed parametric values as follows:

$$P_\infty = \frac{1500}{(1/997)} \left[\frac{(1.19 - 1) \times 3610 \times 300}{1.19} \right]^{1/2} - 1 \times 10^5 = 6.2178 \times 10^8 \,\text{Pa}$$

Now, rearranging for b from the equation (3.7):

$$b = v - \frac{(\gamma - 1)\, C_v T}{P + P_\infty}$$

On substituting the reference property values,the fixed parametric values and the updated value of P_∞ as follows:

$$b = \frac{1}{997} - \frac{(1.19 - 1) \times 3610 \times 300}{1 \times 10^5 + 6.2178 \times 10^8} = 6.7212 \times 10^{-4}\,\text{m}^3\text{/kg}$$

The values of P_∞ and b are thus calculated to be 6.2178×10^8 Pa and 6.7212×10^{-4} m^3/kg respectively. The values of parameters C_p, C_v, γ, and q are kept unaltered from the original NASG formulation. The coefficients for the modified NASG EOS are given in Table 3.2.

Table 3.2: Coefficients for the modified NASG EOS

C_p (J/kgK)	C_v (J/kgK)	γ	P_∞ (Pa)	b (m^3/kg)	q (J/kg)
4285	3610	1.19	6.2178×10^8	6.7212×10^{-4}	-1177788

3.3.1 Evaluation Strategy

For a reliable evaluation of the proposed EOS, density estimates from each EOS is compared with corresponding data from the National Institute of Standards and Technology (NIST). Refer to [68, 250] for the EOS and auxiliary models used by the NIST for generating the thermo-physical data for water. Isothermal density estimates at ten different temperatures between the range 280-370 K and over the pressure range of 1×10^5 Pa- 1×10^9 Pa are generated with the Tait EOS, the Stiffened Gas EOS, the NASG EOS, and the proposed modified version of the NASG EOS. This temperature range is chosen because it lies between the freezing point temperature (273.15 K) and the boiling point temperature (373.15 K) of water at atmospheric pressure. The specified pressure range is chosen because, the highest pressure data available in the NIST database is for 1×10^9 Pa and the lowest range 1×10^5 Pa is set close to the atmospheric pressure. The generated values are compared against the NIST isothermal data at the same temperature over the same pressure range. Accuracy of the EOS at each temperature range is quantified by calculating the average percentage error over the entire pressure range at that temperature. The trend in the variation of error with the temperature range is also analysed. To have a better understanding of the safe range of application of each EOS, the maximum percentage error at each temperature from every EOS is also calculated.

3.4 Results and Discussion

This section outlines major observations of the study. Isothermal density values are generated with the Tait EOS, the Stiffened Gas EOS, the NASG EOS, and the modified NASG EOS at ten different temperatures in the range 280 -370 K, and over the pressure range of 1×10^5 Pa to 1×10^9 Pa. These values are compared against the density values from the NIST isothermal database for the corresponding states. Accuracy of various equations of state at each temperature level is quantified by computing the respective average % error over the complete pressure range. These average % error values are reported in Table 3.3. Conclusions on the reliability of an EOS cannot be arrived at only by knowing the average error over a specified range. Information on maximum deviation of estimated values with EOS from reference values and the respective error bound over this range is also important. This will reassure that at every state point within the specified property limits, the EOS under consideration is equally reliable. The maximum % error in the density estimates with each EOS against the NIST data for all the temperature ranges studied are reported in

Table 3.4.

Table 3.3: Average % error in density estimates with EOSs against the NIST database

Temperature (K)	Average % error			
	Tait	Stiffened Gas	NASG	Modified NASG
280	0.81	40.10	5.62	2.25
290	0.50	41.29	5.03	1.79
300	0.24	43.13	4.51	1.39
310	0.31	39.29	4.20	1.12
320	0.69	35.61	3.92	0.97
330	1.14	32.35	3.66	0.87
340	1.60	29.53	3.41	0.83
350	2.08	26.89	3.18	0.82
360	2.57	24.80	2.97	0.83
370	3.07	22.82	2.78	0.87

From Table 3.3 it is observed that the average % error values associated with Stiffened Gas EOS are extremely large compared to other EOS considered. As an example, the lowest value of average error observed with Stiffened Gas EOS at a temperature of 370 K is above 20 %.The trend observed in the average error with this EOS is such that the error initially shows an increase with increase in temperature from 280 K till 300 K and then shows a continuous decrease with further rise in temperature. The highest average error value of 43.13 % is observed at the temperature of 300 K. The values of maximum % error in density from Table 3.4, clearly suggests the non-reliability of Stiffened Gas EOS for modelling water compressibility. The trend observed in the variation of maximum error with temperature for this EOS, is same as that observed with the average error. The maximum error at all the ten temperatures considered crosses the 50 % bound, and the highest error value reported is 82.67 % at 300 K.

Comparison between the Stiffened Gas EOS, the Tait EOS, the NASG EOS and the proposed modified version of the NASG EOS with the NIST isothermal data for 300 K is shown in Figure 3.1. Isothermal density values predicted by each of the EOS at 300 K over complete pressure range is displayed in the Figure 3.1(a) along with NIST data in continuous bold line. Figure 3.1(b) provides the corresponding % error computed against the NIST data for this temperature. Figures 3.2 and 3.3 display the comparison of densities and associated errors with different EOS for the temperatures of 330 K and 360 K respectively.

Table 3.4: Maximum % error in density estimates with EOSs against the NIST database

Temperature (K)	Maximum % error			
	Tait	Stiffened Gas	NASG	Modified NASG
280	1.22	70.36	7.05	2.40
290	0.93	76.10	6.05	2.06
300	0.66	82.67	5.21	1.78
310	0.56	77.90	4.58	1.53
320	1.00	73.05	4.24	1.40
330	1.47	68.50	3.95	1.99
340	1.96	64.30	3.71	2.51
350	2.50	60.17	3.48	2.95
360	3.08	56.60	3.29	3.32
370	3.79	53.08	3.11	3.63

If the complete density versus pressure plot for Stiffened Gas EOS were to be included in these figures, the respective plots for other state equations could not have been clearly displayed due to the large disparity in the density scales involved. For this reason, only a portion of the density versus pressure plot for this EOS is shown in all these figures. The partly visible data itself implies large deviations associated with Stiffened Gas EOS in comparison to NIST data. The results of Stiffened Gas equation is limited in the error plots also, as the error in density estimates is found to be very large and hence would impede the clear visualisation of results from other EOS.

The average error in density estimates with Tait EOS follows a trend where the maximum accuracy of this EOS is observed at 300 K and the accuracy reduces to either side of the temperature scale as one moves away from 300 K. This observation is attributed to the fact that the parameters P_0 and ρ_0 in Tait EOS is defined at the reference temperature of 300 K. It is also worthwhile to note that Tait EOS is highly accurate over temperature range of 280 - 320 K where the average error is below 1 %. The maximum error in density estimates with Tait EOS also exhibits a similar trend, with the exception that the minimum value is observed against temperature of 310 K. The results from Tait EOS shifting farther away from the NIST data at higher temperatures are clearly depicted in Figures 3.2 and 3.3. However, we could also see that the highest error reported with this EOS for the entire range considered is under 4 %.

From the values in Table 3.3, the NASG EOS shows a steady decrease in both average

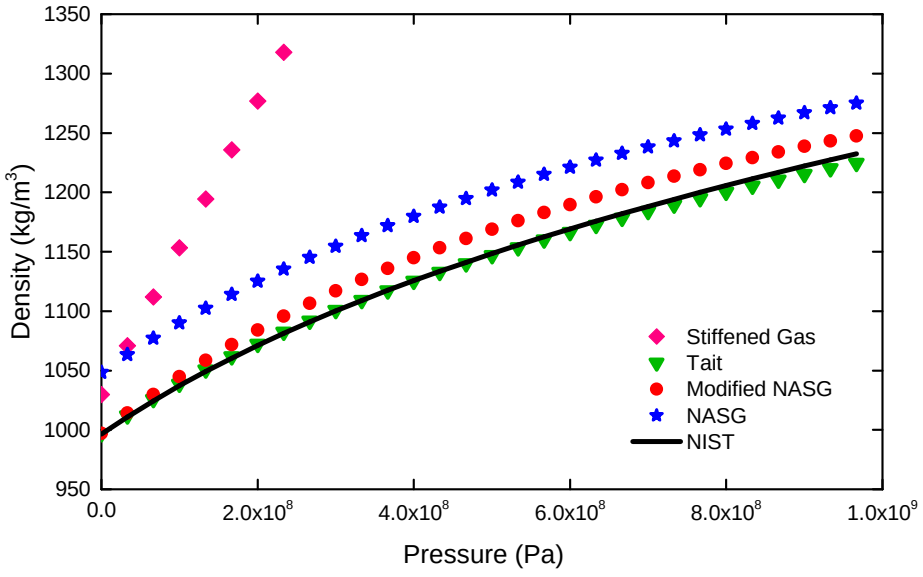

(a)

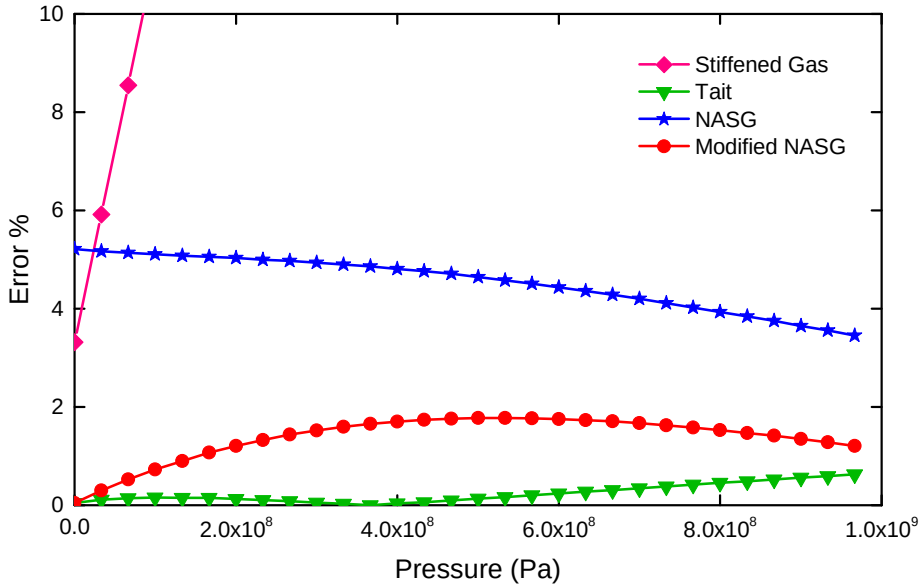

(b)

Figure 3.1: Comparison of EOS with NIST data at 300 K

error and maximum error with increase in the temperature range. This behaviour of NASG EOS is expected because it is originally developed to predict the properties of water close to the saturated liquid line. As the state of liquid moves farther away from the saturation region, accuracy of the property estimates using this EOS diminishes. The average error reaches slightly above the 5 % bound with NASG EOS for temperatures below 300 K. The 5 % bound in maximum error with this EOS is observed for temperatures below 310 K, and

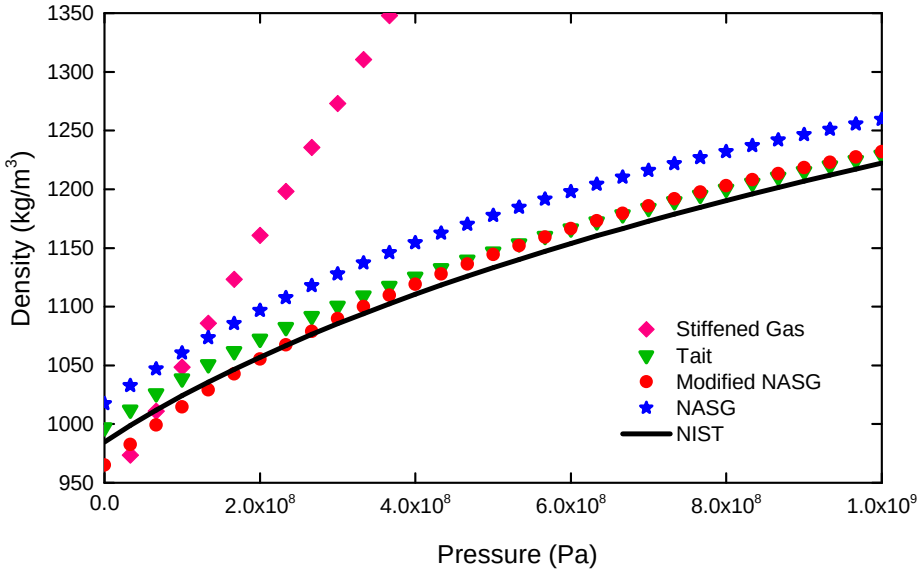

(a)

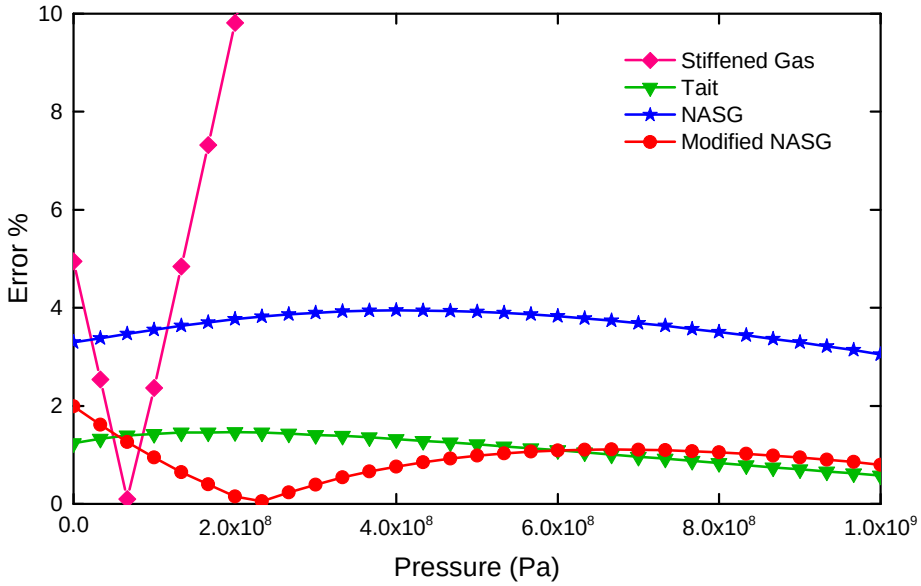

(b)

Figure 3.2: Comparison of EOS with NIST data at 330 K

the highest value of error within the entire range studied is just above 7 %.

It is observed from Table 3.3 that the average error of the modified NASG EOS continuously decreases from 280 K to 350 K, and then slightly increase towards 370 K. However, from Table 3.4 it is observed that maximum error in density estimate for the modified EOS continuously decreases and reaches a minimum at about 320 K and increases thereafter. This is because, the parameters of the modified NASG EOS are recomputed using a new

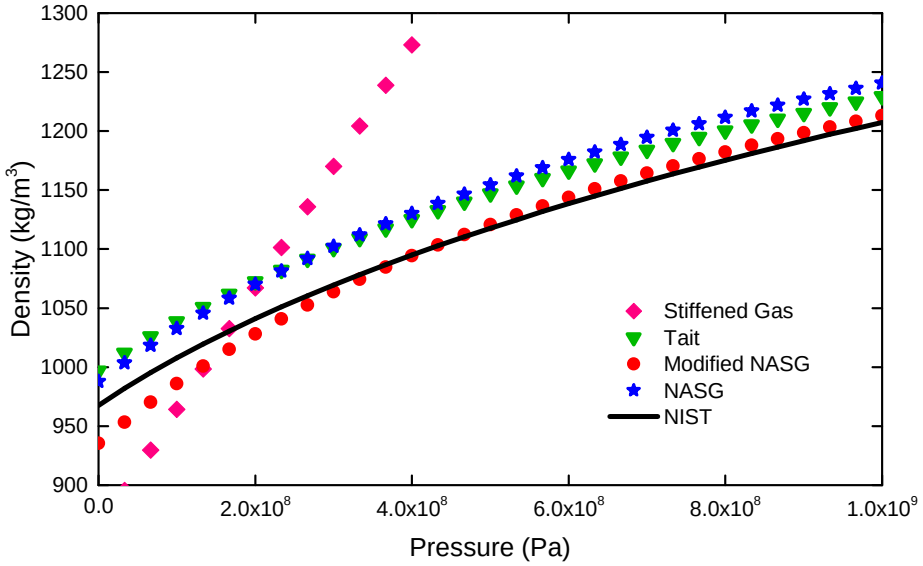

(a)

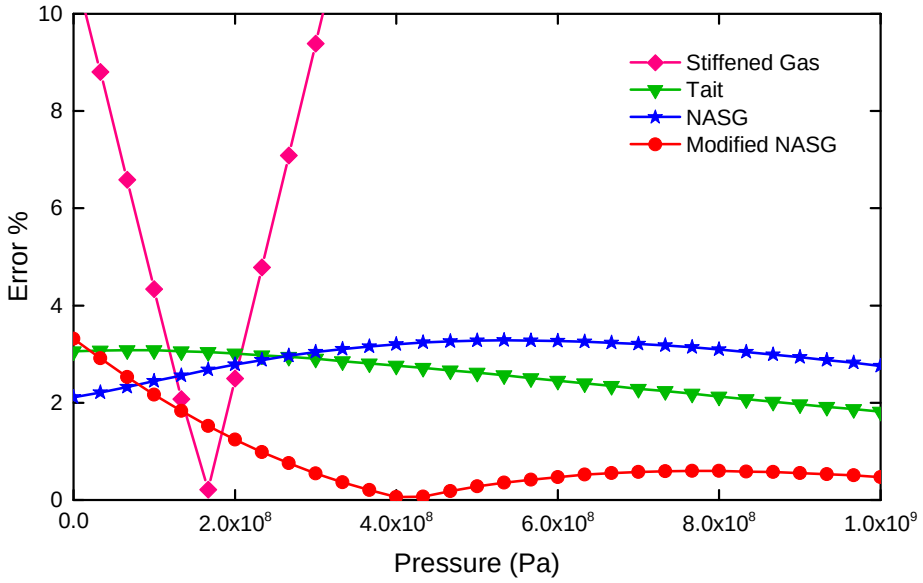

(b)

Figure 3.3: Comparison of EOS with NIST data at 360 K

reference state at the temperature of 300 K and pressure of 1×10^5 Pa, and as the temperature moves farther away from 300 K the accuracy of prediction at lower pressure range decreases resulting in increase of maximum error. This increase in maximum error is not reflected in the average error value up to 350 K. This is because the under-prediction of density with modified NASG EOS occurs only towards the lower pressure range and the error over the remaining range of pressure is very small in magnitude. The density plot and

the error plot at 330 K as given in Figures 3.2(a) and 3.2(b) demonstrate this very clearly.

From the error values reported in Table 3.3 it could be concluded that density estimates using modified NASG EOS is superior to the original version of NASG EOS over the entire temperature range studied. It can also be seen from Figure 3.1 that error estimate in density is superior for the entire range of pressure at 300 K when modified EOS is used. From Figure 3.1 (b), we can see that the maximum error for NASG EOS which is slightly above 5 %, is brought down to below 2 % by the proposed modification to this EOS. The modified NASG EOS is observed to be highly accurate over higher temperature range of 330 K to 370 K with average error below 1 % and is clearly superior to Tait EOS in this temperature range. However, at the temperature ranges close to 300 K, as observed from Fig. 3.1, Tait EOS predicts density closest to NIST data with maximum error below 1 %.

It can be observed from the Figure 3.2, for temperature range close to 330 K, for pressures above 1×10^8 Pa, the modified NASG EOS is much more accurate than Tait EOS, and a major portion of density estimates in this range falls below 1 % error bound. For higher temperatures close to 360 K range, as Figure 3.3 demonstrates, modified NASG is clearly dominant over all the other EOS. Except for lower pressure ranges, this EOS offers density estimates with error below 0.5 %, which is almost one fourth of the error associated with Tait EOS over the same region. From the entire data available in Tables 3.3 and 3.4, we could clearly observe that lowest error bounds are maintained by modified NASG EOS, which falls below 4 % and is also marginally superior to that of Tait EOS.

Reliability of various equations of state in estimating different fluid properties could be elucidated from the quantitative analysis performed here. However, a qualitative analysis is also needed to determine the applicability of these EOS for various flow problems. The Stiffened Gas, the NASG, and the modified NASG, all three are non-isothermal equations of state. However, the Tait EOS, which is amongst the most accurate state equations for water, is isothermal. That is to say that the Tait EOS is incapable of relating variations in fluid temperature to other fluid properties. Because of this drawback, the application of Tait EOS is limited to isothermal and near-isothermal flow cases. Therefore, Tait EOS could not be relied upon for modelling flow problems involving considerable variation in temperature. Though the other three non-isothermal EOS mentioned could relate fluid temperature to other fluid properties, there are also few limitations. As already explained, Stiffened Gas EOS is non-reliable because of the very low accuracy in property estimates. The NASG EOS can be reliably applied for modelling isothermal and non-isothermal flow problems, subject to the limited accuracy of this EOS.

The modified NASG EOS is, therefore, the most suitable choice for modelling com-

pressibility effects in water for isothermal and non-isothermal flow cases, especially where high accuracy is expected in fluid property estimates. For example, we could consider the theoretical problem of a liquid shock tube with water as the tube fluid. For such a non-isothermal compressible-flow problem, where the transient variations in temperature and pressure are expected to be large, the EOS used for modelling compressibility effects in liquid is also expected to robust. An isothermal EOS, irrespective of its accuracy, may not model the complete physics of such a problem.

From the quantitative evaluation of equations of state by comparing them with the NIST data, and by analysing them qualitatively for their applicability, we claim overall superiority of the modified version of NASG EOS over the other three equations of state considered. The high accuracy in density estimates provided by modified NASG EOS over the entire range of pressure and temperature studied, coupled with its ability to capture the physics of problems for wide range of temperature variation, clearly demonstrates the superiority of this equation of state. The modified NASG EOS is hence recommended for situations where high accuracy in density estimation is desired and to model compressible liquid water over the temperature range of 280 K to 370 K and pressure range extending from 1×10^5 Pa to 1×10^9 Pa, within which maximum error is under 4 %.

3.5 Summary

An equation of state (EOS) for compressible water is presented for the application over a wide range of pressure. The proposed EOS is a modified form of Noble Abel Stiffened Gas equation (NASG) which was originally developed for the prediction of saturation properties of water. Three well-known EOS for water viz., the Tait EOS, the Stiffened Gas EOS, and the NASG EOS are used in the comparative study of the proposed EOS. Accuracy of density estimates of the modified EOS is quantified by comparing it with the published NIST data. Evaluative study of the EOS is performed over pressure range of 1×10^5 Pa to 1×10^9 Pa and temperature range of 280 K to 370 K. The analysis reveals supremacy of the modified version of the NASG EOS over the original version for its improved accuracy and suggests its applicability over a wide range of pressure. The accuracy of the proposed EOS is very high and even comparable with that of the Tait EOS at lower temperature range. At higher temperature range from 330 K to 370 K this EOS is found to be far more accurate than Tait EOS. A qualitative analysis is also performed based on the capability of various EOS to model isothermal and non-isothermal flow problems. The combined analysis is used to demonstrate the robustness of modified NASG EOS. The superiority of modified

NASG EOS over Tait EOS in modelling non-isothermal flow problems with high accuracy is also revealed in this study.

Chapter 4

Analytical Solution to the Water Shock Tube: A Benchmark Problem in Compressible Liquid Flows

4.1 Introduction

Developing flow solvers for numerical simulation of compressible liquid flows with sharp change in properties and benchmarking them is a challenging task. This is mainly due to the lack of relevant test case problems for which analytical solution is available. The conventional shock-tube problem of Sod [251] which uses air as working fluid, is the most commonly used test case for benchmarking flow solvers developed for simulation of compressible flows. The main reason for selecting Sod's shock-tube problem is that it has a relatively simple setup and an exact solution [252] available. The application of this test problem, however, is limited to gases, since analytical solution with liquid shock-tube problem is not currently available in the literature. More information on gas shock tube problem such as problem setup, associated flow physics, and its various applications are presented in Section 2.4 of Chapter 2.

In this chapter we attempts to develop an analytical solution for shock tube problem with liquid water as the working fluid. The main pre-requisite for the development of an analytical solution for a problem involving compressible liquid is an equation of state (EOS) for liquid. The liquid EOS plays a crucial role in the development of solution by providing additional relations which are required for mathematical closure. We have earlier developed an equation of state for compressible water called the Modified NASG EOS [253] in Chapter 3. This equation of state is capable of producing high accuracy density estimates

over a wide range of pressure. It is reformulated and combined into the analytical solution for a gas shock tube, to develop the new analytical solution for liquid (water) shock tube problem. Information on various studies and applications related to liquid shocks and shock tube experiments are available in Section 2.5 of Chapter 2.

This chapter is organised as follows. Section 4.2 explains setup of the water shock tube problem. Selection of a suitable equation of state and the steps involved in its reformulation into a simpler form are outlined in Section 4.3. The complete analytical solution procedure including various modified thermodynamic relations are presented in Section 4.4. Important results and observations related to the exact solution developed are explained and discussed in the sections that follow. The expected structure of solution for water shock tube problem and its range of application are explained in Section 4.5. Solutions to water shock tube and air shock tube for a selected problem setup are compared against each other in Section 4.6. Section 4.7 demonstrates the applicability of the developed analytical solution over the complete range of properties specified through solutions obtained for different cases of the problem. Section 4.8 briefly summarises this chapter.

4.2 The Water Shock Tube Problem

The water shock tube problem is a modification of one-dimensional shock tube problem of Sod [251], where fluid inside the shock tube is single phase liquid water. Similar to the case for a gas shock tube, there are two chambers containing liquid at different pressures, separated by a diaphragm. Schematic of the initial problem setup is shown in Figure 4.1.

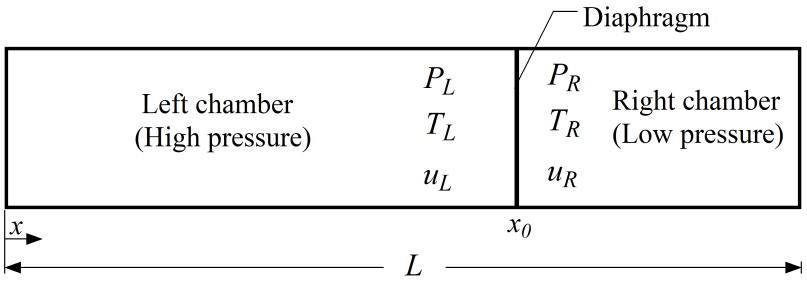

Figure 4.1: Schematic of the Water shock tube problem setup.

A one-dimensional shock tube geometry is used with a length of L. The diaphragm is initially located at a distance of x_0 from the left closed-end boundary. The left chamber of shock tube holds water under comparatively high pressure of P_L and the chamber on the right contains water at lower pressure P_R. Initially, the fluid is assumed to be stationary

with flow velocities in both chambers, $u_L = u_R = 0$. The flow is initially at isothermal conditions inside the entire shock tube, i.e., $T_L = T_R$. Liquid water inside the shock tube is modelled as compressible and densities ρ_L and ρ_R are estimated using a suitable liquid equation of state. The water shock tube problem is solved for flow properties at a time t_A from the rupture of the diaphragm. This time period is selected such that, within this duration no shock reflections or wave interactions are initiated. This is because, with reflection of waves at boundaries and from consequent interactions, the physics of flow becomes very complicated.

Similar to gas shock tube problem, liquid shock tube problem also offers numerous advantages when used as a test problem for benchmarking flow solvers. Simplicity in problem setup is one of its notable advantages as it eases modelling of this problem using a variety of numerical solvers with relatively simple codes. Sufficiency of one-dimensional treatment is another main benefit offered by this problem. From the perspective of flow physics, liquid shock tube problem involves abrupt variations in fluid temperature, pressure, density, speed of sound etc. Additionally, solution to this problem is expected to have flow features like shock, expansion fan, and contact-discontinuity. The above factors make this problem a perfect candidate for using it as a benchmark problem for compressible flow solvers. As a result, numerical solvers tested using this problem are checked for a variety of qualities that are required to conclusively solve this problem.

There are two important considerations for the development of analytical solution to liquid shock tube problem. The first one is to identify a suitable and accurate liquid equation of state to model liquid compressibility effects. The chosen liquid EOS should also smoothly fit into rest of the solution procedure. The second consideration is to develop a relatively simple solution procedure that would be capable of accurately estimating the location of different zones and could also provide corresponding property values over these zones.

4.3 The Equation of State and its Reformulation

Water density is nearly constant up to a few bars of pressure above the atmospheric pressure, however, for pressures above 10 MPa, variation in density cannot be ignored. A suitable liquid equation of state is needed to compute the variations in density, as it could relate pressure and temperature to this fluid property. Generally, liquid water EOS are defined over relatively small pressure ranges over which they are accurate. Tait EOS [81, 85, 245] and Modified NASG EOS [253] are two highly accurate equations of state for water defined

over a wide range of pressure. Since Tait EOS cannot provide proper coupling between fluid density and temperature [253], the Modified NASG EOS has been selected as liquid EOS in the present work.

As the name suggests, the Modified NASG EOS is a modification to Noble-Abel Stiffened Gas equation proposed by Métayer and Saurel [90]. The caloric relation of Modified NASG EOS is given as follows:

$$P = (\gamma - 1)\,\frac{(\varepsilon - q)}{(v - b)} - \gamma P_{\infty} \tag{4.1}$$

The equations for specific volume v and speed of sound c are as follows:

$$v = \frac{(\gamma - 1)\,C_v T}{P + P_{\infty}} + b \tag{4.2}$$

$$c = \left[\frac{\gamma v^2\,(P + P_{\infty})}{v - b}\right]^{1/2} \tag{4.3}$$

We intend to make use of the analytical solution procedure used for a gas shock tube with certain modifications. For this, liquid EOS needs a reformulation similar to that of ideal gas equation of state, $P = \rho RT$, to make it compatible for the analytical solution procedure. Keeping this in mind, specific volume relation in Equation (4.2) can be rearranged as follows:

$$P + P_{\infty} = \frac{(\gamma - 1)\,C_v T}{v - b} \tag{4.4}$$

Further, to simplify expressions used hereafter, we define new variables such as stiffened pressure $\bar{P}$ and stiffened density $\bar{\rho}$ as follows:

$$\bar{P} = P + P_{\infty} \tag{4.5}$$

$$\bar{\rho} = \frac{1}{v - b} \tag{4.6}$$

For a liquid modelled as compressible fluid using a stiffened equation of state, the underlying theory is that, for lower values of absolute pressure P, the absolute liquid density ρ is almost a constant. While, for higher values of P, which is of the order of parameter P_{∞}, liquid density ρ exhibits considerable variation with pressure. For Modified NASG EOS used in this study, by defining two new variables in Equations (4.5) and (4.6), this idea is further simplified. Here, one could just consider that, for the liquid under consideration,

new density variable $\bar{\rho}$ varies based on new pressure variable $\bar{P}$ for all ranges. To take this idea closer to that of an ideal gas, we define a new constant parameter R_W for the liquid that is similar to characteristic gas constant. The liquid constant parameter R_W is defined as follows:

$$R_W = (\gamma - 1)\, C_v \tag{4.7}$$

From the above definitions, Modified NASG EOS in Equation (4.4) takes the form:

$$\bar{P} = \bar{\rho} R_W T \tag{4.8}$$

which has the form of an ideal gas equation of state. Along with this, a stiffened speed of sound ($\bar{c}$) is also defined based on stiffened pressure $\bar{P}$ and stiffened density $\bar{\rho}$ as follows:

$$\bar{c} = \sqrt{\frac{\gamma \bar{P}}{\bar{\rho}}} \tag{4.9}$$

Reformulation of the Modified NASG EOS as mentioned above resulted in two new simplified relations given by Equations (4.8) and (4.9), which will be used in analytical solution procedure. Detailed theories on equations of state, bond energies and heat capacities are available in [254].

4.4 The Analytical Solution

Following the rupture of diaphragm inside shock tube and before the generated shock wave reflects at any of the boundaries, the domain of shock tube is typically composed of five zones as displayed in Figure 4.2. The zones marked as L and R are respectively left and right undisturbed regions where the properties are unchanged from initial conditions. This is because, within this time period, no wave has traversed through these zones. Zone 1 is the region between contact surface and shock, over which shock wave has already traversed. Zone 2 is the region between contact surface and trailing edge of the expansion wave. This is the region through which rarefaction waves have completed propagation. The zone marked E is the region where expansion fan spreads at the given moment. Inside the expansion wave, there is continuous variation of flow properties from values at zone 2 to that at zone L.

Analytical solution procedure described below is in line with the procedure outlined in the reference [252] for gas shock tube problem. The procedure uses several thermodynamic

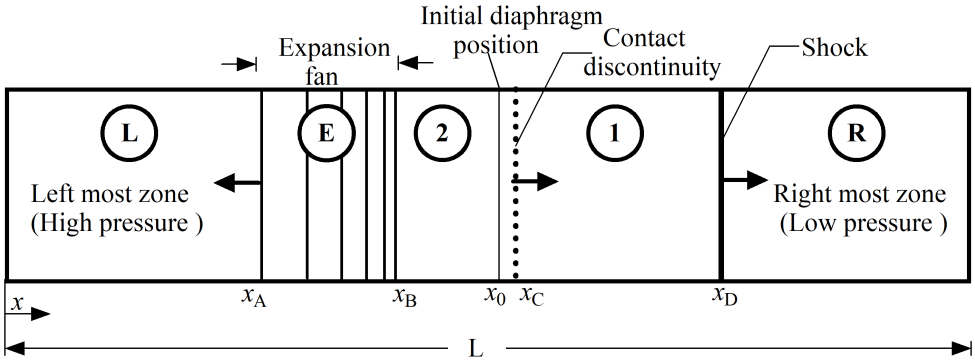

Figure 4.2: Different zone formations inside the shock tube before reflection at boundaries

relations such as isentropic flow relations, equation of state for fluid, Rankine-Hugoniot relation, and acoustic relations for the speed of wave propagation in fluid. The property relations used for gaseous case are reformulated with corresponding relations for liquid case. In the analytical solution procedure, all properties are denoted using appropriate subscripts to identify their location. The solution procedure starts with development of an expression for the unknown pressure ratio P_1/P_R across the shock, from the known diaphragm pressure ratio P_L/P_R. Replacing pressure, density, and speed of sound by corresponding stiffened relations defined above in Equations (4.5) to (4.9), and then following a similar procedure as used in the case of gas shock tube, we arrive at an expression for shock pressure ratio as follows:

$$\frac{\bar{P}_L}{\bar{P}_R} = \frac{\bar{P}_1}{\bar{P}_R}\left[1 - \frac{(\gamma-1)\left(\frac{\bar{c}_R}{\bar{c}_L}\right)\left(\frac{\bar{P}_1}{\bar{P}_R} - 1\right)}{\sqrt{2\gamma}\sqrt{2\gamma + (\gamma+1)\left(\frac{\bar{P}_1}{\bar{P}_R} - 1\right)}}\right]^{-\left[\frac{2\gamma}{\gamma-1}\right]} \tag{4.10}$$

As Equation (4.10) is an implicit expression, standard iterative methods such as Regula-Falsi can be applied to solve shock pressure ratio. From the new shock pressure ratio obtained, the value of $\bar{P}_1$ is calculated by substituting the known value of $\bar{P}_R$. The absolute pressure upstream of the shock can be then computed back using Equation (4.5) as $P_1 = \bar{P}_1 - P_\infty$. The speed of sound at each region is computed from the acoustic relation consistent with EOS given by Equation (4.3). Shock speed, u_S, is calculated from the following relation:

$$u_S = c_R\sqrt{\left(\frac{\gamma+1}{2\gamma}\right)\frac{\bar{P}_1}{\bar{P}_R} + \left(\frac{\gamma-1}{2\gamma}\right)} \tag{4.11}$$

Flow velocity in the upstream region of the shock, u_1, is estimated using the relation:

$$u_1 = \frac{\bar{c}_R}{\gamma}\left(\frac{\bar{P}_1}{\bar{P}_R} - 1\right)\sqrt{\frac{\left(\frac{2\gamma}{\gamma+1}\right)}{\frac{\bar{P}_1}{\bar{P}_R} + \left(\frac{\gamma-1}{\gamma+1}\right)}} \tag{4.12}$$

Stiffened density in the upstream region of the shock, $\bar{\rho}_1$, is computed from modified Rankine-Hugoniot relation as follows:

$$\bar{\rho}_1 = \bar{\rho}_R \frac{\left(\frac{\gamma+1}{\gamma-1}\right)\frac{\bar{P}_1}{\bar{P}_R} + 1}{\left(\frac{\gamma+1}{\gamma-1}\right) + \frac{\bar{P}_1}{\bar{P}_R}} \tag{4.13}$$

Absolute density in the upstream region of the shock, ρ_1, is obtained back using Equation (4.6) as follows:

$$\rho_1 = \frac{\bar{\rho}_1}{1 + b\bar{\rho}_1} \tag{4.14}$$

The specific internal energy ε over all zones is computed using the relation (4.1). Since there are no discontinuities present in flow velocity and pressure across the contact surface, these properties have the same values over zones 1 and 2. Therefore, we have:

$$u_2 = u_1 \quad \text{and} \quad P_2 = P_1 \tag{4.15}$$

The density value over region 2 is computed using isentropic relation across the expansion fan as follows:

$$\bar{\rho}_2 = \bar{\rho}_L \left(\frac{\bar{P}_2}{\bar{P}_L}\right)^{\frac{1}{\gamma}} \tag{4.16}$$

As already mentioned, absolute value of liquid density over this region is computed back using Equation (4.6). After obtaining necessary expressions to compute the required properties over different zones, the major task remaining is to locate various zones at any given time.

Different zones need to be identified and represented in the (x, t) plane. The typical representation of zones in the (x, t) plane for gas shock tube problem was shown in Figure 2.3 in Chapter 2. Liquid shock tube problem has a similar representation of zones on these co-ordinates. All different waves generated are centred at the initial position of the diaphragm, i.e., at (x_0,0). Shock wave and contact discontinuity propagate through uniform

zones. Due to this, they have constant velocities and hence they are displayed as straight lines in the (x, t) diagram. The expansion wave propagates through expansion fan (E), inside which flow parameters vary continuously. We also observed that shock wave and contact discontinuity are propagated to the right of the initial position of the diaphragm, while the expansion fan propagated to its left. Figure 4.3 is the $x - t$ diagram that shows propagation of different waves and characteristics.

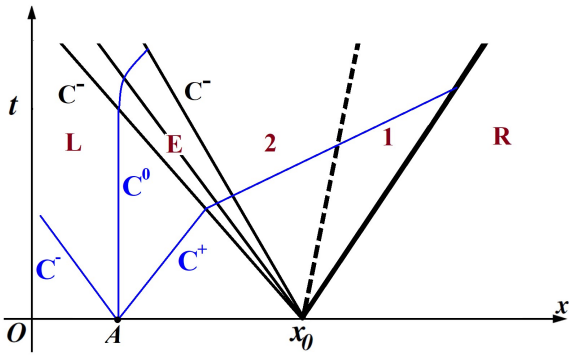

Figure 4.3: The $x - t$ diagram showing the characteristic propagation

While considering the relation of parameters in zone (2) to those in zone (L), we could observe that only C^0 and C^+ characteristics cross the expansion fan to search for information in region (L). The expansion fan (E) is bounded on the left by C^- characteristic originating from point x_0. This characteristic also belongs to region (L), due to which the line of slope $dx/dt = -c_L$. The right extreme of the expansion fan is bounded by another C^- characteristic originating from the same point x_0. However, this characteristic is considered to belong to region (2), resulting in the line of slope, $dx/dt = u_2 - c_2$.

Inside the expansion fan, we know that there will be a continuous variation in properties as we observe with gas shock tube. For a liquid shock tube, we cannot predict whether these changes will be gradual or abrupt. However, we follow the same procedure that is used for a gas shock tube problem. We begin by considering a point (x, t) inside the expansion fan (E) at any time instant t, such that, $x_A \leq x \leq x_B$. This point belongs to a C^- characteristic starting from the initial location of diaphragm x_0 [255], therefore we have:

$$\frac{x - x_0}{t} = u_E(x) - c_E(x) \tag{4.17}$$

From C^+ characteristics originating from zone (L) and entering into the expansion fan (E) we have:

$$c_E(x) + (\gamma - 1)\frac{u_E(x)}{2} = c_L \tag{4.18}$$

Combining Equations (4.17) and (4.18) for isentropic flow inside the expansion fan, we arrive at the following relation for the speed of sound inside the fan:

$$c_E(x) = \frac{2c_L}{1+\gamma} + \left(\frac{1-\gamma}{1+\gamma}\right)\left(\frac{x-x_0}{t}\right) \tag{4.19}$$

Using isentropic relation, the value of stiffened pressure inside the expansion fan is estimated as:

$$\bar{P}_E(x) = \bar{P}_L\left(\frac{c_E(x)}{c_L}\right)^{\frac{2\gamma}{\gamma-1}} \tag{4.20}$$

Subsequently the absolute value of pressure inside the expansion fan is computed using Equation (4.5) as follows:

$$P_E(x) = \bar{P}_E(x) - P_\infty \tag{4.21}$$

Isentropic relation is also used for the calculation of stiffened density values inside expansion wave which are given by:

$$\bar{\rho}_E(x) = \bar{\rho}_L\left(\frac{\bar{P}_E(x)}{\bar{P}_L}\right)^{\frac{1}{\gamma}} \tag{4.22}$$

Absolute values of density inside this zone are obtained back using the relation (4.6) as follows:

$$\rho_E(x) = \frac{\bar{\rho}_E(x)}{1 + b\bar{\rho}_E(x)} \tag{4.23}$$

The specific internal energy values inside the expansion fan are estimated using the relation (4.1). From the computed values of stiffened pressure and stiffened density, stiffened speed of sound for the zone is estimated using Equation (4.9) as follows:

$$\bar{c}_E(x) = \sqrt{\frac{\gamma\bar{P}_E(x)}{\bar{\rho}_E(x)}} \tag{4.24}$$

The velocity inside the expansion fan is computed using Equation (4.18) as:

$$u_E(x) = \left(\frac{2}{\gamma-1}\right)(\bar{c}_L - \bar{c}_E(x)) \tag{4.25}$$

Temperature over different zones in shock tube domain are computed using Equation (4.4) as shown below:

$$T = \frac{(P+P_\infty)(v-b)}{(\gamma-1)\,C_v} \tag{4.26}$$

The extent of different zones in liquid shock tube solution are computed from respective sound speeds and flow velocities available across these zones. The respective relations for the case of a gas shock tube are available in [255], and for liquid shock tube problem these relations are as follows:

$$x_0 = x_0 \text{ (fixed)} \tag{4.27a}$$

$$x_A = x_0 - c_L t \tag{4.27b}$$

$$x_B = x_0 + (u_2 - c_2)\, t \tag{4.27c}$$

$$x_C = x_0 + u_2 t \tag{4.27d}$$

$$x_D = x_0 + u_S t \tag{4.27e}$$

Finally, the analytical solution over the entire solution domain is represented as follows:

$$W(x,t) = \begin{cases} W_L & ; \quad x < x_A \\ W_E & ; \quad x_A \leq x < x_B \\ W_2 & ; \quad x_B \leq x < x_C \\ W_1 & ; \quad x_C \leq x < x_D \\ W_R & ; \quad x \geq x_D \end{cases} \quad \text{where} \quad W(x,t) = \begin{bmatrix} \rho \\ u \\ P \\ T \\ c \end{bmatrix} \tag{4.28}$$

W in Equation (4.28) represents solution vector whose components are required primitive flow variables. This solution vector carries different values based on the zone over which it is defined. As there are five zones in the domain, the vector is also split into five piece-wise solutions as given by Equation (4.28). At any time instant after the rupture of diaphragm, all zones except the expansion zone (E) carry constant value for the solution vector over that entire zone. For the expansion fan, however, the solution is a function of spatial distance inside shock tube domain.

4.5 Structure of Solution and Range of Applicability

In Section 4.3, we have seen the reformulation of Modified NASG EOS to a simpler form similar to an ideal gas equation. In the previous section, Section 4.4, the complete procedure for developing analytical solution for water shock tube problem was discussed. It also showed the inclusion of reformulated EOS into the solution procedure. In Section 4.4, complete analytical solution to water shock tube problem is also presented in the form of

a set of piece-wise solutions applicable over different zones formed in the solution profile. The typical structure of solution profiles for flow properties, viz., velocity, pressure, density, and temperature for a gas shock tube are shown in the Figure 4.4. Based on the piece-wise analytical solution developed for water shock tube problem, we also expect a similar structure of solution. Different zones in the solution profiles are marked L, E, 2, 1, and R as shown in Figure 4.2.

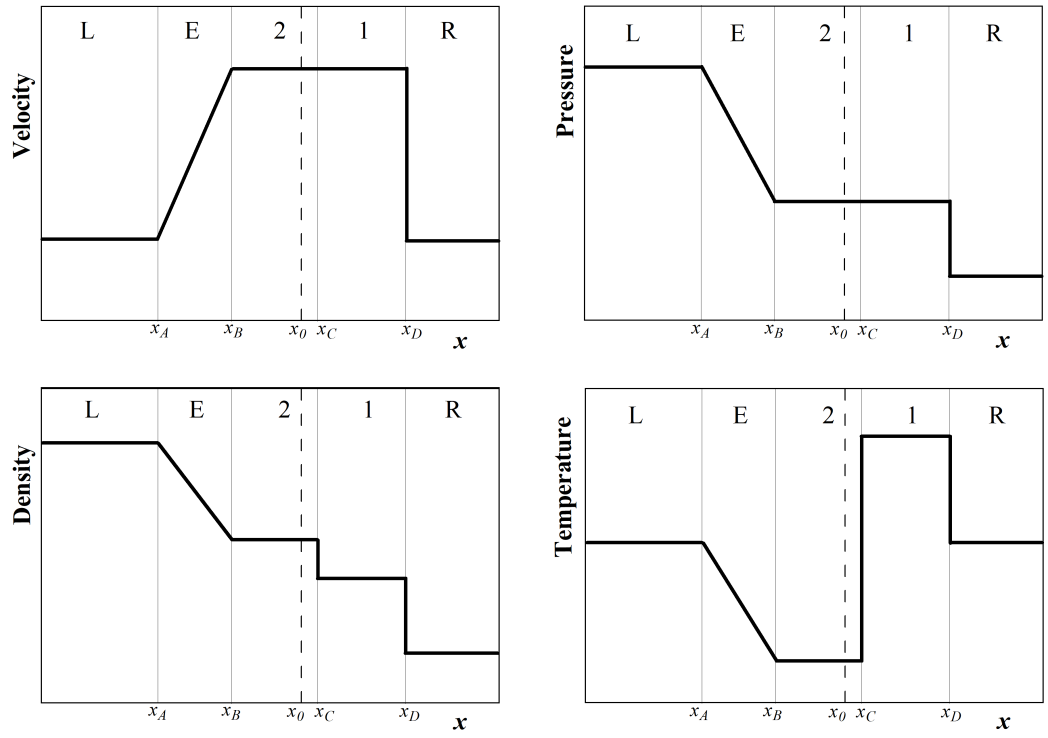

Figure 4.4: The typical structure of analytical solution for the water shock tube problem.

AS we can see form Figure 4.4, the solution is divided into five different zones. It can be observed that all flow variables are discontinuous across the shock. The pressure and velocity remain uniform over the region between the shock and trailing edge of the expansion fan (zones 1 and 2). The properties density and temperature, however, exhibit a jump discontinuity across the contact surface. We could also observe that inside the expansion fan (zone E), all properties vary continuously. Zones L and R are respectively the leftmost and rightmost zones over which no waves have traversed within the duration used in computation. Because of this, the properties in these zones are unaltered from their initial conditions.

Though we are able to obtain the structure of the solution to water shock tube problem, it may be insufficient for complete understanding of the behaviour of the solution. The

scale over which different flow properties change depends on initial pressure ratio across the diaphragm, chemical composition of the gas, shock tube geometry etc. Though the basic structure remains the same, the extent of variation of properties, the sharpness of different flow features etc., may vary. For better understanding of this behaviour we need to obtain and observe the solution profiles for different physical configurations. However, the prerequisite to this is the knowledge of the range of applicability of the newly developed analytical solution itself.

The suitable range of application of the analytical solution for water shock tube problem is the same as the prescribed range for the equation of state of liquid. The range of application of the liquid EOS extends over pressure of 0.1 MPa-1000 MPa and temperature of 273 K-373 K. Outside this range, as we cannot claim reliability of the equation of state, the solution developed using this relation also becomes unreliable. To present the results over this entire specified range, we solved different cases of water shock problem by changing initial conditions. The ranges of properties are selected in such a way that they span the complete applicable range of pressure and temperature.

4.6 Solutions of Water Shock Tube and Air Shock Tube: A Comparison

During the developmental stages of analytical solution to water (liquid) shock tube problem, we have frequently referred to corresponding stages in air (gas) shock tube problem. This is because of the similarities in flow physics and also to understand the salient differences between the cases for a liquid and a gas. Consequently, in the developed analytical solution for liquid case we could again observe many similarities with that of gaseous case. We proceed further and obtain the solution profiles for water shock tube problem for a chosen set of initial physical conditions. Before independently analysing these results, we need to compare them with solution profiles for air shock tube problem. However, for the comparison to be focussed on core parameters, we have to minimise difference associated with physical setup for the two fluids to the maximum possible extent. Therefore, we obtained the solution to water shock tube problem and air shock tube problem for the same one-dimensional shock tube geometry and initial thermodynamic conditions such as pressure and temperature. Moreover, the solution profiles for both cases are obtained after the same duration from the rupture of the diaphragm. The common initial setup used for the two problems is shown in the Figure 4.5.

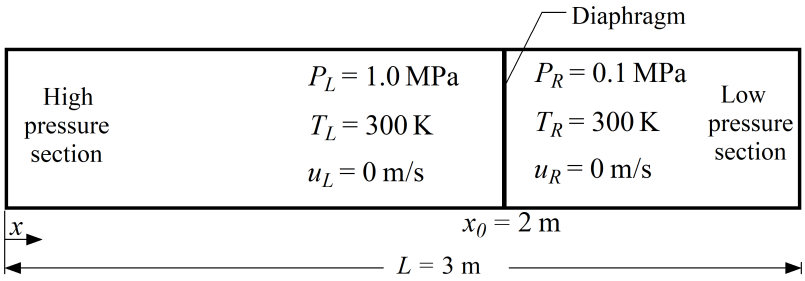

Figure 4.5: The common problem setup for the water and air shock tube cases

The shock tube has a total length of $L = 3\,\text{m}$ and the diaphragm is initially located at a distance of $x_0 = 2\,\text{m}$ from the left closed-end boundary. The pressure in the high pressure driver section towards the left side of the diaphragm, $P_L = 1\,\text{MPa}$ and the driven section pressure $P_R = 0.1\,\text{MPa}$. Initially, the fluids on both sections of the shock tube are stationary and the temperature is 300 K over the entire shock tube domain. The difference in the setup for the two fluids are the fluids themselves and their corresponding fluid densities. The diaphragm is assumed to have undergone an instantaneous rupture. The solution profiles after a duration of $400\,\mu\text{s}$ from this rupture are used for the comparative study. The analytical solutions with two different tube fluids are compared in Figure 4.6.

The profiles for water shock tube are displayed using continuous blue curves while those for air shock tube are represented using red curves. From the figure, the structure of solution profiles for water shock tube is observed to be similar to that of the gas shock tube, with five distinct zones present. However, difference in the spread of zones for the two fluids is notable. Water being the denser fluid has a higher speed of sound in the medium compared to that of air. This leads to more spread out zones for water shock tube case because of the farther wave motion within a given time duration. However, inside the expansion fan, the observation is in contrast to the above. The profiles show a sharper expansion zone with water as the tube fluid, and almost resemble another discontinuity for the selected problem setup. The air shock tube shows a wider expansion fan with a gradual variation of properties. This observation could be attributed to the larger relative variation in the sound speed across the fan for the air medium compared to a minor change for the liquid case. It should also be mentioned that the expansion fan for air shock tube seems to be little sharp compared to what we usually observe in gas shock tube problems. This is due to the short duration after which the solution profiles are selected. For the same air shock tube setup, as the time progresses the expansion region widens and the property variations become more gradual.

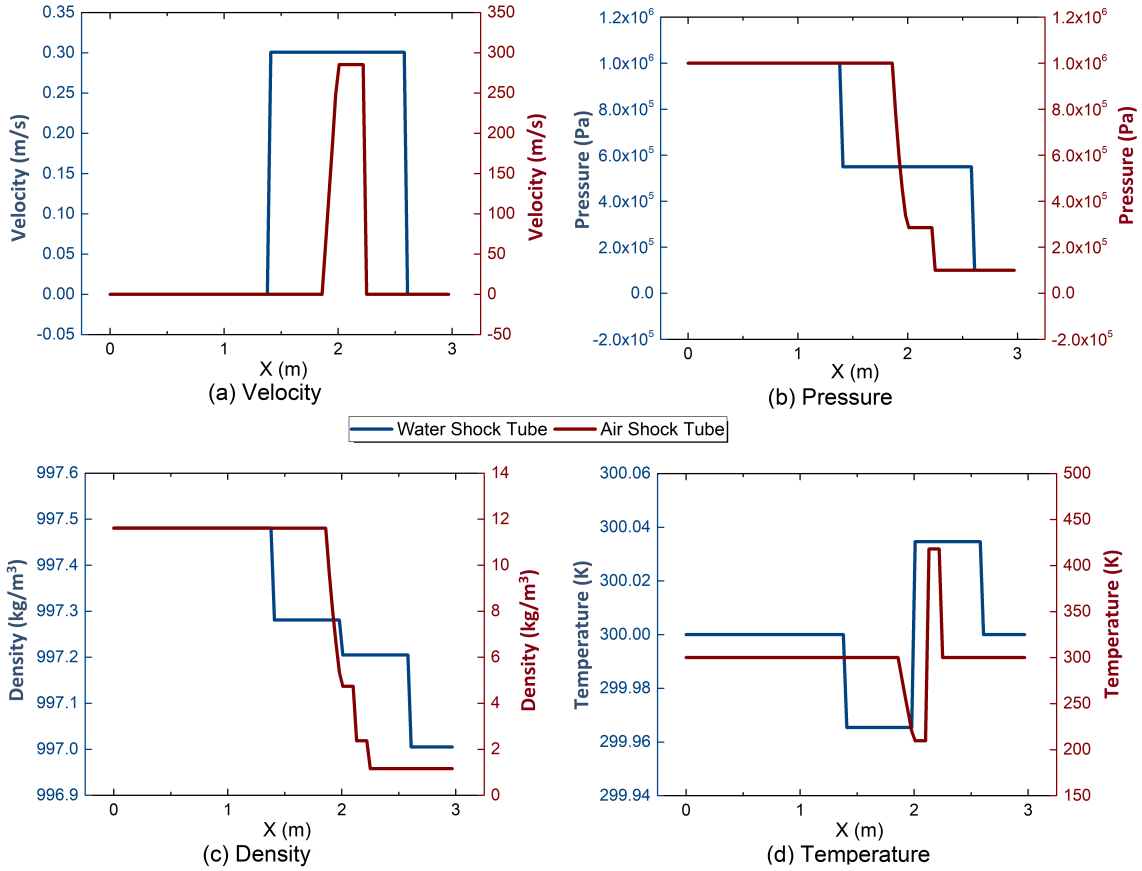

Figure 4.6: Analytical solution profiles for the Water shock tube and the Air shock tube problems for $P_L = 1$ MPa, $P_R = 0.1$ MPa, and $T = 300$ K

On analysing the scales of different property profiles, it could be observed that the properties vary over a wider range for air shock tube problem compared to that of the liquid case. The large variations in the density of air compared to that of water could be attributed to the relatively higher compressibility of the gas. The higher value of specific heat for water is the reason why variation in temperature for this liquid is observed to be substantially lower to that of gas. The maximum value of velocity developed in the zones 1 and 2 is also low for the case of water. The higher velocity observed with the case of air, for the same pressure difference, could be directly associated with the fluid's lower density.

4.7 Analytical Solution Over the Specified Range

As already mentioned in Section 4.5, the range over which analytical solution is claimed to exist is the same as the range of application of equation of state. In this section, we in-

tend to demonstrate the existence of the proposed analytical solution over the same range. This shall be achieved by solving different cases of the problem and presenting these solutions with relevant explanations. The demonstration over complete pressure range and temperature range shall be carried out separately in two steps.

The pressure range over which the proposed solution is expected to exist is 0.1 MPa-1000 MPa. In the previous section, we have already presented solutions up to 1 MPa range. To cover the remaining pressure range, we consider three cases of the shock tube problem. The water shock tube problem with driver section pressures of $P_L = 10$ MPa, 100 MPa, and 1000 MPa, and a driven section pressure of $P_R = 0.1$ MPa are considered. The initial temperature for all the three cases are 300 K. From these initial conditions of temperature and pressure the problems were solved analytically.

The analytical solutions to water shock tube problem corresponding to the driver section pressures of 10 MPa, 100 MPa, and 1000 MPa are shown respectively in the Figures 4.7, 4.8, and 4.9.

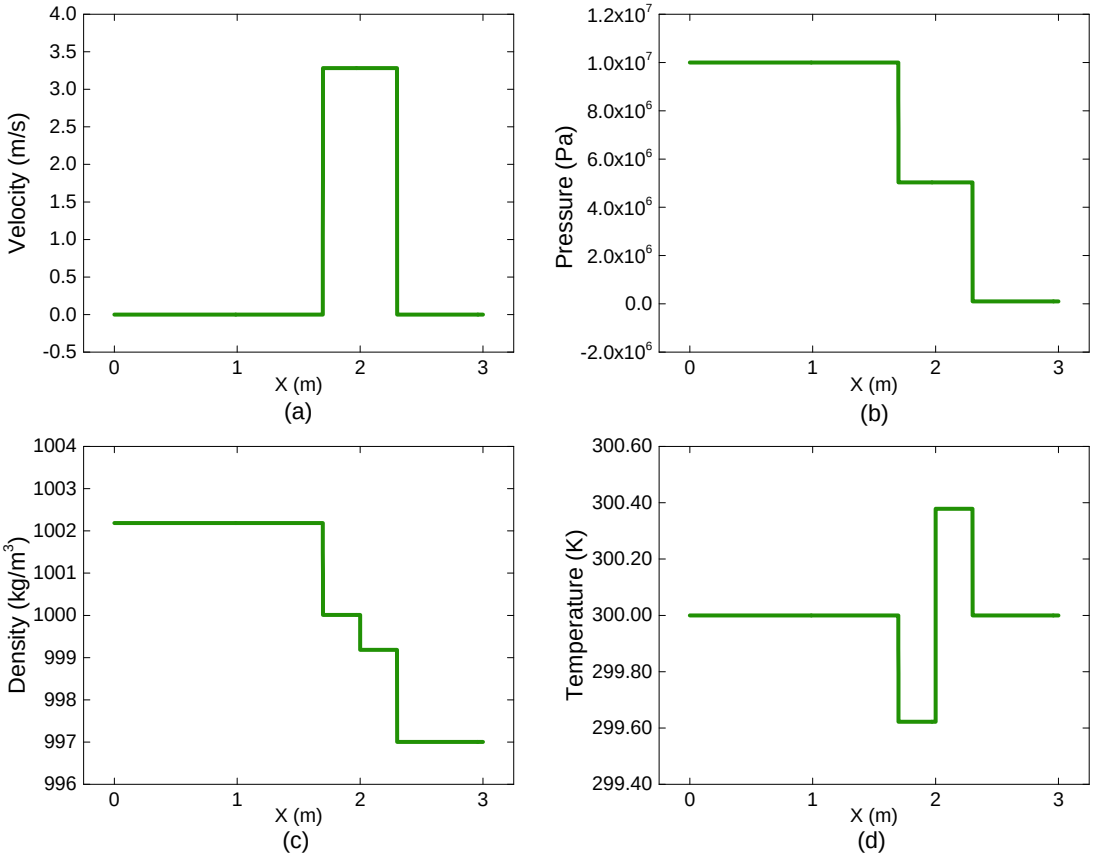

Figure 4.7: Analytical solution profiles for $P_L = 10$ MPa and $T = 300$ K

The figures display spatial distribution of the flow properties viz. velocity, pressure,

density and temperature inside the shock tube domain. The results displayed correspond to the time instant after 200 μ s from the rupture of the diaphragm.

As previously observed for the driver section pressure of $P_L = 1$ MPa, the expansion fan in the solution profiles are not much spread out for the driver section pressures of 10 MPa and 100 MPa. This is clearly observable form Figures 4.7 and 4.8. Such a narrow expansion fan is the consequence of relatively small order of variation in liquid density and wave speed, for the pressure scales involved. However, the results corresponding to the driver section pressure of 1000 MPa displayed in Figure 4.9, shows a spread-out expansion fan. This expansion region is similar to what we commonly observe in gas shock tubes. This observation for the very high pressure case can be attributed to the large initial pressure difference across the diaphragm. For such a large initial pressure difference, liquid density and speed of sound vary over a wider scale resulting in a spread-out expansion zone.

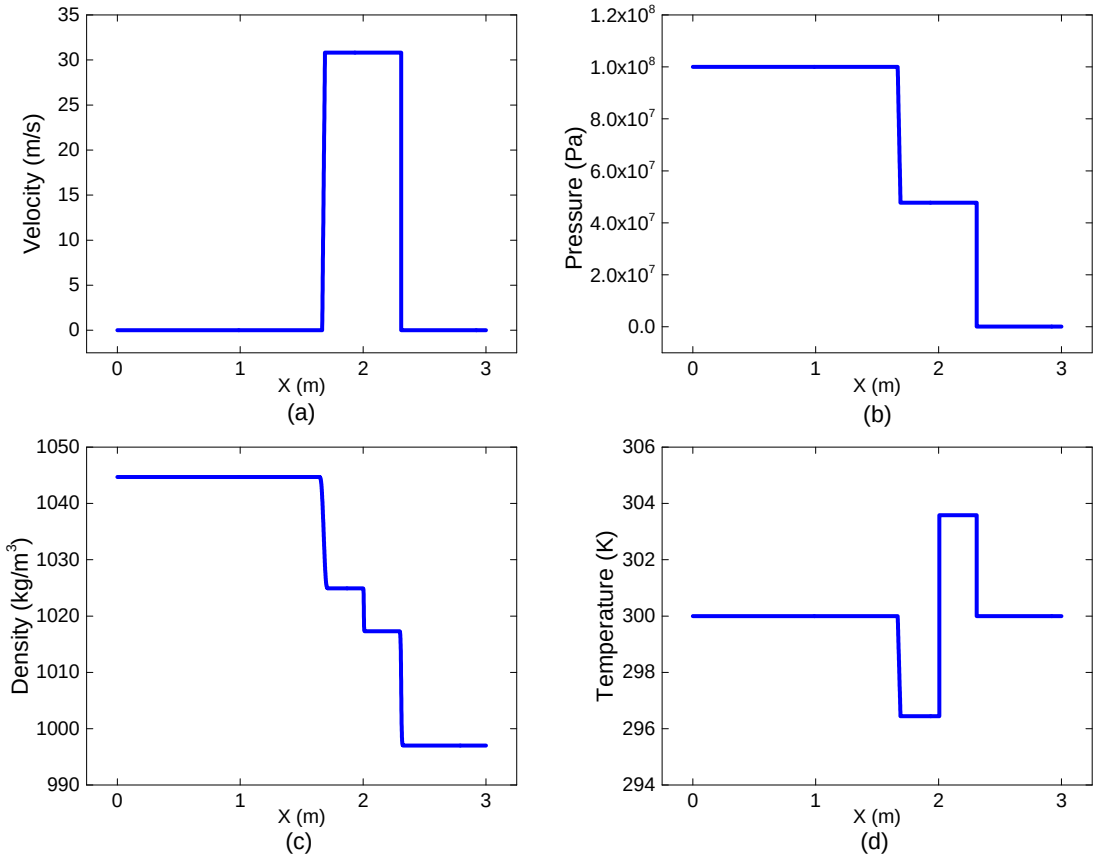

Figure 4.8: Analytical solution profiles for $P_L = 100$ MPa and $T = 300$ K

The change in fluid density across contact discontinuity is correctly captured in solution profiles. This capability is attributed to non-isothermal property of the equation of state used for fluid. The modified NASG EOS establishes a proper coupling between density

and temperature of liquid. The scale over which liquid density varies for different pressure ranges is a clear indication of the impact of higher pressure on liquid compressibility. For the case of $P_L = 10$ MPa, density magnitude inside shock tube varies over the range of $997.0\,\text{kg/m}^3$ to $1002.2\,\text{kg/m}^3$. The maximum value of density in the domain increases to $1044.7\,\text{kg/m}^3$ and $1251.6\,\text{kg/m}^3$ respectively for P_L =100 MPa and 1000 MPa.

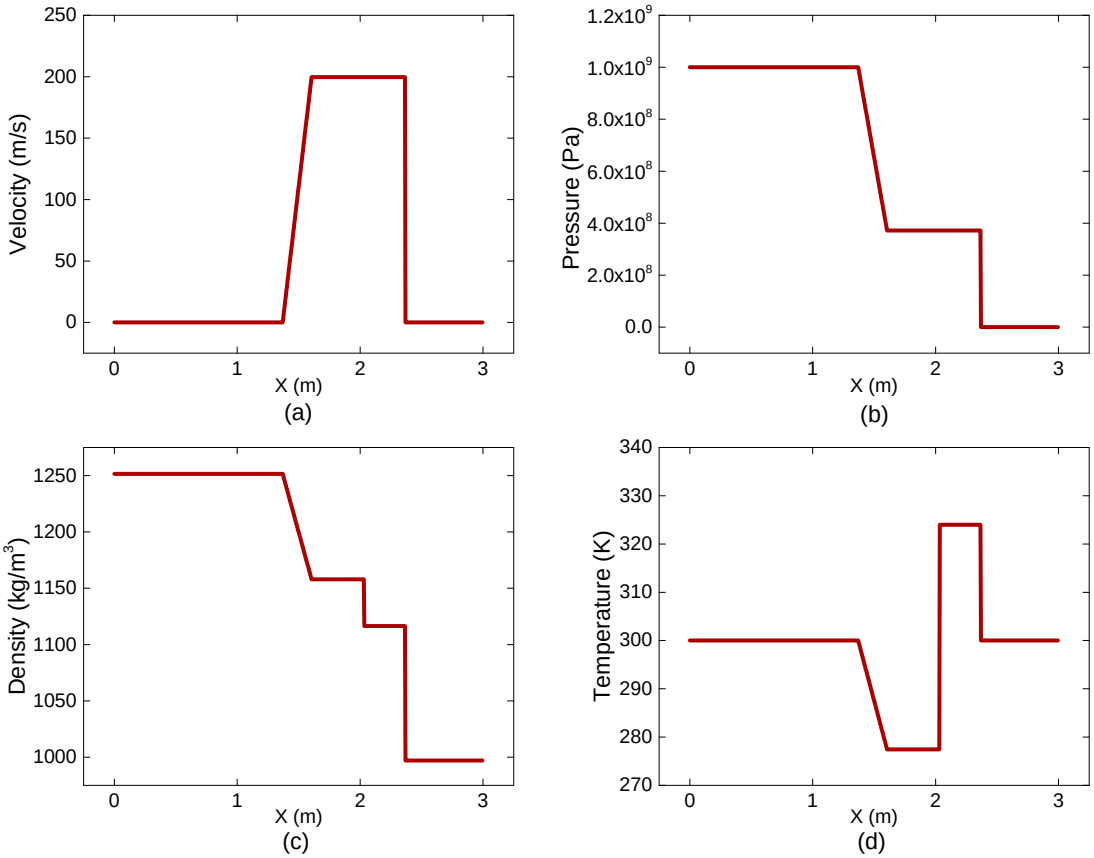

Figure 4.9: Analytical solution profiles for $P_L = 1000$ MPa and $T = 300$ K

For an increase in the initial pressure difference across the diaphragm, there is a corresponding increase observed in the magnitude of velocity in the region between the expansion fan and the shock. The maximum value of velocity developed in the domain for the driver section pressures of 10 MPa, 100 MPa, and 1000 MPa are respectively 3.3 m/s, 30.8 m/s, and 199.7 m/s. The initial diaphragm pressure ratio has a similar effect on the range of temperature variation inside shock tube. For a larger diaphragm pressure ratio, the range of variation of temperature is wider. This is an obvious observation for a fluid that has the pressure proportional to its temperature. For the driver section pressures of 10 MPa, 100 MPa, and 1000 MPa, the range of temperature variation inside shock tube are respectively 299.6 - 300.4 K, 296.4 - 303.6 K, and 277.4 - 324.0 K. These maximum variations in

the temperature are observed in the form of jump discontinuities across contact surface in solution profiles. The solution plots for the three cases discussed here along with associated observations clearly demonstrated the existence of analytical solution to water shock tube problem over complete pressure range of 0.1 MPa - 1000 MPa.

The next step is to demonstrate the existence of analytical solution over specified temperature range of 273 K - 373 K. The study is therefore further extended by considering three different operating temperatures for liquid shock tube problem, within the specified temperature range. The temperature values chosen for these different cases of the shock tube are 280 K, 325 K, and 370 K. A driver section pressure of 500 MPa and a driven section pressure of 0.1 MPa is chosen for all three cases. The pressure values are chosen in such a way that the driver section pressure represents the average value of the pressure range studied and the driven section pressure represents the lowest pressure value in the range considered. The analytical solutions for water shock tube with the three operating temperature ranges are displayed in Figure 4.10.

From the solution profiles displayed in Figure 4.10 for different cases of water shock tube problem, the presence of five typical zones in the shock tube domain are clearly visible. We could also observe the typical flow features like shock wave, contact discontinuity and expansion fan in these profiles. In Figure 4.10(b), the intermediate pressure common to the zones between the shock and expansion fan, do not show much variation for the different cases considered. This is because of the common diaphragm pressure ratio for all the three cases. The temperature profiles shown in Figure 4.10(d), exhibit a clear shift due to the different ranges of temperature selected for the study. Figure 4.10(c) displays density profiles and show that these profiles shift downwards the scale with the increase in operating temperature. Such a downward shift is attributed to the expansion of liquid with increase in temperature, as liquid density varies inversely with this property. The decrease in the density of liquid with an increase in temperature also leads to a higher velocity for the same pressure difference. This trend can be observed form Figure 4.10(a), where the highest velocity is reported for highest temperature range and vice-versa. The structure of the solution remains the same for all three temperature ranges studied. Through this analysis, using results from different temperature ranges, the existence of analytical solution over specified temperature range of 273 K - 373 K is also successfully demonstrated.

The availability of analytical solution has converted water shock tube problem into a simple and powerful test case for the validation of numerical solvers. The developed analytical solution can serve as an easy-to-use benchmark result for testing numerical solutions from various computational algorithms. This capability of the developed solution

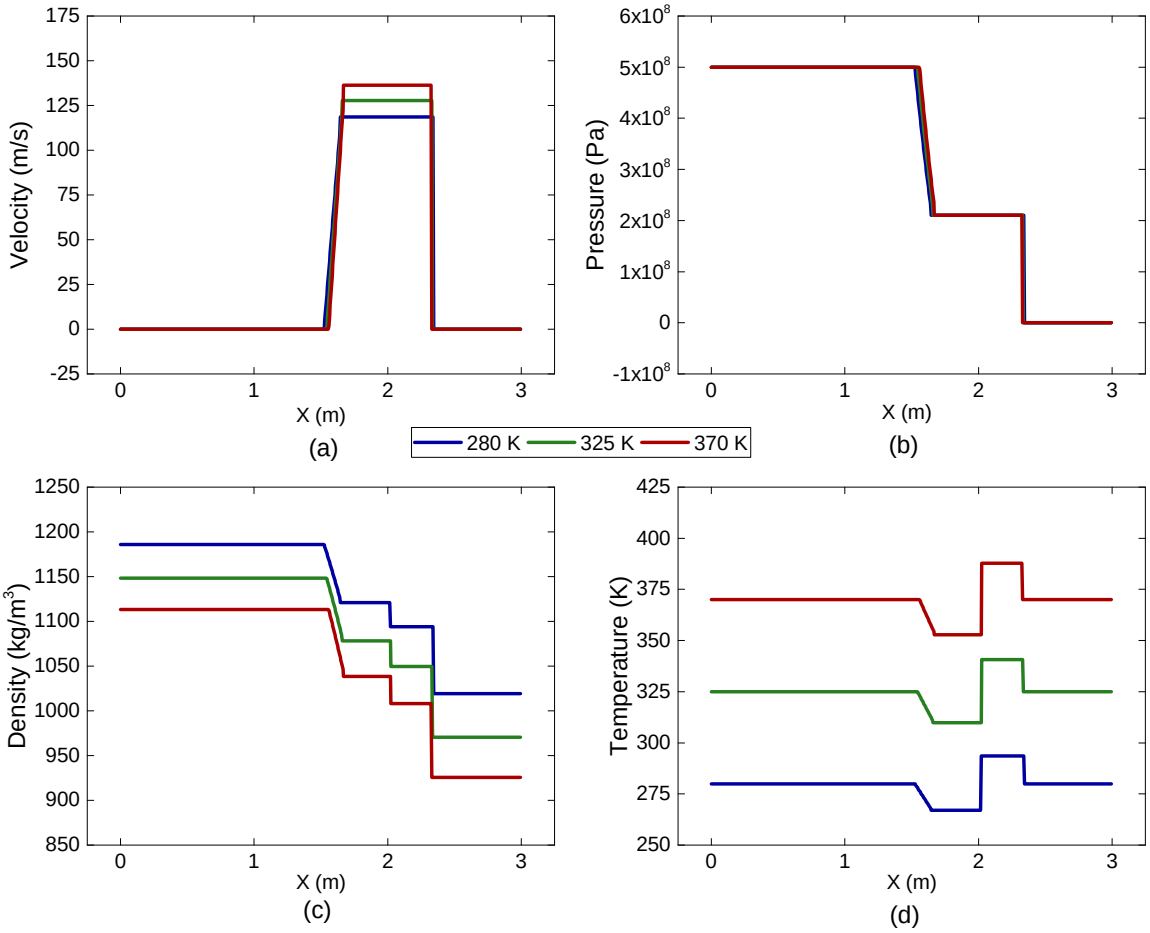

Figure 4.10: Comparison of the analytical solution profiles for $P_L = 500\,\text{MPa}$, $P_R = 0.1\,\text{MPa}$ and $T = 280$ K, $T = 325$ K, and $T = 370$ K

is demonstrated with the help of various numerical methods in the next chapter.

The analytical solution procedure used in this chapter for water shock tube problem can also be considered as a template that could be extended to develop solutions for shock tubes with other liquids. However, this may require appropriate equations of state for the liquids modelled, and a suitable strategy to present the EOS in a standard form. This is to make the EOS compatible with the rest of the solution procedure.

4.8 Summary

The analytical solution for a liquid shock tube with water as the working fluid is successfully developed in this chapter. Liquid water compressibility effects are modelled using the high-accuracy Modified NASG equation of state. The procedure used for developing ana-

lytical solution of a typical gas shock tube is suitably modified by including this EOS for liquid water. Applicability of the suggested analytical solution over a wide range of pressure is demonstrated by obtaining the solution for different driver section pressures. By presenting the results for liquid shock tube problem for three separate operating temperatures, the existence of the analytical solution over the proposed temperature range is also verified. The solution procedure developed could capture the complete physics associated with liquid shock tube problem, with the same ease with which a gas shock tube problem is solved. The solution structure observed for water shock tube problem is compared against that of an air shock tube problem for the same operating conditions. This liquid shock tube problem with an analytical solution can serve as a standard benchmark problem for large variety of compressible liquid flow computational models. The analytical solution procedure outlined in this chapter can be readily extended to other liquids subject to the availability of respective equation of states.

Chapter 5

Numerical Simulation of Water Shock Tube Problem

5.1 Introduction

In this chapter we will numerically solve water shock tube problem with the help of suitable computational algorithm. The numerical results obtained will be validated using the analytical solution already developed in Chapter 4. To understand the major steps required for computationally solving a compressible liquid flow problem, we need to begin with the most basic problem in compressible liquid flows. In this chapter, we begin by numerically solving the air shock tube problem. Details on the air shock tube problem, its problem setup, solution structure, etc. were already discussed in Chapter 2. Information regarding different computational algorithms used for numerically solving this problem is also provided in Chapter 2.

In Section 5.2 of this chapter, the computational capability of some basic Riemann solvers and flux methods are compared by solving Sod's shock tube problem. This comparison is further extended to advanced slope-limiter type Riemann solvers. The optimal computational method for liquid shock tube simulation is determined based on this comparative study. Section 5.3 discusses the selection of a suitable mathematical model and inclusion of liquid compressibility effects into this model. Computational strategy adopted for numerically solving this model is also discussed. In the subsequent section, Section 5.4, numerical results generated from simulation are validated using analytical solution to the problem. Different cases of water shock tube problem are used to compare the two solutions over the specified range of application. Extension of the analytical and numerical solution techniques to water shock tube problems involving slightly complex problem setup is examined in Section 5.5. Section 5.6 considers the inclusion of a few frequently used

equations of state for water into the mathematical model. This section presents numerical results obtained for water shock tube problem using these selected EOS. The relative capabilities and limitations of the equations of state used in modelling compressible effects in liquid are also examined. The last section, 5.7 summarises the contents of this chapter.

5.2 Computational Methods for Solving Gas Shock Tube Problem

In this section we will solve Sod's problem using flux methods such as the Lax Wendroff (two-step) flux [256], the MacCormack flux [257, 258], and some approximate Riemann solver fluxes like the AUSM$^+$-up flux [186] and the HLLC flux [128]. The MacCormack method is a two-step method, with a predictor step followed by a corrector step. The MacCormack and the Lax Wendroff (two-step) flux used in [131] use artificial viscosity for smoothing the solution profiles by controlling the oscillations observed in the solution. In this study, however, these two schemes are used in their most basic form without the addition of artificial viscosity in order to make a more sensible evaluation of these schemes. The two-step Lax Wendroff algorithm is as follows:

$$U_{i+1/2}^{n+1/2} = \frac{1}{2}\left(U_{i+1}^{n} + u_{i}^{n}\right) - \frac{\Delta t}{2\Delta x}\left(F(U_{i+1}^{n}) - F(U_{i}^{n})\right) \tag{5.1a}$$

$$U_{i}^{n+1} = U_{i}^{n} - \frac{\Delta t}{\Delta x}\left(F(U_{i+1/2}^{n+1/2}) - F(U_{i-1/2}^{n+1/2})\right) \tag{5.1b}$$

In the first step $U(x,t)$ is evaluated at half time steps $n+1/2$ and half grid points $i+1/2$. In the second step, values at the next time step $n+1$ are calculated using the data for n and $n+1/2$. The two-step algorithm for MacCormack method is given by:

$$U_{i}^{\overline{n+1}} = U_{i}^{n} - \frac{\Delta t}{\Delta x}(F_{i+1}^{n} - F_{i}^{n}) \tag{5.2a}$$

$$U_{i}^{n+1} = \frac{1}{2}(U_{i}^{n} + U_{i}^{\overline{n+1}}) - \frac{\Delta t}{2\Delta x}(F_{i}^{\overline{n+1}} - F_{i-1}^{\overline{n+1}}) \tag{5.2b}$$

where $F^{\overline{n+1}} = F(U^{\overline{n+1}})$. In the predictor step, provisional values of the conserved variables at an intermediate time level $\overline{n+1}$ is obtained from the property values at the n^{th} time level and the corresponding fluxes are evaluated. In the subsequent corrector step, property values computed at intermediate time level are used to obtain the corrected values of conserved variables and fluxes at the $(n+1)^{th}$ time level. Details of the AUSM$^+$-up and the

HLLC flux methods are presented in Section 2.6. Both these methods have comparatively long algorithms and these are available in Appendix A.

The AUSM$^+$-up flux uses a pressure diffusion term M_P to improve the calculations at low Mach numbers. The definition of M_P is presented in Equation (A.34). The range of the parameters K_P and σ included in the definition of M_P are provided by Equation (A.35). For the present problem, these parameters take up the values of $K_P = 0.3$, $\sigma = 1.0$. A parameter β is used in the definition of the split Mach numbers as visible in the Equation (A.33). This parameter is assigned a fixed value of 0.125 as shown in Equation (A.35). The interface pressure $P_{i+\frac{1}{2}}$ is estimated as in Equation (A.36). Equation (A.38) defines a diffusion term P_U that is used in the calculation of interface pressure. The range of parameter K_U in the definition of P_U is given by Equation (A.39). In the modelling of Sod's problem K_U takes a value of 0.1. The value of the scaling factor f_a is evaluated using the relation (A.31). As suggested in [127], the M_∞ corresponding to initial pressure ratio across the diaphragm is 1.0 which assigns a magnitude of 1.0 for the scaling factor f_a. This value of f_a is substituted in to Equation (A.39) to compute the parameter α.

HLLC flux is used with Godunov's first-order method for computation. The HLLC algorithm starts with the calculation of averaged value of speed of sound and density at cell interfaces as in Equation (A.3). This is followed by the computation of pressure from primitive variable Riemann solver using relation (A.4). The signal wave speeds of the left travelling and the right travelling waves at a cell-interface are estimated using relations (A.8) and (A.9) respectively. The intermediate wave's speed is estimated as shown in Equation (A.10). Based on these signal speeds, different variable vectors at each cell-interface are calculated as shown in equations (A.11) - (A.14). The different flux vectors possible at a cell-interface are computed using relations (A.15) - (A.18). Finally, based on the signal speeds, the HLLC flux at any cell-interface is decided as shown in Equation (A.2).

Solution profiles for the Sod's problem obtained using different flux methods discussed here are presented in Figure 5.1. The problem was solved on a one-dimensional numerical domain with 100 uniform divisions. Data points for the numerical solution from various flux methods are displayed using different markers and analytical solution to the problem is shown using continuous black curves. Sub-figures on the leftmost, the central, and the rightmost columns of Figure 5.1 display density, pressure, and velocity profiles respectively. The results displayed are those after 0.2 units of non-dimensional time from the rupture of the diaphragm. 100 equally spaced numerical data points are used in the plots.

The solution profiles clearly imply non-suitability of the MacCormack and the Lax-Wendroff fluxes in solving the Riemann problem. Both these methods are found to gen-

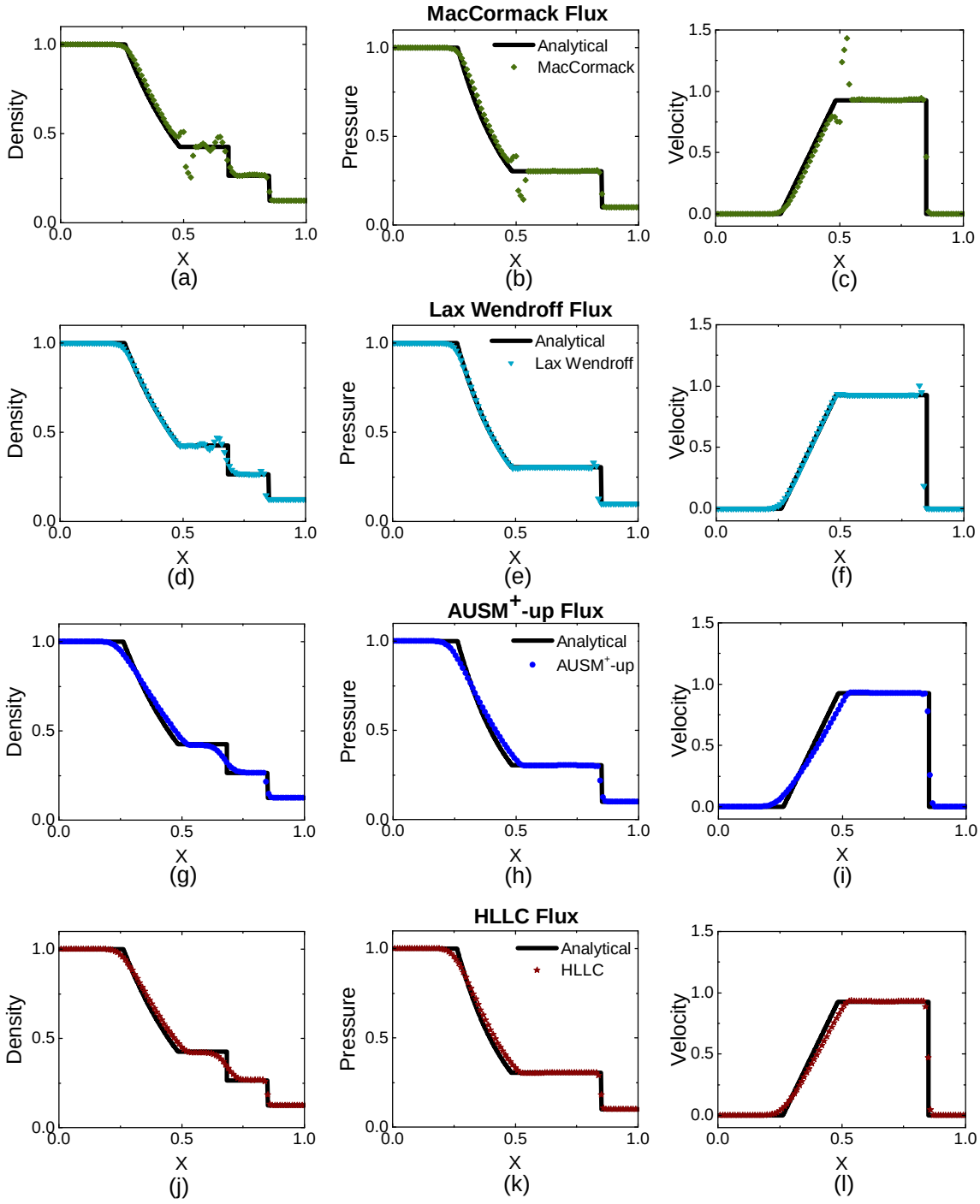

Figure 5.1: Property profiles generated by different flux methods for Sod's problem

erate spurious oscillations near the sharp features in the solution profile. This is a typical observation with second-order accurate numerical flux methods. These dispersive errors in the proximity of high gradients in the solution profile are attributed to the Gibbs phe-

nomenon [259]. Though these two methods resolve the remaining zones of the solution profile with reasonable accuracy, the oscillations cannot be minimised without the inclusion of additional dissipation mechanisms into the algorithm, like artificial viscosity. In the case of two-step Lax-Wendroff flux, the oscillations are generated in the proximity of shock and contact discontinuity, whereas, the MacCormack flux produces oscillations mostly near contact surface and trailing edge of the expansion wave, where it is most severe.

Analyzing the results generated using the AUSM$^+$-up and the HLLC fluxes, we could distinctly observe the advantage offered by these two methods over formerly discussed second-order algorithms. Even with first-order accurate formulations, the AUSM$^+$-up and the HLLC fluxes could produce reasonably accurate solution estimates for gas shock tube problem. Compared to formerly discussed second-order methods, these two flux methods do exhibit a small amount of dissipation near sharp features in the solution. The AUSM$^+$-up and the HLLC fluxes, however, generate highly stable solution profiles that are completely dispersion free. On comparing the two oscillation free Riemann solver flux methods, we could observe that the HLLC flux resolves the profiles slightly better than the AUSM$^+$-up flux. This is due to the more efficient three-wave model of the HLLC algorithm. Closer analysis of solution profiles reveals that all three main features in the solution viz., shock, contact surface and expansion fan are better resolved by the HLLC flux. Moreover, the HLLC algorithm allows a Courant number of 1.0, while the AUSM$^+$-up algorithm is found to become unstable above a Courant number of 0.9, for gas shock tube problem. Similarly, on measuring the speed of computation, the HLLC method was found to be almost 10% to 15% faster compared to the AUSM$^+$-up method,while solving with grid resolutions ranging from 100 divisions to 10,000 divisions. From the comparative analysis carried out on various flux methods in their pure form, we could conclude that the HLLC flux is the most suitable to be used as a Riemann solver for gas shock tube type of problems.

The higher order spatial discretization methods generally exhibit spurious oscillations due to sharp changes in the solution. These large gradients in the solution arise due to the presence of shocks, discontinuities etc. The slope limiters have a major role in limiting the solution gradient near shocks and discontinuities. Details on the MUSCL based slope limited Riemann solvers are presented in Section 2.7. The MUSCL approach uses data reconstruction technique for attaining high–order of accuracy. The HLLC solver which was found to be the best flux method, is used with the MUSCL based approach. The MUSCL schemes used in this study are also TVD schemes as the limited slopes are used in the algorithm. Three different limiting functions are used along with the MUSCL scheme, viz.

the MinMod (MM) limiter [260–262], the Monotonized Central (MC) limiter [158, 191], and the van Albada (VA) limiter [263].

The property profiles generated for Sod's problem by using MUSCL-based HLLC flux Riemann solver that includes different slope limiter algorithms, is displayed in Figure 5.2. Results generated using the MUSCL based HLLC flux without any slope limiter function is also included in this figure. This is to show the improvement brought forward by slope limiters in the solution profiles. The numerical solution profiles are plotted using 100 equally spaced data points. A CFL value of 0.5 was found to be optimal for the MUSCL-HLLC solver with different slope limiters for solving the Sod's problem.

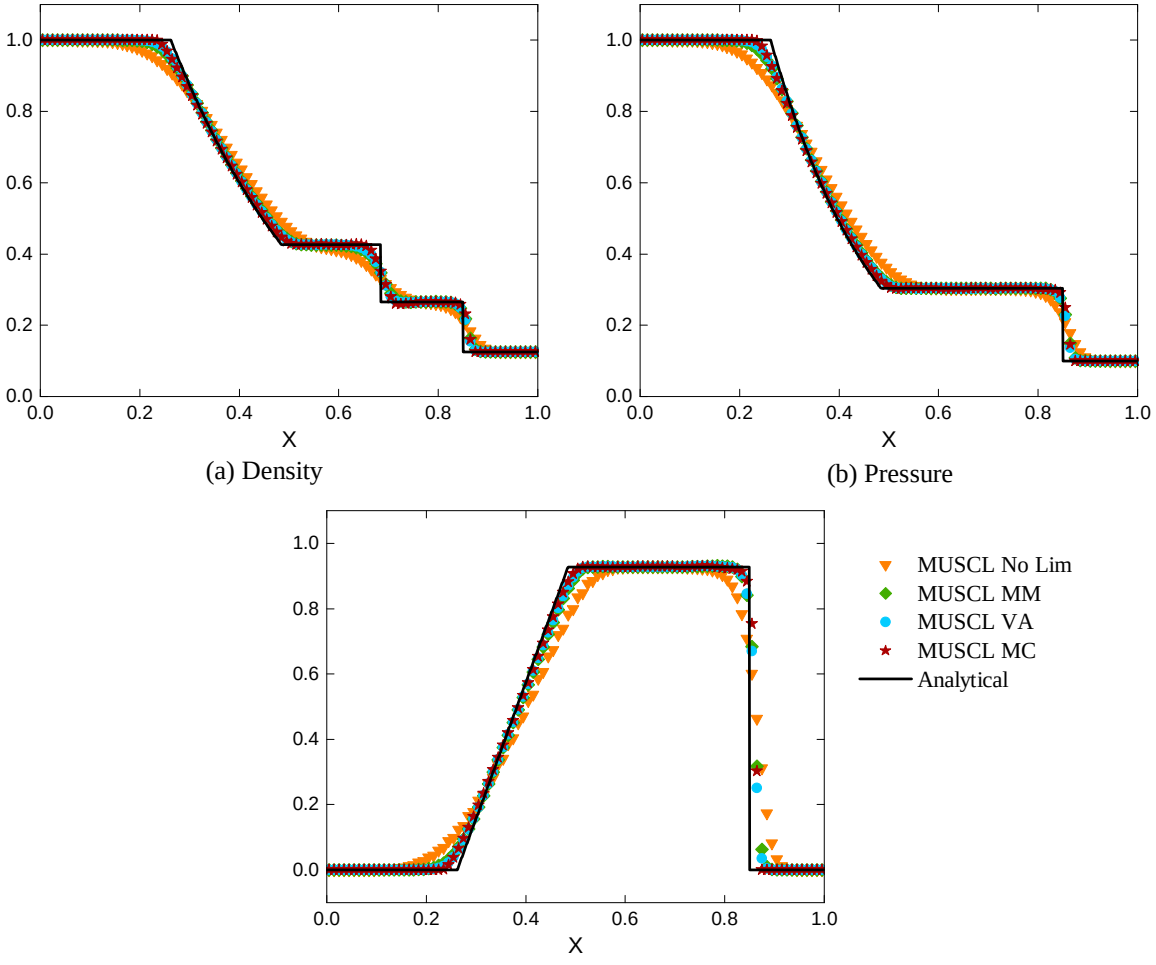

(a) Density

(b) Pressure

(c) Velocity

Figure 5.2: Property profiles generated for Sod's problem by MUSCL-based HLLC solver using various limiters

From the numerical solution profiles displayed using different coloured markers in Figure5.2, we could see that various limiters improve the sharpness and accuracy of the

MUSCL-based HLLC flux. The profiles generated without a limiter algorithm shows heavy dissipation around all sharp features in the solution. The results generated using different limiter algorithms are very close to each other. However, on a closer look we could see that the sharpest reproduction of different property profiles is produced with the MC type limiter algorithm. This solver combination is also the one that produces results closest to analytical solution to the problem. The MM and the VA type limiters are marginally inferior to the MC type limiter.

5.3 Numerical Modelling of Water Shock Tube Problem

The analytical solution procedure discussed in the previous chapter is based on several thermodynamic relations which are applicable for processes taking place inside the shock tube domain. To demonstrate that a numerical solution based on the governing set of partial differential equation matches with the analytical solution, we are numerically solving a mathematical model. This is because, generally, for compressible flow problems, the governing equations for the flow constitute a system of non-linear partial differential equations (PDEs). Such set of equations do not have analytical solution and hence one may have to rely on numerical methods and algorithms to solve them. The numerical modelling of water shock tube problem involves two main steps. The first step is to identify a suitable mathematical model which could provide the desired set of governing equations. The second step is the selection of a computational algorithm to numerically solve the mathematical model based on initial and boundary conditions. These two steps are explained in detail in the following sub-sections.

5.3.1 Selection of the mathematical model

We know that water shock tube problem is a modification of the one-dimensional shock tube problem of Sod [251], with the major difference being the use of liquid water in place of air as the shock tube fluid. The initial problem setup is as shown in Figure 5.3.

In the setup, inside a 3 m long tube, a diaphragm separates liquid water under very high pressure (driver section) from water at a comparatively low pressure (driven section). The fluid chosen for the problem is liquid water and the flow is assumed to be inviscid and non-heat conducting. Since water is treated as a compressible fluid, the governing equations chosen are one-dimensional equations of compressible flow as given in the Sod shock tube problem [251]. The one-dimensional continuity, momentum, and energy equations in

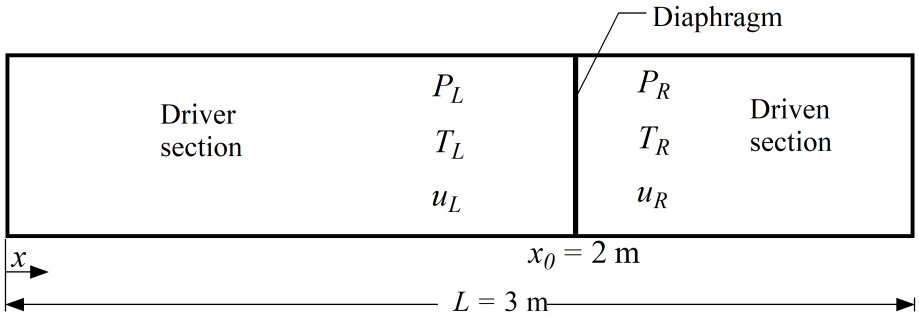

Figure 5.3: The 1D schematic of a liquid shock tube.

conservation form are given by:

$$\frac{\partial \rho}{\partial t} + \frac{\partial (\rho u)}{\partial x} = 0$$

$$\frac{\partial (\rho u)}{\partial t} + \frac{\partial (\rho u^2 + P)}{\partial x} = 0$$

$$\frac{\partial (\rho e)}{\partial t} + \frac{\partial (\rho e u + P u)}{\partial x} = 0$$

As the number of unknowns exceeds the number of equations, the closure of mathematical model is achieved by using a liquid equation of state. The modified NASG EOS is the liquid EOS used. This EOS relates various properties of compressible liquid as given in Equations (3.6) - (3.8). Density values of the liquid are computed from this assigned equation of state using pressure and temperature values.

The one-dimensional compressible flow relations form a non-linear system of PDEs that does not have an analytical solution. Therefore, this system of PDEs is solved numerically for water shock tube problem by using a suitable computational algorithm. The computational strategy employed in solving this problem numerically is discussed in the following subsection.

5.3.2 Computational strategy

The 3 m long shock tube which forms the physical domain of the problem is treated as a one-dimensional domain in the numerical model. For solving the problem numerically, this one-dimensional domain is divided into uniform control volumes. The MUSCL solver with the HLLC flux and the MC type limiter function was found to be the best combination from modelling study on the Sod's problem. This solver combination is used as computational algorithm to numerically solve water shock tube problem. Major assumptions in

the numerical modelling are the following: The flow and the associated variation in all the flow variables are assumed to be one-dimensional. The fluid is considered to be non-viscous and non-heat conducting. The process of rupture of the diaphragm is assumed to be instantaneous or infinitely fast.

A total of six different cases of water shock tube setup are selected for numerical modelling. In the first set, three configurations are selected with initial pressure of water in high pressure chamber to the left of the diaphragm chosen as P_L =10 MPa, 100 MPa, and 1000 MPa. Water in the right chamber is maintained at a fixed pressure value of P_R =0.1 MPa for all three configurations. The diaphragm is initially positioned at a distance of 2 m from the left closed end of the tube. Fluid over the entire domain is assumed to be stationary prior to the rupture of the diaphragm, i.e., $u_L = u_R = 0$. Temperature of the fluid on both sides of the diaphragm are initially at $T_L = T_R = 300$ K.

In the second set, three more configurations are selected with the initial driver section pressure of water fixed at P_L =500 MPa and driven section pressure fixed at P_R =0.1 MPa for all cases. The fluid is again assumed to be stationary at the start of the problem. The three cases correspond to three different operating temperatures of 280 K, 325 K, and 370 K in the shock tube domain.

The 3.0 m long domain is divided into 6,000 uniform control volumes and is marched forward in time until 200 μs is reached. The spatial variations of properties in the domain at the end of computation are compared with the analytical solution. The time duration after which results are sought is carefully decided to avoid reflection of the shock or expansion wave from the boundaries of the domain.

5.4 Validation of the Numerical Results

Liquid shock tube problem is numerically solved and the numerical results generated are compared with the analytical solution to the problem for their validation. The analytical and the numerical solutions to the water shock tube problem corresponding to the driver section pressures of 10 MPa, 100 MPa, and 1000 MPa are shown in Figures 5.4, 5.5, and 5.6 respectively. These figures display the spatial distribution of flow properties viz. velocity, pressure, density and temperature inside the shock tube domain, after a duration of 200 μs from the rupture of the diaphragm. The numerical solution presented is grid-independent, and in the figures, we have used 100 equally spaced data points to plot each solution profile. A CFL value of 0.5 is found to be optimal for time step calculation, and the corresponding time step size is close to 1.5×10^{-7} s.

Property profiles obtained from numerical results suggests that upon the rupture of diaphragm, a shock is formed that propagates to the right of the initial location of the diaphragm and an expansion fan formed propagates to the left. In between these two waves a moving contact discontinuity is formed across which density and temperature exhibit sharp variation. The magnitudes of velocity and pressure are invariant over the region bounded by the trailing edge of expansion fan and the shock. Though the magnitude of variation of properties with water shock tube is different from those observed in air shock tube, the solution structure essentially remains the same.

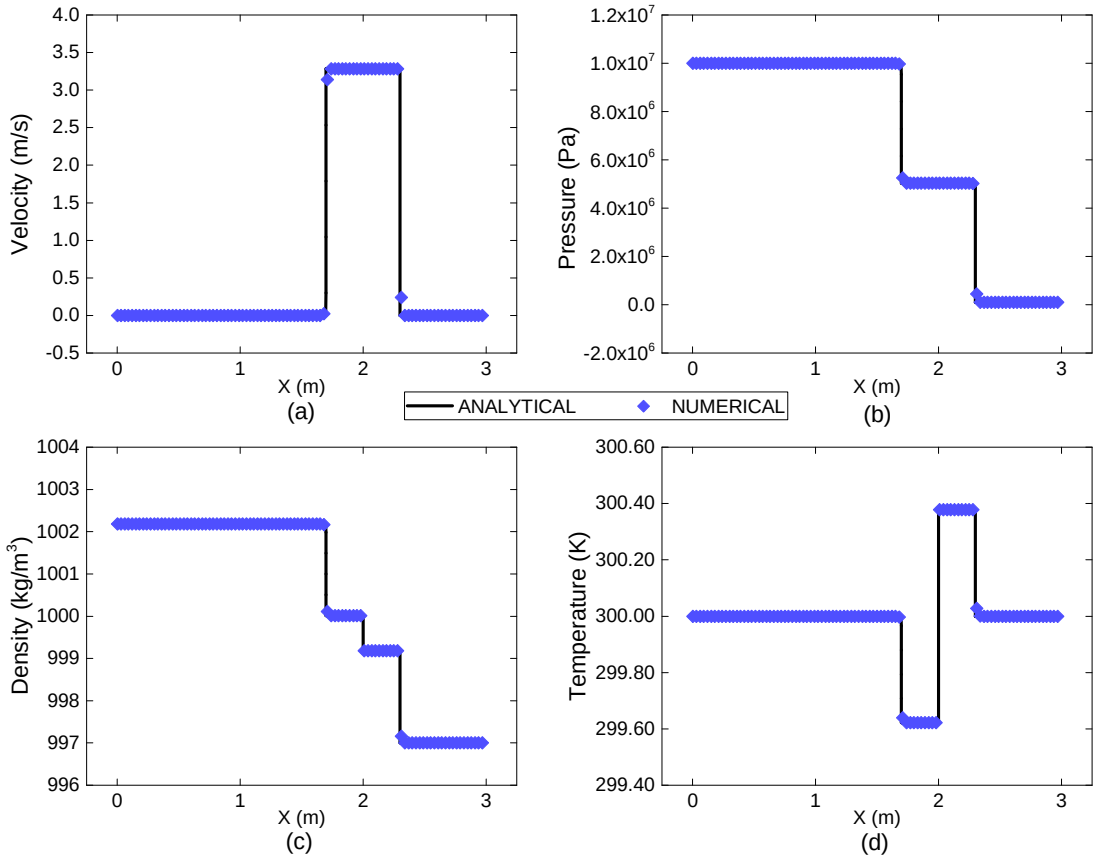

Figure 5.4: Comparison of the analytical and numerical solution profiles for $P_L = 10$ MPa, $P_R = 0.1$ MPa at $T = 300$ K

Scattered symbols are used to plot the numerical data points and the continuous black curves represent analytical solutions. The numerical results obtained for all different driver pressures exhibit very close agreement with their respective analytical solutions. This close match between the numerical and analytical solutions is not limited to the estimated magnitude of properties over different zones. The numerically predicted location of various zones formed in the shock tube domain and flow features such as expansion fan, contact

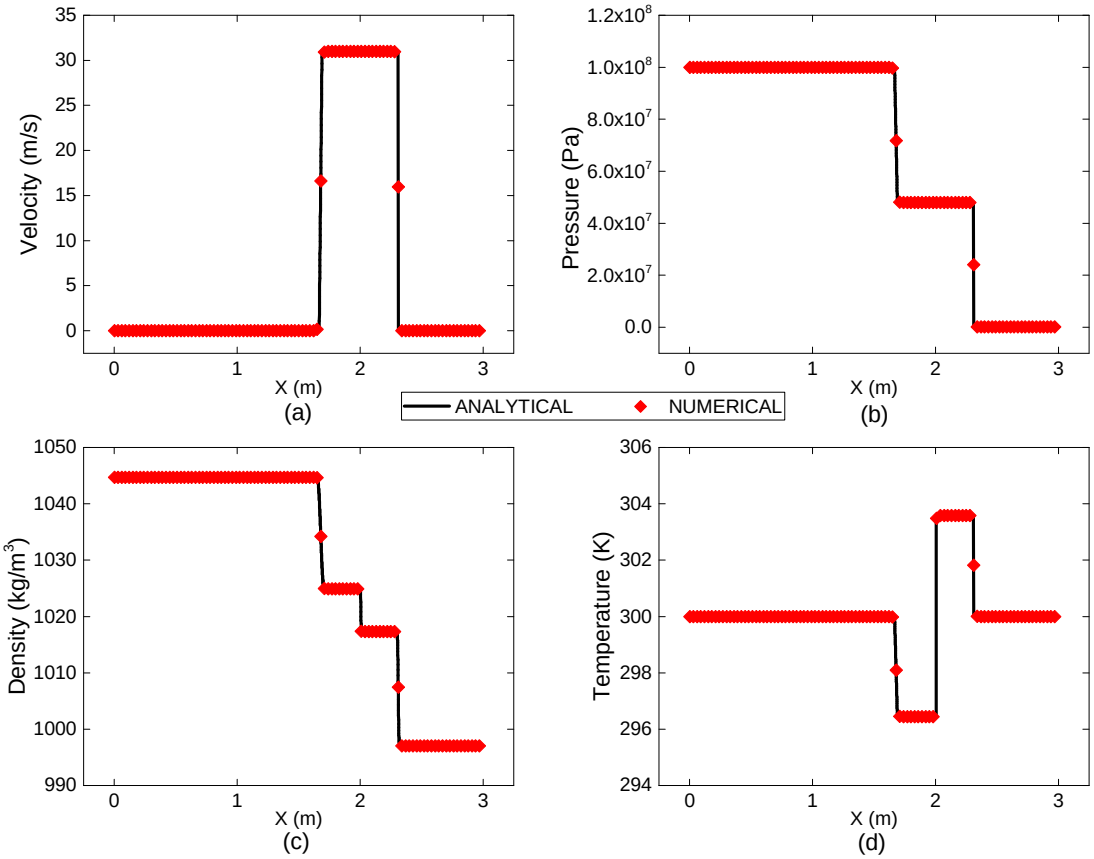

Figure 5.5: Comparison of the analytical and numerical solution profiles for $P_L = 100\,\text{MPa}$, $P_R = 0.1\,\text{MPa}$ at $T = 300\,\text{K}$

discontinuity and shock exhibit an accurate match with the exact solution.

Similar to the observation with analytical solution, the mathematical model used here also has successfully simulated complete physics of the problem. The non-isothermal equation of state used to relate fluid properties also played a crucial role in this. The analytical solution involved a series of fundamental relations that governed different thermodynamic processes occurring inside the shock tube. The numerical solution is, however, obtained by computationally solving a system of partial differential equations (the one-dimensional compressible flow equations) with respective initial and boundary conditions. The high similarity observed for the solutions to the same problem obtained through two different approaches clearly suggest dependability of this solution.

Numerical solutions for the second set of water shock tube problems over different temperature ranges are also obtained. Further, these numerical results are compared against their corresponding analytical solutions. Solution profiles for the initial temperature ranges of 280 K, 325 K, and 370 K are respectively displayed in Figures 5.7, 5.8, and 5.9. As

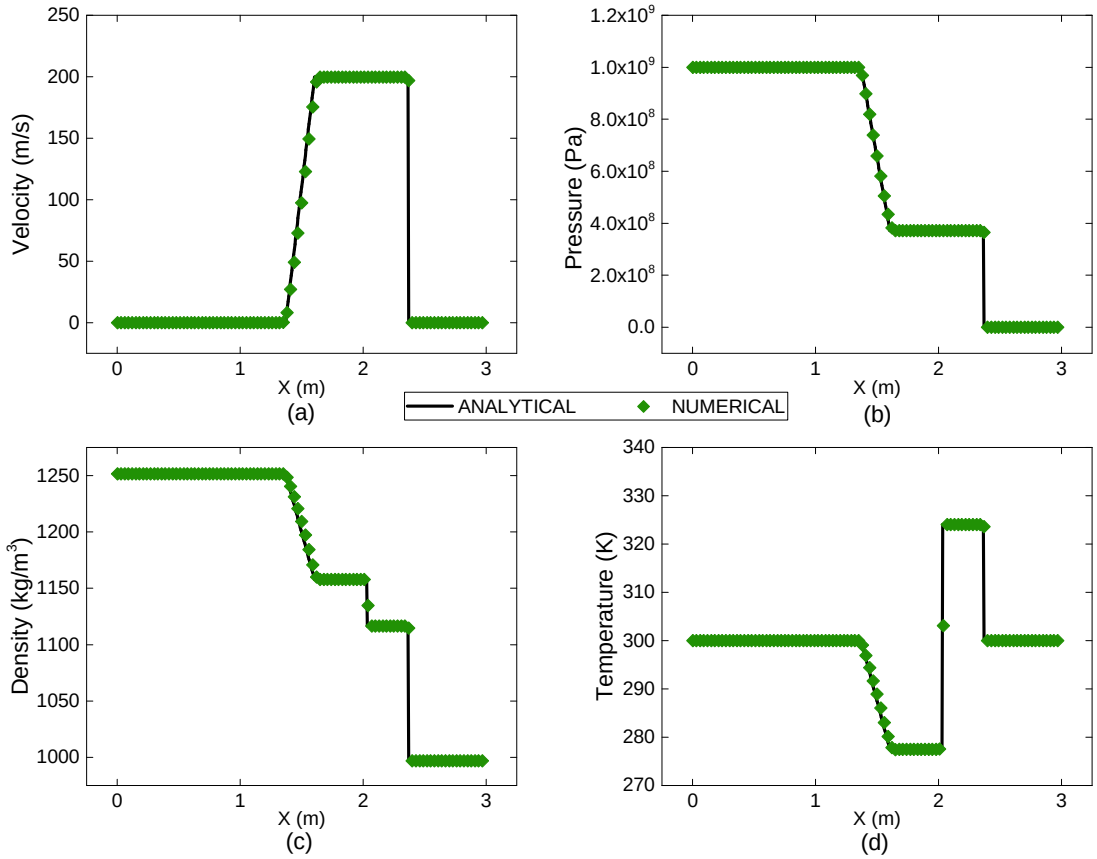

Figure 5.6: Comparison of the analytical and numerical solution profiles for $P_L = 100\,\text{MPa}$, $P_R = 0.1\,\text{MPa}$ at $T = 300\,\text{K}$

already mentioned, all these three cases correspond to a driver section pressure of 500 MPa and a driven section pressure of 0.1 MPa.

All these figures suggest a close agreement between the computational and analytical results. Detailed explanations on the observations related to flow physics and on the values of properties over different zones are presented in Section 4.7 of Chapter 4. The numerical results presented here are grid independent solutions obtained at a resolution of 6,000 divisions and are plotted using 100 equally spaced data points. The optimal CFL value is again found to be close to 0.5.

We have seen some variations in the structure of solution profiles while we modelled cases involving different initial driver section pressures. These variations were observed mostly in relation with the spread of the expansion fan. However, for different operating temperature ranges, such visible variations in the solution structure are absent. This is because of the wider scale over which pressure varies for these cases as compared to the narrower scale of variation for temperature.

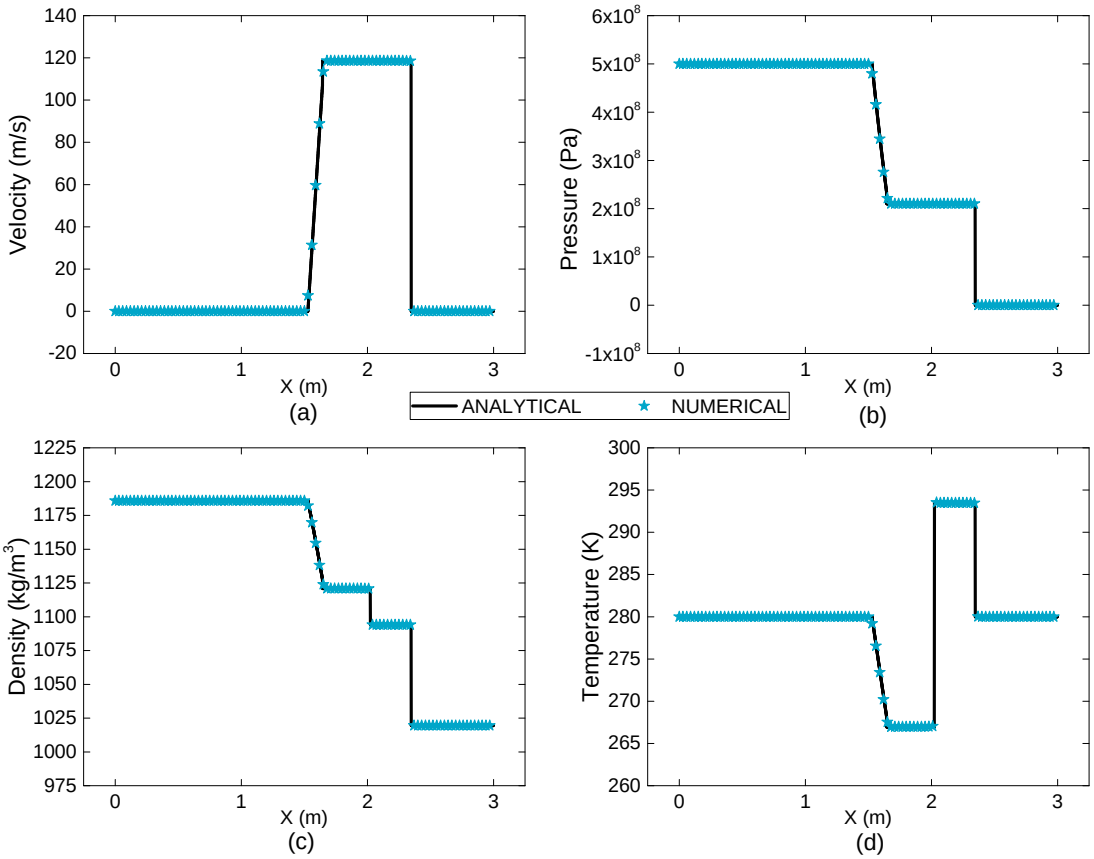

Figure 5.7: Comparison of the analytical and numerical solution profiles for $P_L = 500\,\text{MPa}$, $P_R = 0.1\,\text{MPa}$ at $T = 280\,\text{K}$

We have already seen property profiles for six different cases of water shock tube from the figures displayed. To understand the property magnitudes predicted in the numerical solutions over different zones, for each of these cases modelled, these values are displayed in Tables 5.1 and 5.2.

From the property values reported in Tables 5.1 and 5.2 over different zones, the following observations are made. The flow velocity developed over zones 1 and 2 increases with the rise in driver section pressure. For a fixed value of driven section pressure, the higher value of driver pressure corresponds to a higher diaphragm pressure ratio, and this induces a higher flow velocity. Table 5.2 reports a rise in flow velocity over zones 1 and 2 for an increase in operating temperature, for the same diaphragm pressure ratio. This observation is related to the lower density of liquid at higher temperature.

The difference in pressure values observed over zones 1 and 2 from Table 5.1 for various driver pressure cases is an obvious observation because of the varying diaphragm pressure ratio. As visible from Table 5.2, while the diaphragm pressure ratio is held constant, pres-

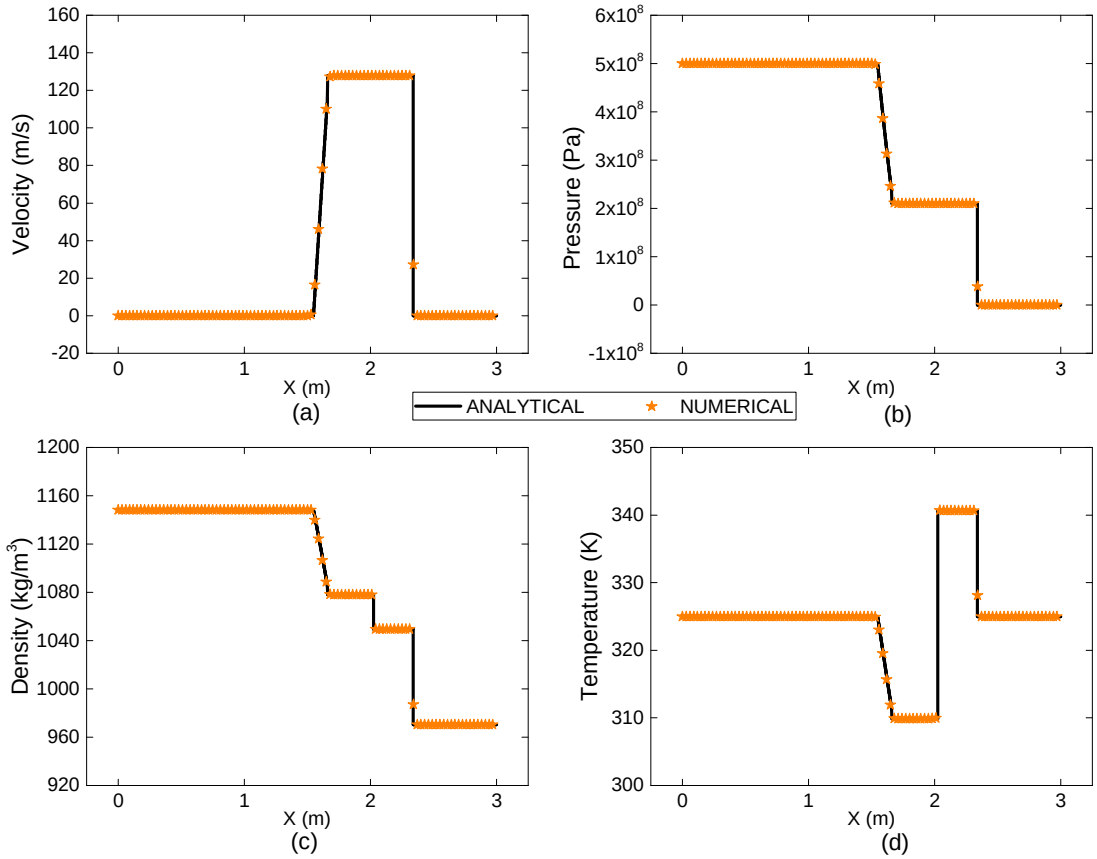

Figure 5.8: Comparison of the analytical and numerical solution profiles for $P_L = 500\,\text{MPa}$, $P_R = 0.1\,\text{MPa}$ at $T = 325\,\text{K}$

sure values over zones 1 and 2 remains nearly the same irrespective of the variations in operating temperature. We could also notice the increase in the density of liquid for higher driver pressures and the maximum density value reported in Table 5.1 is 1251.6 kg/m^3 corresponding to the maximum pressure of 1000 MPa. This is a reliable observation as the equation of state used for the liquid was already shown to be dependable over this pressure range. With the increase in temperature range, a small dip in the density of liquid can be observed over each zone resulting from fluid expansion.

The range over which liquid temperature varies inside the shock tube shows an increase with the rise in the diaphragm pressure ratio. However, such notable variations in the temperature range are not observed for different operating temperature cases. Instead, we could observe a complete upward shift of this range for higher values of operating temperatures. The property values over the expansion zone (E) are not displayed in any of the tables. This is because, unlike other zones with fixed value of properties, the expansion zone has a continuous variation of properties. Property magnitudes over this zone vary between the

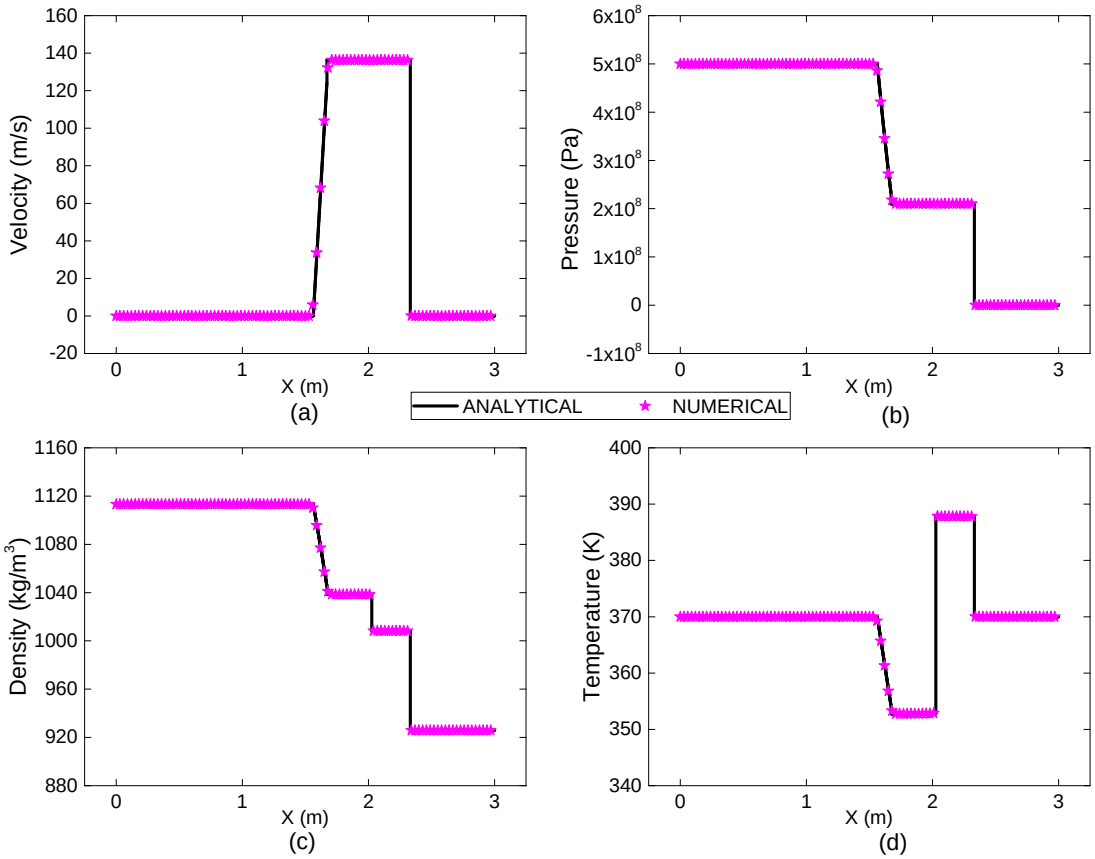

Figure 5.9: Comparison of the analytical and numerical solution profiles for $P_L = 500\,\text{MPa}$, $P_R = 0.1\,\text{MPa}$ at $T = 370\,\text{K}$

values over zone L and zone 2.

More than just a qualitative analysis of results, the comparative study presented in this section demonstrates the ability of the proposed analytical solution to validate numerical results from different computational algorithms. In this section we have discussed different cases of water shock tube problem where either the driver section pressure or the operating temperature is different. We have compared only those cases where either pressure or temperature is different. However, we also need to see the performance of the analytical solution and numerical results for a case where the initial problem setup is slightly more complex. In the next section we are trying to solve such a shock tube problem where all three properties viz., pressure, temperature and velocity are initially discontinuous across the diaphragm.

Table 5.1: Property values over various zones for the water shock tube cases with different driver pressures

Property	Zone	Driver section pressure		
		10 MPa	100 MPa	1000 MPa
Velocity (m/sec)	L	0.0	0.0	0.0
	2	3.3	30.8	199.7
	1	3.3	30.8	199.7
	R	0.0	0.0	0.0
Pressure (MPa)	L	10	100	1000
	2	5.0	48.3	372.1
	1	5.0	48.3	372.1
	R	0.1	0.1	0.1
Density (kg/m^3)	L	1002.2	1044.7	1251.6
	2	1000.0	1024.8	1157.3
	1	999.2	1017.2	1116.9
	R	997.0	997.0	997.0
Temperature (K)	L	300	300	300
	2	299.6	296.4	277.4
	1	300.4	303.6	324.0
	R	300	300	300

5.5 The Effect of Initial Conditions on the Solution of Water Shock Tube Problem

We know that the Sod's problem has a standard initial condition. In this problem, initially, only pressure varies across the diaphragm. The initial temperature is same throughout and the flow is assumed to be stationary over the entire domain. Density of the fluid initially varies based on pressure conditions, as they are related through the relevant EOS. Both the formation of different zones in the solution and the trends observed in property profiles are dependent on the initial conditions for a shock tube problem. For all the different cases of water shock tube problem discussed till now, we have employed a similar set of standard initial conditions. To explore the behaviour of the solution for more complex initial conditions, a new and varied case of water shock tube problem was considered as

Table 5.2: Property values over various zones for the water shock tube cases with different operating temperatures

Property	Zone	Operating temperature		
		280 K	325 K	370 K
Velocity (m/sec)	L	0.0	0.0	0.0
	2	118.6	127.4	136.6
	1	118.6	127.4	136.6
	R	0.0	0.0	0.0
Pressure (MPa)	L	500	500	500
	2	207.7	208.8	210.2
	1	207.7	208.8	210.2
	R	0.1	0.1	0.1
Density (kg/m^3)	L	1184.9	1147.9	1113.1
	2	1121.0	1077.9	1038.5
	1	1093.6	1048.3	1008.4
	R	1018.9	969.7	925.2
Temperature (K)	L	280	325	370
	2	266.9	309.7	352.7
	1	293.4	340.6	387.8
	R	280	325	370

discussed below. The initial setup of this problem is shown in Figure 5.10.

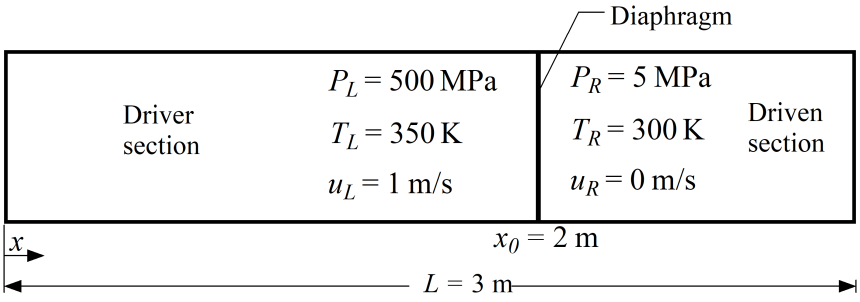

Figure 5.10: 1D schematic of the initial setup for the varied water shock tube problem.

In this problem, as usual, we can see that the pressure is different across the diaphragm. The driver section pressure is 500 MPa and the driven section pressure is 5 MPa. From

Figure 5.10 it may be noted that, we introduced discontinuous initial conditions for both temperature and velocity across the diaphragm. Driver section has a temperature of 350 K and a velocity of 1 m/s, while the driven section temperature is 300 K and the flow in this section is stationary (0 m/s). The shock tube geometry is unaltered from previous cases and has a 3 m long domain.

We intend to explore capability of the analytical solution developed in Chapter 4 to adapt to this slightly complex problem setup. Further, we numerically solve this problem using the same mathematical model described in Section 5.3. The numerical results so obtained are then validated against the analytical solution. Analytical and numerical results for this specific case discussed after 200 μs from the rupture of the diaphragm, are compared in the property plots in Figure 5.11.

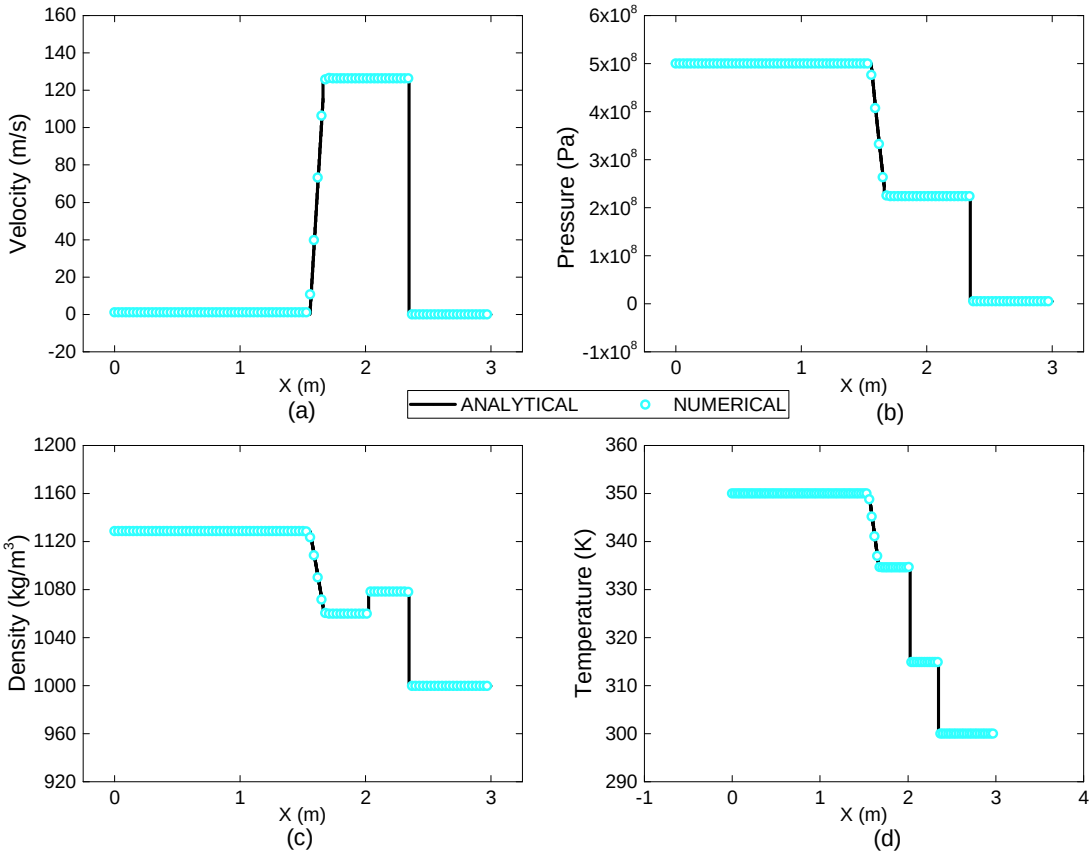

Figure 5.11: Comparison of the analytical and numerical solution profiles for $P_L = 500$ MPa, $P_R = 5$ MPa, $T_L = 350$ K, $T_R = 300$ K, $V_L = 1$ m/s, and $V_R = 0$ m/s,

From Figure 5.11, we could observe that there are some notable variations in the solution profiles compared to standard shock tube problem. While pressure profile does not exhibit any difference in the solution structure, the remaining property profiles do report

certain variations. The temperature profile shows a piece-wise decreasing pattern form the left towards the right of the shock tube domain. Compared to the usual observation where temperature in zone 1 is greater than that of zone 2, here we have the reverse. This is because the initial temperature in zone L is comparatively high compared to that of zone R. Though the rarefaction waves cause a decrease of temperature over zone 2 while the shock wave induces a temperature rise in zone 1, overall both these are insufficient to overcome the high initial temperature difference.

There are also certain notable variations in the density profiles for this problem. Fluid density over zone 1 is usually observed to be lower to that of zone 2, which is not the observed case here. Here we observe that the density over zone 1 is higher than that of zone 2. This observation can be explained as follows. While the higher pressure over zone 2 tends to increase fluid density, the higher value of temperature over this zone has the opposite effect on fluid density. The expansion induced on the liquid by the higher temperature finally results in a lower density in zone 2 compared to that in zone 1. The velocity profile also shows a variation in the velocities on the left most and right most zones based on the initial conditions. However, as we usually observe, the flow velocities over zones 1 and 2 are equalised.

We could conclude that this water shock tube problem with slightly different initial conditions is satisfactorily modelled by the proposed analytical solution procedure. We can now examine the numerical results for the same problem displayed using scattered symbols in Figure 5.11. We see a close match between the numerical and the analytical solution profiles for this problem. This case study of water shock tube simultaneously demonstrates two aspects related to the analytical solution. The first one is versatility of the solution procedure that makes it capable of being applied to slightly modified versions of the shock tube problem. The second aspect is the effective benchmarking capability of the proposed solution for varied flow cases.

5.6 The Effect of EOS on the Solution of Water Shock Tube Problem

We know that modelling of water as a compressible liquid requires relations that connect the properties of water such as pressure, density, temperature etc. These relations should also perform satisfactorily over the property ranges where compressible effects in water become predominant. In this section we present details of the numerical simulation of water

shock tube problem using a few selected equations of state for water. The numerical results obtained were compared based on major observations from the solution profiles. Further, we discuss the merits and demerits associated with each of the specific EOS considered in the comparison. The initial problem setup of the water shock problem used for this study is shown in Figure 5.12.

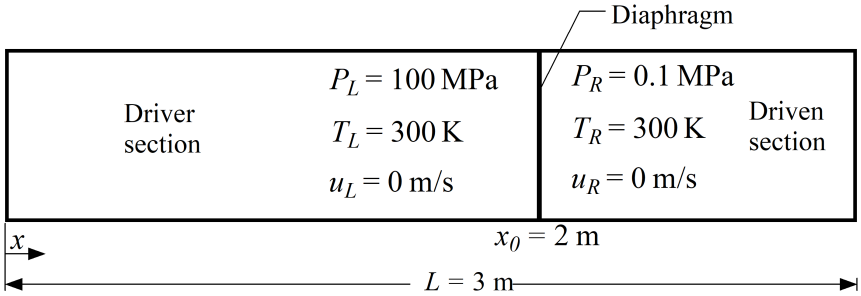

Figure 5.12: 1D schematic of the initial setup for the water shock tube problem for comparing different EOS.

A driver section pressure of 100 MPa and a driven section pressure of 0.1 MPa were considered for the setup. An initial temperature of 300 K and velocity of 0 m/s (stationary) over the complete domain were also preferred.

Four equations of state for liquid water were used in this study to model the compressibility effects in liquid. The Tait EOS and the Stiffened Gas EOS, the two most frequently used EOS for water were considered along with the NASG EOS and the modified version of NASG EOS. The comparatively lucid structure and the ease of incorporation into the flow equations were the two major attributes considered while these EOS were selected for this study. Jolgam et al. in their study of the equations of state for simulation of multi-phase flows [264], use both the Tait EOS and the Stiffened Gas EOS to govern compressible property variations in water. More details on these EOS are available in Section 3.2 of Chapter 3.

The one-dimensional water shock tube problem was numerically solved using each of the four specified EOS for water and the property profiles after 200 μs from the rupture of the diaphragm are plotted in Figure 5.13. Figures 5.13(a) through 5.13(d) display velocity, pressure, density and temperature profiles respectively. The respective numerical values of each of these properties over different zones are enlisted in Table 5.3.

Significant variations observed in the solution profiles obtained with different state equations and are evident from the corresponding property magnitudes reported in Table 5.3. The variations reported are more prominent for density and temperature. Major

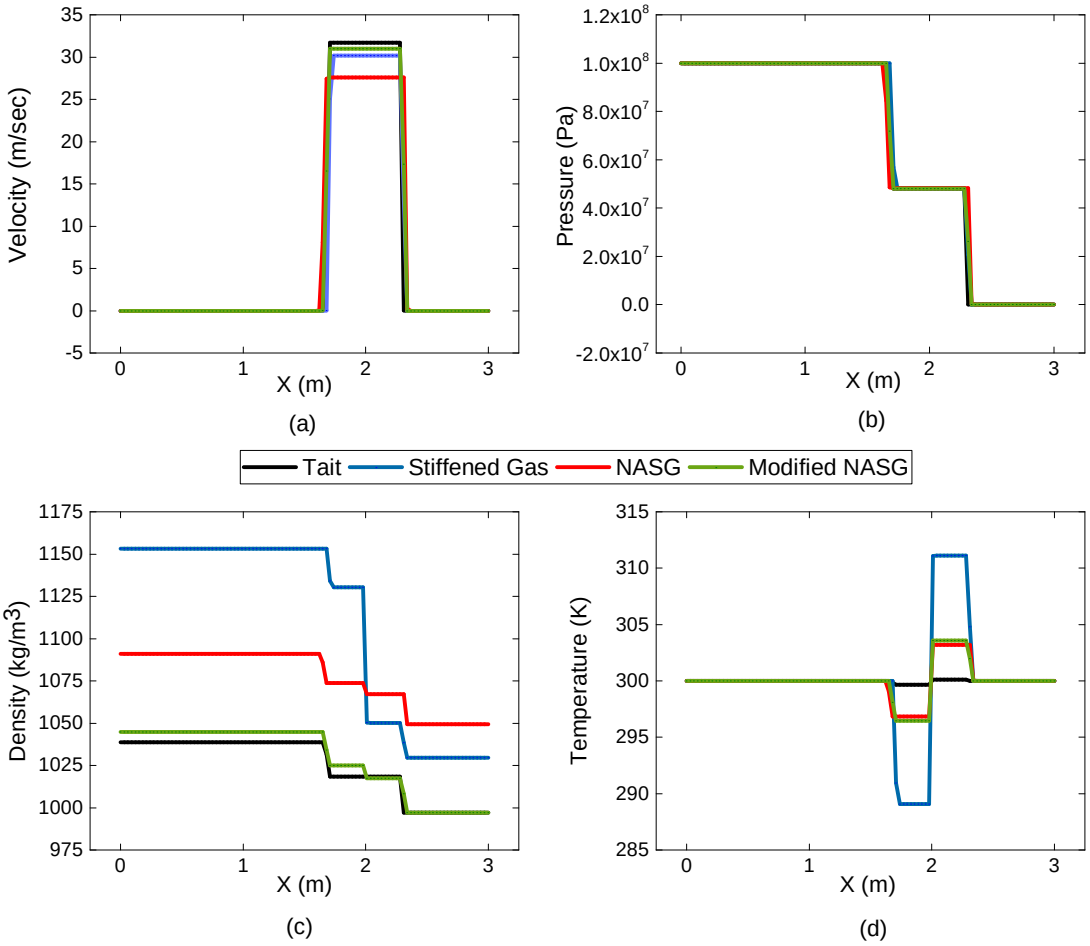

Figure 5.13: Property profiles generated for the water shock tube problem with various EOSs for water.

observations from the analysis are discussed here in detail. The property profiles with Tait equation have not reported any density variation across the contact discontinuity, which is otherwise observed with the other three equations of state. This shortcoming of the EOS may be attributed to the lack of coupling between pressure-density and caloric relations. However, the results reveal that the equation does capture the jump in temperature across the contact surface.

The magnitude of velocity predicted by the Tait and the Stiffened gas equations exhibits very close match for both the cases. The profiles of velocity over its equalised zone stretching over zones 1 and 2 in the plot in Figure 5.13 (a) confirms this claim. However, a slightly lower value is predicted for the same property with the NASG equation. The modified NASG predicts the velocity value close to those from the Tait and the Stiffened gas equations. . The pressure estimates from all four equations of state for the central pressure

Table 5.3: Property values over various zones for the water shock tube cases with different equations of state

Property	Zone	Equation of state			
		Tait	Stiffened Gas	NASG	Modified NASG
Velocity (m/sec)	L	0.0	0.0	0.0	0.0
	2	31.71	30.17	27.6	30.97
	1	31.71	30.17	27.6	30.97
	R	0.0	0.0	0.0	0.0
Pressure (MPa)	L	100	100	100	100
	2	48	48	48	48
	1	48	48	48	48
	R	0.1	0.1	0.1	0.1
Density (kg/m^3)	L	1038.8	1153.1	1090.9	1044.7
	2	1018.3	1130.2	1073.7	1024.9
	1	1018.3	1050.1	1067.0	1017.3
	R	997.0	1029.6	1049.3	997.0
Temperature (K)	L	300	300	300	300
	2	299.66	289.10	296	296.45
	1	300.12	311.13	302.44	303.58
	R	300	300	300	300

equalised zone between the expansion fan and shock vary within a very narrow range. The rounding off gives a value of 48 MPa as the estimated pressure in this region with all the four EOS employed.

The fluid property which exhibits maximum variation in its magnitude with different state equations is the fluid density. Density values of water at a temperature of 300 K and for the pressure ranges of 0.1 MPa and 100 MPa from the NIST database are 996.56 kg/m^3 and 1037.20 kg/m^3 respectively. Density estimates from different equations of state in the zones formed are reported in Table 5.3. The corresponding percentage error in the density prediction with each EOS with respect to the NIST data is presented in Table 5.4.

Of all the state equations employed, Tait equation predicts a density closest to the NIST standard database. Density evaluation with the Stiffened gas equation exhibits the largest deviation from the standard values and the reported error is too large to recommend its use,

Table 5.4: Percentage error in density from each EOS compared to NIST data

Pressure Range (MPa)	% Error in density for EOS			
	Tait	Stiffened gas	NASG	Modified NASG
0.1	0.044	3.32	5.29	0.044
100	0.155	11.18	5.18	0.72

especially at higher pressure ranges. The NASG equation is noticed to perform mid-way between the other two choices. The density estimate error magnitude places it slightly inferior to the Tait equation, whereas the same is an improvement over the Stiffened gas equation. A trend of error growth in density estimates is observed with the Tait and Stiffened gas equations with the increase of pressure range. However, the error associated with the Tait equation is only 0.155% for the pressure range of 100 MPa. For Stiffened gas equation, the estimated density and NIST value exhibit fast-growing divergence with rise in pressure range. The error in density prediction which was under 5% for the 0.1 MPa range, shoots above 10 % for the 100 MPa range with the stiffened gas EOS. This is considerable deviation from the NIST data and this over prediction of density with the Stiffened gas EOS is clearly visible in Figure 5.13 (c). The error percentage is observed to diminish in magnitude with increase in pressure range for the NASG EOS and the maximum error reported is 5.29% at the lowest pressure range of 0.1 MPa. The NASG, primarily being an EOS modelled with the aim of relating pressure, density and caloric properties of saturated water, is expected to show variations while applied with liquid water away from saturation conditions.

The modified NASG equation is observed to produce superior results over its original version as well as the Stiffened gas EOS. Through the refinement of parameters, the state equation emerges adapted for application over a wider expanse away from the saturation conditions. The error in density estimate reducing from 5.29% to a mere 0.044% at the lower pressure range of 0.1 MPa strengthens the claim. Error reported with the original version of the NASG equation for pressure ranges of 0.1 MPa and 100 MPa reduced from 5.29% and 5.18% respectively to 0.044% and 0.72%, which is a clear indication of improvement in accuracy of the EOS with the proposed modification. Thus, the modified NASG EOS is comparable to the accuracy of the Tait equation with the clear advantage of properly coupled pressure-density and caloric relations. The state equation also exhibits the general trend of error growth with higher pressure ranges.

The temperature predicted over different zones also exhibits notable variations with the

EOS used. The lowest variation of temperature range inside the liquid shock tube is predicted by the Tait EOS with the range of variation between 299.66 K-300.12 K. The Stiffened gas EOS reported the highest variation in temperature range which extends between 289.10 K and 311.13 K. The inherent inaccuracies associated with specific heat values of water for the Stiffened gas equation is a possible reason for the excessively extended prediction of temperature range by this EOS. The NASG and modified NASG EOS predicted the range of temperature variation in between the above discussed values, and these values are also close to each other. While the NASG predicts it between 296 K and 302.44 K, the modified NASG provides the temperature estimates in the range of 296.45 K-303.58 K.

Another observation made in the results with different state equations is the variation in the extent of the central zone bounded by expansion wave and shock over which pressure and velocity are equalised. These variations could be attributed to the difference types of EOS used in the formulation of speed of sound. Based on the speed of signal propagation the expanse over which the initial flow conditions are disturbed can vary over a given time period.

On the basis of the reported error in the property estimates in comparison with the NIST standard database as well as from the scrutiny of the relative capability in modelling the complete physics of the flow problem, the modified version of NASG equation substantiates its superiority. The modified NASG EOS is thus recommended in the modelling of liquid water flows involving very wide pressure ranges where compressible effects of the liquid and thermal effects on density are to be considered.

5.7 Summary

In this chapter we presented a comparative study on a few selected computational algorithms by modelling the Sods's shock tube problem. The HLLC was found to be the best flux method in its pure form. This HLLC flux was further combined with the MUSCL-based system along with a few slope limiter algorithms. The MUSCL-HLLC flux with MC type limiter was found to be the optimal solver combination from simulation studies on the one-dimensional Sod's shock tube problem. Further, the chapter discussed the use of one-dimensional equations for compressible flow as the suitable mathematical model for numerically solving water shock tube problem. The selection of modified NASG EOS as the closure relation and its appropriateness in modelling the compressibility effects in water were also explained. The computational strategy employed in the chapter was also discussed along with this. Six different cases of the water shock tube problem were solved

numerically and these numerical results were validated by comparing them against the analytical solutions. Very close agreement was observed between the numerical and analytical solutions for all the cases considered. The six cases were subdivided into three cases each for studying the numerical results under specified range of pressure and temperature. To understand the applicability of the analytical and numerical solution techniques to a slightly varied problem setup, a new case of the water shock tube problem was considered with a somewhat complex initial condition. This study demonstrated the ability of the analytical solution and the numerical methodology used to adapt to a variety of problem setups and their ability to capture the physics of the problem. The last section of the chapter tried to numerically simulate the water shock tube problem using a few selected EOS for water to understand the difference in solution based on the state equation for liquid used. This study provided many valuable observations like the large deviations in results using the Stiffened gas EOS, the incapability of the Tait EOS to model non-isothermal flow cases despite its high accuracy, etc. The study also showed the superiority of the modified NASG EOS in accurately modelling the compressibility effects of liquid water under isothermal and non-isothermal conditions. The close match observed between the analytical and numerical solutions to the water shock tube problem that were achieved using entirely different approaches proved the reliability of the solutions presented. This chapter also demonstrates that the analytical solution developed for liquid shock tube could be successfully used for the validation of numerical solutions obtained with various computational algorithms for compressible liquid flows.

Chapter 6

Hydraulic Surge Estimation: The Concept of Adaptive-Damping

6.1 Introduction

We have discussed several cases where liquids are compressed under extreme pressures in Section 2.2 of Chapter 2. Water in its liquid state finds application in many industrial and nonindustrial systems where the system pressure is extremely high. Under such flow scenarios the compressibility effects in the liquid becomes significant. Hydraulic surges in transfer pipelines triggered by sudden valve closures are commonly observed in industrial, laboratory, and domestic flow situations. The experimentally measured pressure data frequently shows that the maximum pressures reached during a hydraulic surge surpasses the operating pressure by a considerable margin. This information is crucial to the safety of a system and simulation of such flow cases demands high accuracy. The numerical simulation results for such flow situations are usually observed to have deviations from the experimentally measured data. The incapability of the mathematical model to capture certain flow physics is a major cause for such inaccuracies. Treating the liquids to be compressible for high-pressure conditions, usage of advanced pressure damping models, etc., in the mathematical model shall improve simulation accuracy.

In this chapter we present a single-phase mathematical model for the simulation of valve induced hydraulic surges that are non-cavitating or nearly non-cavitating. The proposed model includes two major improvements in relation to flow physics modelling. The first one is that this model considers the compressibility effects in liquid through the inclusion of a dedicated equation of state. The second speciality is that the model includes an adaptive damping technique for surge data prediction by introducing a variable pressure wave damping coefficient.

Section 6.2 discusses the importance of studying and estimating hydraulic surges in different flow systems. This section also explains some catastrophic system failures reported in the literature, that were triggered by the unexpected hydraulic surges in those systems. Section 6.3 describes the particulars of two selected high-pressure rapid valve-closure experiments. The step by step procedure adopted in developing a mathematical model for the simulation of non-cavitating hydraulic surges is explained in Section 6.4. The selection of a suitable mathematical model and the incorporation of the compressible model for the liquid into it are described in the Section 6.5. The proposed mathematical model is presented in Section 6.6 in its corresponding matrix form. The subsequent Section 6.7 describes the computational strategy to numerically simulate hydraulic surge problem using the Split Coefficient Matrix Method (SCM). Results from the simulation using the two-equation compressible-liquid model is presented in Section 6.8, where it is compared with the experimental data along with a discussion of the major observations. Section 6.9 introduces the concept of adaptive damping in pressure surge prediction by defining a new variable pressure wave damping coefficient (VPDC) as a function. The subsequent Section 6.10 presents the simulation results obtained using the two-equation model with the VPDC and discusses the differences observed in the results from those obtained using the same model with a constant pressure wave damping coefficient. The numerical results for transient cases are also thoroughly analysed and compared with the corresponding experimental data. The final Section 6.11 summarises the chapter.

6.2 Hydraulic Surges in Systems

The hydraulic surge in pipes is a widely studied flow phenomenon due to its high practical relevance in water-supply for industrial and non-industrial applications. The importance of studies on the surge in pressure due to events like sudden closure of valves cannot be overemphasised. A thorough analysis of the surge in fluid properties is required for any flow transient for the safety of the structure to avoid hazardous failures. This is why we closely monitor pressure variations at strategic locations in a flow system. The surge data is expected to provide information on the peak pressures reached inside a flow system for a given period of operation. Along with maximum and minimum magnitudes of pressure, the time at which they occur and the exact location inside the flow system where they are expected are also important. This hydraulic surge, or what we commonly call as the water hammer phenomena, is reported to have caused numerous fluid transfer system failures over different parts of the world. The extreme surge in pressure in systems is capable of

causing multiple failures such as rupturing of the pipe fittings, valve failures, failure of heat exchanger components, breaking of the welded joints in pipes, damage to the pipe supports, overstressing of the pressure gauges, etc. The photographs of certain failed components due to hydraulic surges are displayed in Figure 6.1.

(a) Damaged discharge pipe of 12 mm wall thickness

(b) A permanently deformed pipe support

(c) Damaged check valve from pressure surge

Figure 6.1: Photographs of failed components form hydraulic surges

A ruptured cast iron pipe from a water hammer event is displayed in Figure 6.2 (a). The Sayano Shushenskaya Dam incident on 17th of August, 2009, which claimed the lives of 75 people, was reportedly from a turbine draft tube water hammer triggered by a sudden gate valve closure [265]. A liquid ammonia hydraulic shock has led to the catastrophic failure of a 12-inch suction pipe at the Millard Refrigeration Services facility in Theodore, Alabama on 23rd August, 2010 [266]. The rupture of this pipe resulted in the release of large quantities anhydrous ammonia in excess of 32,000 pounds. Figure 6.2 (b) shows the image of the ruptured suction pipe.

(a) A cast-iron pipe ruptured from water hammer

(b) The damaged pipe from Millard Incident

Figure 6.2: Photographs of the ruptured pipes from hydraulic surges

Hydraulic shocks or water hammers are the result of conversion of the kinetic energy of

a flowing fluid into elastic energy. This effect becomes prominent only for sudden accelerations or declaration of a flow. The fluid is deformed at the changing boundary because of the inertia associated with flowing fluid. The fluid deformation is accompanied by corresponding transient variations in pressure. The surge pressure waves thus generated propagates at the speed of sound in the liquid, which is close to 1250 m/s. This high momentum makes the pressure surge very dangerous as it can lead to devastating effects over all parts of the piping system it reaches.

A historical review of water-hammer with column separation is available in [267]. Leishear [268] provides a summary of water hammer-induced pipe failures. Theory and experiments on fluid transients in systems and the studies on various parameters affecting water hammer are available in the books [269, 270]. The work by de Freitas Rachid [271] analyses the damage evolution induced by pressure transients, and the study by Khudayarov and Turaev [272] mathematically simulates non-linear oscillations in viscoelastic pipelines conveying fluid. Modelling and optimising hydraulic transients in water distribution systems, using the classical gradient and heuristic optimisation techniques, are reported by Skulovich et al. in [273]. Numerical detection of cavitation damage level and location on dam spillways is reported in [274]. The recent work by Leishear [275] reveals that water hammer is the main initiator of almost every underground water main breaks.

Provoost [276] carried out an early investigation into cavitation in pipelines due to water hammer. Numerous two-phase cavitation models such as those by Shu [277], Covas et al. [278], Kaliatka et al. [279] are available in the literature for predicting hydraulic surges in pipes. The works by Kucienska et al. [280], Tian et al. [281], and Soares et al. [282] report different two-phase cavitational hammer models. Sadafi et al. describe a generalised interface vaporous cavitation model in [283], while Pinho et al. [284] present a full cavitation model for two-phase water hammer modelling. In these two-phase cavitation models, the gaseous components are modelled as compressible fluids, whereas the liquid component, which is usually water, is invariably treated to be incompressible. There are many practical situations like the displacement of waxy crude oils studied by Frigaard et al. in [285], or the motion of ultrasonic cavitation bubble studied by Qu et al. in [286], where liquid compressibility consideration, though mild, may contribute to the completeness of the model. The simulation of transient flows in viscoelastic pipes with vapour cavitation by Hadj-Taïeb and Hadj-Taïeb [287], employs a compressible model for both liquid and gaseous phases.

For hydraulic surges arising from sudden valve closures at high operating pressures, the cavitation effects are generally absent. For such cases, a comparatively simple mathemat-

ical model is preferred such that it drastically reduces the computational cost to simulate flow transient.

6.3 The Valve-Induced Hydraulic Surge Experiments

We selected two valve-closure experiments with sufficiently high operating pressures such that they are non-cavitating cases and could be safely simulated using a single-phase model. These two high pressure experiments were conducted by Neuhas et al. [288] at the Pilot Plant Pipework (PPP) test rig at Fraunhofer UMSICHT. Experimental and numerical studies on water hammer induced flow transients at the PPP test rig are also available in [289, 290]. The schematic of the PPP experimental setup with measurement points are shown in Figure 6.3.

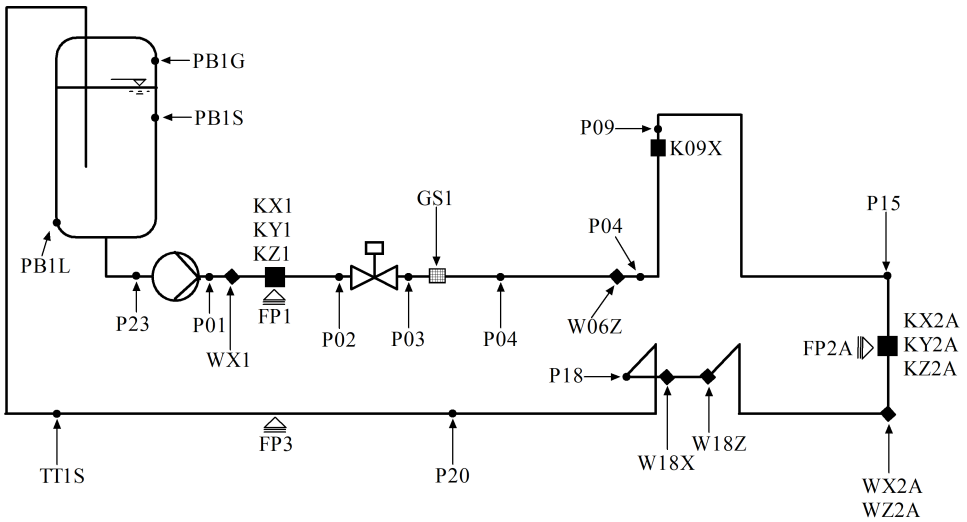

Figure 6.3: Schematic of the Fraunhofer UMSICHT PPP experimental setup with measurement points.

The experimental procedure is as follows. Demineralised tap water from reservoir B1 is pumped into a 110 mm inner diameter and 170 m long steel pipeline. This pumping initially pressurises the entire pipeline to the high pressure maintained inside the reservoir. The valve located between the pressure transducers P02 and P03 closes almost instantaneously at time $t = 0$ while the pump remains running. Due to the sudden closure of the valve, a strong rarefaction wave is generated towards the downstream of it. This wave traverses further downstream towards reservoir B1. Vapour bubbles can form at locations where the fluid pressure goes below its vapour pressure. The rarefaction waves generated oscillate in

the pipe system and undergo multiple reflections at the boundaries until they get dissipated completely.

The two high pressure experiments chosen for validation of the method are Experiment No. 415 and Experiment No. 347 mentioned in [288]. The details of these experiments are provided in Table 6.1.

Table 6.1: Details of the experimental conditions

Experiment No	Fluid Velocity, u [m/s]	Flow Rate, Q [m^3/hr]	Temperature, T [°C]	Pressure, P_R [bar]
415	1.00	33.2	21.9	19.65
347	1.01	33.4	20.3	12.50

The valve closure Experiments No. 415 and No. 347 reported in [288] correspond to the operating pressure ranges of 19.65 bar and 12.50 bar, respectively, with the temperature close to 20 °C. For these two high-pressure experiments, the lowest values of transient pressure measured are well above the saturation pressure of liquid and because of this the effects due to cavitation are absent. The pressure transducer P03 shown in Figure 6.3, located at a distance of 0.2 m downstream of the valve, records the transient pressure data. The experimentally measured pressure values at the location P03 for the Experiment Nos.415 and 347 are displayed in Figures 6.4 and 6.5.

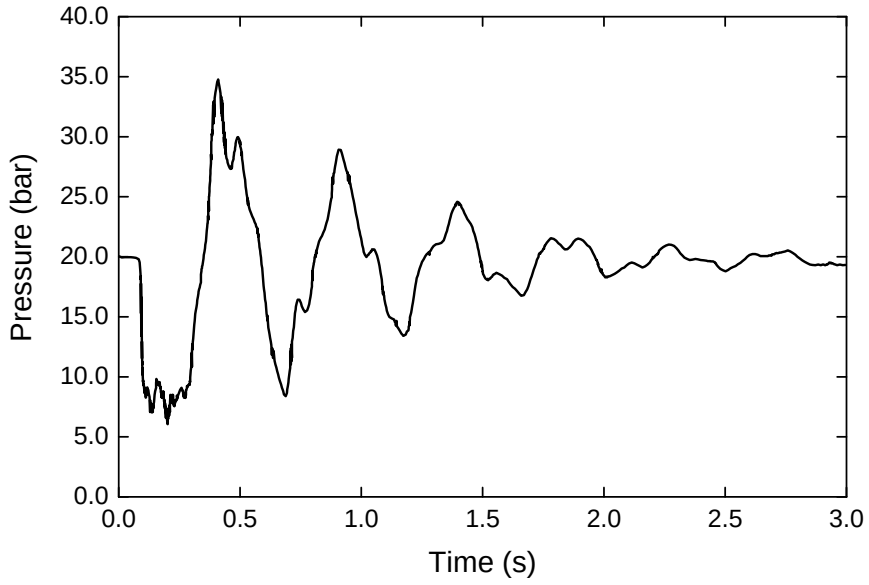

Figure 6.4: The measured pressure values at P03 for experiment 415.

The pressure data was recorded for a duration of 3 seconds from the initiation of the valve closure for Experiment No. 415. However, for Experiment No. 347, the pressure data recording continued till 5 seconds from the valve closure. These durations are also based on the relative time within which the pressure oscillations almost damp down completely inside the system. A strong rarefaction wave is generated just downstream of the valve immediately after its closure as the inertia of moving fluid creates a low-pressure area in the downstream region of the valve. The crests (peaks) and troughs (anti-peaks) seen from the experimental pressure profile indicate the rarefaction waves propagating to and fro along the length of the pipe, undergoing multiple reflections at boundaries. Due to frictional forces in the pipe flow system, these waves lose their energy and dissipate into a steady-state, which is evident from the decreasing amplitude of pressure with time.

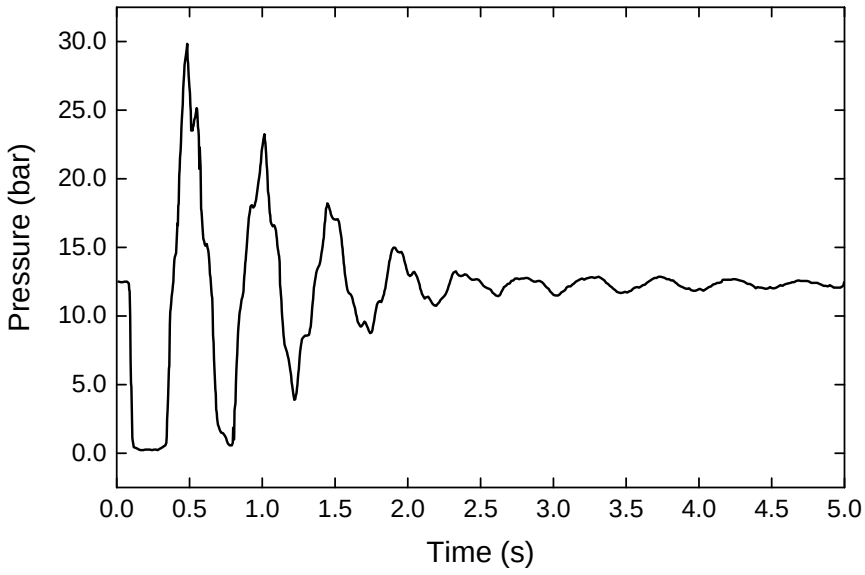

Figure 6.5: The measured pressure values at P03 for experiment 347.

Beginning from an initial condition of 19.65 bar, the pressure during the valve-induced surge reached a maximum value close to 35 bar for Experiment No. 415. The minimum pressure recorded by pressure transducer at P03 is around 6 bar for this experiment which is due to impact of the rarefaction waves generated. In the case of Experiment No. 347, highest pressure recorded by the pressure pick-up is close to 30 bar. These experimentally measured data for the selected cases shall be later used for the validation of the mathematical model we propose.

6.4 Procedure for Model Development

In this chapter, we intend to develop a simplified mathematical model that would be computationally inexpensive to simulate non-cavitating hydraulic surges. The model should also be able to address the compressibility effects in liquid during the surge, in addition to the savings offered in computation. We also intend to incorporate a variable pressure wave damping coefficient (VPDC) to this model to improve the prediction of transient variations in pressure during the surge. The procedure followed to develop the intended model is explained below.

Neuhaus et al. presented a three-equation model in [34] for the calculation of thermo-hydraulic pressure surges in pipes. This is a two-phase model intended for the simulation of cavitational hammers and is a computationally expensive one. This model is to be modified into a two-equation model for single-phase cases. The modified model could then be used for the simulation of hydraulic surges for high-pressure flow cases where cavitation effects are negligible. A suitable equation of state (EOS) for liquid should be further incorporated into this single-phase model to account for the compressibility effects in liquid. The selected EOS should be able to relate fluid density and signal wave speed to pressure. The specific EOS we intend to use is the modified Noble-Abel Stiffened Gas equation of state (modified NASG EOS) [253], which is a highly accurate non-isothermal EOS for liquid water. Further, we will define a variable pressure wave damping coefficient as a replacement to the typical constant friction coefficient. This is to improve the accuracy of numerical solver for predicting oscillations in pressure during the surge. The variable pressure wave damping coefficient would be defined as a tunable function of the local pressure fluctuations.

On finalizing the mathematical model, a suitable computational strategy shall be adopted for the numerical simulation of hydraulic surge associated with sudden valve closure experiments. The Split-Coefficient Matrix (SCM) method [291] that uses characteristic direction based splitting, would be used for modelling wave propagation during fluid transient. The proposed computational model will be then validated by using experimentally measured data reported in [288]. The two-equation model shall be compared to the original three-equation model to showcase model simplification and improvements in saving cost of computation. The flow chart shown below illustrates the research methodology used.

Selection of an existing mathematical model (the three-equation model) for cavitating hydraulic surges.

⇓

Simplifying this mathematical model (to the two-equation model) to make it suitable for non-cavitating hydraulic surges at high operating pressures.

⇓

Inclusion of compressibility effects in liquid by incorporating a suitable EOS for liquid into the model.

⇓

Developing a computational strategy to use this mathematical model to numerically simulate practical flow cases.

⇓

Analysing the results for any variations and improvement with the proposed compressible model.

⇓

Defining a variable pressure wave damping coefficient (VPDC) based on local fluctuations of pressure in the flow field.

⇓

Incorporation of the VPDC into the two-equation compressible-liquid model to provide adaptive damping capability to the solver model.

⇓

Numerically solving the non-cavitating hydraulic surges using the VPDC incorporated two-equation compressible-liquid model.

⇓

Analysing numerical results from the proposed model against the experimental data and numerical results from the original 3-equation model, to understand the improvements brought by this model in the simulation of hydraulic surges.

6.5 The Mathematical Model

This section provides details of the three-equation model for cavitational hammer and its simplification into a two-equation model. The selection of a suitable liquid EOS and its incorporation into mathematical model are also discussed.

6.5.1 The three-equation model

A three-equation two-phase model is proposed by Neuhaus et al. in [34] for numerical simulation of cavitational hammer and related thermo-hydraulic pressure surges. This system

includes separate conservation equations for the mass of each phase (liquid and gas) and a combined momentum equation for both the phases, assuming that there is no slip in velocity between the phases. Below we present the conservation equations for mass in the liquid phase, in the gas phase (air + vapour) and the combined momentum equation for both the phases (in that order).

$$\frac{(1-\alpha)}{{a_L}^2}\frac{\partial P}{\partial t} - \rho_L\frac{\partial \alpha}{\partial t} + \frac{(1-\alpha)u}{{a_L}^2}\frac{\partial P}{\partial x} - \rho_L u\frac{\partial \alpha}{\partial x} + (1-\alpha)\rho_L\frac{\partial u}{\partial x} = -\Gamma_V - \Gamma_A \tag{6.1a}$$

$$\frac{\alpha}{{a_G}^2}\frac{\partial P}{\partial t} + \rho_G\frac{\partial \alpha}{\partial t} + \frac{\alpha u}{{a_G}^2}\frac{\partial P}{\partial x} + \rho_G u\frac{\partial \alpha}{\partial x} + \alpha\rho_G\frac{\partial u}{\partial x} = \Gamma_V + \Gamma_A \tag{6.1b}$$

$$\frac{\partial u}{\partial t} + u\frac{\partial u}{\partial x} + \frac{1}{\rho_M}\frac{\partial P}{\partial x} = -\frac{4\tau}{\rho_M d} \tag{6.1c}$$

where P, u, ρ, and α are respectively the pressure, axial velocity, density, and void fraction of the flow. The symbol a represents speed of propagation of wave in the medium and τ is the shear force due to skin friction. Γ_V denotes mass transfer due to vaporisation/condensation and Γ_A is the mass transfer due to air release, and d is the pipe diameter. The variables x and t ddenotes spatial and temporal coordinates. The subscripts L, G, V, A, and M respectively denote the liquid, gas, vapour, air, and the two-phase mixture. The liquid-gas mixture density, ρ_M, is computed using the following relation:

$$\rho_M = (1-\alpha)\rho_L + \alpha\rho_G \tag{6.2}$$

The flow model also incorporates steady and unsteady friction models as well as the effects of degassing. An optional structural model is also included in the system to take into account the effects of fluid-structure interactions (FSI). The results from this mathematical model are validated against a series of experiments at the Pilot Plant Pipework (PPP), Fraunhofer UMSICHT. The report by Neuhaus et al. [288] shows results from the three-equation mathematical model performing well with two-phase flow cases at low operating pressures. For high operating pressures reported in [288], this model performs satisfactorily only with the incorporation of FSI into it. The simulation results for Experiment Nos. 415 and 347 using the three-equation model are respectively displayed in Figures 6.6 and 6.7.

We could clearly observe variations between the numerical results and the experimentally measured data in the figures. The numerical results displayed are obtained without using FSI algorithm in the mathematical model. The damping down of pressure waves as

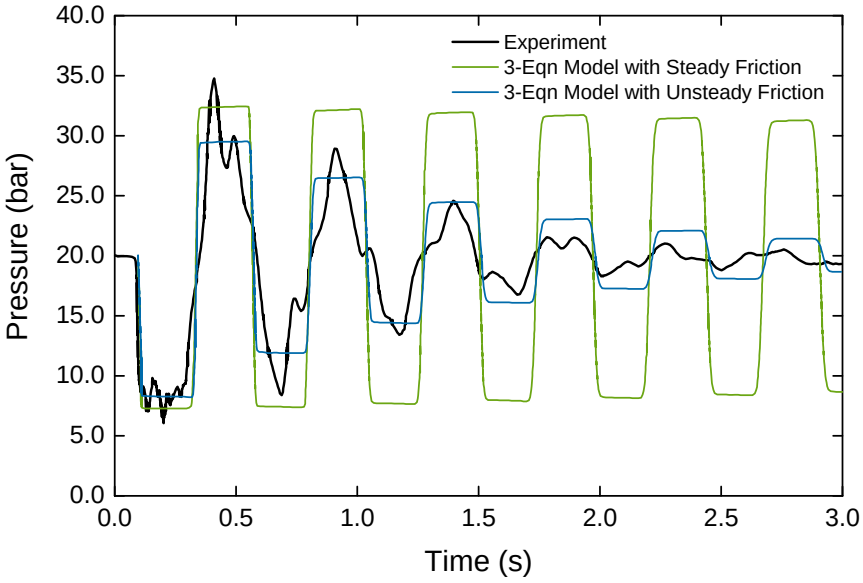

Figure 6.6: Simulation results for Experiment 415 using the 3-Equation model with steady and unsteady friction models

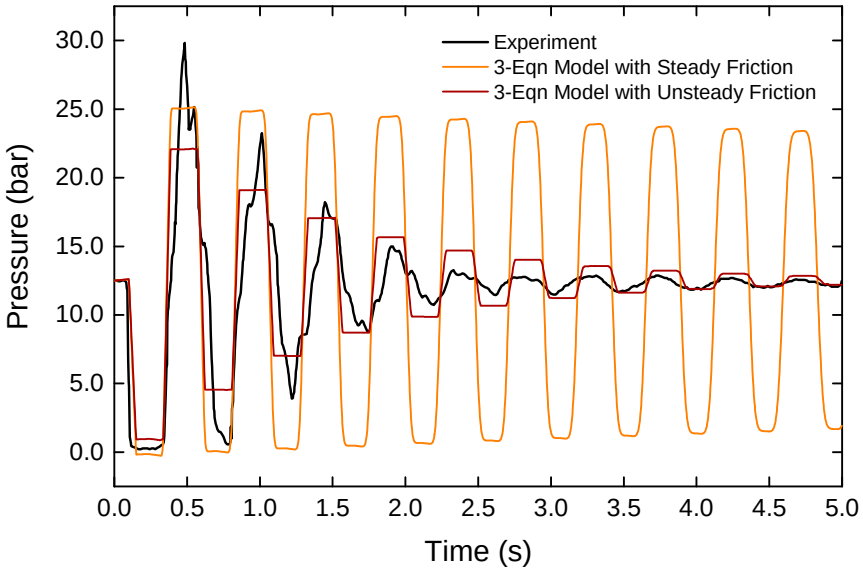

Figure 6.7: Simulation results for Experiment 347 using the 3-Equation model with steady and unsteady friction models

observed in the experiment could not be reproduced by the steady friction model. However, the highest peaks that appear initially in the transient are closely predicted by the steady friction model. Though there exists high inaccuracies in the initial phase of transient predicted, the unsteady friction model correctly indicates dissipation of the pressure waves. While there are notable deviations in amplitudes of peaks and anti-peaks in the numeri-

cal pressure profiles, frequency of transient pressure variations from the simulations are observed to be close to that of the experimental observation.

6.5.2 The two-equation compressible-liquid model

Here we propose a single-phase two-equation model as a modification to the three-equation model described above for flow situations where there are no cavitation effects. The proposed model tries to simulate flow physics without using the FSI algorithm in it, which considerably reduces the computational complexity. For single-phase flow in a horizontal pipe, in the absence of cavitation effects, the three-equation model discussed above reduces to a two-equation system as follows:

$$\frac{1}{a^2}\frac{\partial P}{\partial t} + \frac{u}{a^2}\frac{\partial P}{\partial x} + \rho\frac{\partial u}{\partial x} = 0 \tag{6.3a}$$

$$\frac{\partial u}{\partial t} + u\frac{\partial u}{\partial x} + \frac{1}{\rho}\frac{\partial P}{\partial x} = -\frac{4\tau}{\rho d} \tag{6.3b}$$

Equation (6.1a) reduces to Equation (6.3a), which represents the mass balance for the liquid, and Equation (6.1c) reduces to Equation (6.3b), which represents the momentum balance for the liquid phase. The mass balance for gas phases given by Equation (6.1b) identically satisfies due to single-phase consideration, and the subscripts for flow variables are dropped as only one phase is dealt with in the model. Equations (6.3a) and (6.3b) form a system of PDEs with the dependent variables u, P, and ρ. The temperature is assumed to be constant during the flow process and energy balances are thus automatically satisfied. The density ρ of liquid is treated as a variable using an appropriate compressible model as discussed in Section 6.5.2.1. Initially the shear stress τ is estimated using the same unsteady friction model as used with the three-equation model that uses a constant friction coefficient for pressure wave damping effects. The source term in the momentum equation represents the head losses per unit length due to frictional effects. This term is the sum of the head losses due to steady and unsteady friction.

6.5.2.1 The compressible modelling of water

We know that the accuracy associated with any surge analysis is dependent on the accuracy of data inputs entered in to the system. Only with this accurate input a computation model can faithfully reproduce the real system conditions. Wherever a liquid is exposed to extreme pressure conditions, compressibility effects in that liquid will become significant. In

such situations, we could move a step closer to the actual field conditions by modelling the liquid as a compressible fluid. This shall also improve the simulation accuracy. While we take a closer look at flow transients generated from instantaneous or fast valve closures, we could see that the liquid is frequently exposed to large pressures. This is evident from the surge data for such flow situations, where we closely monitor pressure variations at strategic locations in a flow system. For the selected experimental setups, water is modelled as a compressible liquid because it is subjected to very high pressures both at operating and surge conditions.

The density of liquid water is estimated using the modified NASG equation of state (EOS) proposed in [253]. This EOS relates pressure P, specific volume v, and specific internal energy ε of the liquid as follows:

$$P = (\gamma - 1)\,\frac{(\varepsilon - q)}{(v - b)} - \gamma P_{\infty}$$

The relation for speed of sound in unconfined liquid compatible with the EOS is given as follows:

$$c = \sqrt{\frac{\gamma v^2\,(P + P_{\infty})}{v - b}}$$

Radial expansion of the pipe is considered while estimating the speed of propagation of wave (a) in water using the following relation:

$$a = \frac{1}{\sqrt{\frac{1}{c^2} + (1 - \nu^2)\frac{\rho d}{Es}}} \tag{6.4}$$

In Equation (6.4), ν and E are respectively the Poisson's ratio and the Young's modulus of pipe material, and s is the pipe wall thickness.

6.6 Compact Form of the Mathematical Model

The two-equation model is initially converted to the corresponding matrix form and the resulting matrix system is then solved in a two-step process. The process involves converting the governing equations into characteristic form and solving them using the split coefficient matrix technique. The details are as given below:

The governing relations of the two-equation model given by Equations (6.3a) and (6.3b)

can be written in the compact matrix from as follows:

$$\begin{bmatrix} \frac{1}{a^2} & 0 \\ 0 & 1 \end{bmatrix} \begin{bmatrix} \frac{\partial P}{\partial t} \\ \frac{\partial u}{\partial t} \end{bmatrix} + \begin{bmatrix} \frac{u}{a^2} & \rho \\ \frac{1}{\rho} & u \end{bmatrix} \begin{bmatrix} \frac{\partial P}{\partial x} \\ \frac{\partial u}{\partial x} \end{bmatrix} = \begin{bmatrix} 0 \\ \frac{-4\tau}{\rho d} \end{bmatrix} \tag{6.5}$$

Equation (6.5) is of the form

$$A\frac{\partial U}{\partial t} + B\frac{\partial U}{\partial x} = S \tag{6.6}$$

In Equation (6.6)

$$A = \begin{bmatrix} \frac{1}{a^2} & 0 \\ 0 & 1 \end{bmatrix}, \quad B = \begin{bmatrix} \frac{u}{a^2} & \rho \\ \frac{1}{\rho} & u \end{bmatrix}, \quad S = \begin{bmatrix} 0 \\ \frac{-4\tau}{\rho d} \end{bmatrix}, \quad U = \begin{bmatrix} P \\ u \end{bmatrix} \tag{6.7}$$

Premultiplying Equation (6.7) by A^{-1}, we obtain the following standard form:

$$\frac{\partial U}{\partial t} + C\frac{\partial U}{\partial x} = A^{-1}S \tag{6.8}$$

From the coefficient matrices A and B in Equation (6.7), the corresponding Jacobian matrix C and the eigenvalue matrix $\wedge$ are obtained as follows:

$$C = A^{-1}B = \begin{bmatrix} u & \rho a^2 \\ \frac{1}{\rho} & u \end{bmatrix} \quad \text{and} \quad \wedge = \begin{bmatrix} u-a & 0 \\ 0 & u+a \end{bmatrix} \tag{6.9}$$

Splitting the Jacoian matrix C in Equation (6.9) into the left and the right eigenvector matrices (Z and Z^{-1}), we obtain:

$$C = Z \wedge Z^{-1} = \begin{bmatrix} -\rho a & \rho a \\ 1 & 1 \end{bmatrix} \begin{bmatrix} u-a & 0 \\ 0 & u+a \end{bmatrix} \begin{bmatrix} -\frac{1}{2\rho a} & \frac{1}{2} \\ \frac{1}{2\rho a} & \frac{1}{2} \end{bmatrix} \tag{6.10}$$

In the first step of computation, the source term is excluded from Equation (6.8) and the

resulting equation takes the form:

$$\frac{\partial U}{\partial t} + C\,\frac{\partial U}{\partial x} = 0 \tag{6.11}$$

The split form of the Jacobian matrix C from Equation (6.10) is substituted into Equation (6.11). The resulting equation is premultiplied by Z^{-1} to obtain the following relation:

$$Z^{-1}\frac{\partial U}{\partial t} + \wedge\, Z^{-1}\frac{\partial U}{\partial x} = 0 \tag{6.12}$$

Defining the characteristic vector W as given in [128], such that

$$\partial W = Z^{-1}\partial U \tag{6.13}$$

Equation (6.12) changes to the following relation

$$\frac{\partial W}{\partial t} + \wedge\,\frac{\partial W}{\partial x} = 0 \tag{6.14}$$

Linearizing Equation (6.13) similar to [292] we can compute the characteristic variable vector W using the following relation:

$$W = Z^{-1}U = \begin{bmatrix} -\dfrac{p}{2\rho a} + \dfrac{u}{2} \\ \\ \dfrac{p}{2\rho a} + \dfrac{u}{2} \end{bmatrix} \tag{6.15}$$

Equation (6.11) is thus transformed to the corresponding characteristic form in Equation (6.14).

6.7 The Computational Strategy

In this section we present the computational strategy adopted to numerically solve the mathematical model explained in couple of previous sections. This includes the determination of a suitable computational domain with relevant initial and boundary conditions and the selection of an appropriate numerical algorithm to solve the system of PDEs in the matrix form. These are explained in detail below.

6.7.1 Details of the computational domain

The entire downstream side of the valve up to reservoir B1, as shown in Figure 6.3, which is 149.4 m long, is chosen as the computational domain. In our model, we have not considered fluid-structure interactions in pipe flow. A simplified one-dimensional straight pipe section of the length 149.4 m is assumed for computation as shown in Figure 6.8.

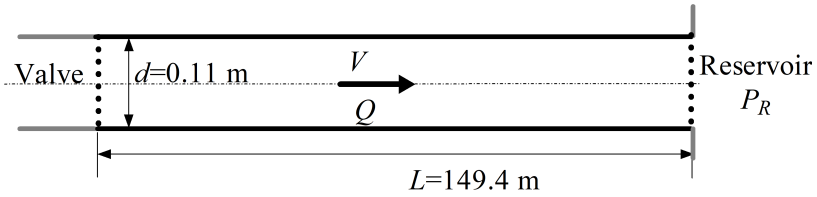

Figure 6.8: Schematic of the computation domain

As we could see, the left end of the domain is the fast closing valve and at the right boundary we have a pressure reservoir. Initially flow is taking place from the left through the fully open valve towards the right to the reservoir maintained at a fixed pressure. The computation starts when the valve closure just begins and continues till the time duration for which corresponding experimental data is available. We assume a fixed initial velocity inside the entire domain as per the experimental specifications. The left boundary is given a transiently varying inflow velocity condition while the right boundary has a fixed pressure outlet condition. The inlet pressure and the outlet velocity are floating variables. At the inlet the velocity is assumed to be linearly decreasing from the initial value to zero over a period of few milliseconds, to replicate the fast valve closure. Reservoir pressure for the experiment is the assigned fixed value of pressure at the right boundary. For the purpose of computation, the one-dimensional domain is divided into equally sized control volumes of size $\triangle x$ m.

6.7.2 The two-step computational algorithm

The solution of two-equation model given by Equation (6.6) is obtained in a two step process. In the first step, the system of equations in the characteristic form excluding the source terms given by Equation (6.14) is solved for an intermediate time step denoted by '$\star$', starting from the n^{th} time step. The semi-discretised form of this equation for the i^{th} spatial grid is as follows:

$$W_i^\star = W_i^n - \triangle t \left[\wedge \frac{\partial W}{\partial x} \right]_i^n \tag{6.16}$$

The split coefficient matrix (SCM) method is used for solving the above system in Equation (6.16).The SCM is a powerful solution technique for wave propagation related fluid flow problems. This technique finds application in different works involving numerical solution of two-phase flow equations such as [293–295]. Recently Zhang et al. [296] used the SCM technique to study axially coupled vibration response of a fluid-conveying pipeline excited by water hammer. The SCM method is used to split eigenvalue matrix $\wedge$ into characteristic speed matrices with positive and negative eigenvalues separated into respective matrices $\wedge^+$ and $\wedge^-$ as follows:

$$\wedge^+ = \frac{\wedge + |\wedge|}{2} \quad \text{and} \quad \wedge^- = \frac{\wedge - |\wedge|}{2} \tag{6.17}$$

Using $\wedge^+$ and $\wedge^-$ from Equation (6.17), the properties are updated to the intermediate time step as follows:

$$W_i^\star = W_i^n - \frac{\triangle t}{\triangle x}\left[\wedge^+ \left(\frac{\partial W}{\partial x}\right)^- + \wedge^- \left(\frac{\partial W}{\partial x}\right)^+\right]_i^n \tag{6.18}$$

An explicit third-order upwind method is used for spatial discretisation of the convective terms in Equation (6.18) as given below:

$$\begin{aligned} W_i^\star = W_i^n - \frac{\triangle t}{\triangle x}\big[\wedge^+ \left(2W_{i+1}^n + 3W_i^n - 6W_{i-1}^n + W_{i-2}^n\right) \\ + \wedge^- \left(-W_{i+2}^n + 6W_{i+1}^n - 3W_i^n - 2W_{i-1}^n\right) \big] \end{aligned} \tag{6.19}$$

On completion of the first step of computation, the primitive variable vector is recovered from characteristic variable vector as $U_i^\star = ZW_i^\star$. In the second step, the effect of source term is integrated into the solution by retaining only the transient and source terms in Equation (6.6) as follows:

$$\frac{\partial U}{\partial t} = A^{-1}S \tag{6.20}$$

and the semi-discretised form of Equation (6.20) is given below:

$$U_i^{n+1} = U_i^\star + \triangle t\left[A^{-1}(U_i^n)S(U_i^n)\right] \tag{6.21}$$

Since there is no source term in the mass balance equation for liquid, only the momentum equation needs to be solved in the source term integration step. From the momentum

equation, the velocity of flow is updated as:

$$u_i^{n+1} = u_i^{\star} - \triangle t \left(\frac{4\tau}{\rho d} \right) \tag{6.22}$$

In Equation (6.22), $u^{\star}$ is the component of primitive variable vector $U^{\star}$.

The single-phase two-equation model can be safely used to simulate hydraulic surges in the two valve closure experiments selected as both of these do not report cavitation effects. However, numerical results from the simulation using the proposed model are to be validated against the corresponding experimental data.

6.8 Results of the Two-Equation Compressible Liquid Model

For the purpose of computation, the one-dimensional domain is divided into 747 uniformly sized control volumes, each of size $\triangle x = 0.2$ m. From stability considerations, a CFL value of 0.03 is found to be optimal and the corresponding time step size $\triangle t$ is calculated to be close to 5×10^{-6} s.

The transient flow problem of sudden valve closure in a steel pipe and the associated pressure surge are mathematically formulated using the proposed two-equation compressible liquid model. This one-dimensional system of equations is solved numerically, and the results are compared against the numerical results computed using the existing three-equation model and with the transient pressure data measured experimentally. The experiment data were those measured using the pressure transducer P03 for Experiment Nos 415 and 347 reported in [288]. In the case of Experiment No. 415, the transient data measured for the first 3 s from the closure of the valve is used, while for Experiment No. 347, the measured data for the first 5 s is considered. The unsteady friction formulation reported in [288] is used with both computational models. An optimised value of 0.18 is used for the constant friction coefficient k in the simulation of these experiments.

The results for Experiment Nos. 415 and 347 are respectively displayed in the Figures 6.9 and 6.10.

The experimentally measured transient pressure profile for both Experiments are plotted using continuous black curves. The continuous blue coloured curve in Figure 6.9 represents the transient pressure profile computed using the three-equation incompressible model [288]. Numerical results obtained from the proposed two-equation compressible liquid model are displayed using magenta coloured curve in Figure 6.9. The numerically computed transient pressure profiles using the three-equation and the two-equation models

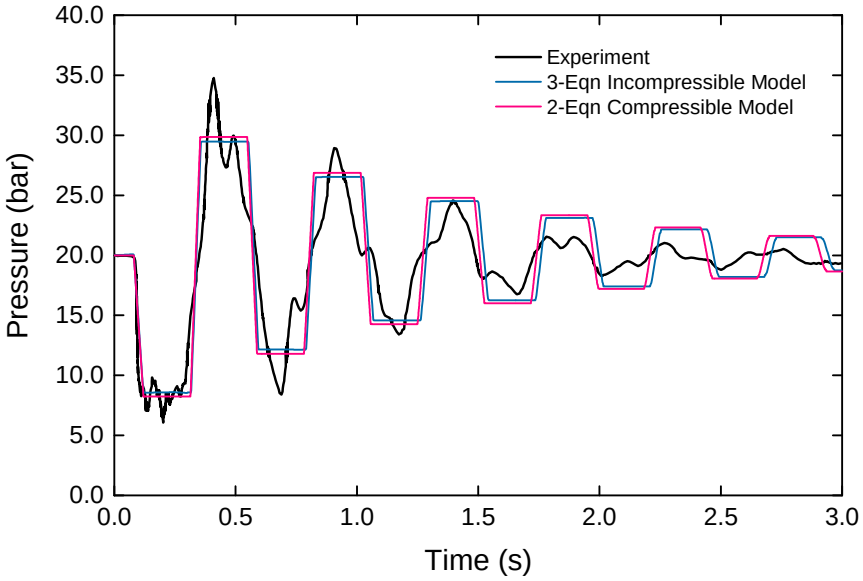

Figure 6.9: Comparison of measured and computed pressure at P03 for experiment 415.

for Experiment No. 347 are shown in Figure 6.10 using green coloured and red coloured curves respectively.

As observed from Figures 6.9 and 6.10, the transient pressure profile predicted by the two-equation model proposed is in good agreement to that obtained from the existing three equation model. However, we should remember that the two-equation model reproduced this numerical solution using a much simplified mathematical formulation with reduced computational cost. On closer observation, one may find that the two-equation model predicts the peak pressures slightly higher than that of the three-equation model throughout the transient. This is visible in both figures. This increase in pressure magnitude could be attributed to the compressible treatment of liquid, which accounts for the increase in density of the liquid at high pressures. The compressible treatment also leads to accurate estimation of wave speeds within the fluid, which adds to the magnitude of calculated surge pressure. We could observe that the crests and troughs in the solution profiles with the proposed two-equation compressible model show a small shift to the left compared to that from the three-equation model. This shift is a result of the higher wave speeds estimated using the two-equation model due to the presence of compressible model in it. The increase in pressure during the surge and the corresponding increase in fluid density are both connected to wave speed through sound speed relation of the liquid EOS used. This increase in wave speeds at higher pressures also increases the frequency of oscillations within the pipe system, which finally appears as a slight leftward shift of the profile.

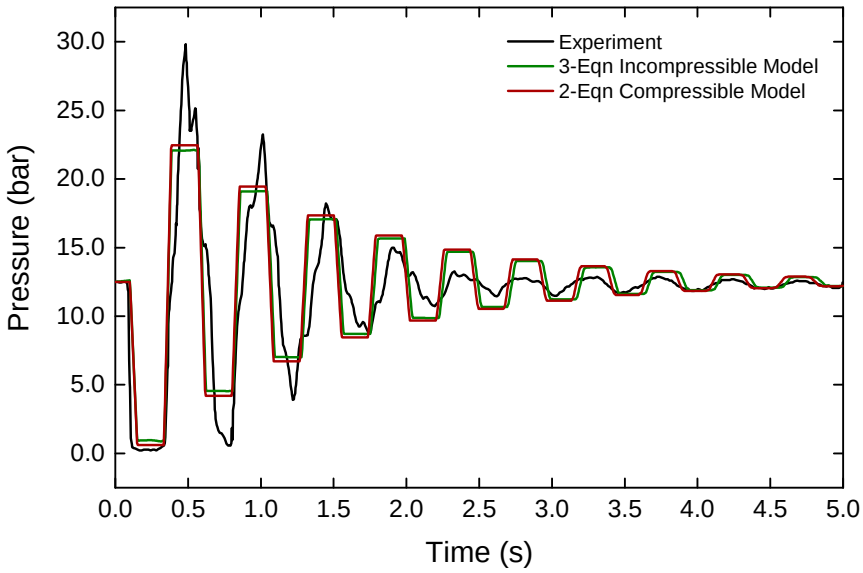

Figure 6.10: Comparison of measured and computed pressure at P03 for experiment 347.

The computed frequency of wave propagation is observed to be in close agreement with the experimental results. However, the amplitude of pressure peaks from the numerical results is not in good agreement with the measured values. The structural interaction with fluid flow, which is not accounted for in the present model, is a possible reason for this disparity in the results. From the experimental and numerical pressure profiles displayed in Figures 6.9 and 6.10, an important observation is made as follows. During the initial phase of the transient, the magnitude of pressure peaks and anti-peaks are highly under-predicted, and at the later phase, they are over-predicted in the numerical results. This observation is due to the over-damping induced by the constant pressure wave damping coefficient for the initial transient phase and vice-versa. This improper damping technique using a constant pressure wave damping coefficient, adds to the variation of numerical results from the measured values. It is thus important to introduce a technique by which the damping could be controlled based on the varying flow conditions. In the following section a new technique is presented for gaining control over the fluctuating flow conditions and to use it to determine the pressure damping coefficient.

6.9 Adaptive Damping of Pressure Waves

It is a common observation that while using a steady shear stress model in modelling fluid hammer problems such as those reported in the works [215,297–300], discrepancies arise in the numerically computed data over experimental or field data measured. A review of some

of the frequently used friction models for liquid transients are presented in Section 2.8. Daily et al. [219] conducted laboratory experiments and found that these discrepancies are positive for accelerating flows and are negative for decelerating flows. A detailed review of the wall shear stress models used in the modelling of hydraulic transients is available in the work of Ghidaoui et al. [301]. The relation of energy loss coefficient with transition geometry of a pipe, flow Reynolds number, and the relative roughness of the wall are outlined by Nosrati et al. in [302]. The friction model used with the three equation model in Equation (6.1) given in [34] defines the shear stress with a quasi-steady friction part (τ_s) and an unsteady friction part (τ_{us}). The unsteady shear stress part of the model takes the following form for single-phase liquid flow case:

$$\tau_{us} = \left(k \, \frac{\rho d}{4} a \right) \text{sign}(u) \left| \frac{\partial u}{\partial x} \right| \tag{6.23}$$

In Equation (6.23), k is the unsteady friction coefficient accounting for damping of pressure waves.

Daily et al. [219] further showed that for an unsteady shear stress model as given in Equation (6.23), the coefficient k is a measure of deviations due to unsteadiness of the wall shear and momentum flux. The extended thermodynamics approach by Axworthy et al. [303] supports this claim and reports the poor agreement between model and data while using a constant value for k.

The disparities in the numerical data is an indication that the mathematical model is unable to adapt to the drastically changing flow conditions. This lack of adaptation means that some important variations in the flow properties during the transient are left unaccounted by the mathematical model. The fluid pressure is a property that undergoes heavy fluctuations in its magnitude during a surge. The other important parameters such as fluid density, signal propagation speed and flow velocity are all related to fluid pressure and hence get altered by the fluctuations in this property. If we could use the captured variations in pressure to make the entire mathematical model adapt to the varying flow conditions, it shall certainly improve simulation accuracy. The pressure wave damping coefficient is a parameter in the unsteady friction model that is usually assigned a constant value throughout the simulation of a flow transient. By redefining this parameter as a function of the calculated fluctuations in the pressure, the mathematical model is expected to suitably adapt to the drastic variations in the flow.

6.9.1 Variable pressure wave damping coefficient

Based on the limitations associated with a constant pressure wave damping coefficient k, we propose to replace it with a variable pressure wave damping coefficient k_v. Unlike the constant coefficient k, the new coefficient k_v is a function that uses the ratio of the magnitude of local pressure fluctuations to maximum possible pressure fluctuation for the cases considered. For the initial operating conditions of pressure P_0, density ρ_0, velocity u_0, and signal speed a_0, the magnitude of maximum possible pressure fluctuation $\triangle p_{max}$ is computed using the well established Joukowsky equation as follows:

$$\triangle P_{max} = \rho_0 a_0 \triangle u = \rho_0 a_0 |u_0 - 0| = \rho_0 a_0 |u_0| \tag{6.24}$$

The importance of Joukowsky relation given by Equation (6.24) in the theory of water hammer is outlined by Ghidaoui in [304] and the historical evolution of this equation is studied by Tijsseling and Anderson [305]. A similar non-dimensional parameter is defined by Wahba [306] using the Joukowsky pressure rise to study the wave attenuation in fluid transients. Walters and Leishear [307] list down those scenarios where Joukowsky equation should not be used to estimate the maximum water hammer pressures.

The magnitude of fluctuation in the pressure at any local point 'i' is calculated as the absolute value of the difference between local pressure P_i and operating pressure P_0. The proposed variable pressure damping coefficient is defined as a function of a parameter called the 'relative local fluctuation of pressure'. The non-dimensional parameter, the 'relative local fluctuation of pressure' ($\triangle P_{RLF}$) is the ratio of the 'magnitude of the local pressure fluctuations' ($|P_i - p_0|$) to the 'maximum possible pressure fluctuation' ($\triangle P_{max}$). The relative local fluctuation of pressure is expressed as follows:

$$\triangle P_{RLF} = \frac{|P_i - P_0|}{\triangle P_{max}} \tag{6.25}$$

At this point it is very important to understand that the surge due to valve-closure at upstream and downstream sides of a closing valve is different in many respects. Because of the differences in the surge physics at these two locations, transient variation of pressure for these locations also show differences. This also means that the damping requirements for pressure waves also vary based on the location where the surge is studied. Therefore, we have to define separate variable pressure damping coefficients for each location. Both valve-closure experiments discussed in this chapter are those at the downstream side of the closing valve. Therefore, we name the variable pressure damping coefficient applicable

for the surge at the downstream of valve as k_{vd}. The variable pressure wave damping coefficient, k_{vd} is defined as follows:

$$k_{vd} = m_1 \left[1 - (\triangle P_{RLF})^{m_2}\right] \tag{6.26}$$

In Equation (6.26), m_1 and m_2 are tunable parameters. While parameter m_1 controls the overall dissipation of the system like the constant parameter k, parameter m_2 could provide the fine-tuning for dissipating trend of the pressure transient. The larger the values of m_1 and m_2, the higher is the dissipation achieved. If the overall dissipation provided by a particular value of m_1 proves to be very high for certain parts of the transient, then by lowering the value of m_2 these unwanted extra dissipation could be avoided in the pressure profiles. The square-bracketed term in Equation (6.26) performs in such a way that, it lowers the dissipation where there are large fluctuations in pressure that carry very important information about the peak pressures reached. During the later phase of the transient where fluctuations are very low, the dissipation offered by mathematical model is usually insufficient and leads to over predicted numerical results. The square bracketed term could offer high dissipation over such conditions and predict numerical results close to the experimental data. With this definition of the variable pressure damping coefficient k_{vd}, the equation for the unsteady part of shear stress can be written as

$$\tau_{us} = \left(k_{vd}\,\frac{\rho d}{4} a\right) \text{sign}(u) \left|\frac{\partial u}{\partial x}\right| \tag{6.27}$$

The quasi-steady part of the shear stress in [34] is given as

$$\tau_s = \frac{f}{4}\frac{\rho}{2} u\,|u| \tag{6.28}$$

where f is the steady Darcy-Weisbach friction coefficient. The value of f is computed from the explicit relation called the Blasius correlation as follows:

$$f = 0.3164 Re^{-0.25} \tag{6.29}$$

where Re is the flow Reynolds number. The Blasius relation [308–310] is a simple approximation for the calculation of Darcy friction factor for the turbulent regime for smooth pipes. It was proposed by Paul Richard Heinrich Blasius in terms of the Moody friction factor, and is valid for Re $\leq 1 \times 10^5$.

The final shear stress (τ) is thus computed as the sum of quasi-steady part (τ_s) and

unsteady part (τ_{us}) as follows:

$$\tau = \frac{f}{4}\frac{\rho}{2}u\,|u| + \left(k_{vd}\,\frac{\rho d}{4}a\right)\,\text{sign}(u)\left|\frac{\partial u}{\partial x}\right| \tag{6.30}$$

The shear stress computed from Equation (6.30) is used to estimate the source term in Equation (6.3b). The newly introduced variable pressure damping coefficient uses relative local fluctuation of pressure, which is a transiently varying quantity. The inclusion of this transient data into the damping coefficient is expected to take care of the deviations due to unsteadiness of the wall shear and momentum flux to some extent.

6.10 Two-Equation Model with Variable Pressure Wave Damping Coefficient

A variable pressure wave damping coefficient is proposed in this study to address deficiencies of the constant wave damping coefficient model. The constant value of wave damping coefficient, which is applied throughout the computation, makes it inflexible to varying flow situations. This fixed amount of damping may prove to be excessive for a particular part of the transient while it could be insufficient for the rest. The definition of the varying pressure wave damping coefficient, k_{vd}, as a function of the relative local pressure fluctuation is outlined in Section 6.9.1.

Magenta curve in Figure 6.11 and red curve in Figure 6.12 display numerical results obtained with the two-equation compressible-liquid model using the variable pressure wave damping coefficient k_{vd} respectively for Experiment Nos. 415 and 347.

In these figures, numerical results from the VPDC included two-equation compressible liquid model are compared against those computed using the two-equation compressible liquid model with a constant pressure wave damping coefficient k. The plots also display the measured values from the field for the corresponding experiments. The comparison shows that the proposed two-equation model with the variable pressure wave damping coefficient improves the result considerably from the model with a constant damping coefficient. This improvement is not only in terms of better estimation of peak pressures but also in closely reproducing the transient trend observed with experimental pressure measurements. The maximum pressure estimated by the proposed computational model using k_{vd} is 1.18 bar (or 4%) higher for Experiment No. 415 and by 1.2 bar(or 5.5%) higher for Experiment No. 347 when compared to the results from two-equation model with the constant k. This is a reasonable improvement in simulation accuracy in quantitative terms. Values

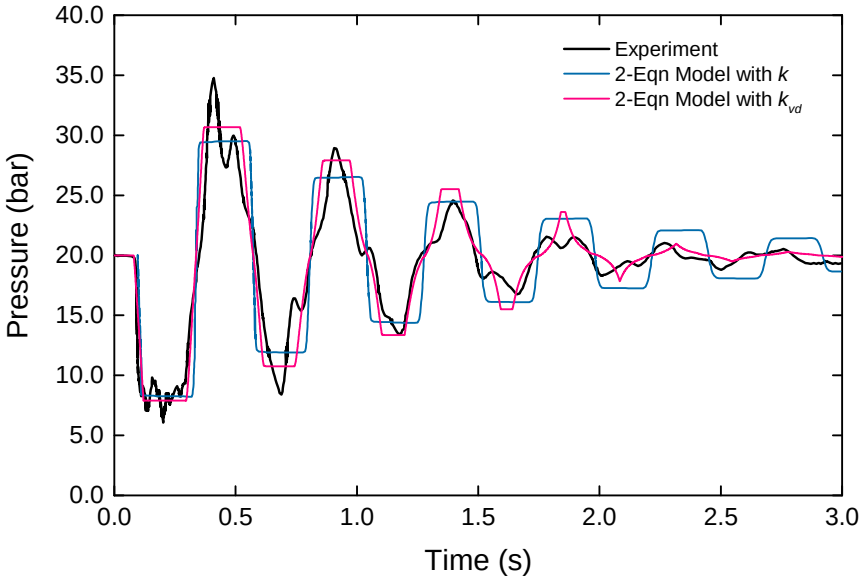

Figure 6.11: Numerical results using the 2-equation compressible-liquid model with k_{vd} for Experiment No. 415.

of the parameters m_1 and m_2 in Equation (6.26) are observed to be optimal in the range 0.3-0.5 for the selected pair of experiments.

The proposed model also numerically reproduced the shape of the pressure profile much closer to the shape of the experimental profile with sharper peaks and anti-peaks. We could see that crests and troughs in the transient pressure profile generated from the model with the constant k shows flat peaks and anti-peaks. This observation is due to the non-adaptation of friction model based on fluctuation of pressure from the mean operating conditions. This extreme flatness of the peaks are reduced to some extent with the inclusion of the VPDC into the friction model. We could observe that towards the later phase of the transients, the sharpness of oscillations from simulation with the VPDC incorporated two-equation model is very close to those observed in the experimental profiles.

The dissipation provided by variable damping coefficient is adaptive to the magnitude of pressure fluctuation at any local point. This capability is imparted through the unique function definition for the parameter k_{vd}. It is visible from numerical pressure profiles in Figures 6.11 and 6.12 that the variable damping coefficient provides a lower damping at the initial stage of the transient where larger pressure peaks are present. Similarly, towards the later phase of the transient the variable damping coefficient adapts to the pressure's diminishing magnitude. This adaptive damping capability improves the accuracy of the computed transient surge data that is crucial to the pipe's and structure's safety. The flexibility added to mathematical model by the inclusion of the VPDC into it, for the prediction of numerical

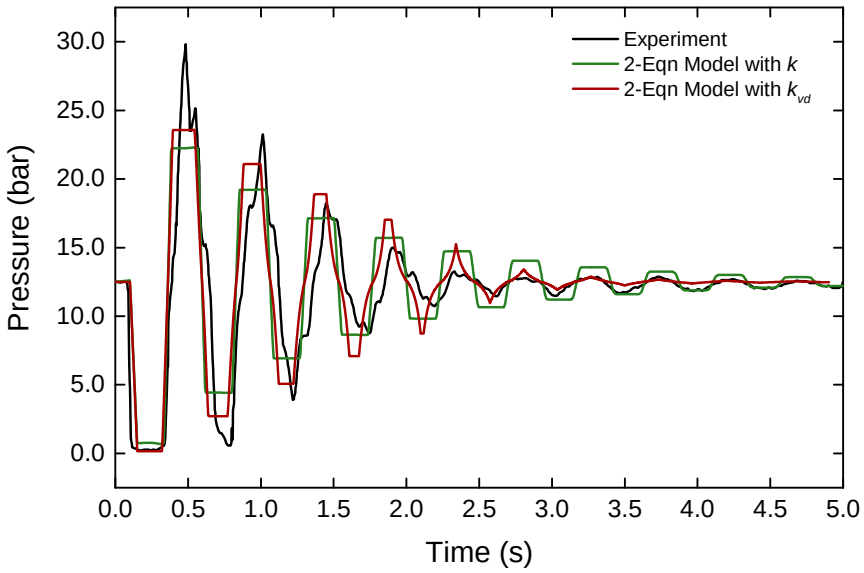

Figure 6.12: Numerical results using the 2-equation compressible-liquid model with k_{vd} for Experiment No. 347.

results much closer to measured field data is notable. This is more prominently observed towards the later part of the transient as visible from Figures 6.11 and 6.12.

The compressible model used for the liquid not only helps in accurate prediction of fluid density but also provides an excellent estimate of wave speeds, both of which are crucial flow parameters varying with pressure. The proposed two-equation model with variable pressure wave damping coefficient is a highly simplified mathematical model capable of accurately estimating transient pressure variations. This model's ability to closely follow transient variations in the experimental pressure profile, even without the inclusion of any fluid-structure interaction (FSI) algorithm, is a substantial improvement over the three-equation model. However, there are visible variations in numerical results during the initial stage of the transients. The main reason for these is that the effects of pipe mountings and support structures are neglected in the computational model. The lack of complete information regarding the exact nature of valve closure is another cause for any mismatches between the simulation results and the measured values.

As observed from the experimental results, the maximum surge in pressure due to the sudden closure of the valve reaches much higher magnitudes than the operating pressure. The compressible model presented in the study, to a particular extent could take this into account by relating these pressures to the corresponding liquid density and signal propagation speed. The variable pressure wave damping coefficient also adds novelty to the model by exhibiting its adaptive damping characteristics in modelling the decaying pressure waves.

The two-equation compressible-liquid model with the adaptive damping capability is quantitatively and qualitatively superior to the existing model for computational applications for high-pressure pipelines for non-cavitating hydraulic surges.

6.11 Summary

This chapter presents the development of an effective mathematical model for the simulation of single-phase non-cavitating hydraulic surges. In the initial sections of the chapter the importance of hydraulic surge studies is highlighted followed by details of two high-pressure valve closure experiments selected from the literature. The simplification of a three-equation model originally developed for the cavitational hammer predictions, to a two-equation model for the simulation of non-cavitating hydraulic surges is outlined in the chapter. Further, the compressible modelling of liquid during the surge phenomena is achieved through the use of a suitable equation of state which relate the fluid properties. The mathematical model is then presented in its corresponding matrix form which was later used while explaining the computational strategy adopted for simulation. A two-level performance analysis of the proposed two-equation model is presented in the chapter. In the first level, the two-equation model with compressible formulation for the liquid is evaluated against the experimentally measured data and the three-equation model of Neuhaus et al., which treats the liquid part as incompressible. The simulation results showed the capability of compressible treatment to accurately compute the varying density and wave speed in the liquid during fluctuating pressure conditions. We also proposed a uniquely defined variable pressure wave damping coefficient that uses the information of local fluctuations in pressure during transients. This new variable pressure wave damping coefficient is superior to the constant friction coefficient, that it adaptively damps the numerically computed transient pressure fluctuations. In the second level of analysis, the variable pressure wave damping coefficient is integrated into the two-equation compressible liquid model, which is then compared for performance against the experimental results as well as the numerical results from the two-equation model with a constant pressure damping coefficient. The adaptive damping capability helps the model to numerically predict the transient pressure with a trend similar to that observed with the experimental data. The flexibility offered by the VPDC to the mathematical model in selectively treating transient pressure gradients is a significant finding of the study. The analysis reveals that the proposed model is computationally inexpensive and provides better accuracy in comparison to the three-equation model. Based on the discussions we could conclude that the proposed model is an effec-

tive computational tool for the modelling and prediction of pressure surges in flow systems where cavitational effects are negligible.

Chapter 7

Further Study on Valve-Induced Transients

7.1 Introduction

In the previous chapter we presented a mathematical model that included compressible modelling of liquid and a variable pressure wave damping coefficient (VPDC) in the unsteady friction model. In this chapter we use this mathematical model to numerically study more valve-induced transients and associated surge characteristics. We will primarily explore the improvements brought into the numerical modelling through the adaptive damping capability incorporated in the VPDC formulation. Three different valve-closure experiments are selected from the literature for numerical study. These experiments are carefully selected such that they involve different pipe materials, wave speeds, geometrical sizes, and operating pressure ranges. In order to perform a comparative performance analysis of this mathematical model, numerical results from the model are also compared against more numerical data sets published in the literature. Numerical results available in literature for the same experiments using other models were also used in the comparative analysis. These experiments were also simulated using a hydraulic surge analysis software package called the 'AFT Impulse'. This is a method of characteristics (MOC) based software platform specifically designed for the simulation of hydraulic transients. The simulation data obtained using the proposed mathematical model is compared against the experimentally measured data. The simulation data is also compared with selected numerical data sets from literature and those generated using the AFT Impulse software.

The chapter also discusses transient variations observed in the pressure jump developed across a valve during its sudden closure with the help of respective numerical results. In relation to this, the effect of duration of valve closure on surge pressure and pressure jump across the closing valve are also explored using the simulation data.

This chapter is organised as follows. The subsequent Section 7.2 discusses the impor-

tance of studying and understanding valve-induced transients and associated surges. Section 7.3 provides details about the valve-closure experiments selected for present numerical study. The mathematical model used and the computational strategy adopted in numerical simulations are explained in the Section 7.4. Some details about the AFT Impulse software and the modelling of hydraulic surges using this platform are presented in Section 7.5. Section 7.6 presents results from the numerical simulation of the selected experiments and discusses the major observations made. The importance of considering pressure jump across a closing valve during a valve-induced transient is explained in Section 7.7. Section 7.8 describes the effect of valve closure duration on pressure jump across the closing valve using the simulation results for cases with different speeds of valve closure.

7.2 Studies on the Valve-Induced Transients

The large variations observed in pressure values during the surges arising from sudden valve closures pose many safety concerns to the systems in which they occur. For example, hydraulic surges and associated flow-induced vibrations arising from the valve closures are very frequently reported from the nuclear power industry. The transient variations of pressure at different strategic locations in systems during valve closure operations are crucial for the structural design and deciding of optimal valve operating conditions. Similar to the impact of peak values of pressure during a valve-induced transient, the lowest values of pressure reached in the system are also important. The lowest values of pressure reported during a transient could provide a better understanding of the chances of cavitation to take place within the system, which is another undesirable effect as far as the structural integrity of the system is concerned. One should also understand that the magnitude of pressure associated with valve-induced surges is not sufficient to completely understand the surge phenomena. The instants at which highest and lowest pressure values are reached in the system, the locations at which they occur, the time period and frequency of the oscillations observed in pressure and the total time taken for pressure waves to completely damp down back to operating conditions have to be accurately estimated for any such transient. For these reasons, the field of valve-induced hydraulic surges is an area of extensive research and has eventually led to a wide range of experimental and computational studies in this field.

Some notable experimental studies on valve-induced surges were carried out by Covas et al. [234], Neuhaus and Dudlik [34], Lee et al. [311], Warda and Elashry [312], Simao et al. [313], Balacco et al. [314], Kodura [315], etc. Computational studies and contributions

related to the impact of sudden closure of valves in the generation of hydraulic transients were made by Ramos et al. [233], Covas et al. [235], Kaliatka and Vaisnoras [316], Barten et al. [290], Nikpour et al. [317], Al-Taliby [318], Tran [319], and Lai et al. [320]. A recent study by Li [321] relates the maximum transient pressures developed during hydraulic transients to the duration of slow valve closures. The study of valve induced pressure transients are also extended to the field of heart health monitoring, where cardiac valve closures and related pressure variations are studied and simulated using various mathematical models. The works by Brockman [322], Bellhouse [323], Lee and Talbot [324], Van Steenhoven and Van Dongen [325], Aluri and Chandran [326], House et al. [327], and Tang et al. [328], are related to the application of valve induced surges for heart health monitoring. Controlled fluid transients are also used as fault and leak detection techniques for pipelines as reported in the works of Wang et al. [329], Vitkovsky et al. [330], Lee et al. [331], Diao et al. [332], Bohorquez et al. [333], and Wang et al. [334]. A review of this technique is presented by Colombo et al. [335]. Details of the various friction models used for computational studies on liquid transients and on different unsteady friction models are presented in the Section 2.8 of Chapter 2.

7.3 Valve-Closure Problems for Numerical Study

The characteristics of a hydraulic surge depends on many parameters such as, geometry of the pipe, pipe material, fluid handled, type of the valve, speed of valve closure, flow velocity inside the pipe, pressure and temperature of the flowing fluid, frictional losses in the flow, and fluid-structure interactions. Here, we select three different experiments from the literature which involve fast valve closures leading to hydraulic surges in the piping systems. The experiments chosen here are such that, some of the parameters listed above vary over a small range, while some others vary over a wider range. Two valve closure experiments by Mitosek and Szymkiewicz [336], and a third experiment by Soares et al. [337] are used in this study to validate numerical results from the proposed mathematical model. The first experiment of Mitosek, which will be hereafter referred to as Mitosek Exp-1, was conducted on a straight steel pipeline of length 72.0 m, while the Mitosek's second experiment, which will be hereafter referred to as Mitosek Exp-2, uses a high density poly ethylene (HDPE) pipe which is arranged in an elliptical loop with a total length of 240 m. Soares et al. conducted their valve closure experiment on a 15.22 m long copper pipe. Other geometrical parameters like pipe inner diameter and pipe wall thickness, and flow parameters like velocity, wave celerity and operating head vary for each of these

experiments. The operating temperature for both the experiments of Mitosek is the same at 287.15 K, whereas the experiment by Soares et al. is conducted at 300 K. The duration of the transient experiments selected for the study varied from 0.5 to 32 s, while the valve closure duration in these experiments ranged between 16.5 to 25 milliseconds. All the experiments considered here are pure single-phase flow cases without cavitation effects. The details of the experiments are provided in Table 7.1.

Table 7.1: Details of the parameters used in the experiments

Parameters	Experiment		
	Mitosek et al.-1	Mitosek et al.-2	Soares et al.
Pipe material	Steel	HDPE	Copper
Pipe length [m]	72.0	240.0	15.22
Pipe diameter [m]	0.042	0.0352	0.020
Pipe thickness [m]	0.0033	0.0024	0.0010
Operating temperature [K]	287.15	287.15	300
Reservoir head [m of H_2O]	51.0	23.1	46.0
Flow velocity [m/s]	0.41	0.86	0.423
Wave Speed [m/s]	1245	335	1255
Valve closure duration [s]	0.025	0.02	0.0165
Experiment duration [s]	8.0	32.0	0.5

We intend to numerically simulate each of these three experiments based on geometrical and flow conditions as described above and analyse the surge data predicted for the cases. The experimentally measured transient pressure data are available for each of these experiments at the upstream position of the closing valve. The experimentally measured transient pressure profiles for Mitosek Exp-1, Mitosek Exp-2, and Soares Exp, are respectively displayed in Figures 7.1, 7.2, and 7.3.

As these figures display, the pressure measured at the location just upstream of the closing valve shows heavy oscillations with many crests (peaks) and troughs (anti-peaks). They also indicate dissipation process of the compression waves inside the system after undergoing multiple reflections at the boundaries. As we discussed, based on geometrical and material properties and for different flow conditions, the characteristics of these oscillations in pressure exhibit variations. The frequency and amplitudes of the oscillations and the time taken for dissipating back to steady operating conditions show differences for the cases. For the experiment by Soares et al., an additional set of pressure data is available

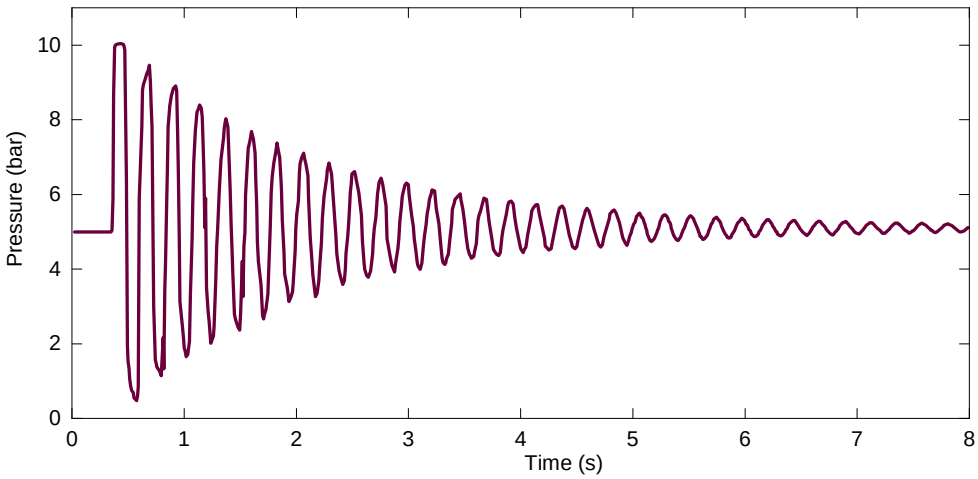

Figure 7.1: Experimental pressure profiles for Mitosek Exp-1 (Steel pipe)

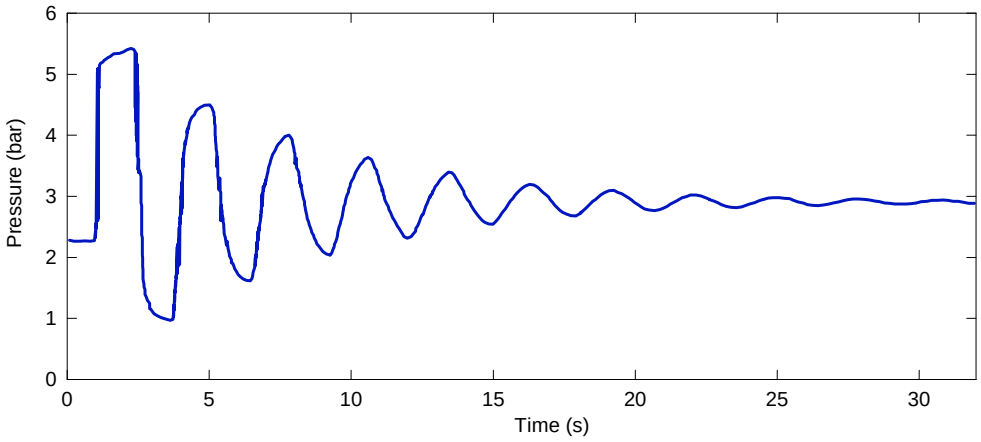

Figure 7.2: Experimental pressure profiles for Mitosek Exp-2 (HDPE pipe)

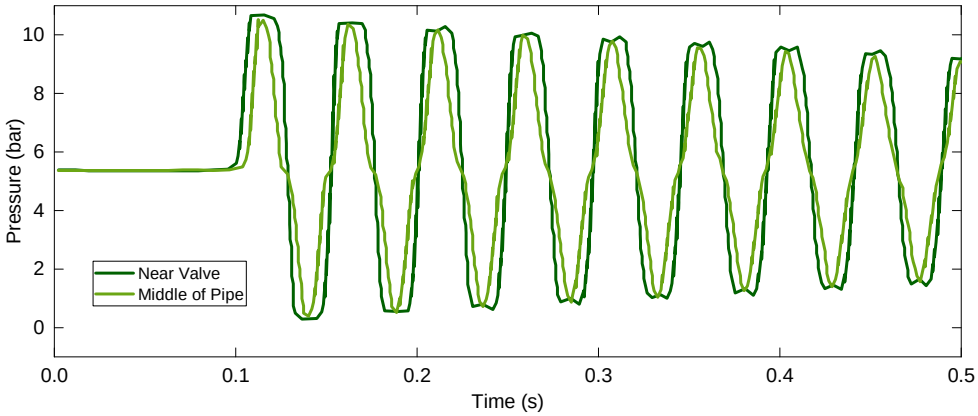

Figure 7.3: Experimental pressure profiles for Soares Exp (Copper pipe)

that is measured at mid-way of the pipe length. The numerical data generated from the simulation for experimental cases will be validated against these respective field data.

7.4 Mathematical Model and Computational Strategy

For numerical simulation of the experiments and associated hydraulic surges, the physical system needs to be converted into corresponding computational model. In this section, firstly, a suitable mathematical model is selected for representing the physical laws that govern flow transients. Further, changes required in the friction model for simulation of the selected set of experiments are discussed. A suitable computational domain is then selected, where we apply the relevant the initial and boundary conditions.

7.4.1 The two-equation compressible liquid model

The two-equation compressible-liquid model, presented in Section 6.5.2 of the previous chapter, is used as the mathematical model for the study of transient flows. The two main physical laws governing the flow, viz., fluid mass balance and momentum balance relations are given as follows:

$$\frac{1}{a^2}\frac{\partial p}{\partial t} + \frac{u}{a^2}\frac{\partial p}{\partial x} + \rho\frac{\partial u}{\partial x} = 0$$

$$\frac{\partial u}{\partial t} + u\frac{\partial u}{\partial x} + \frac{1}{\rho}\frac{\partial p}{\partial x} = -\frac{4\tau}{\rho d}$$

The energy equation need not be solved explicitly for the problem, as the system is considered to be at isothermal conditions.

The transiently varying celerity of pressure waves and the smoothing out of wave fronts are two phenomena observed during flow transient experiments. These physical observations cannot be reproduced by the standard unsteady pipe flow models, even with the usage of modified formulations for shear stresses. A possible method to address the time varying celerity of pressure waves is to model the compressibility effects in the liquid in the pipe. This is the reason why the compressible model used along with the two-equation model for the simulation of hydraulic surges. The wave celerity or the signal propagation speed in the system is finally calculated based on the speed of sound in the fluid, the geometric dimensions of the pipe system and the elastic properties of the pipe material. The procedure to do this is explained in the Section 6.5.2.

7.4.2 Variable pressure wave damping coefficient for adaptive damping

For modelling highly transient flow problems, the friction model used in the mathematical formulation plays a very crucial role. This is mainly due to sudden surge in fluid properties for such transients, where abrupt variations in fluid pressure and flow velocity are observed over a short duration of time. The rapid change in flow properties during the initiation phase of the transient is usually followed by a faster dissipation within the system, which eventually reaches steady state. This necessitates appropriate friction models to accurately simulate transient variation of various flow properties. The application of steady friction models to such highly transient cases could lead to nonphysical results. This is due to the incapability of such models to adapt to varying requirements of dissipation in the system with respect to time and spatial location. There are numerous unsteady friction models available in the literature that could resolve this issue to a good extent by modelling the varying shear stresses during the transient with reasonable accuracy. One could also develop or modify an existing unsteady friction model for higher simulation accuracy by improving its capability to better adapt to the varying dissipation requirements for their respective flow situations.

In the last chapter, we have discussed the shear stress model used by Neuhaus and Dudlik [34] with a quasi-steady part and an unsteady part given as follows:

$$\tau = \frac{f}{4}\frac{\rho}{2}u\left|u\right| + \left(k\,\frac{\rho d}{4}a\right)\text{sign}(u)\left|\frac{\partial u}{\partial x}\right|$$

We have also suggested that the constant pressure wave damping coefficient k in this relation could be replaced by a variable pressure wave damping coefficient k_{vd}. The parameter k_{vd} was specifically defined to improve simulation accuracy of surge prediction for locations downstream of the closing valve. However, while we observe the transient pressure profiles at any location upstream of the closing valve during the surge, as visible in Figures 7.1, 7.2, and 7.3, we could notice that they are different from those observed for the downstream location as seen in Figures 6.4 and 6.5. Therefore, similar to the definition of k_{vd} presented in the previous chapter, we need to define a new variable pressure wave damping coefficient k_{vu} for application at the upstream side of the closing valve during the surge modelling.

Similar to the procedure followed in the last chapter, we intend to replace this constant parameter k, with a variable pressure wave damping coefficient k_{vu}. This variable parame-

ter k_{vu} is also defined as a function of the parameter 'relative local fluctuation of pressure' that is defined in Equation (6.25). This new variable friction coefficient k_{vu} is defined as follows:

$$k_{vu} = m_1 \left[\triangle p_{RLF}\right]^{m_2} = m_1 \left[\frac{|p_i - p_0|}{\triangle p_{max}}\right]^{m_2} \tag{7.1}$$

Here the parameters m_1 and m_2 are tunable and perform the same function as seen with the case of the definition of k_{vd}. However, it could be noted that the definition of the new variable pressure wave damping coefficient k_{vu} in Equation (7.1) is slightly different from that of k_{vd} defined in Equation (6.26). The main difference here is in the square bracketed term. The term '$1 - \triangle p_{RLF}$' for the case of k_{vd} changes to just '$\triangle p_{RLF}$' for k_{vu} within the square brackets. This change is attributed to the difference in pressure wave damping trends observed for the upstream and downstream cases. Based on these different trends, the damping requirements also vary. It is a usual observation that the numerical models are able to correctly predict the first highest peak of such transients. However, as the transient progresses, the numerical results show excess dissipation. The term '$1 - \triangle p_{RLF}$' helps in avoiding such excessive dissipation towards the later phase of the transient, because it lowers the value of k_{vu} for lower value of pressure fluctuations from the operating conditions.

7.4.3 The computational strategy

To carry out the numerical simulation of the experiments, a generalised experimental layout with a straight pipe assumption is used for all the cases. This corresponds to a simplified one-dimensional computational domain. This one-dimensional approach is used because the variations observed in flow variables for the transient cases to be modelled are more or less unidirectional. Ghidaoui et al. [301] state on this that, "rapid flow disturbances, planned or accidental, induce spatial and temporal changes in the velocity and pressure fields in pipe systems and such transient flows are essentially unidirectional since the axial fluxes of mass, momentum and energy are far greater than their radial counterparts." The studies by Mitra and Rouleau [229] on laminar water-hammer and those by Vardy and Hwang [215] on turbulent water-hammer also support this unidirectional approach in the problem formulation. The generalised one-dimensional layout common to all the experiments is presented in Figure 7.4.

The setup consists of a straight pipeline carrying fluid (liquid water) which is connected to a pressurised reservoir at its left end and to a fast closing valve at its right end. The common experimental procedure is as follows. A steady flow is initially setup in the system, where flow velocities inside the pipe and the reservoir head are both maintained constant.

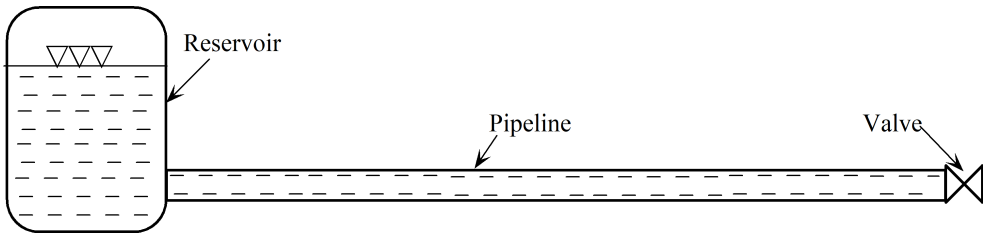

Figure 7.4: The generalized layout for the valve closure experiments

During the steady state operation of the system, the valve at the right end of the pipe is in fully open position. For generating hydraulic transient, this valve is fully closed over a very short duration of time ranging over a few milliseconds. This leads to surge in flow properties in the upstream region of the closing valve, mainly in pressure. Pressure transducers are mounted along the length of the pipe at different locations to measure and record these variations in local fluid pressure. The surge in fluid pressure will be most severe in the region just upstream of the closing valve, as the highest deceleration to the flow takes place in this location. We intend to numerically compute transient pressure variation at this location just upstream of the closing valve for all the experiments considered.

At the left boundary we assign a fixed pressure inlet condition representing the flow from constant pressure reservoir. The closing valve at the right boundary is modelled by assigning linearly decreasing velocity boundary condition over the few milliseconds of valve closure. Beyond this duration, velocity at the right boundary is maintained as zero to emulate situation of the completely closed valve. Velocity at the left boundary and pressure at the right boundary are extrapolated from the computed values from within the domain.

The computational algorithm used here is the very same that is explained in the previous chapter under Section 6.7.2. The governing equations are converted into their respective matrix formulations as outlined in Section 6.6. The complete two-step algorithm, where the split coefficient matrix (SCM) method is used for splitting the eigenvalue matrix into respective characteristic speed matrices as explained below.

7.5 Hydraulic Surge Modelling Using AFT Impulse Software

'Impulse' is hydraulic surge analysis software package developed by the Applied Flow Technology (AFT) Pvt. Ltd. This is a method of characteristics (MOC) based software platform specifically designed for the simulation of hydraulic transients. The selected ex-

periments were also simulated using 'AFT Impulse version 8'. There are steady and unsteady friction models available in the software package. Different valve types could be selected and transient closure functions could also be assigned using this software. The experimental setup for valve closure problem using AFT Impulse software platform is represented in Figure 7.5.

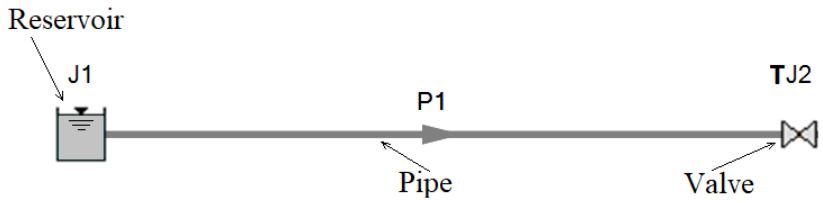

Figure 7.5: The valve closure experiment setup in the AFT Impulse software

The pipe section can be defined by providing details like the pipe material, length, diameter, thickness etc. The wave speed is calculated by the system based on the support type provided. Under the optional tab, the stagnant region steady state pressure is always kept to system pressure, and the initial volume flow rate based on the chosen experiment is provided. Fluid properties are computed using the NIST REFPROP, using which water is selected as the fluid by providing operating pressure and temperature conditions. The NIST database computes corresponding fluid properties like density, dynamic viscosity, vapour pressure, bulk modulus etc. The variable fluid properties option were checked for all the simulations. A ball valve is chosen as the valve type. This valve is assigned a transient boundary condition of closure over a preset duration. The letter 'T' in bold indicates the transient condition assigned to the component. At the left boundary a reservoir is included where we input the fixed liquid surface pressure, the level of water above the pipe centre and the height of the system from the reference line.

For specifying the friction model, the explicit friction factor option under the user specified tab is selected. Based on the initial flow properties, the flow Reynolds number is computed and the corresponding Darcy friction factor is calculated and assigned using relevant correlations. The variable pipe resistance facility was also utilised for the simulations performed. Impulse offers steady, unsteady and advanced unsteady friction models. The advanced unsteady friction model uses the friction model of Bruonne. The valve transient is assigned as a liner decrease of K_V value of the valve from the full open value to zero over the valve closure duration. In the sectioning of pipes, the suggestions provided by the MOC based solver were used. The variation in results and computation time were checked

for different resolution of the pipe sectioning to understand the dependency of the results on spatial resolution. The results were obtained for the pipes at its inlet, outlet and at all intermediate stations.

7.6 Results and Discussions of the Numerical Simulation

The three different experimental situations considered were numerically simulated using the proposed mathematical model. The numerical pressure profiles at the upstream location of the valve for Mitosek's experiment on steel pipe are displayed in Figure 7.6. This figure shows numerical profiles generated using the two-equation compressible model with a constant, k, as well as with the variable pressure wave damping coefficient, k_{vu}. In addition, more numerical data are included in the figure, which include the numerical profiles generated using AFT Impulse platform, with normal unsteady friction model and advanced unsteady friction model of Bruonne. Also, in the figure, the measured data from the experiment is used to compare relative performance of these numerical profiles.

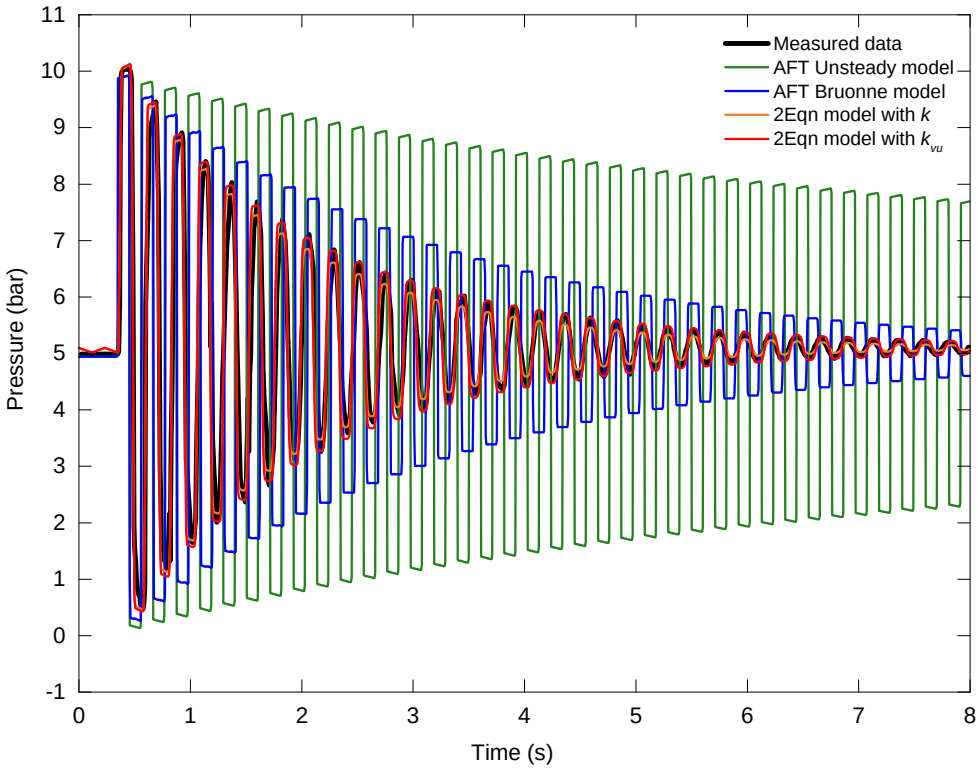

Figure 7.6: Transient pressure profiles for Mitosek's experiment on steel pipe predicted by different models

Numerical results predict initial peaks of the transient with reasonable accuracy. However, as the transient progresses the dissipation of the transient pressure data is found to be insufficient compared to the measured values. The friction factors computed from standard relations are unable to produce the expected damping in pressure. In the case of the Mitosek et al. experiment on steel pipe, the AFT unsteady and the AFT advanced unsteady (Bruonne) friction models show difference in the numerical pressure profiles. In this case, the Bruonne model is observed to offer higher dissipation and better results which are comparatively closer to the measured data. The results from AFT also show a higher pressure oscillation frequency than that of the measured data, that results in sharper oscillations. The two-equation model provides numerical pressure profiles that are very close to the measured values. They are distinctively superior to the results from the AFT Impulse. However, the two-equation model with the VPDC, k_{vu}, produces the closest results to the experimental data, while the same model with a constant k show deviations from the experimental data. To understand the improvements brought by the two-equation model with the inclusion of the VPDC, results from this model with constant k and variable k_{vu} are compared to the measured values in Figure 7.7.

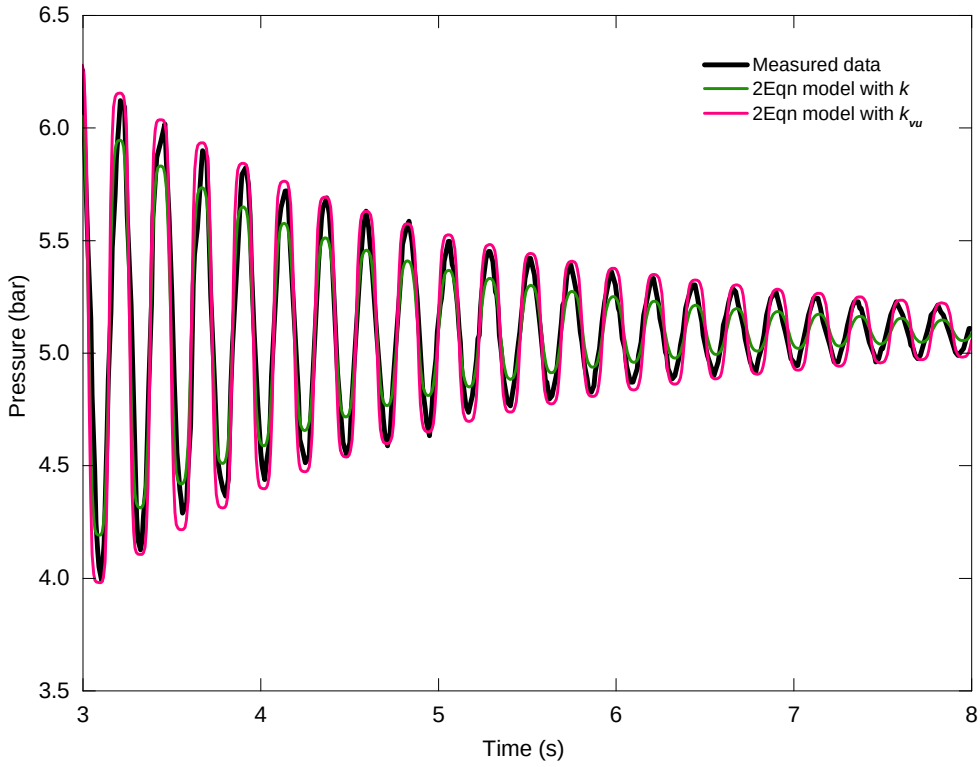

Figure 7.7: Comparison of the transient pressure profiles for Mitosek's experiment on steel pipe using VPDC and constant k

The numerical profile corresponding to the constant k value in Figure 7.7 clearly shows the extra dissipation in the results that is persistent throughout the transient. The replacement of k with k_{vu} in the two-equation model has helped in removing the extra dissipation, and the amplitudes from improved model show a close match with experimental measurements. This close agreement is maintained throughout the transient process. It should also be noted that the results from the two-equation model closely predicts frequency of pressure oscillations in the field data.

The numerical results for Mitosek's experiment on HDPE pipe are presented in Figure 7.8. Solution profiles from the two-equation model are compared against the experimental data and the numerical data sets generated using AFT Impulse. The numerical solution to this problem using the unsteady friction model by Ramos et al. [233] is also included in the comparison.

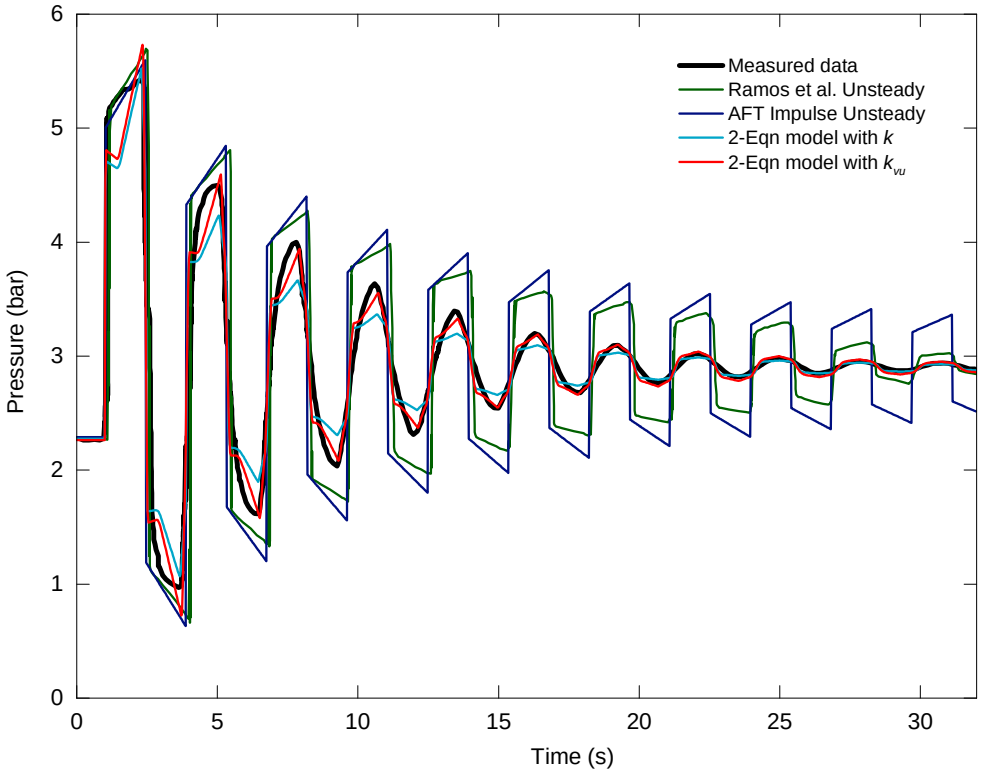

Figure 7.8: Transient pressure profiles for Mitosek's experiment on HDPE pipe predicted by different models

During the simulation of Mitosek's experiment on HDPE pipe using AFT Impulse, we observed that there were no differences in the results generated with the unsteady and the advanced unsteady friction models of this software platform. Though the results from

AFT show a decaying wave pattern, they are considerably over predicted from the experimental values. The unsteady model by Ramos et al. appears to be slightly superior to AFT unsteady model by exhibiting better dissipation in the solution profile. However, this model also shows notable deviations from the measured pressure values. The two-equation model is again the most accurate method and the profiles from this method are separately displayed in Figure 7.9. All models predict oscillation frequency with reasonable accuracy.

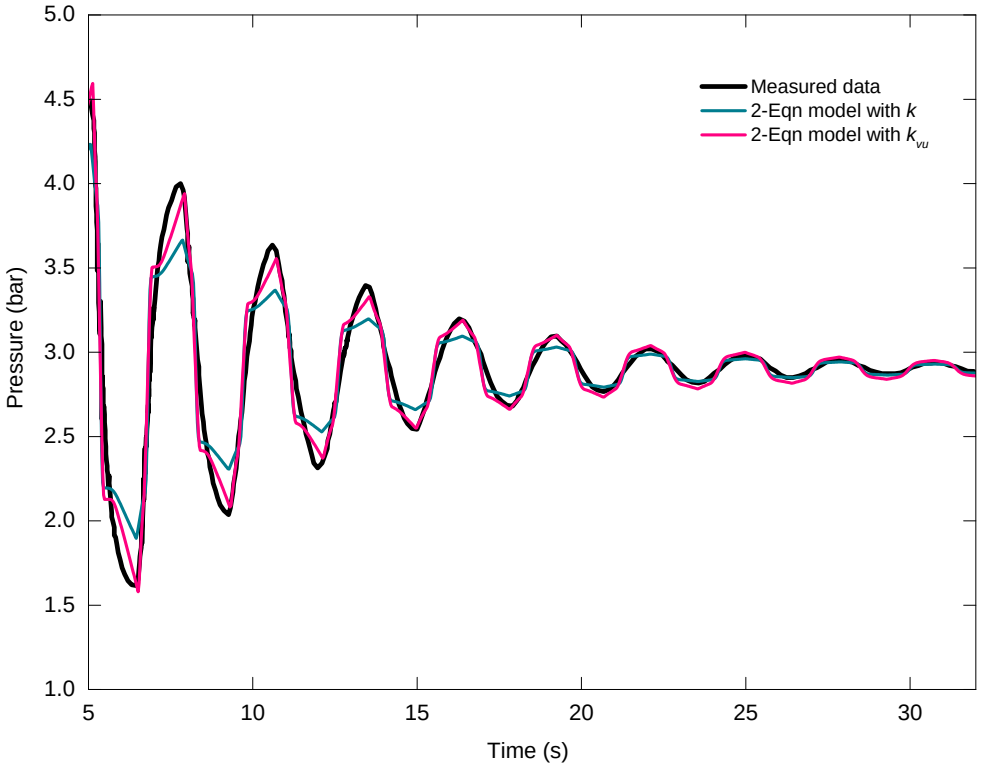

Figure 7.9: Comparison of the transient pressure profiles for Mitosek's experiment on HDPE pipe using VPDC and constant k

The fixed amount of damping provided by the constant coefficient k proves to be excessive for a particular part of the transient while it becomes insufficient for the other. This is why the deviations of numerical data from the measured data, with k are varying for the whole transient. However, the variable coefficient k_{vu} addresses these deficiencies to a good extent and we could see that the profiles generated using it closely follows the measured profile.

Figure 7.10 presents numerically computed transient pressure profiles for the Soares' valve-closure experiment performed on copper pipe. The numerical data from the two-equation model is compared against the experimental data and the simulation data from AFT Impulse.

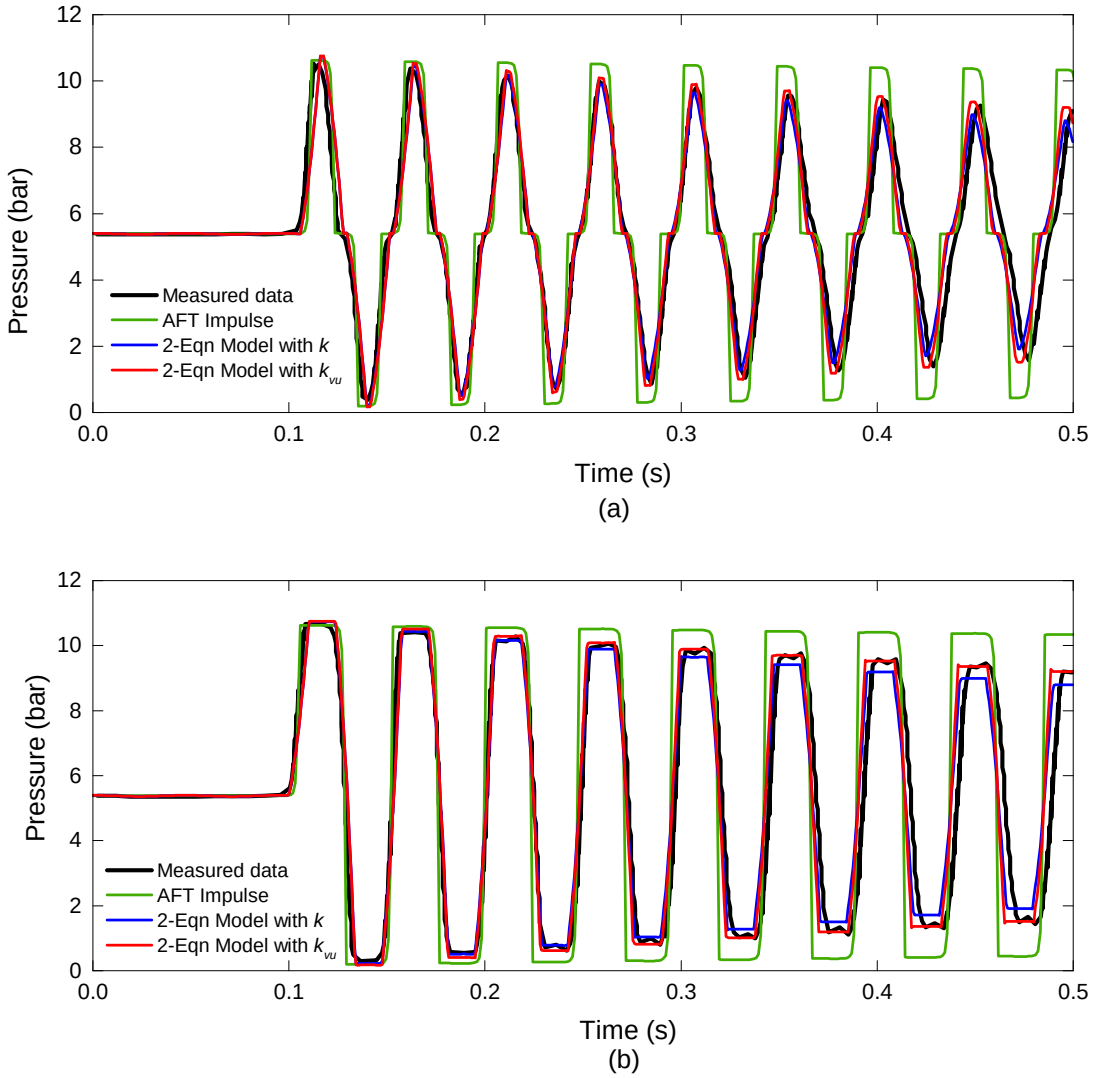

Figure 7.10: Transient pressure profiles for Soares' experiment on copper pipe predicted by different models

As we could see, the results are displayed over two figures. Figure 7.10 (a) displays the transient pressure variation at mid-length location of the 15.22 m long pipe and Figure 7.10 (b) displays the corresponding results at a location just upstream of the closing valve. A zoomed in view of these plots from the two-equation model and the measured values at the two different locations are presented separately in Figure 7.11 for a detailed comparison. The observations are similar to those discussed for the last two experimental cases.

The Impulse software simulates oscillation frequency of pressure surge data close to the measured values. However, the decay of these oscillations are not satisfactorily reproduced

by this software platform. The plots suggest insufficient damping of pressure oscillations by unsteady friction models of this computational tool. The two-equation model is visibly superior with numerical results closely following experimental results.

The adaptive damping capability incorporated to the two-equation model through the inclusion of VPDC is clearly demonstrated in the plots in Figure 7.11. The extra dissipation observed with the constant k is rectified by replacing it with k_{vu}. These numerical profiles generated using k_{vu} are in very close agreement with the experimental profiles at both locations of the system considered. However, the detailed view of the profiles in Figure 7.11 shows that a small phase shift is introduced between numerical and experimental profiles as the transient progresses.

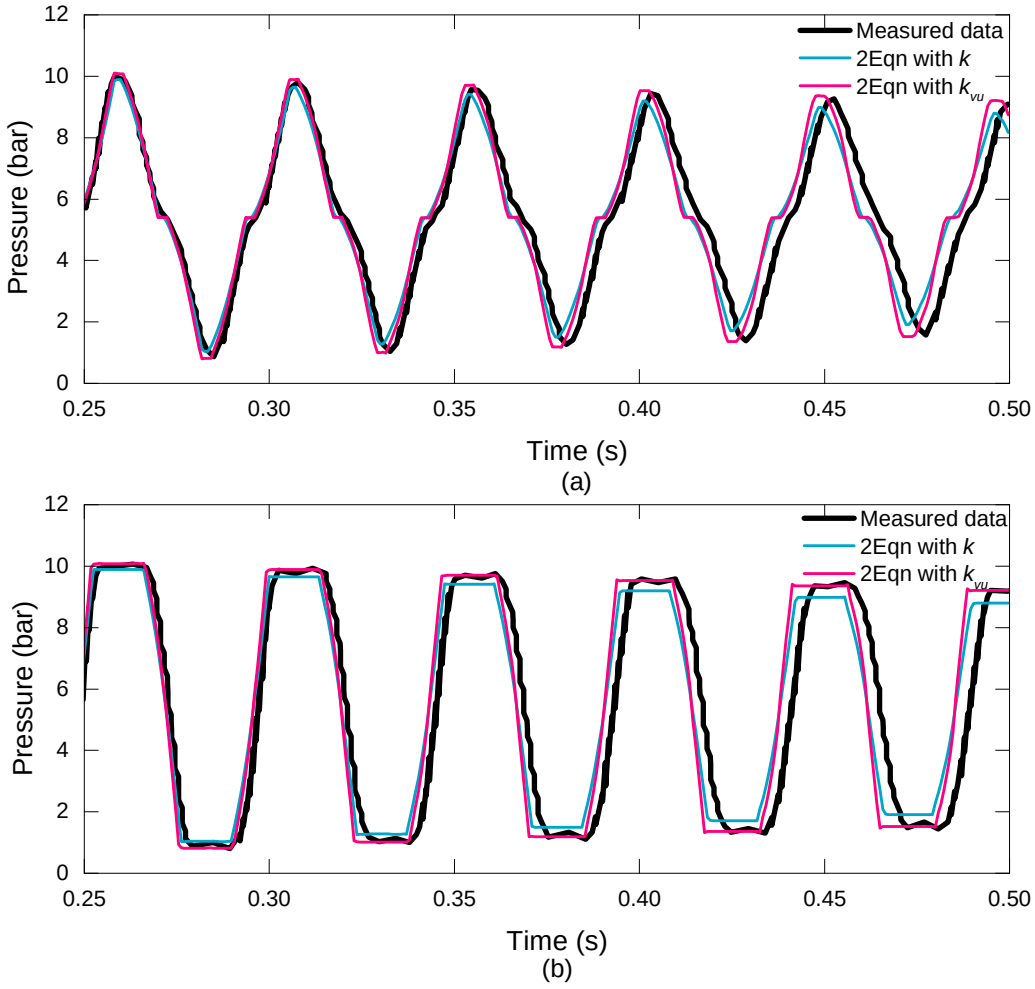

Figure 7.11: Comparison of the transient pressure profiles for Soares' experiment on copper pipe using VPDC and constant k

The fixed value of pressure damping coefficient that is applied throughout the com-

putation makes it inflexible to the varying flow situations. The flexibility added to the mathematical model by VPDC to predict numerical results close to the measured data is notable specifically towards the end of the transients. The value of constant pressure wave damping coefficient k in the unsteady friction model used with the two-equation model for different cases are as follows. For Mitosek's experiment on steel and HDPE pipes, the k values are respectively 0.07 and 0.17, while for Soares' experiment the optimal value of this parameter is found to be 0.025. The following observations were made related to the value of parameters m_1 and m_2 in the variable pressure wave damping coefficient k_{vu} for the experimental cases. It was found that the value of parameter m_1 gave best results when maintained at the same value as that of k for the corresponding experiment. This is because, for all cases considered we could observe a general trend that the two-equation model with k closely predicts the initial peak of the transient and later exhibits high dissipation as the transient progresses. Because of this, the parameter m_1 that is responsible for the overall damping could be assigned the same value as that of k. However, to remove the extra dissipation existing towards the later phase of the transient, the parameter m_2 should be optimised. The optimal values of m_2 for these experiments vary over the range of 0.1 - 0.3.

The modelling of elliptically looped pipe in Soares et al. experiment as a straight pipe for one-dimensional modelling is a limitation of the study and this could also be a possible reason for the mismatches in numerical data and experimentally measured values. The model's ability to follow transient variations in the experimentally measured pressure profile even without an FSI algorithm is a good improvement over the original model. However, the structural interactions and associated vibrations during on-field measurements can cause small variations in the experimental data which may not be accurately captured in numerical simulations.

The step by step procedure for the implementation of Adaptive friction model with variable pressure wave damping coefficient (VPDC) for hydraulic surge simulations is as described below:

From the initial system conditions, compute the 'maximum possible fluctuation in pressure' during surge using the Joukowsky relation.

$\Downarrow$

Compute the parameter, the 'local pressure fluctuation' at each computational volume as the absolute difference between the local pressure and the operating pressure.

$\Downarrow$

Calculate the non-dimensional parameter the 'relative local fluctuation of pressure' (P_{RLF})as the ratio of 'local pressure fluctuation' to the 'maximum possible fluctuation in

pressure'.

⇓

Based on the selected location for modelling surge with respect to the closing valve (upstream or downstream), choose the respective function to calculate the variable pressure wave damping coefficient (VPDC) at each computational volume.

⇓

Calculate the VPDC value at each computational cell and then substitute this value in the unsteady shear stress model to compute the Unsteady shear force at that location.

⇓

Compute the Total shear force at that location by adding the Steady shear force to this Unsteady shear force.

⇓

Use this Total shear force to calculate and update the Source term in the momentum equation, which is then used to update the flow variables in the second step of time marching.

In contrast to the above procedure, the constant damping coefficient, k, is substituted directly to the unsteady stress model during computation to calculate the unsteady shear force. Further, the last two steps in the above procedure are followed.

7.7 Pressure Difference Across a Valve During Valve-Induced Transients

Numerical studies on hydraulic surges at the upstream and the downstream locations of a closing valve generated interest in exploring the varying pressure difference developed across a closing valve during the transient. This is because we could see some variations in the transient pressure during the surge between these two locations. This transient trend in pressure difference across the closing valve is usually neglected during surge analysis. However, this information can yield further insights into understanding the transient and its consequences. For a selected flow setup, the transient pressure at a location upstream and a location downstream of the closing valves were studied simultaneously. The corresponding pressure differences existing across these two locations at each instant of time during the transients were also calculated. The surge data at these two locations were compared to understand the behaviour of the transients based on their location. A 298.8 m long pipe with a valve located at its exact centre, for an initial system pressure of 20 bar was considered

for the study. This is a modification to the case for Experiment No. 415 by Neuhaus and Dudlik. The schematic of this initial flow setup is shown in Figure 7.12.

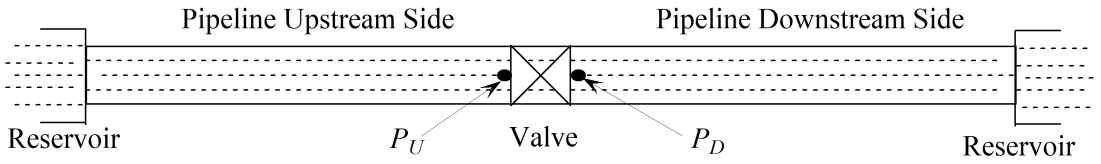

Figure 7.12: Schematic of the theoretical flow setup

Though the flow setup is shown as a straight section, it is assumed to be a closed loop where fluid from a high pressure reservoir flows back to it through a pipeline fitted with a fast closing valve. The valve at the centre of the pipeline changes from a completely open position to completely closed position over a duration of 40 milliseconds. The velocity is linearly reduced from an initial value of 1.0 m/s down to zero over this time period at the valve location. The same mathematical model and computational strategy used in the previous sections are used here for numerical study. Both the compressible model for liquid and the VPDC in the unsteady friction are considered in the model for this study.

7.7.1 Transient pressure across the fast closing valve

Simulation results for transient pressure profiles at the upstream and downstream locations of the closing valve are displayed in Figure 7.13. The results presented were checked for grid-independence. The 298.8 m long one-dimensional domain was divided into 1,494 uniform control volumes with a grid size of $\triangle x = 0.2$ m. A CFL value of 0.03 was found to be optimal with the corresponding time step size, $\triangle t$ close to 5×10^{-6} s.

We have already seen that there are noticeable differences between transient pressure data measured at the upstream and the downstream locations of the valve during hydraulic surge. Numerical pressure profiles from the simulations for these two locations exhibit similar characteristics. The analysis of the structure of pressure profiles at the downstream side of valve results in the following observations. At the downstream location, the pressure profile shows an initial dip from the operating conditions. This initial reduction in pressure is because of the inertia of the flow that carries the fluid forward during valve closure, leading to a low-pressure region close to the valve's downstream side. This lowest value of pressure reached is maintained for a particular duration and is further followed by a sharp rise that takes this property to its peak value. During this dwell period, the compression wave formed reflects from the opposite boundary and reaches back to the valve. The

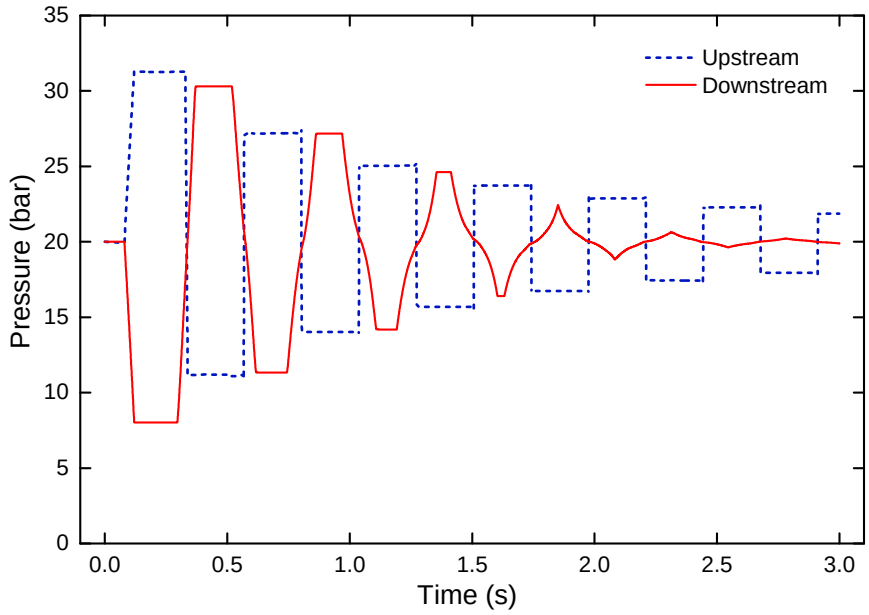

Figure 7.13: Transient pressure at the upstream and the downstream locations of the valve

arrival of compression wave at the valve downstream marks the beginning of abrupt rise in pressure. The oscillation of compression wave inside the system continues while undergoing multiple reflections at the boundary and valve. During the process, energy of the wave is dissipated in overcoming the frictional losses in the system and finally the steady state operating conditions are attained. The frequency of these oscillations are determined by geometrical parameters of the pipe and material parameters of both the pipe and the fluid in it.

Numerical pressure data for transients at the valve upstream, however, show an initial rise in pressure. This is because, during the valve closure, the fluid inertia leads to its accumulation and further to its compression close to the valve upstream. The sudden deceleration of fluid converts the kinetic energy to pressure energy and leads to the creation of a compression front. This compression wave reflects at the closed valve and propagates further upstream of the system. Once this compression wave completely recedes, the valve upstream shows a drastic reduction in pressure. Thus, an oscillating wave motion is set up also in the upstream side of the system similar to the downstream side. The dissipation of the fluctuating pressure back to steady state operating conditions is visible also on the upstream side. The major loss in the circuit, the frictional losses, and the minor losses such as those due to area changes, bends in pipe, etc., can contribute to faster damping down of the pressure oscillations.

The most important observation made is that the surge data on either side of the valve

exhibit a phase shift with each other. The magnitude and frequency of the pressure oscillations are in close range at both these locations. However, the importance of this phase shift and its severity on the safety of the system could be better understood by analysing pressure difference across the valve during the transient. The pressure difference calculated across the closing valve during the transient process is displayed in Figure 7.14.

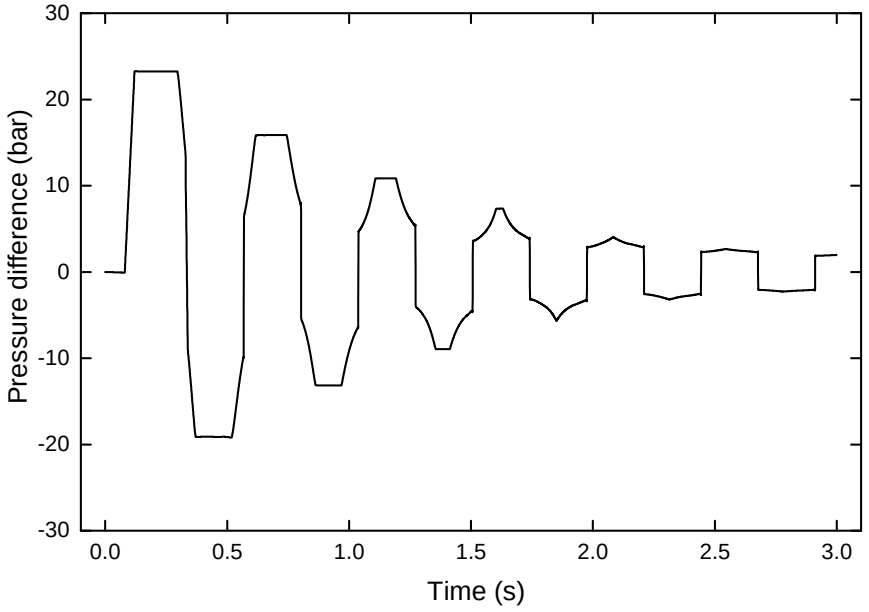

Figure 7.14: Transient variation of pressure difference across the valve

It could be clearly observed from Figure 7.14 that the pressure difference developed across the closing valve could reach very high magnitudes. For example, while the maximum fluctuation of pressure from operating conditions during the surge was computed to be around 12 bar, the maximum pressure difference reported across the valve is close to 23 bar. This is because of the phase shift in pressure oscillations. This is most severe towards the initial part of the transient where highest pressure is developed at the valve upstream and simultaneously lowest pressure is reached at its downstream side. This leads to large pressure differences across the valve.

Actual magnitude of the severity will be understood only when we analyse the scale of pressure difference. Figure 7.14 shows that this pressure difference developed across the valve reverses its direction at the same frequency as that of the oscillations. The high values of pressure differences developed across the valve coupled with these frequent direction changes could become a very serious factor in determining the safety of the valve. It is important to consider this especially for sudden valve closures. The effect of valve closure duration on this pressure difference developed across the valve needs to be explored and is

discussed in the next section.

7.8 Effect of valve closure time on the pressure difference across the valve

The severity of the effects caused by the closure of different valves in pipelines are usually associated with the speed of its closure. Various works and studies related to the impact of valve closure duration on surge characteristics are presented in the Section 2.9 of Chapter 2. As far as the safety and life of valves are concerned, magnitude of the maximum surge pressures during valve transients is important. Another crucial information is the fluctuating magnitude of pressure difference developed across the valve during the transient and the frequency of its oscillation. These oscillations can cause severe damage as they have a similar method of causing damage as observed with the compression wave of a blast wave. We need a reference parameter to understand whether a given valve closure is a slow closure or a fast closure. There is this parameter called the 'pipeline period' or the 'characteristic time period' which is usually denoted as T_C. This is a very important parameter related to the safety of pipelines or fluid transfer lines. For a pipeline system, this is the time taken for a signal to complete one set of to and fro propagation in the system. For a pipeline of length L with signal propagation speed a inside it, the characteristic time period is defined as follows:

$$T_C = \frac{2L}{a} \tag{7.2}$$

If the duration of a valve closure is equal to or shorter than T_C, then that valve closure is considered to be fast or sudden closure. For closure durations of a valve longer than T_C, the closures are considered as slow or gradual closures. For all experimental systems considered previously in this research work, the valve closures were fast. This could be verified from the data furnished in Table 7.2. Here the parameter T_V in the table corresponds to the actual duration of valve closure. We could see that for all the experiments modelled, the value of T_V is lower than the T_C value for the corresponding case.

For valve closing time longer than the characteristic time period, the transient in a system becomes more complicated. This is because of the involvement of several dynamic components in the flow line such as pumps, check valves, control valves etc. For such cases the simulations require a very detailed model to consider all these effects so that the actual behaviour of the transient is closely predicted.

Table 7.2: Details of valve closure durations for different experiments

Experiment	L [m]	a [m/s]	T_C [s]	T_V [s]
Neuhaus et al. No. 415	149.4	1282	0.233	0.040
Neuhaus et al. No. 347	149.4	1279	0.234	0.050
Mitosek et al. Steel	72.0	1245	0.116	0.025
Mitosek et al. HDPE	240.0	333	1.441	0.020
Soares et al. Copper	15.22	1285	0.024	0.016

The Experiment No. 415 of Neuhaus et al., which is the same experiment considered in the previous section, is used to study the effect of valve closure duration on the pressure difference across the closing valve during the transient. The characteristic time period for the selected setup is calculated to be 0.233 seconds. After computing the characteristic time period for the system considered, different valve closure durations were selected such as 0.04 s, 0.15 s, 0.25 s, and 0.50 s. Some of these closures are sudden closures while others are gradual closures. The velocity at the valve location is assumed to be decreasing linearly from the initial value to zero during the period of valve closure. For each of these cases, the pressure at locations just upstream of the valve and just downstream of the valve and the pressure difference across the valve were obtained for the progressing transient.

7.8.1 Numerical results

The simulations are performed for the valve closure experiments with different valve closure durations. Numerical results for the transient variation of pressure at the upstream and downstream locations of the valve were obtained. The transient pressure variation at the upstream side of the valve is displayed in Figure 7.15 and that at the downstream side of the valve is shown in Figure 7.16. Each of these figures show four different pressure profiles corresponding to the four different closure durations of the valve.

The results for different valve closure speeds show the following major observations. The sudden valve closures generate maximum peaks in pressure compared to gradual closures. This is an obvious observation and can be attributed to the faster momentum conversion to pressure head during the sudden deceleration of the flow. The peaks are observed to be more flattened for fast closures compared to the sharp conical peaks observed for gradual valve closures. This is because, with the increase in closure time of the valve,

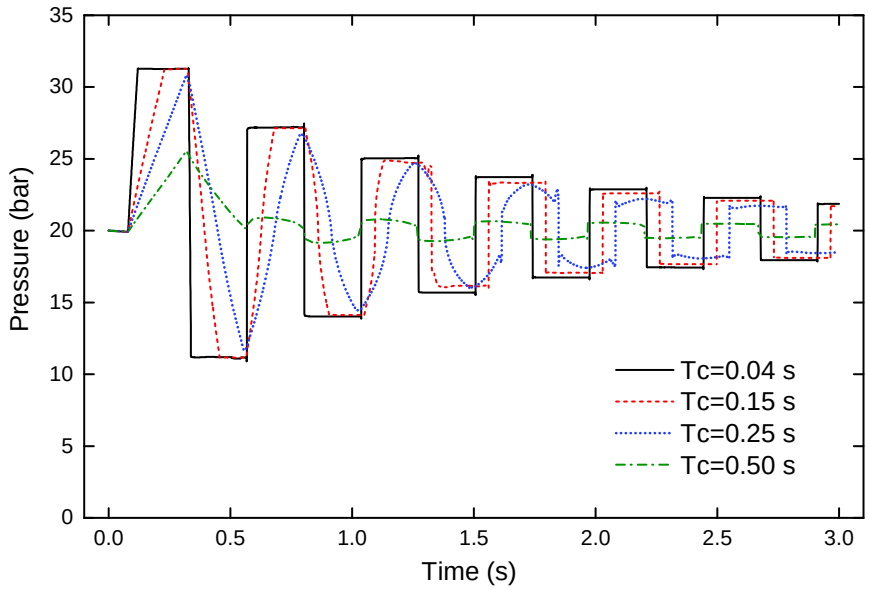

Figure 7.15: Transient variation of pressure at upstream location of valve for different valve closure durations

the rate of declaration reduces and this in turn slows down the rate of rise in the pressure head. A very important observation is that, with increase in the duration of the closure the magnitude of peak pressure shows a substantial decrease only once the duration becomes greater than the characteristic time period. For valve closures faster than this, the variations in peak pressure is observed to be marginal with change in the closure duration.

For sufficiently slower closures, peak pressures are observed to be much below the maximum pressure observed with sudden valve closures. For such slower closures, the dissipation of the pressure waves are also fast and the steady state conditions are reached quickly. There is a small phase shift observed in the oscillations for different closure speeds. The transient pressure profile shows a rightward shift with the increase of valve closure time. This is because, as the valve closure becomes slower, it takes longer time duration for the velocity close to the valve to reach zero. Since magnitude of pressure is dependent on the velocity, this leads to a longer duration for pressure to reach the peak value. This phenomenon is visible in the form of a rightward shift of the transient pressure profiles in Figures 7.15 and 7.16 for slower valve closures .

The transient variations of pressure difference developed across the closing valve during the transient for different closure durations of the valve are displayed in Figure 7.17.

On analysing the effects of valve closure duration on pressure difference across the closing valve, the following observations were made. Increase in the closure time of the

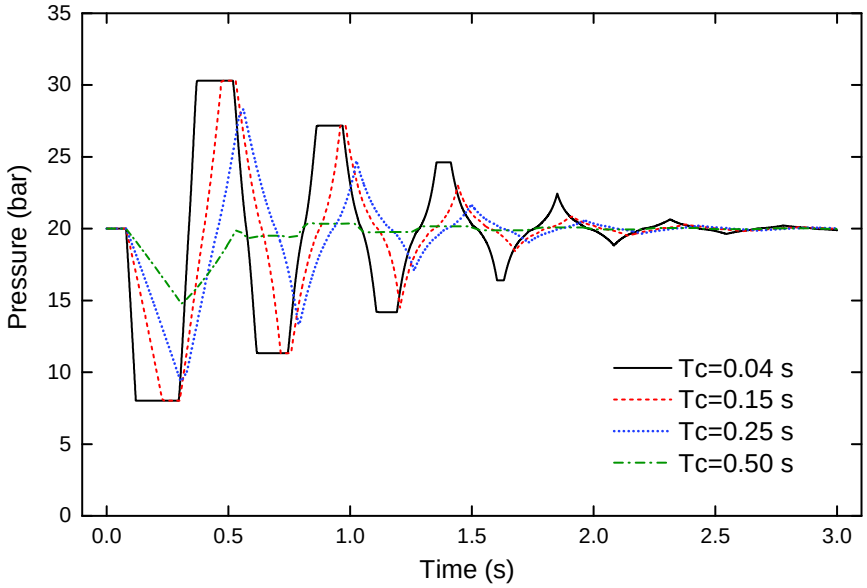

Figure 7.16: Transient variation of pressure at downstream location of valve for different valve closure durations

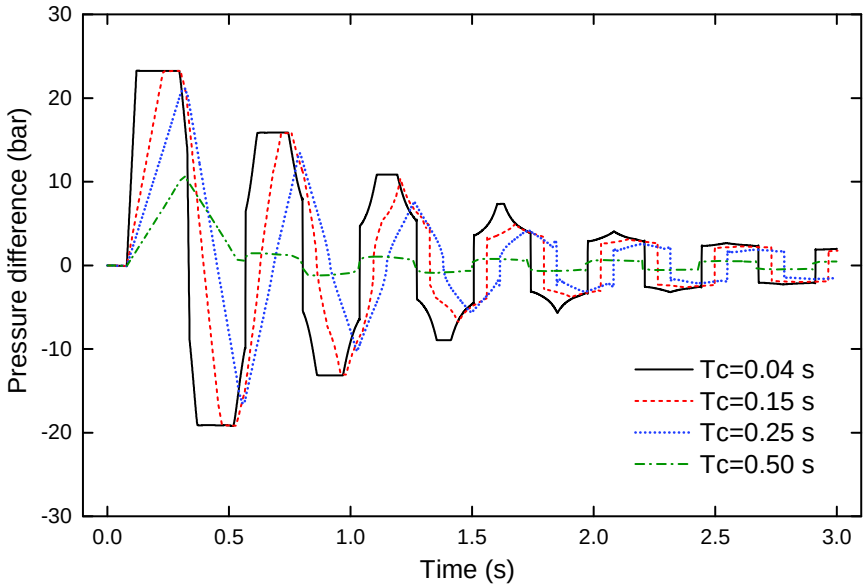

Figure 7.17: Transient variation of pressure difference across the valve for different valve closure durations

valve results in considerable reduction of pressure difference developed across it. This is obvious and as we already explained, could be attributed to the slower deceleration of the flow. Similar to the observation with the case of pressure magnitudes, pressure difference across the valve also shows a substantial fall only once the valve closures become slower

than the characteristic time period of the system. The frequent reversal in the direction of pressure difference is also notable. For the fastest closure considered, the maximum pressure difference developed across the valve is reported to be around 23.2 bar, while for the slowest closure in 0.5 s the maximum pressure difference reduced to 10.5 bar. But it should be noted that for a closure duration of 0.25 s for the valve, which is just higher than the characteristic time period of the system, the maximum pressure difference reported was a high value of 21.1 bar. These large magnitudes of pressure differences and their frequent direction changes are a clear indication of the dangerous pressure conditions to which a valve is subjected during a transient or a surge. Such information should be given due importance while selecting the valve material, fixing a valve closure duration, locating the pipe supports etc.

7.9 Summary

In this chapter, the two-equation compressible-liquid model with adaptive damping capability, proposed and validated in the previous chapter, was used in numerically studying valve-induced hydraulic transients. Three different valve closure experiments were selected from the literature to perform numerical study, based on the varied pipe materials, pipe geometry and the operating conditions involved. A simplified one-dimensional computational domain was selected for numerical simulation. The multi-step computational strategy explained in the previous chapter that used the split-matrix method was adopted here as well. Additionally, an MOC based surge modelling and analysis software platform called AFT Impulse was employed to numerically simulate valve closure problems. Based on the observed difference in the transient trends in surge data on either side of the closing valve, a new definition of the VPDC was presented in this chapter for surge prediction at the upstream locations of a closing valve. Results from the proposed mathematical model were compared against the experimental data. The chapter also used additional numerical data sets in the comparative study such as those from the AFT Impulse platform and some of those that are available in the literature. The improvements brought out to the simulation accuracy through the inclusion of VPDC definition in the mathematical model were highlighted in the discussions. The identified variation in the transient surge data on either side of the closing valve led to the study of pressure difference developed across the valve during the transient valve-induced surge. This study was further extended to understand the effect of valve closure duration on pressure difference across the closing valve.

Chapter 8

Conclusions

The major results and original contributions of this research work are summarised and the important conclusions drawn from the work are presented.

This research work began by addressing the need for accurate compressible models for liquids. In the initial stage of this research, the shortcomings of some of the frequently used equations of state for water were identified. This led to the development of an equation of state for liquid water, called modified NASG EOS, that can be applied over a wide range of pressures and temperatures. This equation of state was thoroughly tested against the NIST database for its accuracy and reliability in modelling compressibility effects in liquid water. It was found during this phase of research that developing a single compressible model for a liquid for application over wide property ranges with reasonable accuracy is a challenging task. Moreover, the necessity that such a model should be able to handle isothermal and non-isothermal cases equally well, makes the process even more challenging.

The research work proceeded by applying the compressible liquid model that we have developed to flow cases to understand the ease of incorporation of the model into existing mathematical models. The modified NASG EOS was thus applied to develop an analytical solution for the water shock tube problem. The shock tube problem was found to have multiple advantages such as the simplicity of problem setup, rich flow physics and features that could make it a good test case. The solution procedure for a gas shock tube was adopted and modified to suit the requirements for water shock tube problem. The equation of state for the liquid has been reformulated to smoothly fit into the procedure. The analytical solution was obtained for a variety of physical configurations of the problem to demonstrate that the solution exists and could be reliably applied for a wide range of pressures and temperatures. Following this, the same theoretical problem of water shock tube was solved numerically by considering the Euler equations as the mathematical flow model.

The numerical results obtained for the problem were then validated using the previously

developed analytical solution. Different varieties of configurations for the water shock tube problem spanning a wide range of pressures and temperatures, were solved numerically and the results were validated using respective analytical solutions. This validation process demonstrated the utility of the analytical solution as a reliable benchmark solution and water shock tube problem as a simple yet powerful test case for various numerical algorithms. Moreover, the close agreement observed between the analytical solution based on thermodynamic relations and the numerical results based on a system of PDE as mathematical model, indicated the dependability of the test case and the solution data itself.

This research further aimed at extending the compressible model to more practical flow situations where liquid compressibility effects are significant. The compressible liquid model was thus applied for the modelling of transient flow problem of hydraulic surge in pipes due to sudden closure of valves. After the selection of an appropriate mathematical model and modifying it suitably for the problems handled, the compressible liquid model was incorporated into it. This mathematical model was then employed to simulate selected valve-induced hydraulic surge cases from the literature. The results showed that the compressible liquid model could bring only small improvements in the simulation results for hydraulic transients. However, the studies indicated that the effectiveness of this compressible model in improving the simulation accuracy is more, with the increase of operating pressure range. It has been identified that the damping of pressure waves during fast transients, by the existing steady and unsteady friction models, is not adequate. This motivated us to the need of developing a new friction model that could improve pressure dissipation mechanism in numerical simulations, by addressing the abrupt changes in flow conditions. It led to the development of a variable pressure wave damping coefficient (VPDC) that could impart adaptive damping capability to unsteady friction models. This VPDC based friction formulation replaced the constant pressure wave damping coefficient based friction formulation in the mathematical model, and was then used to simulate flow transients. The numerical results obtained using the VPDC based friction model when validated with the experimental data demonstrated its capability to adapt to the dissipation requirements of the flow. The results with the new friction formulation produced qualitatively and quantitatively superior results over the older model.

We identified that there are some important differences between the surge characteristics at the upstream and the downstream locations of a fast closing valve. This necessitated the requirement of separate VPDC models for surge estimation at upstream and downstream locations of the valve. The simulation studies on surge at the upstream location of a closing valve, using the proposed mathematical model, and with a commercial software

called the AFT Impulse, produced many important findings. The model with constant pressure wave damping coefficient produced superior results over those from the AFT Impulse and those selected from the literature. However, the results with these constant damping coefficient showed high dissipation as the transient progressed. This suggested the need of a variable pressure wave damping coefficient for the accurate simulation of surge at the upstream location of valve. A variable friction coefficient was thus defined for surge prediction at the upstream location of the valve and was used along with the mathematical model to simulate flow cases. The surge data predicted using the variable damping coefficient showed close match with the experimentally measured values. The VPDC incorporated friction model also removed the extra dissipation that was observed in the numerical solution with the constant damping coefficient. The simulation results showed that the proposed mathematical model for compressible liquid together with adaptive friction model produced superior results over the other models used for the purpose of comparison. The variable damping coefficient addressed the deficiencies of constant damping coefficient to a reasonable extent. The research work also suggested the easy incorporation of the new compressible model and the new friction model into any conventional mathematical model that governs the transient flows of compressible liquids.

The differences found between the surge characteristics at either side of the closing valve motivated to further explore the transient pressure characteristics close to the valve location. We have thus studied the trend of pressure difference developed across a closing valve during a transient and the effect of valve closure duration on this parameter. These were carried out using the full mathematical model that we have developed. The transient variation of pressure difference across the valve showed fluctuations of a larger scale accompanied by frequent flow direction change. This combination can prove to be very crucial in determining the system safety and valve closure characteristics. Variation of the pressure difference existing across a valve for different durations of valve closure is also an important information for determining the optimal operating conditions. The importance of the parameter called the ‘characteristic time period’, in determining the closure speed of valves and variation of peak pressures with closure speed were studied.

8.1 Limitations of the Research

One of the major limitations of the study is the lack of accurate information regarding the exact nature of valve closures for the experimental cases selected, and the effects of fluid-structure interactions in the systems during actual experimental conditions. These are

possible reasons for any mismatches between the experimental data and simulation results. The research was also limited to the case of single-phase flow.

8.2 Scope for Future Work

The compressible model for liquid water developed in this research work could be applied for multi-phase flows, which would improve the simulation accuracy through accurate mixture-density and signal propagation speed predictions. The analytical solution presented for the water shock tube problem can be modified to develop similar exact solutions for different configurations of shock tube problems. The prescribed procedure could also be used for developing analytical solutions for liquids other than water by modifying equations of states appropriately.

Definitions of the variable pressure wave damping coefficients proposed in this research work suggests that the tunable parameters are customisable based on the different cases modelled using them. These definitions of the VPDC could be further refined by performing more experimental studies. This may either provide us with exact values of the tunable parameters that are applicable for wide range of cases, or expressions could be developed for defining the tunable parameters in terms of other relevant flow variables. New compressible-liquid and adaptive-friction models could be incorporated into more existing mathematical models for improving their simulation accuracy and numerical stability.

The research performed only hydraulic surge modelling using the mathematical model we have developed. However, the surges associated with industrial fluids such as crude oil that are frequently subjected to flow transients in transfer pipelines, could also simulated using this model by bringing in suitable modifications.

Bibliography

[1] V. R. Meyer, *Practical high-performance liquid chromatography*. John Wiley & Sons, 2013.

[2] V. R. Meyer, *High Pressure Liquid Chromatography and Ultra-high Pressure Liquid Chromatography of Plants: Basic Concepts*. American Cancer Society, 2014, pp. 1–20.

[3] P. Brown, *High Pressure Liquid Chromatography: Biochemical and Biomedical Applications*. Elsevier, 2012.

[4] A. Cadien, Q. Hu, Y. Meng, Y. Cheng, M. Chen, J. Shu, H. Mao, and H. Sheng, "First-order liquid-liquid phase transition in cerium," *Physical Review Letters*, vol. 110, no. 12, p. 125503, 2013.

[5] H.-k. Mao and R. J. Hemley, "Ultrahigh-pressure transitions in solid hydrogen," *Reviews of modern physics*, vol. 66, no. 2, p. 671, 1994.

[6] J. M. McMahon, M. A. Morales, C. Pierleoni, and D. M. Ceperley, "The properties of hydrogen and helium under extreme conditions," *Reviews of modern physics*, vol. 84, no. 4, p. 1607, 2012.

[7] S. Weir, A. Mitchell, and W. J. Nellis, "Metallization of fluid molecular hydrogen at 140 gpa (1.4 mbar)," *Physical review letters*, vol. 76, no. 11, p. 1860, 1996.

[8] D. Prasad, S. Subrahmanyam, and S. Panda, "Thermal, squeezing and compressibility effects in lubrication of asymmetric rollers." *Tribology in Industry*, vol. 36, no. 3, 2014.

[9] T. Predel, E. Schlücker, P. Wasserscheid, D. Gerhard, and W. Arlt, "Ionic liquids as operating fluids in high pressure applications," *Chemical Engineering & Technol-*

ogy: Industrial Chemistry-Plant Equipment-Process Engineering-Biotechnology, vol. 30, no. 11, pp. 1475–1480, 2007.

[10] K. R. Harris and M. Kanakubo, "High pressure studies of the transport properties of ionic liquids," *Faraday discussions*, vol. 154, pp. 425–438, 2012.

[11] A. Shariati and C. J. Peters, "High-pressure phase equilibria of systems with ionic liquids," *The Journal of supercritical fluids*, vol. 34, no. 2, pp. 171–176, 2005.

[12] Y. Zhao, X. Liu, X. Lu, S. Zhang, J. Wang, H. Wang, G. Gurau, R. D. Rogers, L. Su, and H. Li, "The behavior of ionic liquids under high pressure: A molecular dynamics simulation," *The Journal of Physical Chemistry B*, vol. 116, no. 35, pp. 10 876–10 884, 2012.

[13] E. Boucher and J. MURRELL, *Properties of liquids and solutions*. Wiley, 1982.

[14] Y. Taniguchi, K. Hara, and M. Senoo, *High pressure liquids and solutions*. Elsevier, 2013.

[15] H.-K. Mao, X.-J. Chen, Y. Ding, B. Li, and L. Wang, "Solids, liquids, and gases under high pressure," *Reviews of Modern Physics*, vol. 90, no. 1, p. 015007, 2018.

[16] B. G. Schwacha, "Liquid cutting of hard materials," May 23 1961, US Patent 2,985,050.

[17] R. Chadwick and J. Robertson, "Energy absorber for high pressure fluid jets," May 1 1973, US Patent 3,730,040.

[18] M. Lesser and J. Field, "The impact of compressible liquids," *AnRFM*, vol. 15, pp. 97–122, 1983.

[19] H. Ramezanzadeh, A. Ramiar, M. Yousefifard, and M. Ghasemian, "Numerical analysis of sinusoidal and step pulse velocity effects on an impinging jet quenching process," *Journal of Thermal Analysis and Calorimetry*, pp. 1–19, 2019.

[20] B. Le Méhauté and S. Wang, *Water Waves Generated by Underwater Explosion*. World Scientific, 1996.

[21] M. Liu, G. Liu, K. Lam, and Z. Zong, "Smoothed particle hydrodynamics for numerical simulation of underwater explosion," *Computational Mechanics*, vol. 30, no. 2, pp. 106–118, 2003.

[22] T. Li, S. Wang, S. Li, and A. M. Zhang, "Numerical investigation of an underwater explosion bubble based on fvm and vof," *Applied Ocean Research*, vol. 74, pp. 49–58, 2018.

[23] V. Gurovich, A. Virozub, A. Rososhek, S. Bland, R. Spielman, and Y. E. Krasik, "Quasi-isentropic compression using compressed water flow generated by underwater electrical explosion of a wire array," *Journal of Applied Physics*, vol. 123, no. 18, p. 185902, 2018.

[24] R. O. Cleveland and J. A. McAteer, "The physics of shock wave lithotripsy," *Smith's textbook on endourology*, vol. 1, pp. 529–558, 2007.

[25] G. L. Cheing and H. Chang, "Extracorporeal shock wave therapy," *Journal of Orthopaedic & Sports Physical Therapy*, vol. 33, no. 6, pp. 337–343, 2003.

[26] L. A. Crum and R. A. Roy, "Sonoluminescence," *Physics Today*, vol. 47, no. 9, pp. 22–30, 1994.

[27] F. R. Young, *Sonoluminescence*. CRC press, 2004.

[28] J. Heiderich and R. E. Todd, "Along-stream evolution of gulf stream volume transport," *Journal of Physical Oceanography*, 2020.

[29] A. J. Jamieson, "The five deeps expedition and an update of full ocean depth exploration and explorers," *Marine Technology Society Journal*, vol. 54, no. 1, pp. 6–12, 2020.

[30] W. Chen, G. Chen, D. Jeng, and L. Xu, "Ocean bottom hydrodynamic pressure due to vertical seismic motion," *International Journal of Geomechanics*, vol. 20, no. 9, p. 06020025, 2020.

[31] C. Houqun, "Seismic safety analysis of tall concrete dams, investigation and insights on critical challenges," *Earthquake Engineering and Engineering Vibration*, vol. 19, no. 3, pp. 533–539, 2020.

[32] B. Pastina, J. Isabey, and B. Hickel, "The influence of water chemistry on the radiolysis of the primary coolant water in pressurized water reactors," *Journal of nuclear materials*, vol. 264, no. 3, pp. 309–318, 1999.

[33] A. Berg, U. Iben, A. Meister, and J. Schmidt, "Modeling and simulation of cavitation in hydraulic pipelines based on the thermodynamic and caloric properties of liquid and steam," *Shock Waves*, vol. 14, no. 1-2, pp. 111–121, 2005.

[34] T. Neuhaus and A. Dudlik, "Experiments and comparing calculations on thermohydraulic pressure surges in pipes," *Kerntechnik*, vol. 71, no. 3, pp. 87–94, 2006.

[35] N. Philip, "Adiabatic and isothermal compressibilities of liquids," in *Proceedings of the Indian Academy of Sciences-Section A*, vol. 9, no. 2. Springer, 1939, pp. 109–120.

[36] P. W. Bridgman *et al.*, "Physics of high pressure," 1952.

[37] V. L'vov and A. Mikhailov, "Sound and hydrodynamic turbulence in a compressible liquid," *Zh. Eksp. Teor. Fiz*, vol. 74, pp. 1445–1457, 1978.

[38] S. Tanaka, N. Arihara, M. A. Al-Marhoun *et al.*, "Effects of oil compressibility on production performance of fractured reservoirs evaluated by streamline dual-porosity simulation," in *SPE EUROPEC/EAGE Annual Conference and Exhibition*. Society of Petroleum Engineers, 2010.

[39] D. Fuster, C. Dopazo, and G. Hauke, "Liquid compressibility effects during the collapse of a single cavitating bubble," *The Journal of the Acoustical Society of America*, vol. 129, no. 1, pp. 122–131, 2011.

[40] S. Merouani, O. Hamdaoui, and N. Kerabchi, "Liquid compressibility effect on the acoustic generation of free radicals," *Journal of Applied Water Engineering and Research*, pp. 1–15, 2020.

[41] Z. Paszota, "Effect of the working liquid compressibility on the picture of volumetric and mechanical losses in a high pressure displacement pump used in a hydrostatic drive," *Polish Maritime Research*, vol. 19, no. 2, pp. 3–10, 2012.

[42] N. Henry, "String out and compressibility effect on pressure rise in a shut-in well," 2019.

[43] R. Egashira and T. Kanagawa, "Effects of liquid compressibility on mathematical well-posedness of two-fluid model equation for bubbly flows," in *Proceedings of the 12th Asia Pacific Physics Conference (APPC12)*, 2014, p. 015051.

[44] Y.-n. Zhang, Q. Min, and X.-z. Du, "Effects of liquid compressibility on bubble-bubble interactions between oscillating bubbles," *Journal of Hydrodynamics*, vol. 28, no. 5, pp. 832–839, 2016.

[45] X. Deng, S. Inaba, B. Xie, K.-M. Shyue, and F. Xiao, "High fidelity discontinuity-resolving reconstruction for compressible multiphase flows with moving interfaces," *Journal of Computational Physics*, vol. 371, pp. 945 – 966, 2018.

[46] B. Re and R. Abgrall, "Non-equilibrium model for weakly compressible multi-component flows: the hyperbolic operator," in *International Seminar on Non-Ideal Compressible-Fluid Dynamics for Propulsion & Power*. Springer, 2018, pp. 33–45.

[47] V. Shokri and K. Esmaeili, "Effect of liquid phase compressibility on modeling of gas-liquid two-phase flows using two-fluid model," *Thermal Science*, vol. 23, no. 5 Part B, pp. 3003–3013, 2019.

[48] M. J. Klein, "The historical origins of the van der waals equation," *Physica*, vol. 73, no. 1, pp. 28–47, 1974.

[49] P. Perrot, *A to Z of Thermodynamics*. Oxford University Press on Demand, 1998.

[50] A. Kaplun and A. Meshalkin, "Simple fundamental equation of state for liquid, gas, and fluid of argon, nitrogen, and carbon dioxide," *Thermophysics and Aeromechanics*, vol. 24, no. 4, pp. 513–522, 2017.

[51] J. R. Maw, "A relatively simple analytical equation of state for liquid metals," in *AIP Conference Proceedings*, vol. 1426, no. 1. American Institute of Physics, 2012, pp. 779–782.

[52] H. Ichikawa, T. Tsuchiya, and Y. Tange, "The p-v-t equation of state and thermodynamic properties of liquid iron," *Journal of Geophysical Research: Solid Earth*, vol. 119, no. 1, pp. 240–252, 2014.

[53] E. M. Mansour, "Equation of state," in *Inverse Heat Conduction and Heat Exchangers*. IntechOpen, 2020.

[54] A. Maghari and F. ZiaMajidi, "Prediction of thermodynamic properties of pure ionic liquids through extended saft-back equation of state," *Fluid Phase Equilibria*, vol. 356, pp. 109–116, 2013.

[55] X. Ji and C. Held, "Modeling the density of ionic liquids with epc-saft," *Fluid Phase Equilibria*, vol. 410, pp. 9–22, 2016.

[56] M. Chorążewski, E. B. Postnikov, B. Jasiok, Y. V. Nedyalkov, and J. Jacquemin, "A fluctuation equation of state for prediction of high-pressure densities of ionic liquids," *Scientific reports*, vol. 7, no. 1, pp. 1–9, 2017.

[57] M. H. Rice and J. M. Walsh, "Equation of state of water to 250 kilobars," *The Journal of Chemical Physics*, vol. 26, no. 4, pp. 824–830, 1957.

[58] E. Nowak, "A rational equation of state for water and water vapor in the critical region," 1964.

[59] G. Gurtman, J. Kirsch, and C. Hastings, "Analytical equation of state for water compressed to 300 kbar," *Journal of Applied Physics*, vol. 42, no. 2, pp. 851–857, 1971.

[60] F. H. Ree, "Equation of state of water," California Univ., Livermore (USA). Lawrence Livermore Lab., Tech. Rep., 1976.

[61] C.-T. Chen, R. A. Fine, and F. J. Millero, "The equation of state of pure water determined from sound speeds," *The Journal of Chemical Physics*, vol. 66, no. 5, pp. 2142–2144, 1977.

[62] H. Halbach and N. D. Chatterjee, "An empirical redlich-kwong-type equation of state for water to 1,000 c and 200 kbar," *Contributions to Mineralogy and Petrology*, vol. 79, no. 3, pp. 337–345, 1982.

[63] E. A. Mueller and K. E. Gubbins, "An equation of state for water from a simplified intermolecular potential," *Industrial & engineering chemistry research*, vol. 34, no. 10, pp. 3662–3673, 1995.

[64] S. Wiryana, L. Slutsky, and J. Brown, "The equation of state of water to 200 c and 3.5 gpa: model potentials and the experimental pressure scale," *Earth and Planetary Science Letters*, vol. 163, no. 1-4, pp. 123–130, 1998.

[65] C. Jeffery and P. Austin, "A new analytic equation of state for liquid water," *The Journal of chemical physics*, vol. 110, no. 1, pp. 484–496, 1999.

[66] P. Hill, R. C. MacMillan, and V. Lee, "A fundamental equation of state for heavy water," *Journal of Physical and Chemical Reference Data*, vol. 11, no. 1, pp. 1–14, 1982.

[67] S. Herrig, M. Thol, A. H. Harvey, and E. W. Lemmon, "A reference equation of state for heavy water," *Journal of Physical and Chemical Reference Data*, vol. 47, no. 4, p. 043102, 2018.

[68] W. Wagner and A. Pruß, "The iapws formulation 1995 for the thermodynamic properties of ordinary water substance for general and scientific use," *Journal of physical and chemical reference data*, vol. 31, no. 2, pp. 387–535, 2002.

[69] J. Chen, J.-g. Mi, Y.-m. Yu, and G. Luo, "An analytical equation of state for water and alkanols," *Chemical engineering science*, vol. 59, no. 24, pp. 5831–5838, 2004.

[70] K. Davitt, E. Rolley, F. Caupin, A. Arvengas, and S. Balibar, "Equation of state of water under negative pressure," *The Journal of chemical physics*, vol. 133, no. 17, p. 174507, 2010.

[71] M. French, T. R. Mattsson, N. Nettelmann, and R. Redmer, "Equation of state and phase diagram of water at ultrahigh pressures as in planetary interiors," *Physical Review B*, vol. 79, no. 5, p. 054107, 2009.

[72] R. I. Nigmatulin and R. K. Bolotnova, "Wide-range equation of state of water and steam: Simplified form," *High Temperature*, vol. 49, no. 2, pp. 303–306, 2011.

[73] V. Holten, J. V. Sengers, and M. A. Anisimov, "Equation of state for supercooled water at pressures up to 400 mpa," *Journal of Physical and Chemical Reference Data*, vol. 43, no. 4, p. 043101, 2014.

[74] G. Pallares, M. A. Gonzalez, J. L. F. Abascal, C. Valeriani, and F. Caupin, "Equation of state for water and its line of density maxima down to- 120 mpa," *Physical Chemistry Chemical Physics*, vol. 18, no. 8, pp. 5896–5900, 2016.

[75] F. J. Millero, C.-T. Chen, A. Bradshaw, and K. Schleicher, "A new high pressure equation of state for seawater," *Deep Sea Research Part A. Oceanographic Research Papers*, vol. 27, no. 3-4, pp. 255–264, 1980.

[76] N. Fofonoff, "Physical properties of seawater: A new salinity scale and equation of state for seawater," *Journal of Geophysical Research: Oceans*, vol. 90, no. C2, pp. 3332–3342, 1985.

[77] J. Nycander, M. Hieronymus, and F. Roquet, "The nonlinear equation of state of sea water and the global water mass distribution," *Geophysical Research Letters*, vol. 42, no. 18, pp. 7714–7721, 2015.

[78] F. J. Millero, "History of the equation of state of seawater," *Oceanography*, vol. 23, no. 3, pp. 18–33, 2010.

[79] A. T. J. Hayward, "Compressibility equations for liquids: a comparative study," *British Journal of Applied Physics*, vol. 18, no. 7, p. 965, 1967.

[80] Y.-H. Li, "Equation of state of water and sea water," *Journal of Geophysical Research*, vol. 72, no. 10, pp. 2665–2678, 1967.

[81] P. Tait, "Physics and chemistry of the voyage of hms challenger," *Vol. II, Part IV, SP LXI*, 1888.

[82] G. Tammann, "Über die abhängigkeit der volumina von lösungen vom druck," *Zeitschrift für Physikalische Chemie*, vol. 17, no. 1, pp. 620–636, 1895.

[83] J. R. Macdonald, "Some simple isothermal equations of state," *Reviews of Modern Physics*, vol. 38, no. 4, p. 669, 1966.

[84] O. Tumlirz, *Die Zustandsgleichung der Flüssigkeiten bei hohem Drucke*, 1909.

[85] J. Dymond and R. Malhotra, "The tait equation: 100 years on," *International Journal of Thermophysics*, vol. 9, no. 6, pp. 941–951, 1988.

[86] A. I. Burshtein, *Introduction to thermodynamics and kinetic theory of matter*. John Wiley & Sons, 2008.

[87] R. Davis, "Further comments on thermodynamic response of mie-gruneisen materials," in *Physics of condensed matter*. Springer, 1973, pp. 63–70.

[88] L. Huang, "Numerical simulation model on irreversibility of shock-wave process," 2013.

[89] F. Harlow and A. Amsden, "Fluid dynamics, los alamos national laboratory," Technical Report, LA-4700, Tech. Rep., 1971.

[90] O. Le Métayer and R. Saurel, "The noble-abel stiffened-gas equation of state," *Physics of Fluids*, vol. 28, no. 4, p. 046102, 2016.

[91] M. J. Morley and D. M. Williamson, "Shock/reload response of water and aqueous solutions of ammonium nitrate," in *AIP Conference Proceedings*, vol. 1426, no. 1. American Institute of Physics, 2012, pp. 775–778.

[92] A. N. Maiboroda, "Planing on the surface of a compressible fluid," *International Journal of Fluid Mechanics Research*, vol. 33, no. 3, pp. 286–302, 2006.

[93] R. Saurel and R. Abgrall, "A simple method for compressible multifluid flows," *SIAM Journal on Scientific Computing*, vol. 21, no. 3, pp. 1115–1145, 1999.

[94] G. Allaire, S. Clerc, and S. Kokh, "A five-equation model for the simulation of interfaces between compressible fluids," *Journal of Computational Physics*, vol. 181, no. 2, pp. 577–616, 2002.

[95] O. Le Métayer, J. Massoni, P. SMASH, R. Saurel, P. SMASH *et al.*, "Elaborating equations of state of a liquid and its vapor for two-phase flow models; elaboration des lois d'etat d'un liquide et de sa vapeur pour les modeles d'ecoulements diphasiques," *International Journal of Thermal Sciences*, vol. 43, 2004.

[96] T. FlÅtten, A. Morin, and S. T. Munkejord, "On solutions to equilibrium problems for systems of stiffened gases," *SIAM Journal on Applied Mathematics*, vol. 71, no. 1, pp. 41–67, 2011.

[97] B. Jasiok, E. B. Postnikov, and M. Chorążewski, "The prediction of high-pressure volumetric properties of compressed liquids using the two states model," *Physical Chemistry Chemical Physics*, vol. 21, no. 29, pp. 15 966–15 973, 2019.

[98] D. Dolan, M. Knudson, C. Hall, and C. Deeney, "A metastable limit for compressed liquid water," *Nature Physics*, vol. 3, no. 5, pp. 339–342, 2007.

[99] M. Yasutomi, *The Physics of Liquid Water*. Jenny Stanford Publishing, 2020.

[100] I. Glass, "Shock tubes. part i. theory and performance of simple shock tubes," *UTIA Review, No. 12 Part I*, 1958. [Online]. Available: http://resolver.tudelft.nl/uuid:316a7629-ad4e-445b-b3e5-df690b684584

[101] J. K. Wright, *Shock tubes*. Methuen Monographs on Physical Subjects, John Wiley & Sons, 1961.

[102] R. E. Duff and A. N. Blackwell, "Explosive driven shock tubes," *Review of Scientific Instruments*, vol. 37, no. 5, pp. 579–586, 1966. [Online]. Available: https://aip.scitation.org/doi/abs/10.1063/1.1720256

[103] W. Jost, "J. n. bradley, shock waves in chemistry and physics. 370 s. methuen, london, john wiley and sons, new york, 1962, 370 s. preis: 63 s," *Zeitschrift für Elektrochemie, Berichte der Bunsengesellschaft für physikalische Chemie*, vol. 66, no. 8-9, pp. 770–770, 1962. [Online]. Available: https://onlinelibrary.wiley.com/doi/abs/10.1002/bbpc.19620660841

[104] A. G. Gaydon and I. R. Hurle, *The shock tube in high-temperature chemical physics*. Chapman and Hall, 1963.

[105] J. V. Becker, "Re-entry from space," *Scientific American*, vol. 204, no. 1, pp. 49–57, 1961. [Online]. Available: http://www.jstor.org/stable/24940739

[106] C. C. HORSTMAN and M. I. KUSSOY, "Free-flight measurements of aerodynamic viscous effects on lifting re-entry bodies." *Journal of Spacecraft and Rockets*, vol. 4, no. 8, pp. 1064–1069, 1967. [Online]. Available: https://doi.org/10.2514/3.29019

[107] K. Itoh, S. Ueda, H. Tanno, T. Komuro, and K. Sato, "Hypersonic aerothermodynamic and scramjet research using high enthalpy shock tunnel," *Shock Waves*, vol. 12, no. 2, pp. 93–98, 2002. [Online]. Available: https://doi.org/10.1007/s00193-002-0147-0

[108] G. Yamada, T. Suzuki, H. Takayanagi, and K. Fujita, "Development of shock tube for ground testing reentry aerothermodynamics," *Transactions of the Japan Society for Aeronautical and Space Sciences*, vol. 54, no. 183, pp. 51–61, 2011. [Online]. Available: https://doi.org/10.2322/tjsass.54.51

[109] H. Tanno, M. KODERA, K. Tomoyuki, S. Kazuo, T. Masahiro, and I. Katsuhiro, *Aeroheating measurements on a reentry capsule model in free-piston shock tunnel HIEST*, 2010, vol. 9. [Online]. Available: https://arc.aiaa.org/doi/abs/10.2514/6.2010-1181

[110] R. Haoui, "Physico-chemical state of the air at the stagnation point during the atmospheric reentry of a spacecraft," *Acta Astronautica*, vol. 68, no. 11, pp. 1660 – 1668, 2011. [Online]. Available: http://www.sciencedirect.com/science/article/pii/S0094576511000038

[111] H. Tanno, T. Komuro, K. Sato, K. Itoh, and T. Yamada, *Free-flight tests of reentry capsule models in free-piston shock tunnel*, 2013, p. 2979. [Online]. Available: https://arc.aiaa.org/doi/abs/10.2514/6.2013-2979

[112] H. Tanno, K. Sato, T. Komuro, and K. Itoh, *Free-flight aerodynamic tests of reentry vehicles in high-temperature real-gas flow (Invited)*, 2014, p. 3109. [Online]. Available: https://arc.aiaa.org/doi/abs/10.2514/6.2014-3109

[113] G. Yamada, M. KAJINO, and K. Ohtani, "Experimental and numerical study on radiating shock tube flows for spacecraft reentry flights," *Journal of Fluid Science and Technology*, vol. 14, pp. JFST0022–JFST0022, 01 2019.

[114] M. Chavko, W. A. Koller, W. K. Prusaczyk, and R. M. McCarron, "Measurement of blast wave by a miniature fiber optic pressure transducer in the rat brain," *Journal of Neuroscience Methods*, vol. 159, no. 2, pp. 277 – 281, 2007. [Online]. Available: http://www.sciencedirect.com/science/article/pii/S0165027006003360

[115] I. Cernak, "The importance of systemic response in the pathobiology of blast-induced neurotrauma," *Frontiers in Neurology*, vol. 1, p. 151, 2010. [Online]. Available: https://www.frontiersin.org/article/10.3389/fneur.2010.00151

[116] J. A. Ogden, A. Tóth-Kischkat, and R. Schultheiss, "Principles of shock wave therapy." *Clinical Orthopaedics and Related Research (1976-2007)*, vol. 387, pp. 8–17, 2001.

[117] R. O. Cleveland and O. A. Sapozhnikov, "Modeling elastic wave propagation in kidney stones with application to shock wave lithotripsy," *The Journal of the Acoustical Society of America*, vol. 118, no. 4, pp. 2667–2676, 2005.

[118] N. Fomin, "110 years of experiments on shock tubes," *Journal of Engineering Physics and Thermophysics*, vol. 83, no. 6, pp. 1118–1135, 2010. [Online]. Available: https://doi.org/10.1007/s10891-010-0437-9

[119] I. Glass and G. Patterson, "A theoretical and experimental study of shock-tube flows," *Journal of the Aeronautical Sciences*, vol. 22, no. 2, pp. 73–100, 1955.

[120] H. Pain and E. Rogers, "Shock waves in gases," *Reports on progress in physics*, vol. 25, no. 1, p. 287, 1962.

[121] R. M. NEREM and G. H. STICKFORD, "Shock-tube studies of equilibrium air radiation," *AIAA Journal*, vol. 3, no. 6, pp. 1011–1018, 1965.

[122] R. Kern and K. Xie, "Shock tube studies of gas phase reactions preceding the soot formation process," *Progress in energy and combustion science*, vol. 17, no. 3, pp. 191–210, 1991.

[123] D. F. Davidson and R. K. Hanson, "Real gas corrections in shock tube studies at high pressures," *Israel journal of chemistry*, vol. 36, no. 3, pp. 321–326, 1996.

[124] K. Chojnicki, A. Clarke, and J. Phillips, "A shock-tube investigation of the dynamics of gas-particle mixtures: Implications for explosive volcanic eruptions," *Geophysical research letters*, vol. 33, no. 15, 2006.

[125] J. Ananthu and N. A. Kumar, "Shock tube performance studies with different driver and driven gases using numerical simulation," in *Recent Asian Research on Thermal and Fluid Sciences*. Springer, 2020, pp. 533–542.

[126] R. Kumar and A. Nedungadi, "Using gas-driven shock tubes to produce blast wave signatures," *Frontiers in neurology*, vol. 11, p. 90, 2020.

[127] J. John and T. Keith, *Gas Dynamics, 3rd edition*. Pearson, London, 2006.

[128] E. F. Toro, *Riemann solvers and numerical methods for fluid dynamics: a practical introduction*. Springer Science & Business Media, 2013.

[129] G. B. Whitham, *Linear and nonlinear waves*, 2011, vol. 42.

[130] L. Landau and E. Lifshitz, *Fluid Mechanics, Pargamon*. Oxford, 1987.

[131] "A survey of several finite difference methods for systems of nonlinear hyperbolic conservation laws," *Journal of Computational Physics*, vol. 27, no. 1, pp. 1 – 31, 1978. [Online]. Available: http://www.sciencedirect.com/science/article/pii/0021999178900232

[132] I. Campbell and A. Pitcher, "Shock waves in a liquid containing gas bubbles," *Proceedings of the Royal Society of London. Series A. Mathematical and Physical Sciences*, vol. 243, no. 1235, pp. 534–545, 1958.

[133] A. Campbell, W. Davis, and J. Travis, "Shock initiation of detonation in liquid explosives," *The Physics of Fluids*, vol. 4, no. 4, pp. 498–510, 1961.

[134] J. M. Walsh and M. H. Rice, "Dynamic compression of liquids from measurements on strong shock waves," *The Journal of Chemical Physics*, vol. 26, no. 4, pp. 815–823, 1957.

[135] G. Lyzenga, T. J. Ahrens, W. Nellis, and A. Mitchell, "The temperature of shock-compressed water," *The Journal of Chemical Physics*, vol. 76, no. 12, pp. 6282–6286, 1982.

[136] L. Al'Tshuler, G. Doronin, and G. K. Kim, "Viscosity of shock-compressed fluids," *Journal of Applied Mechanics and Technical Physics*, vol. 27, no. 6, pp. 887–894, 1986.

[137] C. H. Cooke and T.-J. Chen, "On shock capturing for pure water with general equation of state," *Communications in applied numerical methods*, vol. 8, no. 4, pp. 219–233, 1992.

[138] I. Lee and S. Finnegan, "Prediction of shock response of pyrotechnic mixtures from thermal analysis," *Journal of Thermal Analysis and Calorimetry*, vol. 50, no. 5-6, pp. 707–717, 1997.

[139] P. Celliers, G. Collins, D. Hicks, M. Koenig, E. Henry, A. Benuzzi-Mounaix, D. Batani, D. Bradley, L. Da Silva, R. Wallace *et al.*, "Electronic conduction in shock-compressed water," *Physics of Plasmas*, vol. 11, no. 8, pp. L41–L44, 2004.

[140] D. Dolan and Y. Gupta, "Nanosecond freezing of water under multiple shock wave compression: Optical transmission and imaging measurements," *The Journal of chemical physics*, vol. 121, no. 18, pp. 9050–9057, 2004.

[141] D. Dolan, J. Johnson, and Y. Gupta, "Nanosecond freezing of water under multiple shock wave compression: Continuum modeling and wave profile measurements," *The Journal of chemical physics*, vol. 123, no. 6, p. 064702, 2005.

[142] K. Takayama, H. Yamamoto, and H. Shimokawa, "Underwater shock wave research applied to therapeutic device developments," *Journal of Engineering Physics and Thermophysics*, vol. 86, no. 4, pp. 963–975, 2013.

[143] D. Batani, K. Jakubowska, A. Benuzzi-Mounaix, C. Cavazzoni, C. Danson, T. Hall, M. Kimpel, D. Neely, J. Pasley, M. R. Le Gloahec *et al.*, "Refraction index of shock compressed water in the megabar pressure range," *EPL (Europhysics Letters)*, vol. 112, no. 3, p. 36001, 2015.

[144] A. B. Gojani, K. Ohtani, K. Takayama, and S. Hosseini, "Shock hugoniot and equations of states of water, castor oil, and aqueous solutions of sodium chloride, sucrose and gelatin," *Shock Waves*, vol. 26, no. 1, pp. 63–68, 2016.

[145] D. Kang, J. B. Nah, M. Cho, and S. Xiao, "Shock wave generation in water for biological studies," *IEEE Transactions on Plasma Science*, vol. 42, no. 10, pp. 3231–3238, 2014.

[146] G. Ben-Dor, O. Igra, and T. Elperin, *Handbook of shock waves, three volume set*. Elsevier, 2000.

[147] A.-L. Biance, F. Chevy, C. Clanet, G. Lagubeau, and D. Quéré, "On the elasticity of an inertial liquid shock," *Journal of Fluid Mechanics*, vol. 554, p. 47, 2006.

[148] M. Kubecka, A. Obrusník, and Z. Bonaventura, "Simulation of shock-waves in water induced by nanosecond-laser pulse," in *Proceedings of the* 45^{th} *Conference on Plasma Physics*. European Physical Society, 2018, p. P4.3006.

[149] M. Armstrong and S. Bastea, "System and method for rapid, high throughput, high pressure synthesis of materials from a liquid precursor," May 28 2020, uS Patent App. 16/203,177.

[150] X. Song, B. Li, and L. Xie, "Experimental investigation on the properties of liquid film breakup induced by shock waves," *Chinese Physics B*, 2020.

[151] P. Debnath and K. Pandey, "Numerical analysis of detonation combustion wave in pulse detonation combustor with modified ejector with gaseous and liquid fuel mixture," *Journal of Thermal Analysis and Calorimetry*, pp. 1–12, 2020.

[152] J. Kaiser, J. Winter, S. Adami, and N. Adams, "Investigation of interface deformation dynamics during high-weber number cylindrical droplet breakup," *International Journal of Multiphase Flow*, p. 103409, 2020.

[153] C. Ash, "The shattering effect on rain," *Science*, vol. 369, no. 6501, pp. 265–265, 2020.

[154] E. M. El-Said, M. M. Awad, and M. Abdulaziz, "A comprehensive review on pressurized thermal shock: predictive, preventive and safety issues," *Journal of Thermal Analysis and Calorimetry*, pp. 1–20, 2020.

[155] L. Li, X.-x. Lu, X.-b. Ren, Y.-j. Ren, S.-t. Zhao, and X.-f. Yan, "The mechanism of liquid dispersing from a cylinder driven by central dynamic shock loading," *Defence Technology*, 2020.

[156] B. Riemann, *Über die Fortpflanzung ebener Luftwellen von endlicher Schwingungsweite*. Dieterich, 1860.

[157] E. F. Toro, *Shock-capturing methods for free-surface shallow flows*. Wiley-Blackwell, 2001.

[158] R. J. LeVeque *et al.*, *Finite volume methods for hyperbolic problems*. Cambridge university press, 2002, vol. 31.

[159] V. Guinot, *Godunov-type schemes: an introduction for engineers*. Elsevier, 2003.

[160] S. K. Godunov, "A difference method for numerical calculation of discontinuous solutions of the equations of hydrodynamics," *Matematicheskii Sbornik*, vol. 89, no. 3, pp. 271–306, 1959.

[161] C. Kong, "Comparison of approximate riemann solvers," *A dissertation of the degree of Master of Science in Mathematical and Numerical Modeling of the Atmoshere and Oceans, Department of Mathematics, University of Reading*, vol. 54, 2011.

[162] M. Ivings, D. Causon, and E. Toro, "On riemann solvers for compressible liquids," *International Journal for Numerical Methods in Fluids*, vol. 28, no. 3, pp. 395–418, 1998.

[163] P. Roe, *Numerical algorithms for the linear wave equation*. Royal Aircraft Establishment, 1981.

[164] P. Roe and J. Pike, "Efficient construction and utilisation of approximate riemann solutions," in *Proc. of the sixth int'l. symposium on Computing methods in applied sciences and engineering, VI*, 1985, pp. 499–518.

[165] L. Sainsaulieu, "Finite volume approximation of two phase-fluid flows based on an approximate roe-type riemann solver," *Journal of computational Physics*, vol. 121, no. 1, pp. 1–28, 1995.

[166] L. Giraud and G. Manzini, "Parallel implementations of 2d explicit euler solvers," *Journal of computational physics*, vol. 123, no. 1, pp. 111–118, 1996.

[167] R. J. LeVeque and K.-M. Shyue, "Two-dimensional front tracking based on high resolution wave propagation methods," *Journal of Computational Physics*, vol. 123, no. 2, pp. 354–368, 1996.

[168] F. Rieper, "A low-mach number fix for roe's approximate riemann solver," *Journal of Computational Physics*, vol. 230, no. 13, pp. 5263–5287, 2011.

[169] C. E. Castro and E. F. Toro, "Roe-type riemann solvers for general hyperbolic systems," *International Journal for Numerical Methods in Fluids*, vol. 75, no. 7, pp. 467–486, 2014.

[170] R. Martins, J. Leandro, and S. Djordjević, "A well balanced roe scheme for the local inertial equations with an unstructured mesh," *Advances in Water Resources*, vol. 83, pp. 351–363, 2015.

[171] S. Osher and S. Chakravarthy, "Upwind schemes and boundary conditions with applications to euler equations in general geometries," *Journal of Computational Physics*, vol. 50, no. 3, pp. 447–481, 1983.

[172] B. Engquist and S. Osher, "One-sided difference approximations for nonlinear conservation laws," *Mathematics of Computation*, vol. 36, no. 154, pp. 321–351, 1981.

[173] T. W. Roberts, "The behavior of flux difference splitting schemes near slowly moving shock waves," *Journal of Computational Physics*, vol. 90, no. 1, pp. 141–160, 1990.

[174] S. Billett and E. Toro, "Restoring monotonicity of slowly-moving shocks computed with godunov-type schemes," *NASA STI/Recon Technical Report N*, vol. 93, p. 24075, 1992.

[175] A. Harten, P. D. Lax, and B. V. Leer, "On upstream differencing and godunov-type schemes for hyperbolic conservation laws," *SIAM Review*, vol. 25, no. 1, pp. 35–61, 1983. [Online]. Available: http://www.jstor.org/stable/2030019

[176] B. Einfeldt, "On godunov-type methods for gas dynamics," *SIAM Journal on Numerical Analysis*, vol. 25, no. 2, pp. 294–318, 1988. [Online]. Available: http://www.jstor.org/stable/2157317

[177] B. Einfeldt, C.-D. Munz, P. L. Roe, and B. Sjögreen, "On godunov-type methods near low densities," *Journal of computational physics*, vol. 92, no. 2, pp. 273–295, 1991. [Online]. Available: https://doi.org/10.1007/BF02425037

[178] E. F. Toro, M. Spruce, and W. Speares, "Restoration of the contact surface in the HLL-Riemann solver," *Shock Waves*, vol. 4, no. 1, pp. 25–34, jul 1994.

[179] J. L. Steger and R. Warming, “Flux vector splitting of the inviscid gasdynamic equations with application to finite-difference methods,” *Journal of computational physics*, vol. 40, no. 2, pp. 263–293, 1981.

[180] B. Van Leer, “" flux-vector splitting for the euler equations", proceedings of the 8th international conference on numerical methods in fluid dynamics,” *Lecture Notes in Physics*, vol. 70, 1982.

[181] M.-S. Liou and C. J. Steffen, “A new flux splitting scheme,” *Journal of Computational Physics*, vol. 107, no. 1, pp. 23 – 39, 1993. [Online]. Available: http://www.sciencedirect.com/science/article/pii/S0021999183711228

[182] M.-S. Liou, “A sequel to ausm: Ausm+,” *Journal of Computational Physics*, vol. 129, no. 2, pp. 364 – 382, 1996. [Online]. Available: http://www.sciencedirect.com/science/article/pii/S0021999196902569

[183] Y. Wada and M.-S. Liou, “An accurate and robust flux splitting scheme for shock and contact discontinuities,” *SIAM Journal on Scientific Computing*, vol. 18, no. 3, pp. 633–657, 1997. [Online]. Available: https://doi.org/10.1137/S1064827595287626

[184] M. Hajžman, J. Vimmr, and O. Bublík, “On the modelling of compressible inviscid flow problems using ausm schemes,” 2007.

[185] M.-S. Liou, “The evolution of ausm schemes,” *Defence Science Journal*, vol. 60, no. 6, 2010.

[186] M.-S. Liou, “A sequel to ausm, part ii: Ausm+-up for all speeds,” *J. Comput. Phys.*, vol. 214, no. 1, p. 137–170, May 2006. [Online]. Available: https://doi.org/10.1016/j.jcp.2005.09.020

[187] C.-H. Chang and M.-S. Liou, “A robust and accurate approach to computing compressible multiphase flow: Stratified flow model and ausm+-up scheme,” *Journal of Computational Physics*, vol. 225, no. 1, pp. 840 – 873, 2007. [Online]. Available: http://www.sciencedirect.com/science/article/pii/S0021999107000071

[188] K. Kitamura, “Numerical flux functions for ideal gases,” in *Advancement of Shock Capturing Computational Fluid Dynamics Methods*. Springer, 2020, pp. 21–67.

[189] B. Van Leer, “Towards the ultimate conservative difference scheme i. the quest of monotonicity,” in *Proceedings of the Third International Conference on Numerical Methods in Fluid Mechanics*. Springer, 1973, pp. 163–168.

[190] B. Van Leer, "Towards the ultimate conservative difference scheme. ii. monotonicity and conservation combined in a second-order scheme," *Journal of computational physics*, vol. 14, no. 4, pp. 361–370, 1974.

[191] B. Van Leer, "Towards the ultimate conservative difference scheme iii. upstream-centered finite-difference schemes for ideal compressible flow," *Journal of Computational Physics*, vol. 23, no. 3, pp. 263–275, 1977.

[192] B. Van Leer, "Towards the ultimate conservative difference scheme. iv. a new approach to numerical convection," *Journal of computational physics*, vol. 23, no. 3, pp. 276–299, 1977.

[193] B. Van Leer, "Towards the ultimate conservative difference scheme. v. a second-order sequel to godunov's method," *Journal of computational Physics*, vol. 32, no. 1, pp. 101–136, 1979.

[194] A. Rizzi *et al.*, "Numerical implementation of solid-body boundary conditions for the euler equations," *ZAMM*, vol. 58, pp. 301–304, 1978.

[195] B. Van Leer, "On the relation between the upwind-differencing schemes of godunov, engquist–osher and roe," *SIAM Journal on Scientific and Statistical Computing*, vol. 5, no. 1, pp. 1–20, 1984.

[196] C. Hirsch, "Numerical computation of internal and external flows, volume 1: Fundamentals of numerical discretization," *John Wiley and Sons*, vol. 9, p. 10, 1988.

[197] J. P. Boris and D. L. Book, "Flux-corrected transport. i. shasta, a fluid transport algorithm that works," *Journal of computational physics*, vol. 11, no. 1, pp. 38–69, 1973.

[198] D. L. Book, J. P. Boris, and K. Hain, "Flux-corrected transport ii: Generalizations of the method," *Journal of Computational Physics*, vol. 18, no. 3, pp. 248–283, 1975.

[199] J. P. Boris and D. L. Book, "Flux-corrected transport. iii. minimal-error fct algorithms," *Journal of Computational Physics*, vol. 20, no. 4, pp. 397–431, 1976.

[200] A. HARTEN, "High resolution schemes for hyperbolic conservation laws," *Journal of Computational Physics*, vol. 49, pp. 357–393, 1983.

[201] P. K. Sweby, "High resolution schemes using flux limiters for hyperbolic conservation laws," *SIAM journal on numerical analysis*, vol. 21, no. 5, pp. 995–1011, 1984.

[202] F. Kemm, "A comparative study of tvd-limiters—well-known limiters and an introduction of new ones," *International Journal for Numerical Methods in Fluids*, vol. 67, no. 4, pp. 404–440, 2011.

[203] G. Luttwak and J. Falcovitz, "Slope limiting for vectors: A novel vector limiting algorithm," *International Journal for Numerical Methods in Fluids*, vol. 65, no. 11-12, pp. 1365–1375, 2011.

[204] V. Aizinger, "A geometry independent slope limiter for the discontinuous galerkin method," in *Computational Science and High Performance Computing IV*. Springer, 2011, pp. 207–217.

[205] Y. Liu, W. Zhang, and X. Zheng, "An accuracy preserving limiter for the high-order discontinuous galerkin method on unstructured grids," *Computers & Fluids*, vol. 192, p. 104253, 2019.

[206] M. E. Ladonkina, O. A. Nekliudova, and V. F. Tishkin, "Limiting functions affecting the accuracy of numerical solution obtained by discontinuous galerkin method," in *Advances in Theory and Practice of Computational Mechanics*. Springer, 2020, pp. 63–76.

[207] K. Kitamura and A. Hashimoto, "Simple a posteriori slope limiter (post limiter) for high resolution and efficient flow computations," *Journal of Computational Physics*, vol. 341, pp. 313–340, 2017.

[208] M. D. Bragin, Y. A. Kriksin, and V. F. Tishkin, "Discontinuous galerkin method with entropic slope limiter for euler equations," *Matematicheskoe modelirovanie*, vol. 32, no. 2, pp. 113–128, 2020.

[209] J. Velechovsky, M. Francois, and T. Masser, "Direction-aware slope limiter for three-dimensional cubic grids with adaptive mesh refinement," *Computers & Mathematics with Applications*, vol. 78, no. 2, pp. 670–687, 2019.

[210] H.-F. Duan, M. Ghidaoui, P. J. Lee, and Y.-K. Tung, "Unsteady friction and visco-elasticity in pipe fluid transients," *Journal of hydraulic research*, vol. 48, no. 3, pp. 354–362, 2010.

[211] Y. A. Cengel, *Fluid mechanics*. Tata McGraw-Hill Education, 2010.

[212] W. Zielke, "Frequency-dependent friction in transient pipe flow," 1968.

[213] A. K. Trikha, "An efficient method for simulating frequency-dependent friction in transient liquid flow," 1975.

[214] A. E. Vardy and J. M. Brown, "Transient, turbulent, smooth pipe friction," *Journal of hydraulic research*, vol. 33, no. 4, pp. 435–456, 1995.

[215] A. E. Vardy and K.-L. Hwang, "A characteristics model of transient friction in pipes," *Journal of Hydraulic Research*, vol. 29, no. 5, pp. 669–684, 1991.

[216] A. Vardy and J. Brown, "Transient turbulent friction in smooth pipe flows," *Journal of Sound and Vibration*, vol. 259, no. 5, pp. 1011–1036, 2003.

[217] A. Vardy and J. Brown, "Efficient approximation of unsteady friction weighting functions," *Journal of Hydraulic Engineering*, vol. 130, no. 11, pp. 1097–1107, 2004.

[218] A. Vardy and J. Brown, "Transient turbulent friction in fully rough pipe flows," *Journal of Sound and Vibration*, vol. 270, no. 1-2, pp. 233–257, 2004.

[219] J. Daily, W. Hankey Jr, R. Olive, and J. Jordaan Jr, "Resistance coefficients for accelerated and decelerated flows through smooth tubes and orifices," MASSACHUSETTS INST OF TECH CAMBRIDGE, Tech. Rep., 1955.

[220] B. Brunone, U. Golia, and M. Greco, "Modelling of fast transients by numerical methods," in *Proceedings of the 9th International Conference on Hydraulic Transients with Water Column Separation, Valencia, Spain*, 1991, pp. 273–281.

[221] B. Brunone, U. Golia, and M. Greco, "Some remarks on the momentum equation for fast transients," in *Proceedings of the International Meeting on Hydraulic Transients with Column Separation*, 1991, pp. 201–209.

[222] M. Carstens and J. E. Roller, "Boundary-shear stress in unsteady turbulent pipe flow," *Journal of the Hydraulics Division*, vol. 85, no. 2, pp. 67–81, 1959.

[223] E. L. Holmboe and W. T. Rouleau, "The effect of viscous shear on transients in liquid lines," 1967.

[224] M. Schultz, "The influence of unsteady friction on the propagation of pressure waves in tunnels," in *Proc. of 6th Int. Symp. on Aerodynamics and Ventilation of Vehicle Tunnels*, vol. 123, 1988.

[225] A. Bergant, A. Ross Simpson, and J. Vìtkovsk, "Developments in unsteady pipe flow friction modelling," *Journal of Hydraulic Research*, vol. 39, no. 3, pp. 249–257, 2001.

[226] A. Adamkowski and M. Lewandowski, "Experimental examination of unsteady friction models for transient pipe flow simulation," 2006.

[227] J. P. Vítkovskỳ, A. Bergant, A. R. Simpson, and M. F. Lambert, "Systematic evaluation of one-dimensional unsteady friction models in simple pipelines," *Journal of Hydraulic Engineering*, vol. 132, no. 7, pp. 696–708, 2006.

[228] R. NOROOZ, H. SHAMLOO, and M. MOUSAVIFARD, "A review of one-dimensional unsteady friction models for transient pipe flow," *Cumhuriyet Üniversitesi Fen-Edebiyat Fakültesi Fen Bilimleri Dergisi*, vol. 36, no. 3, pp. 2278–2288, 2015.

[229] A. Mitra and W. Rouleau, "Radial and axial variations in transient pressure waves transmitted through liquid transmission lines," 1985.

[230] I. Jelev, "The damping of flow and pressure oscillations in water hammer analysis," *Journal of Hydraulic Research*, vol. 27, no. 1, pp. 91–114, 1989.

[231] C. P. Liou, "Maximum Pressure Head Due to Linear Valve Closure," *Journal of Fluids Engineering*, vol. 113, no. 4, pp. 643–647, 12 1991.

[232] B. Brunone, B. W. Karney, M. Mecarelli, and M. Ferrante, "Velocity profiles and unsteady pipe friction in transient flow," *Journal of water resources planning and management*, vol. 126, no. 4, pp. 236–244, 2000.

[233] H. Ramos, D. Covas, A. Borga, and D. Loureiro, "Surge damping analysis in pipe systems: modelling and experiments," *Journal of hydraulic Research*, vol. 42, no. 4, pp. 413–425, 2004.

[234] D. Covas, I. Stoianov, H. Ramos, N. Graham, and C. Maksimovic, "The dynamic effect of pipe-wall viscoelasticity in hydraulic transients. part i—experimental analysis and creep characterization," *Journal of Hydraulic Research*, vol. 42, no. 5, pp. 517–532, 2004.

[235] D. Covas, I. Stoianov, J. F. Mano, H. Ramos, N. Graham, and C. Maksimovic, "The dynamic effect of pipe-wall viscoelasticity in hydraulic transients. part ii—model development, calibration and verification," *Journal of Hydraulic Research*, vol. 43, no. 1, pp. 56–70, 2005.

[236] D. Y. Choi, J. Kim, D.-J. Lee, and D. Kim, "Pressure measurements with valve-induced transient flow in water pipelines," *Urban Water Journal*, vol. 12, no. 3, pp. 200–206, 2015.

[237] E. Perez and A. El-Bayoumi, "Valve characteristics and their effect on transient surge pressures in delivery terminals," in *International Pipeline Conference*, vol. 50266. American Society of Mechanical Engineers, 2016, p. V002T02A005.

[238] S. Yang, D. Wu, Z. Lai, and T. Du, "Three-dimensional computational fluid dynamics simulation of valve-induced water hammer," *Proceedings of the Institution of Mechanical Engineers, Part C: Journal of Mechanical Engineering Science*, vol. 231, no. 12, pp. 2263–2274, 2017.

[239] B. S. Jung and B. Karney, "A practical overview of unsteady pipe flow modeling: from physics to numerical solutions," *Urban Water Journal*, vol. 14, no. 5, pp. 502–508, 2017.

[240] G. Bertaglia, M. Ioriatti, A. Valiani, M. Dumbser, and V. Caleffi, "Numerical methods for hydraulic transients in visco-elastic pipes," *Journal of fluids and structures*, vol. 81, pp. 230–254, 2018.

[241] P. Azoury, M. Baasiri, and H. Najm, "Effect of valve-closure schedule on water hammer," *Journal of Hydraulic Engineering*, vol. 112, no. 10, pp. 890–903, 1986.

[242] M. R. Bazargan-Lari, R. Kerachian, H. Afshar, and S. N. Bashi-Azghadi, "Developing an optimal valve closing rule curve for real-time pressure control in pipes," *Journal of Mechanical Science and technology*, vol. 27, no. 1, pp. 215–225, 2013.

[243] M. I. Yuce and A. F. Omer, "Hydraulic transients in pipelines due to various valve closure schemes," *SN Applied Sciences*, vol. 1, no. 9, pp. 1–11, 2019.

[244] R. H. Cole and R. Weller, "Underwater explosions," *Physics Today*, vol. 1, p. 35, 1948.

[245] R. Saurel, J. P. Cocchi, and P. B. Butler, "Numerical study of cavitation in the wake of a hypervelocity underwater projectile," *Journal of Propulsion and Power*, vol. 15, no. 4, pp. 513–522, 1999.

[246] D. S. Lemons and C. M. Lund, "Thermodynamics of high temperature, mie–gruneisen solids," *American Journal of Physics*, vol. 67, no. 12, pp. 1105–1108, 1999.

[247] J.-M. Ghidaglia and A. A. Mrabet, "A regularized stiffened-gas equation of state," *Journal of Applied Analysis & Computation*, vol. 8, no. 3, pp. 675–689, 2018.

[248] C. K. Batchelor and G. Batchelor, *An introduction to fluid dynamics*. Cambridge university press, 2000.

[249] G. A. Hirn and G. Zeuner, *Analytical and Experimental Exposure of the Heat Metallic Theme*, 1862.

[250] A. Saul and W. Wagner, "A fundamental equation for water covering the range from the melting line to 1273 k at pressures up to 25 000 mpa," *Journal of Physical and Chemical Reference Data*, vol. 18, no. 4, pp. 1537–1564, 1989.

[251] G. A. Sod, "A survey of several finite difference methods for systems of nonlinear hyperbolic conservation laws," *Journal of Computational Physics*, vol. 27, no. 1, pp. 1–31, 1978.

[252] T. G. Keith and J. E. John, *Gas Dynamics*. Pearson Education Inc, 2006.

[253] J. Chandran and A. Salih, "A modified equation of state for water for a wide range of pressure and the concept of water shock tube," *Fluid Phase Equilibria*, vol. 483, pp. 182–188, 2019.

[254] L. Beda, "Chemical thermodynamics," *Journal of thermal analysis*, vol. 44, no. 2, pp. 513–516, Feb 1995.

[255] I. Danaila, P. Joly, S. M. Kaber, and M. Postel, Eds., *Gas Dynamics: The Riemann Problem and Discontinuous Solutions: Application to the Shock Tube Problem*. Springer New York, 2007, pp. 213–233.

[256] R. D. Richtmyer, *A survey of difference methods for non-steady fluid dynamics*. National Center for Atmospheric Research Boulder, Colorado, 1963, vol. 63.

[257] R. MacCormack, "The effect of viscosity in hypervelocity impact cratering, tech," paper AIAA-69-354, Tech. Rep., 1969.

[258] R. W. MacCormack, "Numerical solution of the interaction of a shock wave with a laminar boundary layer," in *Proceedings of the Second International Conference on Numerical Methods in Fluid Dynamics*, M. Holt, Ed. Berlin, Heidelberg: Springer Berlin Heidelberg, 1971, pp. 151–163.

[259] A. J. Jerri, *The Gibbs phenomenon in Fourier analysis, splines and wavelet approximations*. Springer Science & Business Media, 2013, vol. 446.

[260] P. L. Roe, "Some contributions to the modelling of discontinuous flows," in *ams*, 1985, pp. 163–193.

[261] P. L. Roe, "Characteristic-based schemes for the euler equations," *Annual review of fluid mechanics*, vol. 18, no. 1, pp. 337–365, 1986.

[262] H. YEE, "A class of high resolution explicit and implicit shock-capturing method," *NASA-TM 101088*, 1988.

[263] G. van Albada, B. van Leer, W. Roberts *et al.*, "A comparative study of computational methods in cosmic gas dynamics," *Astronomy and Astrophysics*, vol. 108, pp. 76–84, 1982.

[264] S. Jolgam, A. Ballil, A. Nowakowski, and F. Nicolleau, "On equations of state for simulations of multiphase flows," in *World Congress on Engineering 2012. July 4-6, 2012. London, UK.*, vol. 3. International Association of Engineers, 2012, pp. 1963–1968.

[265] F. Hamill, "Sayano shushenskaya accident – presenting a possible direct cause," *International Water Power & Dam Construction*, 2010.

[266] J. Ranson, "Key lessons for preventing hydraulic shock in industrial refrigeration systems," *Safety Bulletin*, 2015.

[267] A. Bergant, A. R. Simpson, and A. S. Tijsseling, "Water hammer with column separation: A historical review," *Journal of fluids and structures*, vol. 22, no. 2, pp. 135–171, 2006.

[268] R. A. Leishear, "Summary of Water Hammer-Induced Pipe Failures," in *Fluid Mechanics, Water Hammer, Dynamic Stresses, and Piping Design*. ASME Press, 01 2013.

[269] E. B. Wylie, V. L. Streeter, and L. Suo, *Fluid transients in systems*. Prentice Hall Englewood Cliffs, NJ, 1993, vol. 1.

[270] A. Bergant and A. S. Tijsseling, *Parameters affecting water hammer wave attenuation, shape and timing*. Citeseer, 2001.

[271] F. B. de Freitas Rachid, R. M. S. da Gama, and H. da Costa Mattos, "Modelling of hydraulic transient in damageable elasto-viscoplastic piping systems," *Applied mathematical modelling*, vol. 18, no. 4, pp. 207–215, 1994.

[272] B. Khudayarov and F. Z. Turaev, "Mathematical simulation of nonlinear oscillations of viscoelastic pipelines conveying fluid," *Applied Mathematical Modelling*, vol. 66, pp. 662–679, 2019.

[273] O. Skulovich, L. Perelman, and A. Ostfeld, "Modeling and optimizing hydraulic transients in water distribution systems," *Procedia Engineering*, vol. 70, pp. 1558–1565, 2014.

[274] E. Fadaei-Kermani, G. Barani, and M. Ghaeini-Hessaroeyeh, "Numerical detection of cavitation damage on dam spillway," *Civil Engineering Journal*, vol. 2, no. 9, pp. 484–490, 2016.

[275] R. A. Leishear, "Water hammer causes water main breaks," *Journal of Pressure Vessel Technology*, vol. 142, no. 2, 2020.

[276] G. Provoost and N. Waterloopkundig Laboratorium (Delft, *Investigation Into Cavitation in a Prototype Pipeline Caused by Water Hammer*, ser. Delft Hydraulics Laboratory. Delft Hydraulics Laboratory, 1976. [Online]. Available: https://books.google.co.in/books?id=ItgbHQAACAAJ

[277] J.-J. Shu, "Modelling vaporous cavitation on fluid transients," *International Journal of Pressure vessels and piping*, vol. 80, no. 3, pp. 187–195, 2003.

[278] D. Covas, I. Stoianov, H. Ramos, N. Graham, Č. Maksimović, and D. Butler, "Water hammer in pressurized polyethylene pipes: conceptual model and experimental analysis," *Urban Water Journal*, vol. 1, no. 2, pp. 177–197, 2004.

[279] A. Kaliatka, E. Uspuras, and M. Vaisnoras, "Benchmarking analysis of water hammer effects using relap5 code and development of rbmk-1500 reactor main circulation circuit model," *Annals of Nuclear Energy*, vol. 34, no. 1-2, pp. 1–12, 2007.

[280] B. Kucienska, J.-M. Seynhaeve, and M. Giot, "Friction relaxation model for fast transient flows application to water hammer in two-phase flow–the waha code," *International journal of multiphase flow*, vol. 34, no. 2, pp. 188–205, 2008.

[281] W. Tian, G. Su, G. Wang, S. Qiu, and Z. Xiao, "Numerical simulation and optimization on valve-induced water hammer characteristics for parallel pump feedwater system," *Annals of Nuclear Energy*, vol. 35, no. 12, pp. 2280–2287, 2008.

[282] A. K. Soares, D. I. Covas, and N. J. Carriço, "Transient vaporous cavitation in viscoelastic pipes," *Journal of Hydraulic Research*, vol. 50, no. 2, pp. 228–235, 2012.

[283] M. Sadafi, A. Riasi, and S. A. Nourbakhsh, "Cavitating flow during water hammer using a generalized interface vaporous cavitation model," *Journal of fluids and structures*, vol. 34, pp. 190–201, 2012.

[284] J. Pinho, M. Lema, P. Rambaud, and J. Steelant, "Multiphase investigation of water hammer phenomenon using the full cavitation model," *Journal of Propulsion and Power*, vol. 30, no. 1, pp. 105–113, 2014.

[285] I. Frigaard, G. Vinay, and A. Wachs, "Compressible displacement of waxy crude oils in long pipeline startup flows," *Journal of non-newtonian fluid mechanics*, vol. 147, no. 1-2, pp. 45–64, 2007.

[286] W. Qu, Y. Xie, Y. Shen, J. Han, M. You, and T. Zhu, "Simulation on the effects of various factors on the motion of ultrasonic cavitation bubble," *Mathematical Modelling of Enineering Problems*, vol. 4, no. 4, pp. 173–178, 2017.

[287] L. Hadj-Taïeb and E. Hadj-Taïeb, "Numerical simulation of transient flows in viscoelastic pipes with vapour cavitation," *International Journal of Modelling and Simulation*, vol. 29, no. 2, pp. 206–213, 2009.

[288] T. Neuhaus, A. Dudlik, and A. S. Tijsseling, "Experiments and corresponding calculations on thermohydraulic pressure surges in pipes," *External research report*, 2005.

[289] A. Dudlik, H.-M. Prasser, A. Apostolidis, and A. Bergant, "Water hammer induced by fast-acting valves: Experimental studies at pilot plant pipework," *Multiphase Science and Technology*, vol. 20, no. 3-4, 2008.

[290] W. Barten, A. Jasiulevicius, A. Manera, R. Macian-Juan, and O. Zerkak, "Analysis of the capability of system codes to model cavitation water hammers: Simulation of umsicht water hammer experiments with trace and relap5," *Nuclear Engineering and Design*, vol. 238, no. 4, pp. 1129–1145, 2008.

[291] S. Chakravarthy, D. Anderson, and M. Salas, "The split coefficient matrix method for hyperbolic systems of gasdynamic equations," in *18th Aerospace Sciences Meeting*, 1980, p. 268.

[292] J. Peng, C. Zhai, G. Ni, H. Yong, and Y. Shen, "An adaptive characteristic-wise reconstruction weno-z scheme for gas dynamic euler equations," *Computers & Fluids*, vol. 179, pp. 34–51, 2019.

[293] P. Romstedt, "A split-matrix method for the numerical solution of two-phase flow equations," *Nuclear science and engineering*, vol. 104, no. 1, pp. 1–9, 1990.

[294] D. Lu, H. Simpson, and A. Gilchrist, "The application of split-coefficient matrix method to transient two phase flows," *International Journal of Numerical Methods for Heat & Fluid Flow*, 1996.

[295] Z. Wang, G. Su, S. Qiu, and W. Tian, "Preliminary study on split coefficient matrix method for two-phase flow equation solving," *Atomic Energy Science and Technology*, vol. 49, no. 6, pp. 1045–1050, 2015.

[296] T. Zhang, Z. Tan, H. Zhang, J. Fan, and Z. Yang, "Axial coupled response characteristics of a fluid-conveying pipeline based on split-coefficient matrix finite difference method," *Zhendong yu Chongji/Journal of Vibration and Shock*, vol. 37, pp. 148–154, 03 2018.

[297] W. F. Silva-Araya and M. H. Chaudhry, "Computation of energy dissipation in transient flow," *Journal of Hydraulic Engineering*, vol. 123, no. 2, pp. 108–115, 1997.

[298] G. Pezzinga, "Quasi-2d model for unsteady flow in pipe networks," *Journal of Hydraulic Engineering*, vol. 125, no. 7, pp. 676–685, 1999.

[299] G. Pezzinga, M. S. Ghidaoui, D. H. Axworthy, M. Zhao, and D. A. McInnis, "Extended thermodynamics derivation of energy dissipation in unsteady pipe flow," *Journal of Hydraulic Engineering*, vol. 127, no. 10, pp. 888–890, 2001.

[300] M. S. Ghidaoui and S. Mansour, "Efficient treatment of the vardy–brown unsteady shear in pipe transients," *Journal of Hydraulic Engineering*, vol. 128, no. 1, pp. 102–112, 2002.

[301] M. S. Ghidaoui, M. Zhao, D. A. McInnis, and D. H. Axworthy, "A review of water hammer theory and practice," *Appl. Mech. Rev.*, vol. 58, no. 1, pp. 49–76, 2005.

[302] K. Nosrati, A. Tahershamsi, and S. H. S. Taheri, "Numerical analysis of energy loss coefficient in pipe contraction using ansys cfx software," *Civil Engineering Journal*, vol. 3, no. 4, pp. 288–300, 2017.

[303] D. H. Axworthy, M. S. Ghidaoui, and D. A. McInnis, "Extended thermodynamics derivation of energy dissipation in unsteady pipe flow," *Journal of Hydraulic Engineering*, vol. 126, no. 4, pp. 276–287, 2000.

[304] M. S. Ghidaoui, "On the fundamental equations of water hammer," *Urban Water Journal*, vol. 1, no. 2, pp. 71–83, 2004.

[305] A. S. Tijsseling and A. Anderson, "The joukowsky equation for fluids and solids," *Eindhoven University of Technology, Eindhoven, The Netherlands, CASA-Report*, no. 0608, 2006.

[306] E. Wahba, "Modelling the attenuation of laminar fluid transients in piping systems," *Applied Mathematical Modelling*, vol. 32, no. 12, pp. 2863–2871, 2008.

[307] T. W. Walters and R. A. Leishear, "When the joukowsky equation does not predict maximum water hammer pressures," *Journal of Pressure Vessel Technology*, vol. 141, no. 6, 2019.

[308] E. K. Vakkilainen, "4 - steam–water circulation design," in *Steam Generation from Biomass*, E. K. Vakkilainen, Ed. Butterworth-Heinemann, 2017, pp. 87 – 114.

[309] O. Arsenyeva, J. Tran, and E. Y. Kenig, "Thermal and hydraulic performance of pillow-plate heat exchangers," in *28th European Symposium on Computer Aided Process Engineering*, ser. Computer Aided Chemical Engineering, A. Friedl, J. J.

Klemeš, S. Radl, P. S. Varbanov, and T. Wallek, Eds. Elsevier, 2018, vol. 43, pp. 181 – 186.

[310] K. Ermis, "Chapter 2.26 - experimental and numerical investigations of condensation heat transfer in multiport tubes," in *Exergetic, Energetic and Environmental Dimensions*, I. Dincer, C. O. Colpan, and O. Kizilkan, Eds. Academic Press, 2018, pp. 657 – 676.

[311] T. Lee, H. Low, D. Nguyen, and W. Neo, "Experimental study of check valves performances in fluid transient," *Proceedings of the Institution of Mechanical Engineers, Part E: Journal of Process Mechanical Engineering*, vol. 223, no. 2, pp. 61–69, 2009.

[312] H. Warda and Y. Elashry, "Towards an improved understanding of water-hammer column-separation due to rapid valve closure," in *Pressure Vessels and Piping Conference*, vol. 49262, 2010, pp. 379–395.

[313] M. Simão, J. Mora-Rodriguez, and H. M. Ramos, "Mechanical interaction in pressurized pipe systems: experiments and numerical models," *Water*, vol. 7, no. 11, pp. 6321–6350, 2015.

[314] G. Balacco, C. Apollonio, and A. F. Piccinni, "Experimental analysis of air valve behaviour during hydraulic transients," *Journal of Applied Water Engineering and Research*, vol. 3, no. 1, pp. 3–11, 2015.

[315] A. Kodura, "An analysis of the impact of valve closure time on the course of water hammer," *Archives of Hydro-Engineering and Environmental Mechanics*, vol. 63, no. 1, pp. 35–45, 2016.

[316] A. Kaliatka and M. Vaisnoras, "Simulation of water hammer experiments using relap5 code," in *Proceedings of the International Conference on Nuclear Energy for New Europe, Bled, Slovenia*, 2005, pp. 541–549.

[317] M. Nikpour, A. Nazemi, A. H. Dalir, F. Shoja, and P. Varjavand, "Experimental and numerical simulation of water hammer," *Arabian Journal for Science and Engineering*, vol. 39, no. 4, pp. 2669–2675, 2014.

[318] W. Al-Taliby, "Modeling force main systems for surge analysis and studying dynamic response due to water hammer," Ph.D. dissertation, 2015.

[319] P. D. Tran, "Pressure transients caused by air-valve closure while filling pipelines," *Journal of Hydraulic Engineering*, vol. 143, no. 2, p. 04016082, 2017.

[320] Z. Lai, Q. Li, B. Karney, S. Yang, D. Wu, and F. Zhang, "Numerical simulation of a check valve closure induced by pump shutdown," *Journal of Hydraulic Engineering*, vol. 144, no. 12, p. 06018013, 2018.

[321] G. Li, "Surge phenomenon during slow valve closures in short pipelines," in *Pipelines 2020*. American Society of Civil Engineers Reston, VA, 2020, pp. 60–67.

[322] S. K. Brockman, "Mechanism of the movements of the atrioventricular valves," *The American journal of cardiology*, vol. 17, no. 5, pp. 682–690, 1966.

[323] B. Bellhouse, "Velocity and pressure distributions in the aortic valve," *Journal of Fluid Mechanics*, vol. 37, no. 3, pp. 587–600, 1969.

[324] C. Lee and L. Talbot, "A fluid-mechanical study of the closure of heart valves," *Journal of Fluid Mechanics*, vol. 91, no. 1, pp. 41–63, 1979.

[325] A. Van Steenhoven and M. Van Dongen, "Model studies of the aortic pressure rise just after valve closure," *Journal of fluid mechanics*, vol. 166, pp. 93–113, 1986.

[326] S. Aluri and K. Chandran, "Numerical simulation of mechanical mitral heart valve closure," *Annals of biomedical engineering*, vol. 29, no. 8, pp. 665–676, 2001.

[327] D. R. Hose, A. J. Narracott, J. M. Penrose, D. Baguley, I. P. Jones, and P. V. Lawford, "Fundamental mechanics of aortic heart valve closure," *Journal of biomechanics*, vol. 39, no. 5, pp. 958–967, 2006.

[328] H. Tang, J. Gao, and Y. Park, "Heart valve closure timing intervals in response to left ventricular blood pressure," 2013.

[329] X.-J. Wang, M. F. Lambert, A. R. Simpson, J. A. Liggett, and J. P. V ı´ tkovskỳ, "Leak detection in pipelines using the damping of fluid transients," *Journal of Hydraulic Engineering*, vol. 128, no. 7, pp. 697–711, 2002.

[330] J. P. Vítkovskỳ, M. F. Lambert, A. R. Simpson, and J. A. Liggett, "Experimental observation and analysis of inverse transients for pipeline leak detection," *Journal of Water Resources Planning and Management*, vol. 133, no. 6, pp. 519–530, 2007.

[331] P. J. Lee, H.-F. Duan, J. Tuck, and M. Ghidaoui, "Numerical and experimental study on the effect of signal bandwidth on pipe assessment using fluid transients," *Journal of Hydraulic Engineering*, vol. 141, no. 2, p. 04014074, 2015.

[332] X. Diao, G. Shen, J. Jiang, Q. Chen, Z. Wang, L. Ni, A. Mebarki, and Z. Dou, "Leak detection and location in liquid pipelines by analyzing the first transient pressure wave with unsteady friction," *Journal of Loss Prevention in the Process Industries*, vol. 60, pp. 303–310, 2019.

[333] J. Bohorquez, B. Alexander, A. R. Simpson, and M. F. Lambert, "Leak detection and topology identification in pipelines using fluid transients and artificial neural networks," *Journal of Water Resources Planning and Management*, vol. 146, no. 6, p. 04020040, 2020.

[334] X. Wang, J. Lin, and M. S. Ghidaoui, "Usage and effect of multiple transient tests for pipeline leak detection," *Journal of Water Resources Planning and Management*, vol. 146, no. 11, p. 06020011, 2020.

[335] A. F. Colombo, P. Lee, and B. W. Karney, "A selective literature review of transient-based leak detection methods," *Journal of hydro-environment research*, vol. 2, no. 4, pp. 212–227, 2009.

[336] M. Mitosek and R. Szymkiewicz, "Wave damping and smoothing in the unsteady pipe flow," *Journal of Hydraulic Engineering*, vol. 138, no. 7, pp. 619–628, 2012.

[337] A. K. Soares, N. Martins, and D. I. Covas, "Investigation of transient vaporous cavitation: experimental and numerical analyses," *Procedia Engineering*, vol. 119, pp. 235–242, 2015.

List of Publications

Refereed Journals

1. Jishnu Chandran R, & A Salih (2019). A modified equation of state for water for a wide range of pressure and the concept of water shock tube, *Fluid Phase Equilibria 483 (2019) 182-188*, Elsevier. DOI: https://doi.org/10.1016/j.fluid.2018.11.032

2. Jishnu Chandran R, & A Salih (2020). An adaptively-damped compressible-liquid model for non-cavitating hydraulic surges, *International Journal of Engineering, Transactions A: Basics 33 (2020)10 2047-2056*, Materials and Energy Research Center. DOI: 10.5829/IJE.2020.33.10A.23

3. Jishnu Chandran R, & A Salih (2020). A pressure-based compressible-liquid flow model for computation of instantaneous valve closure in pipes, *Science and Technology Journal 7 (2019)2 60-66*, Mizoram University.
DOI: https://doi.org/10.22232/stj.2019.07.02.07

4. Jishnu Chandran R, & A Salih (2020). A comparative performance analysis of HLLC and AUSM^{+}-up Riemann Solvers, *Cankaya University Journal of Science and Engineering 17 (2020)2 108-117*, Cankaya University.

5. Jishnu Chandran R, & A Salih (2021). Development of a benchmark solution in compressible liquid flows: Analytical solution to the water shock tube problem, *Journal of Thermal Analysis and Calorimetry*, Springer. DOI: https://doi.org/10.1007/s10973-021-10871-7

Refereed Conferences

1. Jishnu Chandran R, & A Salih (2016). A Comparative Study of AUSM Scheme with Some Common Finite Difference Schemes in Solving One-Dimensional Shock-

Tube Problem, *Proceedings of the 6^{th} International and $43^{r}d$ National Conference on Fluid Mechanics and Fluid Power, 2016, 1-3.*

2. Jishnu Chandran R, & A Salih (2017). Water Shock tube simulation with Tait equation of state, *Proceedings of the 24^{th} National and 2^{nd} International ISHMT-ASTFE Heat and Mass Transfer Conference*,ISHMT Digital Library. Begell House Inc., 2017, 2203-2209. DOI: 10.1615/IHMTC-2017.3080

3. Jishnu Chandran R, & A Salih (2018). Equivalence of Density-Based and a Customized Pressure-Based Approach for Compressible Modelling of Instant Valve Closure in Irrigation Pipes, *Proceedings of the 7^{th} International and $45^{t}h$ National Conference on Fluid Mechanics and Fluid Power, 2018, 1-4.*

Communicated Works

1. Jishnu Chandran R, & A Salih (2021). The Adaptive damping technique: Improving the simulation accuracy of hydraulic transients, *International Journal of Mathematical, Engineering and Management Sciences*, IJMEMS.

2. Jishnu Chandran R, & A Salih (2021). Numerical Studies on Liquid Shock Tube Problem, *International Journal of Thermal Sciences*, Elsevier.

Appendix A

The HLLC and AUSM$^+$-up algorithms

The details of the algorithms of HLLC and AUSM$^+$-upare briefly described here. The interested reader may refer to [128] and [186] for a more detailed description of the HLLC and the AUSM$^+$-up schemes respectively.

A.1 HLLC Scheme

The HLLC scheme can be written in the following generic way:

$$U_i^{n+1} = U_i^n + \frac{\Delta t}{\Delta x}\left(F_{i+\frac{1}{2}}^{hllc} - F_{i-\frac{1}{2}}^{hllc}\right) \tag{A.1}$$

where

$$F_{i+\frac{1}{2}}^{hllc} = \begin{cases} F_{Li+\frac{1}{2}}, & \text{if } 0 \le S_{Li+\frac{1}{2}} \\ F_{*Li+\frac{1}{2}}, & \text{if } S_{Li+\frac{1}{2}} \le 0 \le S_{*i+\frac{1}{2}} \\ F_{*Ri+\frac{1}{2}}, & \text{if } S_{*i+\frac{1}{2}} \le 0 \le S_{Ri+\frac{1}{2}} \\ F_{Ri+\frac{1}{2}}, & \text{if } S_{Ri+\frac{1}{2}} \le 0 \end{cases} \tag{A.2}$$

To start with, the averaged value of the speed of sound and density at the cell interfaces is computed:

$$\overline{a}_{i+\frac{1}{2}} = \frac{a_i + a_{i+1}}{2} \quad \text{and} \quad \overline{\rho}_{i+\frac{1}{2}} = \frac{\rho_i + \rho_{i+1}}{2} \tag{A.3}$$

The pressure from Primitive Variable Riemann Solver (PVRS) is obtained at each cell interface as follows

$$P_{pvrs_{i+\frac{1}{2}}} = \frac{1}{2}(p_i + p_{i+1}) - \frac{1}{2}(u_{i+1} - u_i)\overline{\rho}_{i+\frac{1}{2}}\overline{a}_{i+\frac{1}{2}} \tag{A.4}$$

from which the pressure in the starred region is computed:

$$P_{*i+\frac{1}{2}} = \max(P_{pvrs_{i+\frac{1}{2}}}, 0). \tag{A.5}$$

Based on the comparison of the pressure at each point, with the starred pressure defined there, the quantities q_L and q_R are defined as follows:

$$q_{Li+\frac{1}{2}} = \begin{cases} 1, & \text{if } P_{*i+\frac{1}{2}} \leq p_i \\ \left[1 + \dfrac{\gamma+1}{2\gamma}\left(\dfrac{P_{*i+\frac{1}{2}}}{p_i} - 1\right)\right]^{\frac{1}{2}}, & \text{if } P_{*i+\frac{1}{2}} > p_i \end{cases} \tag{A.6}$$

$$q_{Ri+\frac{1}{2}} = \begin{cases} 1, & \text{if } P_{*i+\frac{1}{2}} \leq p_{i+1} \\ \left[1 + \dfrac{\gamma+1}{2\gamma}\left(\dfrac{P_{*i+\frac{1}{2}}}{p_{i+1}} - 1\right)\right]^{\frac{1}{2}}, & \text{if } P_{*i+\frac{1}{2}} > p_{i+1} \end{cases} \tag{A.7}$$

The wave speed estimates for the two signal waves i.e., the left and right traveling waves respectively are obtained through the relations

$$S_{Li+\frac{1}{2}} = u_i - a_i q_{Li+\frac{1}{2}} \tag{A.8}$$

$$S_{Ri+\frac{1}{2}} = u_{i+1} - a_{i+1} q_{Ri+\frac{1}{2}} \tag{A.9}$$

The intermediate wave speed S_* is then computed in terms of S_L and S_R using the following expression

$$S_{*i+\frac{1}{2}} = \frac{p_{i+1} - p_i + \rho_i u_i (S_{Li+\frac{1}{2}} - u_i) - \rho_{i+1} u_{i+1} (S_{Ri+\frac{1}{2}} - u_{i+1})}{\rho_i (S_{Li+\frac{1}{2}} - u_i) - \rho_{i+1} (S_{Ri+\frac{1}{2}} - u_{i+1})} \tag{A.10}$$

Next, we compute the following vectors at each cell interface:

$$U_{Li+\frac{1}{2}} = \begin{bmatrix} \rho_i \\ \rho_i u_i \\ \rho e_i \end{bmatrix} \tag{A.11}$$

$$U_{*Li+\frac{1}{2}} = \rho_i \left(\frac{S_{Li+\frac{1}{2}} - u_i}{S_{Li+\frac{1}{2}} - S_{*i+\frac{1}{2}}} \right) \begin{bmatrix} 1 \\ S_{*i+\frac{1}{2}} \\ e_i + (S_{*i+\frac{1}{2}} - u_i) \left[S_{*i+\frac{1}{2}} + \frac{p_i}{\rho_i (S_{Li+\frac{1}{2}} - u_i)} \right] \end{bmatrix} \tag{A.12}$$

$$U_{*Ri+\frac{1}{2}} = \rho_{i+1} \left(\frac{S_{Ri+\frac{1}{2}} - u_{i+1}}{S_{Ri+\frac{1}{2}} - S_{*i+\frac{1}{2}}} \right) \begin{bmatrix} 1 \\ S_{*i+\frac{1}{2}} \\ e_{i+1} + (S_{*i+\frac{1}{2}} - u_{i+1}) \left[S_{*i+\frac{1}{2}} + \frac{p_{i+1}}{\rho_{i+1} (S_{Ri+\frac{1}{2}} - u_{i+1})} \right] \end{bmatrix} \tag{A.13}$$

$$U_{Ri+\frac{1}{2}} = \begin{bmatrix} \rho_{i+1} \\ \rho_{i+1} u_{i+1} \\ \rho_{i+1} e_{i+1} \end{bmatrix} \tag{A.14}$$

Finally, various fluxes are computed as follows:

$$F_{Li+\frac{1}{2}} = \begin{bmatrix} \rho_i u_i \\ \rho_i u_i^2 + p_i \\ u_i (\rho_i e_i + p_i) \end{bmatrix} \tag{A.15}$$

$$F_{*Li+\frac{1}{2}} = F_{Li+\frac{1}{2}} + S_{Li+\frac{1}{2}} (U_{*Li+\frac{1}{2}} - U_{Li+\frac{1}{2}}) \tag{A.16}$$

$$F_{*Ri+\frac{1}{2}} = F_{Ri+\frac{1}{2}} + S_{Ri+\frac{1}{2}} (U_{*Ri+\frac{1}{2}} - U_{Ri+\frac{1}{2}}) \tag{A.17}$$

$$F_{Ri+\frac{1}{2}} = \begin{bmatrix} \rho_{i+1} u_{i+1} \\ \rho_{i+1} u_{i+1}^2 + p_{i+1} \\ u_{i+1} (\rho_{i+1} e_{i+1} + p_{i+1}) \end{bmatrix} \tag{A.18}$$

Based on the signal speeds the corresponding fluxes are chosen as shown in Equation(A.2).

A.2 AUSM$^+$-up Scheme

As in the case of basic AUSM scheme, the generic form of AUSM$^+$-up algorithm may be written as

$$U_i^{n+1} = U_i^n - \frac{\Delta t}{\Delta x}\left(F_{i+\frac{1}{2}}^n - F_{i-\frac{1}{2}}^n\right) \tag{A.19}$$

where

$$F_{i+\frac{1}{2}} = F_{i+\frac{1}{2}}^{(c)} + F_{i+\frac{1}{2}}^{(p)} \tag{A.20}$$

The inviscid flux vector F is split into two physically distinct parts; the convective part, $F^{(c)}$ and the pressure part, $F^{(p)}$. The equations for $F^{(c)}$ and $F^{(p)}$ are given by

$$F_{i+\frac{1}{2}}^{(c)} = u_{i+\frac{1}{2}} \begin{bmatrix} \rho \\ \rho u \\ \rho e + p \end{bmatrix}_{L/R} = M_{i+\frac{1}{2}} a_{i+\frac{1}{2}} \begin{bmatrix} \rho \\ \rho u \\ \rho e + p \end{bmatrix}_{L/R} \tag{A.21}$$

$$F_{i+\frac{1}{2}}^{(p)} = \begin{bmatrix} 0 \\ p_{i+\frac{1}{2}} \\ 0 \end{bmatrix} \tag{A.22}$$

Speed of sound and Mach number at each node are given by the relations

$$a_i = \sqrt{\gamma \frac{p_i}{\rho_i}} \quad \text{and} \quad M_i = \frac{u_i}{a_i}. \tag{A.23}$$

The speed of sound at each cell interfaces is calculated as either simple average,

$$a_{i+\frac{1}{2}} = \frac{a_i + a_{i+1}}{2} \tag{A.24}$$

or from the critical speed of sound using the isoenergetic equation

$$a_i^* = \sqrt{\frac{2\gamma}{\gamma+1}\frac{p_i}{\rho_i} + \frac{\gamma-1}{\gamma+1}u_i^2} \tag{A.25}$$

$$\hat{a}_i = \frac{(a_i^*)^2}{\max(a_i^*, |u_i|)} \tag{A.26}$$

$$a_{i+\frac{1}{2}} = \min(\hat{a}_i, \hat{a}_{i+1}) \tag{A.27}$$

and the following quantities are defined and computed at each cell interface:

$$M_{Li+\frac{1}{2}} = \frac{u_i}{a_{i+\frac{1}{2}}}, \quad M_{Ri+\frac{1}{2}} = \frac{u_{i+1}}{a_{i+\frac{1}{2}}} \tag{A.28}$$

$$\overline{M}_{i+\frac{1}{2}} = \frac{1}{2}\left(M^2_{Li+\frac{1}{2}} + M^2_{Ri+\frac{1}{2}}\right) \tag{A.29}$$

The values of M_0 at cell-interface can now be computed as

$$M^2_{0\,i+\frac{1}{2}} = \min\left(1, \max(\overline{M}^2_{i+\frac{1}{2}}, M^2_\infty)\right) \tag{A.30}$$

where $M_\infty = 1.0$ for the given pressure ratio across the diaphragm. The factor f_a at each cell interface is then computed from relation

$$f_{a i+\frac{1}{2}} = M_{0 i+\frac{1}{2}}(2 - M_{0 i+\frac{1}{2}}) \tag{A.31}$$

The interface Mach number and interface pressure terms are both computed using a comparatively lengthy procedure through the following set of relations. First we define the interface Mach number:

$$M_{i+\frac{1}{2}} = \mu^+_{(4)}\left(M_{Li+\frac{1}{2}}\right) + \mu^-_{(4)}\left(M_{Ri+\frac{1}{2}}\right) + M_{Pi+\frac{1}{2}} \tag{A.32}$$

where, the split Mach numbers are fourth degree $\mu^\pm_{(4)}$ polynomial functions of $M_{L/R}$. They are defined as follows:

$$\mu^\pm_{(4)}(M) = \begin{cases} \dfrac{1}{2}(M \pm |M|), & \text{if } |M| \geq 1.0, \\ \pm\dfrac{1}{4}(M \pm 1)^2\left[1 + 4\beta(M \mp 1)^2\right], & \text{otherwise} \end{cases} \tag{A.33}$$

$$M_{Pi+\frac{1}{2}} = -K_P \max\left(1 - \sigma\overline{M}^2_{i+\frac{1}{2}}, 0\right)\frac{p_{i+1} - p_i}{\rho_{i+\frac{1}{2}} a^2_{i+\frac{1}{2}}} \tag{A.34}$$

where

$$0 \leq K_P \leq 1, \quad \sigma \leq 1, \quad \beta = \frac{1}{8}, \quad \rho_{i+\frac{1}{2}} = \frac{\rho_i + \rho_{i+1}}{2}. \tag{A.35}$$

The pressure diffusion term M_P in the computation is introduced with the motive to improve the calculations at low Mach numbers and for multiphase flows.

The interface pressure term is then defined as

$$P_{i+\frac{1}{2}} = P^{+}_{(5)}\left(M_{Li+\frac{1}{2}}\right) p_i + P^{-}_{(5)}\left(M_{Ri+\frac{1}{2}}\right) p_{i+1} + P_{Ui+\frac{1}{2}} \tag{A.36}$$

where the fifth degree polynomial $P^{\pm}_{(5)}$ function of $M_{L/R}$ are used as given below:

$$P^{\pm}_{(5)}(M) = \begin{cases} \dfrac{1}{2}\left(1 \pm \dfrac{M}{|M|}\right), & \text{if } |M| \geq 1.0, \\ \pm\dfrac{1}{4}(M \pm 1)^2\left[(\pm 2 - M) + 4\alpha M(M \mp 1)^2\right], & \text{otherwise} \end{cases} \tag{A.37}$$

$$P_{Ui+\frac{1}{2}} = -K_U P^{+}_{(5)}\left(M_{Li+\frac{1}{2}}\right) P^{-}_{(5)}\left(M_{Ri+\frac{1}{2}}\right)(\rho_i + \rho_{i+1})(f_{a i+\frac{1}{2}} a_{i+\frac{1}{2}})(u_{i+1} - u_i) \tag{A.38}$$

where

$$0 \leq K_U \leq 1, \quad \alpha_{i+\frac{1}{2}} = \frac{3}{16}\left(-4 + 5 f^{\,2}_{a_{i+\frac{1}{2}}}\right) \tag{A.39}$$

A diffusion term P_U is included in the calculation of interface pressure.

The final inter cell flux is given by

$$F_{i+\frac{1}{2}} = F^{(c)}_{i+\frac{1}{2}} + F^{(p)}_{i+\frac{1}{2}} \tag{A.40}$$

where

$$F^{(c)}_{i+\frac{1}{2}} = \begin{cases} M_{i+\frac{1}{2}} a_{i+\frac{1}{2}} \begin{bmatrix} \rho \\ \rho u \\ \rho e + p \end{bmatrix}_i, & \text{if } M_{i+\frac{1}{2}} \geq 0, \\ M_{i+\frac{1}{2}} a_{i+\frac{1}{2}} \begin{bmatrix} \rho \\ \rho u \\ \rho e + p \end{bmatrix}_{i+1}, & \text{otherwise} \end{cases} \tag{A.41}$$

$$F^{(p)}_{i+\frac{1}{2}} = \begin{bmatrix} 0 \\ P_{i+\frac{1}{2}} \\ 0 \end{bmatrix} \tag{A.42}$$

Appendix B

Analytical Solution to One-Dimensional Shock Tube (SOD's) Problem

The complete steps involved in the analytical solution procedure for a one-dimensional gas shock tube is provided here. The exact solution to the one-dimensional shock tube problem includes determining the extent of each of the five zones in space at any given point of time from the rupture of the diaphragm. The zones once identified in space, the corresponding set of relations is applied at each region. Determination of the zone interfaces, however, requires the shock and flow velocity in zone '1', both of which is computed from the shock pressure ratio (p_1/p_R). The calculation of shock pressure ratio requires the solution of the implicit equation

$$\frac{p_L}{p_R} = \frac{p_1}{p_R}\left[1 - \frac{(\gamma-1)\left(\frac{a_R}{a_L}\right)\left(\frac{p_1}{p_R}-1\right)}{\sqrt{2\gamma}\sqrt{2\gamma+(\gamma+1)\left(\frac{p_1}{p_R}-1\right)}}\right]^{-2\gamma/(\gamma-1)} \tag{B.1}$$

where (p_L/p_R) is the initial pressure ratio and (a_R/a_L) is the initial ratio of sound speed across the diaphragm before rupture. Equation (B.1) cannot be rewritten explicitly for the shock pressure ratio (p_1/p_R) and is hence solved iteratively using the Regula-Falsi method.

Shock speed (S) is obtained from the shock pressure ratio using the relation

$$S = a_R\sqrt{\left(\frac{\gamma+1}{2\gamma}\right)\frac{p_1}{p_R} + \left(\frac{\gamma-1}{2\gamma}\right)}. \tag{B.2}$$

The symbols p, V, ρ, a, and ε represents the fluid pressure, velocity, density, sound speed, and the specific internal energy respectively. The zone notation is used as subscripts with

each of these properties to denote the zone over which it is defined. The fluid properties over zone '1' is computed as follows.
The pressure,

$$p_1 = \left(\frac{p_1}{p_R}\right) p_R \tag{B.3a}$$

where, the shock pressure ratio is from the solution of equation (B.1).
Fluid velocity

$$V_1 = \frac{a_R}{\gamma}\left(\frac{p_1}{p_R} - 1\right)\sqrt{\frac{\left(\frac{2\gamma}{\gamma+1}\right)}{\frac{p_1}{p_R}\left(\frac{\gamma-1}{\gamma+1}\right)}}, \tag{B.3b}$$

the density ρ_1 is computed from the following form of the Rankine-Hugoniot relation

$$\frac{\rho_1}{\rho_R} = \frac{\frac{(\gamma+1)}{(\gamma-1)}\frac{p_1}{p_R} + 1}{\frac{(\gamma+1)}{(\gamma-1)} + \frac{p_1}{p_R}}, \tag{B.3c}$$

the speed of sound

$$a_1 = \sqrt{\frac{\gamma p_1}{\rho_1}}, \tag{B.3d}$$

and the specific internal energy

$$\varepsilon_1 = \left(\frac{1}{\gamma-1}\right)\frac{p_1}{\rho_1}. \tag{B.3e}$$

The fluid pressure and velocity are equalized over the zones 1 and 2 and hence for zone 2 only the density and internal energy values need to be computed. The set of relations for zone 2 are

$$p_2 = p_1 \tag{B.4a}$$

$$V_2 = V_1 \tag{B.4b}$$

$$\rho_2 = \rho_L\left(\frac{p_2}{p_L}\right)^{\frac{1}{\gamma}} \tag{B.4c}$$

$$a_2 = \sqrt{\frac{\gamma p_2}{\rho_2}} \tag{B.4d}$$

$$\varepsilon_2 = \left(\frac{1}{\gamma-1}\right)\frac{p_2}{\rho_2} \tag{B.4e}$$

The properties inside the expansion wave i.e., zone 'E' are computed using another set of relations. Unlike the other zones, the property values in zone 'E' are not constant throughout, instead, they vary linearly in space. The set of relations applicable across the expansion wave is

$$V_E(x,t) = \frac{2}{\gamma+1}\left(a_L + \frac{x-x_0}{t}\right) \tag{B.5a}$$

$$a_E(x,t) = a_L - (\gamma-1)\frac{V_E}{2} \tag{B.5b}$$

$$p_E(x,t) = p_L\left(\frac{a_E}{a_L}\right)^{\frac{2\gamma}{\gamma-1}} \tag{B.5c}$$

$$\rho_E(x,t) = \gamma\frac{p_E}{{a_E}^2} \tag{B.5d}$$

$$\varepsilon_E(x) = \frac{1}{\gamma-1}\frac{p_E}{\rho_E} \tag{B.5e}$$

where t is the time elapsed since the diaphragm rupture. The unaffected zones on the extreme left and right are marked as 'L' and 'R' respectively. The computation of properties for these two zones are not required as the expansion wave and shock are yet to reach zone 'L' and 'R' respectively and thus the initial conditions in these regions continue uninterrupted. Therefore, for zone 'L' the property values are p_L, ρ_L, V_L, a_L, and ε_L and that for zone 'R' are p_R, ρ_R, V_R, a_R, and ε_R.

It may be noted that the property values at the different zones do not complete the analytical solution. The extent of each zone in space also needs to be determined. This is achieved by computing the values of x_1, x_2, x_3, and x_4 with respect to the initial position of diaphragm x_0. The relations used for the same are:

$$x_1 = x_0 - a_L t \tag{B.6a}$$

$$x_2 = x_0 + (V_2 - a_2)t \tag{B.6b}$$

$$x_3 = x_0 + V_2 t \tag{B.6c}$$

$$x_4 = x_0 + St \tag{B.6d}$$

where S is the shock speed computed using equation (B.2). The structure of solution for

the entire domain is thus,

$$W(x) = \begin{cases} W_L & \text{if } x < x_1 \\ W_E & \text{if } x_1 \leq x < x_2 \\ W_2 & \text{if } x_2 \leq x < x_3 \\ W_1 & \text{if } x_3 \leq x < x_4 \\ W_R & \text{if } x_4 \leq x \end{cases} \tag{B.7a}$$

where W is the vector of flow property variable defined as

$$W_k = \begin{bmatrix} p_k \\ \rho_k \\ V_k \\ a_k \\ \varepsilon_k \end{bmatrix} \quad , \quad k = R, 1, 2, E, L \tag{B.7b}$$